Università Politecnica delle Marche

Doctoral School of Engineering Sciences

Industrial Engineering - curriculum in Mechanical Engineering

Exploring State-Space Substructuring for time-domain dynamic substructuring applications

Rafael da Silva Oliveira Dias

Advisors:
Prof. Milena Martarelli
Prof. Paolo Chiariotti

Abstract

This thesis aims at developing novel methodologies to mitigate the limitations of the state-of-the art State-Space Substructuring (SSS) techniques and of the state-of-the-art approaches to estimate state-space models from experimentally acquired data. Moreover, we also aim at demonstrating the benefit of using state-space models and SSS methods to tackle time-domain Transfer Path Analysis (TPA) applications.

In this thesis, the dual SSS formulation (also, denoted Lagrange Multiplier State-Space Substructuring method (LM-SSS)) is extended to directly perform dynamic substructuring (DS) operations with displacement and velocity state-space models. A novel coupling form, tagged Unconstrained Coupling Form (UCF), specially tailored to perform DS operations with LM-SSS is derived. With respect to the coupling forms previously presented in literature, UCF holds the advantages of only requiring the computation of a single nullspace and not demanding the typical difficult selection of a subspace from a nullspace. Then, novel post-processing procedures to eliminate the redundant states originated from the performance of DS operations with LM-SSS are proposed to enable the computation of minimal-order coupled models. An additional post-processing procedure is presented to avoid a manual elimination of the redundant degrees of freedom (DOFs) of the coupled state-space models computed with LM-SSS. By comparing LM-SSS enhanced by the proposed post-processing procedures with two state-of-the-art approaches, it is straightforward that LM-SSS entails the advantages of both, without presenting any of their drawbacks. Subsequently, a novel primal state-space assembly formulation is derived. Afterwards, a novel SSS technique, named LM-SSS via compatibility relaxation, is developed to allow the inclusion of connecting elements (CEs) into SSS operations via compatibility relaxation. Post-processing procedures to eliminate the extra states originated from the performance of coupling operations with this method are also derived, enabling the computation of minimal-order coupled models. A discussion on how to compute models of CEs to be used with LM-SSS via compatibility relaxation in analytical, numerical and experimental contexts is conducted. To estimate these models in an experimental context, the state-space realization of the Inverse Substructuring (IS) method is derived.

Then, a novel method to impose Newton's second law on estimated state-space models that does not rely on the use of undamped residual compensation modes (RCMs) is introduced. Thereby, this technique enables the computation of models strictly verify-

ing this physical law that are suitable for being used in time-domain analysis. Besides this benefit, by comparing this method with a state-of-the-art approach, it is evident that the method here derived holds the additional advantage of permitting the enforcement of Newton's second law by using RCMs presenting lower natural frequencies. Subsequently, a novel strategy to impose stability on unstable coupled models resultant from the performance of DS operations with non-passive models is proposed. This approach has the important advantage of not necessarily rely on iterative algorithms.

Afterwards, the developed methodologies are validated on numerical and experimental substructuring cases. The identified state-space models representative of the substructures/assemblies under study showed to be highly accurate, while respecting Newton's second law. This clearly demonstrates the robustness of the proposed approach to force state-space models to obey Newton's second law. Reliable decoupling/coupling results are obtained with LM-SSS enhanced by the developed post-processing procedures and by using the estimated models transformed into UCF. The primal state-space assembly formulation also showed to lead to accurate primally assembled/disassembled results. Moreover, the state-space realization of IS showed to be capable of computing reliable models representative of the CEs, provided that they verify the underlying assumptions of IS. The LM-SSS via compatibility relaxation method also demonstrated to be able to accurately include the models of the CEs identified with the state-space realization of IS into the coupling operations. On top of this, it is evident that the proposed approach to impose stability on unstable coupled state-space models is reliable. Indeed, it turned out to lead to the determination of accurate stable coupled models from unstable coupled models resultant from the performance of several DS operations.

Then, a local approach to compute interpolating Linear Parameter-Varying (LPV) models is presented and validated on numerical and experimental examples. The state-space realizations of the matrix-inverse classical Transfer Path Analysis (TPA) and of the in-situ component-based TPA methods are presented. Subsequently, novel applications of LPV models in TPA are proposed and validated on an analytical assembly made of a source and a passive system. The dynamics of both systems is time-dependent. In a first instance, an interpolating LPV model describing the dynamics of the passive system is used with the matrix-inverse classical TPA method to estimate the time-domain connecting force acting on the interface between the source and the passive system. It is found that the estimated connecting force is accurate and can be used to perform reliable estimations of the responses on DOFs belonging to the passive system. Then, interpolated models computed from the LPV models describing the dynamics of the source and passive systems are coupled at each time-sample by using LM-SSS to obtain coupled models representative of the dynamics of the assembled structure. These coupled models are used with the in-situ component-based TPA method to estimate the time-domain equivalent force of the source. It is found that the estimated equivalent force is accurate and can be used to perform reliable estimations of the responses on the passive side of assemblies made of the same source connected to any passive system.

Sommario

Questa tesi mira a sviluppare nuove metodologie per mitigare i limiti presenti nello stato dell'arte in relazione alle tecniche di State-Space Substructuring (SSS) e degli approcci per stimare i modelli State-Space da dati acquisiti sperimentalmente. Inoltre, si vuole dimostrare il vantaggio dell'uso dei modelli state-space e dei metodi SSS per affrontare applicazioni Transfer Path Analysis (TPA) nel dominio del tempo.

In questa tesi, la formulazione SSS duale (anche denominata Lagrange Multiplier State-Space Substructuring (LM-SSS)) viene estesa per eseguire direttamente operazioni di dynamic substructuring (DS) con modelli state-space di spostamento e velocità. Viene derivata una nuova forma di accoppiamento, denominata Unconstrained Coupling Form (UCF), appositamente studiata per eseguire operazioni DS con LM-SSS. Rispetto alle forme di accoppiamento precedentemente discusse in letteratura, la UCF presenta il vantaggio di richiedere il calcolo di un solo nullspace e di non richiedere la tipica e difficile selezione di un sottospazio da un nullspace. Vengono poi discusse nuove procedure di post-processing per eliminare gli stati ridondanti derivanti dall'esecuzione di operazioni DS con LM-SSS. In questo modo, è possibile calcolare modelli accoppiati di ordine minimo. Viene presentata un'ulteriore procedura di post-processing per evitare l'eliminazione manuale dei gradi di libertà (DOF) ridondanti dei modelli accoppiati con LM-SSS. Confrontando LM-SSS, potenziato dalle procedure di post-processing proposte, con due approcci considerati ad aggi il reiferimento di letteratura, è evidente che LM-SSS presenta i vantaggi di entrambi, senza presentare alcuno dei loro svantaggi. Successivamente, viene derivata una nuova formulazione denominata primal state-space assembly. In seguito, viene sviluppata una nuova tecnica SSS, denominata LM-SSS via compatibility relaxation, per consentire l'inclusione degli elementi di connessione (CE) nelle operazioni SSS tramite compatibility relaxation. Vengono inoltre derivate procedure di post-processing per eliminare gli stati extra originati dall'esecuzione di operazioni di accoppiamento con questo metodo, consentendo il calcolo di modelli accoppiati di ordine minimo. Si discute su come calcolare modelli di CE da utilizzare con LM-SSS tramite il rilassamento di compatibilità in contesti analitici, numerici e sperimentali. Per stimare questi modelli in un contesto sperimentale, è stata derivata una realizzazione state-space del metodo Inverse Substructuring (IS).

Viene poi introdotto un nuovo metodo per imporre la seconda legge di Newton su modelli state-space che non si basa sull'uso di modi di compensazione residui (RCM)

non smorzati. In questo modo, è possibile calcolare modelli che verificano questa legge fisica e che sono adatti a essere utilizzati nell'analisi del dominio del tempo. Oltre a questo vantaggio, confrontando questo metodo con lo stato dell'arte, è evidente che il metodo qui derivato ha l'ulteriore vantaggio di consentire l'applicazione della seconda legge di Newton utilizzando RCM che presentano frequenze naturali più basse. Successivamente, viene proposta una nuova strategia per imporre la stabilità ai modelli accoppiati instabili risultanti dall'esecuzione di operazioni DS con modelli non passivi. Questo approccio ha l'importante vantaggio di non basarsi necessariamente su algoritmi iterativi.

Successivamente, le metodologie sviluppate sono state validate su casi di studio numerici e sperimentali. I modelli state-space identificati, rappresentativi delle sottostrutture/assiemi oggetto di studio, si sono dimostrati altamente accurati, pur rispettando la seconda legge di Newton. Ciò dimostra la robustezza dell'approccio proposto per forzare i modelli state-space a rispettare la seconda legge di Newton. Risultati affidabili di disaccoppiamento/accoppiamento si ottengono con LM-SSS migliorato dalle procedure di post-processing sviluppate e utilizzando i modelli stimati trasformati in UCF. La formulazione primal state-space assembly ha dimostrato di portare a risultati accurati primal assembled/disassembled. Inoltre, la realizzazione state-space di IS ha dimostrato di essere in grado di calcolare modelli affidabili rappresentativi degli CE, a condizione di verificare le ipotesi di base di IS. Il metodo di rilassamento della compatibilità LM-SSS ha anche dimostrato di essere in grado di includere accuratamente i modelli degli CE identificati con la formulazione state-space di IS nelle operazioni di accoppiamento. Inoltre, è evidente che l'approccio proposto per imporre la stabilità ai modelli state-space accoppiati instabili porta alla determinazione di modelli di coppia stabili accurati da modelli state-space accoppiati instabili risultanti dall'esecuzione di diverse operazioni di DS.

Viene quindi presentato un approccio locale per il calcolo di modelli interpolanti a variazione di parametri lineari (LPV), validato su esempi numerici e sperimentali. Vengono presentate le formulazioni state-space dei metodi matrix-inverse classical TPA e in-situ component-based TPA. Successivamente, viene proposta e validata una nuova applicazione dei modelli LPV nella TPA su una struttura assemblata analitica composta da una sorgente e da un sistema passivo. La dinamica di entrambi i sistemi è tempovariante. In un primo momento, un modello LPV interpolante che descrive la dinamica del sistema passivo viene utilizzato con il metodo matrix-inverse classical TPA per stimare la forza di connessione nel dominio del tempo che agisce sull'interfaccia tra la sorgente e il sistema passivo. La forza di connessione che si ottiene è accurata e può essere utilizzata per eseguire stime affidabili delle risposte sui DOF appartenenti al sistema passivo. Quindi, i modelli interpolati calcolati dai modelli LPV che descrivono la dinamica della sorgente e dei sistemi passivi vengono accoppiati ad ogni campione temporale utilizzando LM-SSS per ottenere modelli accoppiati rappresentativi della dinamica della struttura assemblata. Questi modelli accoppiati vengono utilizzati con il

metodo in-situ component based TPA per stimare la forza equivalente della sorgente nel dominio del tempo. Si scopre che la forza equivalente stimata è accurata e può essere utilizzata per eseguire stime affidabili delle risposte sul lato passivo degli assiemi costituiti dalla stessa sorgente collegata a qualsiasi sistema passivo.

Acknowledgements

The present PhD thesis represents the outcome of the research activities performed at the Polytechnic University of Marche over the last three years. This journey turned out to be an amazing adventure that provided me the opportunity to perform research on interesting mechanical engineering topics and to incredibly extend my network. Yet, this experience would not have been so pleasant without the support of many people. Thus, it is now the moment to thank them all.

First of all, I would like to acknowledge my supervisors, Prof. Milena Martarelli and Prof. Paolo Chiariotti, for giving me the opportunity to work in such an amazing and challenging project and for their supervision and guidance throughout my PhD. A big thanks goes also to all the colleagues of the Mechanical and Thermal measurements group at Polytechnic University of Marche.

I would also like to express gratitude to Siemens Software NV, especially Mr. Fabio Bianciardi and Dr. Mahmoud El-Khafafy, for their supervision and guidance during my secondments. Moreover, I want to acknowledge BMW Group, especially Dr. Arthur Hülsmann, for his support during my research stay.

The support of the European Commission through the Marie Sklodowska-Curie project ECO-DRIVE (Grant Agreement n° 858018) is also gratefully acknowledge. A big thanks goes as well to all the research fellows involved in this project.

Finally, I would also like to thank my family and my girlfriend Inês for their endless patience and support throughout this journey.

Rafael da Silva Oliveira Dias
Ancona, Italy, November 2023

Contents

List of Figures

List of Tables

Nomenclature

Acronyms

AKF   Augmented Kalman Filter

CE   Connecting Element

CMS   Component Mode Synthesis

DOF   Degree of freedom

DS   Dynamic Substructuring

EMA   Experimental Modal Analysis

FBS   Frequency Based Substructuring

FOC   Fixed operating condition

FOH   First-order-hold

FRF   Frequency Response Function

IDM   Interface Deformation Mode

IS   Inverse Substructuring

LM-FBS Lagrange Multiplier Frequency-Based Substructuring

LM-SSS Lagrange Multiplier State-Space Substructuring

LPV   Linear Parameter-Varying

LSFD   Least-squares frequency domain

LTI   Linear Time-Invariant

MCFS   Modal Constraints for Fixture and Subsystem

MIMO   Multiple input multiple output

ML-MM   Maximum Likelihood Modal Model method

MVU   Minimum-Variance Unbiased estimator

OPAX Operational Path Analysis with eXogenous Inputs

OTPA Operational Transfer Path Analysis

pLSCF Polyreference Least-Squares Complex Frequency-domain

PolyMAX Polyreference least-squares complex frequency-domain

PTIM-MP Precise time-step integration method for Markov parameters

RCM   Residual Compensation Mode

SACF Coupling form proposed by Sjövall and Abrahamsson in [8]

SISO   Single Input Single Output

SSS   State-Space Substructuring

SVD   Singular Value Decomposition

TPA   Transfer Path Analysis

UCF   Unconstrained coupling form

VPT   Virtual Point Transformation

VPT-SS State-space realization of VPT

Subscripts

$\bullet_{\alpha M \beta}$ Variable associated with the structure made of α and β linked by M

$\bullet_{\alpha}$ Substructure α

$\bullet_{\beta}$ Substructure β

$\bullet_{AB}$ Structure made of active system A connected to passive system B

$\bullet_{AC}$ Structure made of active system A connected to passive system C

$\bullet_{A}$ Active component A

$\bullet_{B}$ Passive system B

$\bullet_{CB}$ RCMs associated with $[C_{full}][B_{full}]$

$\bullet_{cdf}$ State-space model transformed into complex diagonal form

$\bullet_{C}$ Passive system C

$\bullet_{D}$ Block diagonal matrix

$\bullet_{F_A M F_B}$ Variable associated with the structure made of F_A and F_B linked by M

$\bullet_{F_A}$ Fixture A

$\bullet_{F_B}$ Fixture B

$\bullet_{full}$ Complete state-space model

$\bullet_{ib}$ Model representative of the in-band modes

$\bullet_i$ i^{th} output

$\bullet_j$ j^{th} input

$\bullet_{k_f}$ k^{th} discrete frequency

$\bullet_k$ k^{th} discrete time sample

$\bullet_{LR}$ RCMs associated with $[LR]$

$\bullet_{M\alpha}$ Side of M that is linked to substructure α

$\bullet_{M\beta}$ Side of M that is linked to substructure β

$\bullet_M$ Variable associated with connecting elements

$\bullet_m$ Vector/matrix transformed into modal domain

$\bullet_{neg}$ Matrix transformed into negative form

$\bullet_{or}$ Original coupled state-space mode

$\bullet_{pcp}$ Model composed by pairs of complex conjugate poles

$\bullet_P$ Substructure P

$\bullet_{rp}$ Model composed by real poles

$\bullet_r$ Variable associated with the rth mode

$\bullet_{sc}$ Coherently scaled state-space matrix

$\bullet_{st}$ Stable state-space model

$\bullet_S$ Variable associated with structures

$\bullet_{UR}$ RCMs associated with $[UR]$

$\bullet_{ut}$ Unstable state-space model

Superscripts

$\bullet^\dagger$ Pseudoinverse of a matrix

$\bullet^{accel}$ Variable associated with an acceleration state-space model

$\bullet^{apm}$ Variable associated with a state-space model representative of apparent mass

$\bullet^{disp}$ Variable associated with a displacement state-space model

$\bullet^{eq}$ Equivalent forces

$\bullet^{INL}$ Model forced to verify Newton's second law

$\bullet^{inv}$ Matrix of an inverted state-space model

$\bullet^{I}$ Internal DOF

$\bullet^{i}$ i^{th} fixed operating condition

$\bullet^{J}$ Interface DOF

$\bullet^{op}$ State-space model constructed with optimized modal parameters

$\bullet^{stbz}$ State-space model forced to be stable

$\bullet^{T}$ Transpose of a vector/matrix

$\bullet^{vel}$ Variable associated with a velocity state-space model

Roman letters

B_C Mapping matrix

B_T State mapping matrix

H^{accel} Accelerance FRF matrix

H^{vel} Mobility FRF matrix

H_{ref} Reference FRF matrix

H_{target} Target FRF matrix

L_C Boolean localization matrix

L_T State Boolean localization matrix

P_x Error covariance matrix associated with the state vector

R_u Input Interface Deformation Mode matrix

R_y Output Interface Deformation Mode matrix

T_m Matrix responsible for transforming modal coordinates into physical coordinates

T_{SJ} Coupling matrix

x_{min} State vector of a minimal-order coupled model

Z^{α} Dynamic stiffness matrix

Z^{A} Apparent mass matrix

A   State matrix

B   Input matrix

C   Output matrix

D   Feedthrough matrix

G   Connecting forces vector in frequency domain

g   Connecting forces vector

H   FRF matrix

I   Identity matrix

j   Unit imaginary number ($j = \sqrt{-1}$)

K   Stiffness matrix

L   Modal participation factors matrix

l   Modal participation factor vector

LR   Lower residual matrix

M   Mass matrix

N   Nullspace of a matrix

P   Left eigenvectors of a matrix

Q   Covariance matrix associated with process noise

q   State vector defined in modal coordinates

R   Covariance matrix associated with measurement noise

T   Transformation matrix

t   Time

U   Input vector in frequency domain

u   Input vector

UR   Upper residual matrix

V   Damping matrix

W   Right eigenvectors of a matrix

X   State vector in frequency domain

x   State vector

Y   Output vector in frequency domain

y   Output vector

z   State vector transformed into coupling form

Greek letters

β Scheduling parameter β

Δ Parameterized value of a scheduling parameter

η Output vector defined in the modal domain

γ Gaussian distributed independent stochastic variable

Λ Diagonal matrix composed by the poles of a system

λ Pole of a system

Λ_C Lagrange multipliers vector in frequency domain

ω Frequency

ω_d Damped natural frequency

ω_n Natural frequency

Ψ Mode shapes matrix

ψ Mode shape vector

σ Singular values of a matrix

θ Gaussian distributed independent stochastic variable

ξ_n Damping ratio

Other symbols

$\bar{\bullet}$ Coupled vector/matrix

$\otimes$ Kronecker matrix product

$\breve{\bullet}$ Vectors/matrices of an interpolating LPV model

$\bullet^{-1}$ Inverse of a matrix

$\ddot{\bullet}$ Second order time derivative

$\dot{\bullet}$ First order time derivative

$\hat{\bullet}$ Maximum value of scheduling parameter $\bullet$

$\Im(\bullet)$ Imaginary part of a variable

$\Re(\bullet)$ Real part of a variable

$\tilde{\bullet}$ Coupled vector/matrix associated with an unique set of DOFs

$\underline{\bullet}$ Minimum value of scheduling parameter $\bullet$

$diag[\bullet]$ Column vector containing the diagonal elements of matrix $[\bullet]$

$vec[\bullet]$ Column vector obtained by stacking all columns of matrix $[\bullet]$

Chapter 1

Introduction

1.1 Research Context and Motivation

To ease the characterization of the dynamic behaviour of complex structures, we may think on diving them into several simple substuctures. Then, by characterizing the dynamics of each of those simple substructures and by coupling them, a characterization of the dynamic behaviour of the initial complex structure can be obtained. The approach just described is commonly addressed in literature as dynamic substructuring (DS). This concept can be exploited with substructures numerically or experimentally characterized. Additionally, DS also provides us the possibility of coupling together numerically and experimentally characterized substructures. In this thesis, our attention will be focused on the application of DS with experimentally characterized substructures.

Nowadays, when dealing with experimentally characterized substructures, the DS concept is mainly exploited in frequency domain. Yet, some applications would profit from the use of DS in time-domain. For example, applications involving transient phenomena, involving the characterization of the dynamics of mechanical systems presenting non-linear or time-varying dynamic behaviour and real-time substructuring applications. In fact, there are many mechanical systems that when operating under regular conditions promote relevant changes on the dynamic behaviour of their components. A classical example of these components are the rubber mounts, whose dynamics depends on several external factors, such as on the temperature at which they are submitted and on the value of the static pre-load applied on them.

To tackle this kind of applications, one may think of using state-space models to characterize the dynamics of each component and then, couple them by exploiting SSS methods. In fact, this strategy seems promising for several reasons. First of all, these

models are known to be well-suited to deal with problems formulated in time-domain. Secondly, the state-space models can be used to characterize mechanical systems, whose dynamics depends on different external factors. Indeed, there are many approaches proposed in literature based on state-space models that are adequate to characterize components, whose dynamics depends on different factors. On top of this, these models are also well-known for being excellent choices to tackle real-time substructuring applications. However, the state-of-the-art methodologies are not completely adequate to experimentally estimate state-space models that are suitable for being exploited in DS operations. Moreover, the family of SSS methods is still under investigation, not being so well established in literature as, for example, the Component Mode Synthesis (CMS) and Frequency Based Substructuring (FBS) methods. For these reasons, the computation of accurate stable coupled state-space models by performing coupling operations with models representative of real mechanical systems and estimated experimentally, for example, from experimentally acquired Frequency Response Functions (FRFs), continues to be challenging.

In the following, we detail the challenges to be overcome to ease the computation of accurate stable coupled models from the performance of DS operations with experimentally estimated state-space models. Moreover, we refer the kind of time-domain TPA applications that we aim at tackling by using state-space models and SSS methods.

State-Space Substructuring

Two of the most well-known state-of-the-art SSS approaches are the methods presented by Su and Juang in [9] and by Sjövall and Abrahamsson in [8]. The method derived by Su and Juang is capable of coupling an unlimited number of substructures at same time. However, it presents two important drawbacks. On the one hand, it is not capable of computing minimal-order coupled models. On the other hand, it requires the performance of two different matrix inversions. Conversely, the method proposed by Sjövall and Abrahamsson enables the computation of minimal-order coupled models and only requires the computation of a single matrix inversion. Nonetheless, this method is only capable of coupling two substructures at same time. In addition, this approach requires the previous transformation of state-space models into the coupling form proposed in [8]. The transformation matrix involved on the transformation of state-space models into this coupling form requires the selection of a subspace from the nullspace of the input matrix of the model to be transformed. The selection of this subspace is hard to be performed and strongly influences the performance of the transformation. To ease the computation of coupled state-space models, a novel coupling form and novel post-processing procedures are proposed in section 2.3 to define a SSS approach that merges the advantages of both of these state-of-the-art SSS methods, while mitigating their limitations.

Moreover, the SSS methods available in literature only allow the inclusion of the

dynamics of CEs into coupling operations by treating them as others substructures to be coupled. Even though this methodology does not pose any important disadvantages, when dealing with CEs analytically or numerically characterized, it definitely presents drawbacks, when the CEs are to be experimentally characterized. In an experimental context, it is typical to test CEs with fixtures attached to their ends. Therefore, to obtain a state-space model characterizing the dynamics of a CE by considering it as a regular structure, we are required to decouple the dynamics of the fixtures used to test it. Hence, we are demanded to determine models representative of these fixtures, which might involve the performance of additional experimental modal characterization tests. Furthermore, the performance of decoupling operations to remove the dynamics of the fixtures leads to the identification of state-space models representative of CEs that are contaminated by pairs of spurious modes. In practice, there is generally no a-priori knowledge on the dynamics of the substructures to be identified by decoupling operations. Thus, the identification and subsequent elimination of these spurious modes is many times hard or even infeasible to be performed. The use of state-space models contaminated by spurious states to include the dynamics of CEs into coupling operations is not recommended, because it leads to the computation of coupled modes spoiled by spurious states. Moreover, due to the contamination by spurious modes, the performance of calculations with these coupled models and with the identified models of the CEs will demand higher computational effort.

To overcome the disadvantages associated with the inclusion of CEs into the coupling SSS operations by treating them as regular structures, we may think on including them into these operations via compatibility relaxation. In this way, we could include the dynamics of CEs by exploiting state-space models representative of their diagonal dynamic stiffness terms. The inverse substructuring (IS) method could be particularly useful to compute these models, because it enables the determination of the diagonal dynamic stiffness terms of CEs from the dynamic stiffness of the assembly, where they are included, provided that these components verify the assumptions underlying IS. Thus, it could be possible to experimentally determine state-space models representative of CEs without performing decoupling operations and hence, free of spurious states. Moreover, in this scenario, we would not be required to determine state-space models representative of the fixtures used to experimentally characterize the CEs. Thereby, in section 2.5, a novel SSS method to include CEs via compatibility relaxation into SSS coupling operations is proposed. Furthermore, the state-space realization of IS is derived to experimentally determine state-space models representative of CEs to be included into this novel SSS technique.

Estimation of state-space models

To be suitable for DS operations, the state-space models must present FRFs that closely match the FRFs of the mechanical systems that they represent. On top of this,

these models must be stable, reciprocal (in case that the substructures that they represent are reciprocal), obey Newton's second law, passive and have to present outputs and inputs collocated at the interfaces of the substructures involved in the DS operations. The state-space models defined in analytical and numerical contexts generally verify these criteria. However, the experimental identification of state-space models that verify all this criteria is not straightforward. In particular, the computation of models verifying Newton's second law and passivity remains challenging.

The identification of state-space models verifying Newton's second law is mandatory, otherwise these models cannot be properly differentiated. Thereby, state-space models that do not respect Newton's second law cannot be properly transformed into coupling form, which makes the computation of minimal-order coupled models infeasible, in case that the state-space models involved in the DS operations are not defined in the physical domain (common situation in practice). Moreover, the acceleration FRFs of state-space models violating this physical law cannot be correctly determined. The state-of-the-art approaches to impose Newton's second law on state-space models either impose this physical law in a weak sense or make use of undamped residual compensation modes (RCMs) to strictly impose it. On the one hand, state-space models that do not strictly obey Newton's second law are not suitable for being used in SSS operations. On the other hand, the inclusion of undamped modes on state-space models is not recommended, because the performance of time-domain simulations with models composed by undamped modes may lead to numerical instabilities. To overcome the limitations of the state-of-the-art approaches, in section 3.3.2, we propose a novel method to strictly impose Newton's second law on state-space models without relying on the use of undmaped RCMs.

The estimation of state-space models verifying passivity is also fundamental, because the performance of DS operations with non-passive models generally leads to the computation of unstable coupled state-space models. Many algorithms to impose passivity on state-space models have already been proposed in literature. These algorithms are often clustered under the labels optimal and sub-optimal. Nevertheless, none of these groups of algorithms is completely adequate to estimate passive state-space models to be involved on SSS operations, because they either lead to the computation of state-space models with limited accuracy (case of the sub-optimal algorithms) or they demand high computational effort (case of the optimal algorithms). This might prevent the use of SSS methods in applications that require a fast computation of accurate stable coupled state-space models. In [4], a direct method to impose passivity on state-space models that does not belong to any of the groups of techniques mentioned above was proposed. However, this approach may lead to the computation of passive models presenting poor accuracy and not being globally passive (i.e. that are not passive in the entire frequency axis). To surpass these difficulties, in section 3.5, we propose a novel approach to compute accurate stable coupled state-space models directly from unstable coupled models originated from the performance of SSS operations with non-passive

models. In this way, we avoid the need of imposing passivity on state-space models.

State-space models and SSS methods in TPA

As discussed in section 1.1, the state-space formulation is well-suited to deal with problems formulated in time-domain and to take into account possible time-domain variations on the dynamics of mechanical systems by exploiting, for instance, interpolating Linear Parameter-Varying (LPV) models. Thus, we intend to take advantage of these characteristics of the state-space formulation to apply TPA methods on applications involving structures/components, whose dynamics changes over time. In chapter 5, two time-domain TPA applications involving mechanical systems presenting time-domain variations on their dynamical behaviour are tackled by using state-space models and SSS methods.

1.2 Research Objectives

The aim of this thesis is to develop novel methodologies to mitigate the limitations of the state-of-the art SSS techniques and of the state-of-the-art approaches to experimentally estimate state-space models. Moreover, we also aim at demonstrating the benefit of using state-space models and SSS methods to tackle time-domain TPA applications. To accomplish these objectives, the state-of-the-art must be extended by the following innovations:

- Develop a novel State-Space Substructuring (SSS) methodology that entails the advantages of the state-of-the-art methods, while overcoming their main limitations;

- Develop a novel methodology to enable the introduction of the dynamics of CEs into SSS operations via compatibility relaxation;

- Derive a novel approach to determine state-space models of CEs to be included into the coupling SSS operations via compatibility relaxation;

- Address the limitation of the state-of-the art approaches to force identified state-space models to obey Newton's second law, by developing a novel approach that strictly imposes this physical law without relying on the use of undamped RCMs;

- Develop a novel method that enables the computation of accurate stable coupled state-space models from the performance of DS operations with non-passive state-space models;

- Investigate and demonstrate the benefit of using state-space models and SSS methods for time-domain Transfer Path Analysis (TPA) applications.

1.3   Thesis Contributions

The novel contributions of this thesis with respect to the state-of-the-art are listed as follows:

- The dual SSS formulation (also denoted LM-SSS) is extended to directly couple displacement and velocity state-space models. In this way, we can directly compute displacement and velocity coupled models with LM-SSS, avoiding the need of performing matrix inversions to compute displacement and velocity coupled models from the correspondent acceleration coupled model;

- A novel coupling form tagged Unconstrained Coupling Form (UCF) is presented. UCF is specially tailored to conduct DS operations with LM-SSS, holding the advantage of transforming state-space models into coupling form without relying on the selection of a subspace from a nullspace, which is many times difficult to be performed. UCF is validated on numerical and experimental substructuring cases;

- Novel post-processing procedures to eliminate the redundant states originated from the performance of DS operations with LM-SSS are proposed. These approaches enable the computation of minimal-order coupled models with LM-SSS. Numerical and experimental substructuring cases are exploited to validate these post-processing procedures;

- To avoid a manual elimination of the redundant DOFs originated from the performance of coupling operations with LM-SSS, a novel post-processing procedure is proposed to retain a unique set of DOFs from the computed coupled state-space models. This post-processing procedure is validated on numerical and experimental substructuring cases;

- A novel primal state-space assembly formulation is introduced. This approach is validated on numerical and experimental substructuring cases;

- A novel SSS technique enabling the inclusion of the dynamics of CEs into LM-SSS formulation via compatibility relaxation is derived. This approach enables the inclusion of the dynamics of CEs by using state-space models representative of their diagonal apparent mass terms. The accuracy of this coupling approach is evaluated on numerical and experimental substructuring cases;

- Novel post-processing procedures to eliminate the extra states originated from the performance of coupling operations with LM-SSS via compatibility relaxation are presented. Thereby, enabling the computation of minimal-order coupled models with this SSS method. These post-processing procedures are validated on numerical and experimental substructuring cases;

- The state-space realization of the Inverse Substructuring (IS) method is derived. This method enables the determination of state-space models representative of the diagonal apparent mass terms of connecting elements (CEs) from state-space models representative of the dynamics of the assemblies where they are included. The accuracy of this method is evaluated on numerical and experimental substructuring cases;

- A novel method to impose Newton's second law on state-space models without relying on the use of undamped RCMs is presented. This approach is validated to force several state-space models representative of analytical and real mechanical systems to obey Newton's second law.

- A novel methodology to impose stability on unstable coupled state-space models is proposed. Thus, making it possible to compute accurate stable coupled models from the performance of DS operations with non-passive state-space models. This methodology is validated to impose stability on an unstable coupled state-space model resultant from the performance of several DS operations with non-passive models representative of real mechanical systems.

- Novel strategies to apply both matrix-inverse classical TPA and in-situ component-based TPA methods in time-domain, when dealing with assemblies composed by sources and passive systems presenting time-varying dynamics are presented. These methodologies are numerically validated.

1.4 Thesis Outline

Part of the content of this thesis has already been published in [1], [3], [10], [2], [6], [11], [7]. However, those topics have been extended in this document to provide the reader with a more detailed and comprehensive description of the work done. The present document is organized according to the following structure:

Chapter 1 presents the motivation of the thesis, the defined research activities and its contributions with respect to the state-of-the-art.

Chapter 2 discusses some state-of-the-art dynamic substructuring techniques belonging to the groups of Component Mode Synthesis (CMS), Frequency Based Substructuring and State-Space Substructuring (SSS) methods. The state-of-the-art LM-SSS method is extended to directly couple displacement and velocity state-space models. A novel coupling form, specially, tailored to perform DS operations with LM-SSS is presented. Novel post-processing procedures to eliminate the redundant states originated from the performance of DS operations with this technique and hence, to compute minimal-order coupled models are proposed. An additional post-processing procedure is outlined to eliminate the redundant DOFs from the coupled state-space models computed with LM-SSS without relying on a manual elimination. A comparison of the

LM-SSS method enhanced by the proposed post-processing procedures with two state-of-the-art SSS techniques is also conducted. A novel primal state-space assembly formulation is introduced. The inclusion of state-space models representative of connecting elements (CEs) into the dual SSS formulation via compatibility relaxation is discussed, leading to the development of a novel SSS coupling method, named Lagrange Multiplier State-Space Substructuring via compatibility relaxation. Novel post-processing procedures to eliminate the extra states originated from the performance of DS operations with this technique are proposed. A discussion on strategies to compute state-space models representative of diagonal apparent mass terms of CEs is conducted and the state-space realization of the Inverse Substructuring approach is derived.

Chapter 3 presents a state-of-the-art methodology to construct state-space models from modal parameters directly estimated from experimentally acquired FRFs. A discussion on the need of constructing state-space models verifying Newton's second law is also conducted, being proposed a novel technique to impose this physical law on state-space models. The proposed novel technique is compared with a state-of-the-art approach. The state-space realization of the Virtual Point Transformation (VPT) method is presented and a novel strategy to impose stability on unstable coupled state-space models is developed.

Chapter 4 exploits numerical and experimental substructuring cases to validate the novel methodologies proposed in chapters 2 and 3.

Chapter 5 presents a local methodology to construct interpolating LPV models. This technique is validated on numerical and experimental examples. The use of interpolating LPV models together with the matrix-inverse classical TPA and with the in-situ component-based TPA methods is proposed to determine time-domain connecting and equivalent forces, respectively, when dealing with mechanical systems, whose dynamics changes over time. These approaches are validated by exploiting a numerical example.

Chapter 6 presents the conclusions of this thesis and proposes future research activities.

Chapter 2

Dynamic Substructuring

2.1 Introduction

Dynamic Substructuring (DS) is a methodology used to characterize the dynamic behaviour of complex assembled structures. This methodology relies on the belief that the characterization of a given complex structure can be easily performed by, firstly, characterizing each of its constituent parts and, then, coupling them to obtain an accurate representation of the initial complex structure. Over the last decades, this methodology received much attention, which lead to the development of several DS techniques [12]. In literature, these techniques are usually clustered in three main groups. The group of the Component Mode Synthesis (CMS) techniques, the group of the Frequency Based Substructuring (FBS) methods and the group of the State-Space Substructuring (SSS) approaches.

In section 2.2, we will start by presenting state-of-the art approaches belonging to the groups of CMS, FBS and SSS methods (sections 2.2.1, 2.2.2 and 2.2.3, respectively). Then, novel procedures to mitigate the limitations of the Lagrange Multiplier State-Space Substructuring (LM-SSS) method are outlined in section 2.3, while a novel primal state-space assembly formulation is developed in section 2.4. Finally, the inclusion of connecting elements into the LM-SSS formulation via compatibility relaxation is discussed in section 2.5, leading to the development of two novel techniques, namely, the LM-SSS via compatibility relaxation method and the state-space realization of the inverse substructuring (IS) approach.

2.2 State-of-the-art

2.2.1 Component Mode Synthesis

The group of CMS methods was the first kind of investigated DS techniques and became popular among the scientific community as a reduction method for finite-element models [12]. When performing DS operations with CMS methods, the dynamical be-

haviour of each of the substructures is represented by a set of modes [13]. Different methods have been proposed to define reliable sets of modes that properly model the mechanical behaviour of the substructures. One of the most famous methods is the Craig-Bampton approach proposed in [14], which uses fixed-interface and constraint modes to characterize each of the substructures. Yet, there are other techniques that use other kind of modes. For example, the techniques proposed in [15],[16] that make use of free-interface modes with and without residual flexibility.

The CMS methods can be used to rigidly couple components by imposing strict compatibility between their interfaces, i.e. no relative displacement between the interfaces of the substructures is allowed (see [12]). Alternatively, these methods can also be used to couple substructures, whose interfaces are not rigidly coupled, i.e. that may present some relative displacement between them. For example, substructures that are connected by connecting elements (CEs), such as screws and rubber mounts. To perform the coupling of this kind of substructures, two possible approaches can be followed. Either we characterize the CE responsible for connecting the substructures and we include it in the coupling operation as a regular substructure or, we perform coupling by relaxing the compatibility conditions [17]. By following the second strategy, the compatibility conditions are no longer defined by imposing null relative displacement between the interfaces of the substructures to be coupled. Instead, these conditions are established through the relation between the relative displacement of the interfaces of the connected structures and the connecting forces acting on the CE (see [18], [19], [20]).

Overall, this kind of methods are easy to apply, when performing DS operations with numerically modelled substructures, for example modelled by using finite element models. However, when dealing with experimentally characterized components these techniques cannot be directly applied, because they require the use of system identification algorithms (see, for instance, [21],[22]) to identify modal parameters that well describe the dynamics of the substructures [23].

Primal Formulation

To present the primal assembly formulation in the modal domain, we will start by analyzing the assembled structure composed by two substructures denoted α and β shown in figure 2.1.
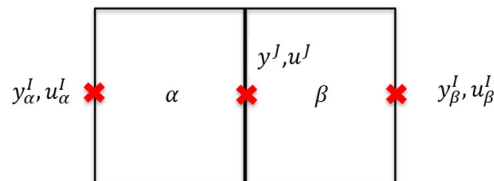
Figure 2.1: Assembled structure composed by two different substructures [1].

By virtually separating the assembled structure presented in figure 2.1, the connecting forces acting on the interface DOFs of both substructures can be observed as depicted in figure 2.2.
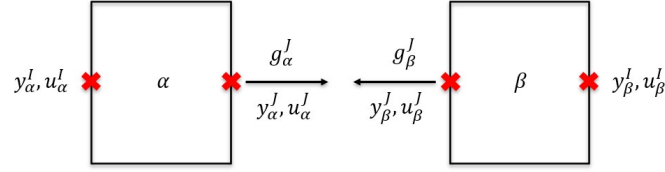
Figure 2.2: Substructures composing the assembly shown in figure 2.1 virtually separated [1].

The connecting forces represented in figure 2.2 present the same intensity, but different directions, hence we can represent these forces as follows

$$\{g(t)\} = \begin{Bmatrix} g_\alpha(t) \\ g_\beta(t) \end{Bmatrix} = -[B_C]^T \{\lambda_C(t)\} \tag{2.1}$$

where, $\{\lambda_C(t)\}$ denotes a vector composed by Lagrange Multipliers that represent the intensity of the connecting forces [24], while $[B_C]$ is a signed Boolean mapping matrix (see [24],[25],[12],[26]). This matrix must be constructed by assigning negative unitary values to the coefficients associated with the interface DOFs of one of the substructures and by assigning positive unitary values to the coefficients related to the interface DOFs of the other substructure. The value of the coefficients associated with the internal DOFs of the substructures must be set to zero. Subscripts α and β denote vectors/matrices associated with substructures α and β, respectively. Vectors $\{g_\alpha(t)\}$ and $\{g_\beta(t)\}$ are composed by the connecting forces acting on each of the substructures. These vectors are given below.

$$\{g_\alpha(t)\} = \begin{Bmatrix} 0 \\ g_\alpha^J(t) \end{Bmatrix} \tag{2.2a} \qquad \{g_\beta(t)\} = \begin{Bmatrix} 0 \\ g_\beta^J(t) \end{Bmatrix} \tag{2.2b}$$

Note that expression (2.1) can be easily generalized and remains valid, when performing coupling operations involving an unlimited number of substructures.

At this point, let us assume that the mass, damping and stiffness matrices of both substructures is known. Thereby, by generalizing for coupling an unlimited number of substructures, we may define a set of coupled differential equations as follows

$$[M_D]\{\ddot{y}(t)\} + [V_D]\{\dot{y}(t)\} + [K_D]\{y(t)\} = \{u(t)\} + \{g(t)\} \tag{2.3}$$

where, $[M_D]$, $[V_D]$, $[K_D]$, $\{y(t)\}$, $\{u(t)\}$ and $\{g(t)\}$ are given as follows

$$\{y(t)\} = \begin{Bmatrix} y_\alpha(t) \\ y_\beta(t) \\ \vdots \end{Bmatrix}, \quad \{u(t)\} = \begin{Bmatrix} u_\alpha(t) \\ u_\beta(t) \\ \vdots \end{Bmatrix}, \quad \{g(t)\} = \begin{Bmatrix} g_\alpha(t) \\ g_\beta(t) \\ \vdots \end{Bmatrix}$$

$$[M_D] = \begin{bmatrix} M_\alpha & & \\ & M_\beta & \\ & & \ddots \end{bmatrix}, \quad [V_D] = \begin{bmatrix} V_\alpha & & \\ & V_\beta & \\ & & \ddots \end{bmatrix}, \quad [K_D] = \begin{bmatrix} K_\alpha & & \\ & K_\beta & \\ & & \ddots \end{bmatrix} \tag{2.4}$$

where, $\{y(t)\}$ and $\{u(t)\}$ are vectors composed by the displacement responses of the DOFs and by the external applied forces on the DOFs, respectively. Matrices $[M]$, $[V]$ and $[K]$ denote mass, damping and stiffness matrices, respectively. Subscript D denotes block diagonal matrices.

Let us further assume that the exact relation between physical and modal coordinates is given as follows:

$$\left\{ y(t) \right\} = \left[T_{m,D} \right] \left\{ \eta(t) \right\} \tag{2.5}$$

with,

$$\left[T_{m,D} \right] = \begin{bmatrix} T_{m,\alpha} & & \\ & T_{m,\beta} & \\ & & \ddots \end{bmatrix}, \quad \{\eta(t)\} = \begin{Bmatrix} \eta_\alpha(t) \\ \eta_\beta(t) \\ \vdots \end{Bmatrix} \tag{2.6}$$

where, $[T_m]$ is a matrix responsible for transforming the modal coordinates of a given substructure into the physical domain, while vector $\{\eta(t)\}$ is composed by the modal coordinates of a given substructure.

By using expression (2.5) and expression (2.3) pre-multiplied by $[T_{m,D}]^T$, we may rewrite the set of coupled differential equations (expression (2.3)) in modal domain as follows

$$[M_{m,D}] \{\ddot{\eta}(t)\} + [V_{m,D}] \{\dot{\eta}(t)\} + [K_{m,D}] \{\eta(t)\} = \{u_m(t)\} + \{g_m(t)\} \tag{2.7}$$

where, matrices $[M_{m,D}]$, $[V_{m,D}]$, $[K_{m,D}]$, $\{u_m(t)\}$ and $\{g_m(t)\}$ are given below.

$$[M_{m,D}] = [T_{m,D}]^T [M_D][T_{m,D}], \quad [V_{m,D}] = [T_{m,D}]^T [V_D][T_{m,D}]$$
$$[K_{m,D}] = [T_{m,D}]^T [K_D][T_{m,D}] \tag{2.8}$$
$$[u_m(t)] = [T_{m,D}]^T [u(t)], \quad [g_m(t)] = [T_{m,D}]^T [g(t)]$$

To be coupled, the substructures must respect both compatibility and equilibrium conditions. The compatibility condition states that the physical motion of the inter-

face DOFs of both substructures must be the same. Hence, these conditions can be, mathematically, defined as given below.

$$[B_C] \{y(t)\} = \{0\} \tag{2.9}$$

By using expression (2.5), expression (2.9) can be also defined in the modal domain as:

$$[B_{C,m}] \{\eta(t)\} = \{0\} \tag{2.10}$$

where, $[B_{C,m}]$ is given hereafter.

$$[B_{C,m}] = [B_C] [T_{m,D}] \tag{2.11}$$

However, when performing coupling by using a primal formulation, the compatibility condition is imposed by retaining the unique set of DOFs [12]. Thereby, this condition must be defined as follows

$$\{\eta(t)\} = [L_{C,m}] \{\tilde{\eta}(t)\} , \forall \{\tilde{\eta}(t)\} \tag{2.12}$$

where, $\{\tilde{\eta}(t)\}$ represents the unique set of coupled DOFs represented in the modal domain and $[L_{C,m}]$ represents a Boolean localization matrix defined in the modal domain. The set of unique DOFs $\{\tilde{\eta}(t)\}$ must verify the compatibility conditions given in expression (2.10), thus the following identities must be verified.

$$[B_{C,m}] \{\eta(t)\} = [B_{C,m}] [L_{C,m}] \{\tilde{\eta}(t)\} = \{0\} \tag{2.13}$$

It is evident that expression (2.13) will be verified, in case that $[L_{C,m}]$ is computed from the nullspace of $[B_{C,m}]$ as given below [24],[12].

$$[L_{C,m}] = null \left([B_{C,m}]\right) \tag{2.14}$$

The equilibrium conditions state that the sum of the connecting forces at the matching DOFs must be null [9],[27]. This means that the connecting forces acting on matching interface DOFs belonging to different structures must present the same intensity and opposite direction (hence, must cancel each other). In this way, the equilibrium conditions can be defined by the following expression.

$$[L_{C,m}]^T \{g_m(t)\} = \{0\} \tag{2.15}$$

To prove that the set of equations (2.15) holds, we may start by pre-multiplying expression (2.1) by $[T_{m,D}]^T$ as follows.

$$[T_{m,D}]^T \{g(t)\} = - [T_{m,D}]^T [B_C]^T \{\lambda_C(t)\} \tag{2.16}$$

By using expression (2.8) and expression (2.11) together with the transpose matrix property $(AB)^T = B^T A^T$ [28], we may rewrite expression (2.16) as given below.

$$\{g_m(t)\} = -[B_{C,m}]^T \{\lambda_C(t)\} \tag{2.17}$$

From expression (2.17), it is straightforward that expression (2.15) can be rewriten as follows.

$$-[L_{C,m}]^T [B_{C,m}]^T \{\lambda_C(t)\} = \{0\} \tag{2.18}$$

As matrix $[L_{C,m}]$ is the nullspace of $[B_{C,m}]$ (see expression (2.14)), we may write the following expression.

$$[B_{C,m}] [L_{C,m}] = \{0\} \tag{2.19}$$

By using once again the transpose matrix property $(AB)^T = B^T A^T$ [28] and expression (2.19), we may define the identities given below.

$$([B_{C,m}] [L_{C,m}])^T = [L_{C,m}]^T [B_{C,m}]^T = \{0\} \tag{2.20}$$

Thus, $[L_{C,m}]^T$ is the nullspace of $[B_{C,m}]^T$ and, hence expression (2.15) holds.

By imposing both compatibility and equilibrium conditions (expressions (2.12) and (2.15), respectively) in expression (2.7), we may arrive to the following set of coupled differential equations:

$$\left[\tilde{M}_m\right] \{\ddot{\tilde{\eta}}(t)\} + \left[\tilde{V}_m\right] \{\dot{\tilde{\eta}}(t)\} + \left[\tilde{K}_m\right] \{\tilde{\eta}(t)\} = \{\tilde{u}_m(t)\} \tag{2.21}$$

where,

$$\begin{aligned}
[\tilde{M}_m] = [L_{C,m}]^T[M_{m,D}][L_{C,m}], \quad [\tilde{V}_m] = [L_{C,m}]^T[V_{m,D}][L_{C,m}] \\
[\tilde{K}_m] = [L_{C,m}]^T[K_{m,D}][L_{C,m}], \quad [\tilde{u}_m(t)] = [L_{C,m}]^T[u_m(t)]
\end{aligned} \tag{2.22}$$

Dual Formulation

A dual formulation can also be used to set-up the coupled differential equations of motion in the modal domain. By using expressions (2.17), (2.10) and (2.7) and by dropping $[\bullet]$, $\{\bullet\}$ and (t) for ease of readability, the dual assembled differential equations can be defined as follows

$$\begin{cases}
M_{m,D}\ddot{\eta} + V_{m,D}\dot{\eta} + K_{m,D}\eta + B_{C,m}^T \lambda_C = u_m \\
B_{C,m}\eta = 0
\end{cases} \tag{2.23}$$

where, this set of differential equations can also be established in matrix form as given below.

$$\begin{bmatrix} M_{m,D} & 0 \\ 0 & 0 \end{bmatrix} \begin{Bmatrix} \ddot{\eta} \\ \lambda_C \end{Bmatrix} + \begin{bmatrix} V_{m,D} & 0 \\ 0 & 0 \end{bmatrix} \begin{Bmatrix} \dot{\eta} \\ \lambda_C \end{Bmatrix} + \begin{bmatrix} K_{m,D} & B_{C,m}^T \\ B_{C,m} & 0 \end{bmatrix} \begin{Bmatrix} \eta \\ \lambda_C \end{Bmatrix} = \begin{Bmatrix} u_m \end{Bmatrix} \quad (2.24)$$

Decoupling

Decoupling is widely used in DS to identify the dynamic behaviour of components that are part of an assembled structure. This DS operation requires the dynamic behavior of the assembled structure and of the remaining components to be known. One of the main applications of decoupling operations is the dynamic characterization of parts that are difficult or even impossible to be tested separately. To perform decoupling, we can follow the procedures discussed above. However, the mass, damping and stiffness matrices (either represented in the physical or modal domains) of the substructures to be decoupled must be, previously, multiplied by -1 [29].

Nevertheless, in practice it is sometimes difficult to perform measurements at the interface between the substructure to be decoupled and the component to be identified. To circumvent this difficulty, we may, for instance, exploit the Modal Constraints for Fixture and Subsystem (MCFS) method presented in [30]. This approach enables the use of information obtained from measurements performed on internal points of the assembled structure belonging to the substructure to be decoupled. To perform decoupling MCFS constrains the motion of the assembly and of the substructure to be decoupled by using weak modal constraints to avoid high sensitivity to measurement errors. This method demonstrated to be reliable to perform decoupling operations, leading to the identification of accurate modal basis representative of the dynamics of real mechanical systems (see, [29]).

Substructuring via compatibility relaxation

The strategy proposed in [18] to perform coupling of substructures, whose interfaces are not rigidly connected, will be here presented. To start, let us consider the following two substructures connected by a CE M depicted in figure 2.3.
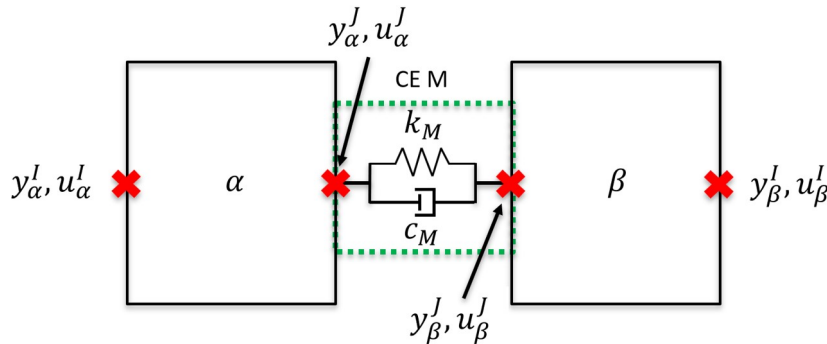
Figure 2.3: Assembled structure composed by two substructures connected by a connecting element [2].

By virtually separating the assembly shown in figure 2.3, we may observe the connecting forces responsible for keeping the substructures coupled (see figure 2.4).
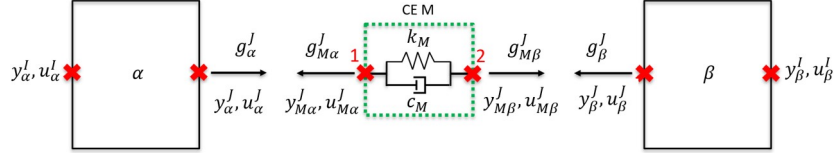
Figure 2.4: Substructures composing the structure depicted in figure 2.3 virtually separated [2].

To exploit the strategy proposed in [18], we must assume that the CE is massless and that there are no cross couplings between its DOFs. In other words, each DOF on one of the interfaces of the CE must be only coupled to one DOF on the other interface (being both DOFs associated with the same direction). If these conditions hold, we may define the following relations [17]:

$$
\begin{aligned}
[M_{M,11}] = [M_{M,12}] = [M_{M,21}] = [M_{M,22}] = [0] \\
[V_{M,11}] = -[V_{M,12}] = -[V_{M,21}] = [V_{M,22}] = [V_M] \\
[K_{M,11}] = -[K_{M,12}] = -[K_{M,21}] = [K_{M,22}] = [K_M]
\end{aligned}
\tag{2.25}
$$

where, subscript M denotes variables related to the CE M depicted in figures 2.3 and 2.4, while the first number in subscript refers to the outputs and the second to the inputs of each variable. The number 1 denotes that the outputs or/and inputs are associated with the DOFs on the side $M\alpha$ of the CE, whereas the number 2 means that the outputs or/and inputs are associated with the DOFs on the $M\beta$ side (see figure 2.4).

The assembly depicted in figure 2.3 is composed by two substructures connected by a CE. Thus, relative displacement between the interface of both substructures is allowed. This relative displacement is a direct consequence of the connecting forces that act at the interfaces of the CE. Thereby, by generalizing to couple an unlimited number of substructures connected by an unlimited number of CEs, we may define a relation between these connecting forces and the relative displacement between the interfaces of the connected substructures as follows [18]:

$$
\{\lambda_C(t)\} = [V_{M,D}] [B_C] \{\dot{y}(t)\} + [K_{M,D}] [B_C] \{y(t)\}
\tag{2.26}
$$

where,

$$
[V_{M,D}] = \begin{bmatrix} V_{M_1} & & \\ & V_{M_2} & \\ & & \ddots \end{bmatrix}, \quad [K_{M,D}] = \begin{bmatrix} K_{M_1} & & \\ & K_{M_2} & \\ & & \ddots \end{bmatrix}
\tag{2.27}
$$

where, subscripts M_1 and M_2 denote variables associated with different CEs.

As the CEs are assumed to be massless, the force equilibrium condition defined in expression (2.1) is still valid [18],[20],[17]. In this way, by imposing the compatibility conditions (see expression (2.26)) in expression (2.3), by exploiting the relation given in (2.1) and by dropping [•], {•} and (t) for ease of readability, we may establish the following set of differential equations.

$$M_D \ddot{y} + V_D \dot{y} + K_D y + B_C^T(V_{M,D} B_C \dot{y} + K_{M,D} B_C y) = u \qquad (2.28)$$

After some mathematical manipulations, the following set of coupled differential equations can be defined.

$$M_D \ddot{y} + (V_D + B_C^T V_{M,D} B_C)\dot{y} + (K_D + B_C^T K_{M,D} B_C)y = u \qquad (2.29)$$

By exploiting expressions (2.5) and (2.8), expression (2.29) can also be represented in the modal domain as given hereafter.

$$T_{m,D}^T M_D T_{m,D} \ddot{\eta} + T_{m,D}^T (V_D + B_C^T V_{M,D} B_C) T_{m,D} \dot{\eta}$$
$$+ T_{m,D}^T (K_D + B_C^T K_{M,D} B_C) T_{m,D} \eta = u_m \qquad (2.30)$$

2.2.2   Frequency Based Substructuring

In the Frequency Based Substructucturing (FBS) methods, the substructures to be coupled are characterized by their impedance (i.e. for instance, dynamic stiffness or apparent mass) or admittance (e.g. receptance, mobility or accelerance FRFs). Thereby, this group of methods is typically exploited when performing DS operations with experimentally characterized substructures.

The first developed FBS methods relied on the performance of coupling by primally assembling the impedance of the substructures involved in the DS operations (see [31]). However, when performing experimental modal characterization tests, we usually measure admittance instead of impedance. Thus, the performance of coupling by primally assembling the impedance of the substructures requires in general the previous inversion of their FRFs. On top of that, after performing coupling, an additional matrix inversion is required, in case that the determination of the coupled FRFs is of interest. The performance of so many matrix inversions makes this kind of methods numerically inefficient and prone to noise amplification [12].

A more suitable technique to perform DS was developed in [32]. This method showed to be able to directly couple sets of measured FRFs belonging to an unlimited number of structures at same time. In addition, it also showed to be numerically efficient, because to perform coupling by using this approach, we are just required to calculate the inverse of a single matrix of dimension $n_J \times n_J$ (where, n_J represents the number of interface DOFs). However, this approach demonstrated to be complex

to be used in practice. For this reason, the method proposed in [32] was rewritten in a more straightforward fashion in [23], giving arise to the development of the well-known Lagrange Multiplier Frequency Based Substructuring (LM-FBS). This method makes use of a dual assembly formulation representing a simpler version of the approach proposed by Jetmundsen et al. in [32]. Due to its accuracy and simplicity, LM-FBS method is usually the method of choice, when DS operations with FRFs are to be performed (see, for example, [27],[33]).

When dealing with substructures connected by CEs, we may follow two different approaches. On the one hand, we may treat the CEs as other substructures to be coupled, on the other hand, we may include the dynamics of the CEs via compatibility relaxation ([33],[34],[35]). To implement the second approach, we may exploit the approach proposed in [20]. This approach represents the frequency based realization of the approach proposed in [18] and presented in section 2.2.1. Thus, it is developed by assuming that the CEs are massless and that no cross couplings between their DOFs exist. By performing these assumptions, a new variant of LM-FBS method that enables the inclusion of CEs via compatibility relaxation can be formulated. In this new variant of LM-FBS, the compatibility conditions must allow relative displacement between the interfaces of the substructures to be coupled. These coupling conditions must be derived from the relation between the connecting forces acting on the CEs and the relative displacement between the interfaces of the connected components.

Primal Formulation

To demonstrate how to perform primal assembly in the frequency domain let us apply a Fourier transform on the expression (2.3) representative of a coupled set of differential equations as follows

$$[Z_D(j\omega)]\{Y(j\omega)\} = \{U(j\omega)\} + \{G(j\omega)\} \qquad (2.31)$$

with,

$$[Z_D(j\omega)] = \begin{bmatrix} Z_\alpha & & \\ & Z_\beta & \\ & & \ddots \end{bmatrix} = -\omega^2[M_D] + j\omega[V_D] + [K_D] \qquad (2.32)$$

where, $[Z]$ represents a dynamic stiffness matrix, while $\{Y(j\omega)\}$ is a vector composed by the displacements of the DOFs in the frequency domain. Vectors $\{U(j\omega)\}$ and $\{G(j\omega)\}$ are composed by the external applied forces and by the connecting forces in the frequency domain, respectively.

Before moving on, it is worth noting that expressions (2.1) and (2.9) are still valid in the frequency domain. Thereby, we may define the following mathematical relations.

$$\{G(j\omega)\} = -[B_C]^T \{\Lambda_C(j\omega)\} \tag{2.33}$$

$$[B_C]\{Y(j\omega)\} = \{0\} \tag{2.34}$$

As mentioned in section 2.2.1, when using a primal assembly formulation, the compatibility condition is imposed by retaining the unique set of DOFs, whereas the equilibrium condition must be enforced by imposing the mutual cancellation of the connecting forces acting on the matching interface DOFs. Thereby, the compatibility condition must be defined as follows [24][12]

$$\{Y(j\omega)\} = [L_C]\left\{\tilde{Y}(j\omega)\right\}, \forall \left\{\tilde{Y}(j\omega)\right\} \tag{2.35}$$

where, $\{\tilde{Y}(j\omega)\}$ represents the unique set of coupled DOFs represented in the physical domain and $[L_C]$ represents a so-called Boolean localization matrix. Vector $\{\tilde{Y}(j\omega)\}$ must respect the compatibility conditions, thus the following identities must hold.

$$[B_C]\{Y(j\omega)\} = [B_C][L_C]\left\{\tilde{Y}(j\omega)\right\} = \{0\} \tag{2.36}$$

By observing expression (2.36), it is evident that this expression will hold, in case that $[L_C]$ is computed from the nullspace of $[B_C]$ as given below [24][12].

$$[L_C] = null\left([B_C]\right) \tag{2.37}$$

The equilibrium conditions can be, mathematically, established as given below [24],[12].

$$[L_C]^T\{G(j\omega)\} = \{0\} \tag{2.38}$$

To prove that the relations given in equation (2.38) are verified, we must rewrite them by using expression (2.33) as follows.

$$-[L_C]^T[B_C]^T\{\Lambda_C(j\omega)\} = \{0\} \tag{2.39}$$

As matrix $[L_C]$ is the nullspace of $[B_C]$ (see expression (2.37)), we may define the following expression.

$$[B_C][L_C] = \{0\} \tag{2.40}$$

By using the transpose matrix property $(AB)^T = B^T A^T$ [28] and expression (2.40), we arrive to the identities given below.

$$([B_C][L_C])^T = [L_C]^T[B_C]^T = \{0\} \tag{2.41}$$

Thereby, we may conclude that $[L_C]^T$ is the nullspace of $[B_C]^T$ and, hence expression (2.38) holds.

At this point, to primally assemble the dynamic stiffness matrices of each substructure, we must start by imposing the compatibility condition (see expression (2.35)) on expression (2.31) as follows

$$\{U(j\omega)\} + \{G(j\omega)\} = [Z_D(j\omega)][L_C]\left\{\tilde{Y}(j\omega)\right\} \tag{2.42}$$

by pre-multiplying expression (2.42) by $[L_C]^T$ and by imposing the equilibrium conditions defined in expression (2.38), yields:

$$\left\{\tilde{U}(j\omega)\right\} = [\tilde{Z}(j\omega)]\left\{\tilde{Y}(j\omega)\right\} \tag{2.43}$$

where, $[\tilde{Z}(j\omega)]$ and $\left\{\tilde{U}(j\omega)\right\}$ represent the primally assembled dynamic stiffness matrices and the vector composed by the unique set of external applied forces in the frequency domain, respectively. These variables are given hereafter.

$$\left[\tilde{Z}(j\omega)\right] = [L_C]^T [Z_D(j\omega)] [L_C] \tag{2.44}$$

$$\left\{\tilde{U}(j\omega)\right\} = [L_C]^T \{U(j\omega)\} \tag{2.45}$$

To comoute the coupled set of receptance FRFs, we are only required to invert the primally assembled dynamic stiffness matrices as follows

$$\left[\tilde{H}(j\omega)\right] = [\tilde{Z}(j\omega)]^{-1} \tag{2.46}$$

where, $[\tilde{H}(j\omega)]$ denotes a coupled set of receptance FRFs, which is composed by the unique set of DOFs.

It is worth mentioning that, even though we have presented the primal assembly formulation in the frequency domain by coupling dynamic stiffness, it continues to be valid to couple other kinds of impedance, such as apparent mass.

Dual Formulation

To demonstrate how to perform dual assembly in the frequency domain, let us start by using expressions (2.31), (2.33) and (2.34), to define the following system of equations:

$$\begin{cases} [Z_D(j\omega)]\{Y(j\omega)\} = \{U(j\omega)\} - \left[B_C^T\right]\{\Lambda_C(j\omega)\} \\ [B_C]\{Y(j\omega)\} = \{0\} \end{cases} \tag{2.47}$$

by solving the first set of equations to obtain the value of $\{Y(j\omega)\}$ and by dropping $[\bullet]$, $\{\bullet\}$ and $(j\omega)$ for ease of readability, yields:

$$\begin{cases} Y = H_D(U - B_C^T \Lambda_C) \\ B_C Y = 0 \end{cases} \tag{2.48}$$

where, $[H_D(j\omega)]$ is given below.

$$[H_D(j\omega)] = [Z_D(j\omega)]^{-1} \tag{2.49}$$

After performing some mathematical manipulations with the system of equations given in expression (2.48), we may define the following relations.

$$\begin{cases} Y = H_D \left(I - B_C^T \left(B_C H_D B_C^T \right)^{-1} B_C H_D \right) U \\ \Lambda_C = \left(B_C H_D B_C^T \right)^{-1} B_C H_D U \end{cases} \tag{2.50}$$

The first set of equations of the system of equations (2.50) can be used to define an expression to calculate the coupled FRFs as follows

$$[\bar{H}(j\omega)] = \frac{\{\bar{Y}(j\omega)\}}{\{\bar{U}(j\omega)\}} = H_D \left(I - B_C^T \left(B_C H_D B_C^T \right)^{-1} B_C H_D \right) \tag{2.51}$$

where, $[\bar{H}(j\omega)]$ denotes the coupled set of FRFs. Expression (2.51) enables the computation of coupled FRFs in a dual manner. A physical interpretation of this expression can be found in [12]. This coupling approach was proposed by de Klerk et al. in [23], where it was tagged as Lagrange Multiplier Frequency Based Substructucturing (LM-FBS) method.

Unlike the primal assembly formulation, the dual assembly formulation does not impose compatibility by retaining the unique set of DOFs. Thus, for each pair of coupled DOFs, $[\bar{H}(j\omega)]$ will present two interface outputs and two interface inputs, whose physical meaning is the same. To remove these redundant interface outputs and inputs, for each pair of coupled DOFs we must remove a row and a column of $[\bar{H}(j\omega)]$ associated with one of those outputs and inputs, respectively.

In alternative, to avoid the manual elimination of the redundant interface outputs and inputs, we can use the previously defined Boolean localization matrix (see equation (2.37)) to retain a unique set of outputs and inputs [27]. Thereby, let us use expression (2.45) to define the following relation:

$$\{U(j\omega)\} = \left([L_C]^T \right)^\dagger \left\{ \tilde{U}(j\omega) \right\} \tag{2.52}$$

where, superscript † denotes the Moore-Penrose pseudoinverse of a matrix. By using expressions (2.51), (2.35) and (2.52), we can define the following expression.

$$[L_C] \{\tilde{Y}(j\omega)\} = [\bar{H}(j\omega)] \left([L_C]^T \right)^\dagger \left\{ \tilde{U}(j\omega) \right\} \tag{2.53}$$

Finally, expression (2.53) can be rewritten as follows

$$\{\tilde{Y}(j\omega)\} = \left[\tilde{H}(j\omega)\right]\left\{\tilde{U}(j\omega)\right\} \tag{2.54}$$

where, $\left[\tilde{H}(j\omega)\right]$ represents the coupled FRFs, which are composed by unique sets of outputs and inputs. $\left[\tilde{H}(j\omega)\right]$ is given below.

$$\left[\tilde{H}(j\omega)\right] = [L_C]^\dagger\left[\bar{H}(j\omega)\right]\left([L_C]^T\right)^\dagger \tag{2.55}$$

Note that, even though we have presented the LM-FBS method by coupling receptance FRFs, it continues to be valid to couple other kinds of FRFs, such as mobility and accelerance.

Decoupling

To perform decoupling, we may exploit the Inverse Coupling approach [36]. By following this method, the primal assembly formulation presented above is still valid. However, we should multiply the impedance matrices of the substructures to be decoupled by −1. Similarly, to perform decoupling by using LM-FBS, the procedures presented above still hold, but the FRFs of the substructures to be decoupled must be multiplied by −1.

Nevertheless, different strategies can be followed to perform decoupling. One can, for example, decouple a substructure from an assembled system by enforcing the compatibility and equilibrium conditions at the interface DOFs, hence by following the presented procedures to perform coupling operations, but by using the impedance or admittance of the substructure to be decoupled multiplied by −1. However, when performing decoupling operations with assemblies/substructures described by their experimentally acquired FRFs, this approach is known for amplifying possible measurement errors, leading to inaccurate results. In an attempt to increase the robustness of the decoupling operations, information measured at internal DOFs may also be included. This leads, in general, to an improvement of the observability, controlability and conditioning of the problem [37]. Thereby, decreasing the sensitivity of the decoupling operations to measurement errors [38]. Detailed discussions on different approaches to perform decoupling in frequency domain can be found, for instance, in [36],[38],[27],[39],[37].

Substructuring via compatibility relaxation

Here, we will derive the variant of the LM-FBS method (see section 2.2.2) proposed in [20] that enables the inclusion of CEs into the coupling operations via compatibility relaxation. To start, let us analyze the assembled structure composed by two substructures connected by a CE depicted in figure 2.3. We will assume that this CE is massless and that no cross couplings between its DOFs exists. If these conditions hold, the relations given below are valid [17].

$$[Z_{M,11}(j\omega)] = -[Z_{M,12}(j\omega)] = -[Z_{M,21}(j\omega)] = [Z_{M,22}(j\omega)] = [Z_M(j\omega)] \qquad (2.56)$$

As substructures α and β are connected through the CE M, relative displacement between their interfaces is allowed. This relative displacement is associated with the connecting forces acting on the interfaces of the CE (see figure 2.4). Thus, by generalizing for coupling an unlimited number of substructures connected by an unlimited number of CEs, we may determine the relative displacement between the interfaces of the connected substructures as given hereafter [18].

$$[B_C]\{Y(j\omega)\} = [Z_{M,D}(j\omega)]^{-1}\{\Lambda_C(j\omega)\} \qquad (2.57)$$

where, matrix $[Z_{M,D}(j\omega)]$ is given below.

$$[Z_{M,D}(j\omega)] = \begin{bmatrix} Z_{M_1}(j\omega) & & \\ & Z_{M_2}(j\omega) & \\ & & \ddots \end{bmatrix} \qquad (2.58)$$

Expression (2.57) defines the compatibility conditions, mathematically. The local equilibrium conditions given by the first set of equations of the system of equations (2.47) are still valid, because the CE is assumed to be massless [17]. Thus, by using the top set of equations of the system of equations (2.47) and expression (2.57), we may define the following system of equations

$$\begin{cases} [Z_D(j\omega)]\{Y(j\omega)\} = \{U(j\omega)\} - [B_C^T]\{\Lambda_C(j\omega)\} \\ [B_C]\{Y(j\omega)\} = [Z_{M,D}(j\omega)]^{-1}\{\Lambda_C(j\omega)\} \end{cases} \qquad (2.59)$$

by solving the first set of equations of the system of equations (2.59) to find the value of $\{Y(j\omega)\}$ and by pre-multiplying the resultant expression by $[B_C]$, we may define the following expression.

$$[B_C]\{Y(j\omega)\} = [B_C][H_D(j\omega)]\{U(j\omega)\} - [B_C][H_D(j\omega)][B_C^T]\{\Lambda_C(j\omega)\} \qquad (2.60)$$

By using expression (2.60) and by dropping $[\bullet]$, $\{\bullet\}$ and $(j\omega)$, we may rewrite the second set of equations of the system of equations (2.59) as follows

$$Z_{M,D}^{-1}\Lambda_C = B_C H_D U - B_C H_D B_C^T \Lambda_C \qquad (2.61)$$

after performing some mathematical manipulations, we may arrive to the following relation:

$$\Lambda_C = \left(H_{M,D} + B_C H B_C^T\right)^{-1} B_C H U \tag{2.62}$$

where, $[H_{M,D}]$ is given below.

$$H_{M,D} = Z_{M,D}^{-1} \tag{2.63}$$

By using expression (2.62) and after performing some mathematical manipulations, we may rewrite the first set of equations of the system of equations (2.59) as given below.

$$Y = H_D U - H_D B_C^T \left(H_{M,D} + B_C H_D B_C^T\right)^{-1} B_C H_D U \tag{2.64}$$

Thus, we can define an expression that enables the computation of coupled FRFs by exploiting LM-FBS via compatibility relaxation as given below.

$$[\tilde{H}(j\omega)] = \frac{\{\tilde{Y}(j\omega)\}}{\{\tilde{U}(j\omega)\}} = H_D \left(I - B_C^T \left(H_{M,D} + B_C H_D B_C^T\right)^{-1} B_C H_D\right) \tag{2.65}$$

Note that, as the used compatibility conditions to develop this variant of the LM-FBS formulation do not impose null relative displacement between the interfaces of the coupled substructures (see expression (2.135)), the computed coupled FRFs will be composed by unique sets of coupled outputs and inputs. Hence, there is no need to eliminate outputs and inputs from the obtained coupled FRFs. Moreover, it is also worth mentioning that expression (2.65) can be used to couple any kind of FRFs, such as receptance, mobility and accelerance.

2.2.3   State-Space Substructuring

The State-Space Substructuring (SSS) techniques make use of state-space models to represent the dynamics of the components to be coupled. These approaches are suitable to perform coupling with numerically and experimentally characterized substructures.

One of the first SSS techniques was proposed by Su and Juang in [9] (for this reason, from now on it will be denoted as classical SSS). To implement this approach, we must start by constructing an uncoupled state-space model by concatenating in a block diagonal form the models of the substructures to be coupled. Then, to mathematically define the coupling conditions (compatibility and equilibrium), a coupling matrix is exploited. Finally, by imposing these conditions on the constructed uncoupled state-space model, a coupled state-space model can be computed. This approach revealed to be simple and to be able to successfully couple an unlimited number of substructures at same time. However, this method also revealed to present two important limitations. On the one hand, classical SSS requires the computation of two matrix inversions, on the other hand, this approach is unable to compute minimal-order coupled models.

Thereby, the computed coupled models will contain redundant states. These redundant states do not perturb the input-output transfer functions of the coupled state-space model [9]. Nevertheless, the computation of minimal-order coupled models is still interesting for two main reasons. Firstly, minimal-order coupled state-space models are free of redundant states, hence they are composed by a lower number of states. For this reason, the computational effort required to perform calculations with them is lower. Secondly, minimal-order coupled models are more elegant representations of the dynamics of coupled structures.

When performing DS operations, we must eliminate one interface DOF for each pair of connected DOFs. Thus, to obtain a minimal-order coupled model, for each pair of connected DOFs, we must eliminate one state and its respective first order derivative [9]. Thereby, the number of states included in a minimal-order coupled state-space model is $n - 2n_J$ (where, n is the sum of the number of states of the state-space models of the coupled substructures, while n_J is the number of interface outputs). By coupling models represented in the physical domain (whose states and outputs present the same physical meaning, hence composed by $2n_o$ states (where, n_o denotes the number of outputs)), the states, which before coupling represented matching interface outputs, will be representative of the correspondent coupled interface outputs (the same is valid for the respective first order derivatives). Hence, the coupled model will include pairs of states and respective first order derivatives, whose physical meaning is the same. To compute a minimal-order coupled model, we cannot simply eliminate from the coupled model one state for each pair of states, whose physical meaning is the same, because each of these states contributes to the dynamics of the coupled model. Thus, to properly compute a minimal-order coupled model, this state elimination must guarantee that the contribution of each eliminated state is retrieved by the one kept in the coupled model. Two post-processing procedures to perform this operation will be discussed in section 2.3.3.

In contrast, when the state-space models are estimated from experimentally acquired data (e.g. from measured FRFs), they are usually represented in the modal domain (see, for instace, [40],[10]). For this reason, it is difficult to point out the states that correspond to matching interface DOFs, which turns the elimination of the redundant states infeasible. To circumvent this difficulty, one could think on transforming the identified state-space models from the modal domain into the physical domain. However, as argued in [41],[42], the transformation of models identified from experimental data into the physical domain is not feasible. For these models $n >> n_o$ is usually verified, consequently, the transformation of these state-space models into physical domain would impose a tremendous constraint in the models to force them to be composed by $2n_o$ states.

An approach to compute minimal-order coupled state-space models was proposed by Sjövall and Abrahamsson in [8]. In their work, they suggested to couple the state-space models of the substructures, previously, transformed into the so-called coupling form.

The coupling form is based on the application of a similarity state vector transformation that enables the partial transformation of the state vector of the state-space models into physical domain. After performing this similarity transformation, the state vector of the state-space models is composed by the first derivative of the interface outputs, by the interface outputs and by $n - 2n_J$ internal states.

When represented in coupling form, the first block row of the state equation of the state-space models represents a second order differential equation. Thereby, coupling can be performed by directly summing those first block rows [41],[43]. Performing coupling in this way is feasible, because the coupling form proposed in [8] guarantees that the interface inputs of the models do not contribute to the response of their internal states. Thus, the internal states are not involved on the coupling operation, being the state-space matrix terms associated with them only correctly placed on the coupled state-space model [41].

This coupling method demonstrated to be able to solve the problems pointed to classical SSS. On the one hand, the coupled model can be computed by performing a single matrix inversion and, on the other hand, a minimal order coupled model is directly computed. Nevertheless, this approach imposes the limitation of coupling just two substructures at same time. In addition, the construction of the transformation matrix to transform the state-space models into coupling form is not straightforward, because it requires the choice of a subspace from a nullspace. In [41], Gibanica showed that this choice is difficult to be performed and that it strongly affects the performance of the transformation.

In [41], Gibanica developed a novel SSS method by porting the SSS approach proposed in [8] into the general framework presented in [12]. This method turned out to be able to couple an unlimited number of substructures at same time. However, it requires the performance of two matrix inversions to compute the coupled state-space model.

Recently, Kammermeier et al. developed a novel SSS method in [44] based on a dual assembly formulation. This method was later labelled as Lagrange Multiplier State-Space Substructuring (LM-SSS) in [1]. LM-SSS is able to couple an unlimited number of substructures at same time and only requires the performance of a single matrix inversion to compute coupled state-space models. Thus, LM-SSS combines the advantage of coupling an unlimited number of structures (pointed to classical SSS) with the advantage of requiring a single matrix inversion to compute the coupled model (pointed to the method developed in [8]).

However, LM-SSS presents some important limitations. As this method makes use of a dual assembly formulation, the full set of interface DOFs is retained during the performance of coupling operations. Hence, we are required to eliminate the redundant DOFs from the coupled state-space models obtained with LM-SSS. In addition, this approach is unable to compute minimal-order coupled state-space models and it is only capable of coupling acceleration state-space models (i.e. state-space models, whose output vector elements are accelerations, respectively). Hence, if we are interested on

computing a displacement or a velocity coupled model (i.e. state-space models, whose output vector elements are displacements and velocity, respectively), we are forced to firstly compute an acceleration coupled model with LM-SSS. Then, the correspondent displacement or velocity coupled models can be obtained from the acceleration one (see [45]). However, the computation of displacement and velocity coupled models from acceleration ones is not convenient, because it involves the inversion of the state matrix of the coupled model.

Despite the limitations here pointed to LM-SSS, in section 2.3 it will be shown that they can be mitigated by using tailored post-processing procedures. In this way, LM-SSS will combine the advantages of the methods proposed in [9],[8] without presenting any important disadvantage or limitation. Thus, becoming a very promising SSS approach. This is the reason why, in the following, we will present the dual assembly formulation in the state-space domain (also named LM-SSS). Additionally, we will also discuss how to perform decoupling by using this approach.

Note that, in contrast with sections 2.2.1 and 2.2.2, here we will not present a primal state-space assembly formulation neither the extension of the dual assembly formulation to include CEs via compatibility relaxation. These techniques will be, respectively, presented in sections 2.4 and 2.5. This is justified by the fact that these approaches were not part of the state-of-the-art, before the performance of the research activities described in this document. These formulations were, actually, developed in one of the authors' publications (i.e. in [2]).

Dual Formulation

In this section, we will present the dual assembly State-Space Substructuring formulation [44], also known as Lagrange Multiplier State-Space Substructuring (LM-SSS) method [1].

The first step to derive the LM-SSS method is the construction of a so-called diagonal coupled state-space model. This model can be constructed by concatenating the state-space matrices of each state-space model of each substructure to be coupled in a block diagonal form. Moreover, we must also consider the connecting forces that act on the interface of the coupled substructures and that are responsible for keeping the components coupled (see figure 2.2). Thereby, assuming that an unlimited number of substructures is intended to be coupled, we can define the diagonal coupled state-space model as follows

$$
\begin{aligned}
\{\dot{x}_S(t)\} &= [A_{S,D}]\{x_S(t)\} + [B_{S,D}]\left(\{u(t)\} - \{g(t)\}\right) \\
\{\ddot{y}(t)\} &= \left[C_{S,D}^{accel}\right]\{x_S(t)\} + \left[D_{S,D}^{accel}\right]\left(\{u(t)\} - \{g(t)\}\right)
\end{aligned}
\tag{2.66}
$$

with,

$$\{x_S(t)\} = \begin{Bmatrix} x_\alpha(t) \\ x_\beta(t) \\ \vdots \end{Bmatrix}, \{y(t)\} = \begin{Bmatrix} y_\alpha(t) \\ y_\beta(t) \\ \vdots \end{Bmatrix}$$

$$\{u(t)\} = \begin{Bmatrix} u_\alpha(t) \\ u_\beta(t) \\ \vdots \end{Bmatrix}, \{g(t)\} = \begin{Bmatrix} g_\alpha(t) \\ g_\beta(t) \\ \vdots \end{Bmatrix} \tag{2.67}$$

$$[A_{S,D}] = \begin{bmatrix} A_\alpha & & \\ & A_\beta & \\ & & \ddots \end{bmatrix}, \quad [B_{S,D}] = \begin{bmatrix} B_\alpha & & \\ & B_\beta & \\ & & \ddots \end{bmatrix}$$

$$[C_{S,D}^{accel}] = \begin{bmatrix} C_\alpha^{accel} & & \\ & C_\beta^{accel} & \\ & & \ddots \end{bmatrix}, \quad [D_{S,D}^{accel}] = \begin{bmatrix} D_\alpha^{accel} & & \\ & D_\beta^{accel} & \\ & & \ddots \end{bmatrix} \tag{2.68}$$

$\{x(t)\} \in \mathbb{R}^{n \times 1}$ represents the state vector, $\{u(t)\} \in \mathbb{R}^{n_i \times 1}$ represents the input vector, whose elements are the external applied forces and $\{\ddot{y}(t)\} \in \mathbb{R}^{n_o \times 1}$ represents the acceleration output vector. $[A] \in \mathbb{R}^{n \times n}$, $[B] \in \mathbb{R}^{n \times n_i}$, $[C] \in \mathbb{R}^{n_o \times n}$ and $[D] \in \mathbb{R}^{n_o \times n_i}$ represent, respectively, state, input, output and feedthrough matrices. Superscript *accel* denotes a state-space matrix of an acceleration state-space model, while subscript S denotes state vectors and state-space matrices of state-space models representative of the dynamics of substructures.

By using expression (2.1), expression (2.66) can be rewritten as given below.

$$\{\dot{x}_{S,D}(t)\} = [A_{S,D}]\{x_{S,D}(t)\} + [B_{S,D}](\{u(t)\} - [B_C]^T\{\lambda_C(t)\})$$
$$\{\ddot{y}(t)\} = [C_{S,D}^{accel}]\{x_{S,D}(t)\} + [D_{S,D}^{accel}](\{u(t)\} - [B_C]^T\{\lambda_C(t)\}) \tag{2.69}$$

To couple the substructures, we must impose continuity at their interface. This condition was already, mathematically, defined in expression (2.9). However, here we are working with state-space models, whose outputs represent accelerations, thus equation (2.9) must be set-up in terms of accelerations.

$$[B_C]\{\ddot{y}(t)\} = \{0\} \tag{2.70}$$

Besides the compatibility requirement at the interface, the coupled substructures have to verify the local equilibrium conditions defined by the output equation of the state-space model given in expression (2.69). By solving these equations to determine $\{u(t)\}$, we may obtain the expression given below.

$$\{u(t)\} = [D_{S,D}^{accel}]^{-1}(\{\ddot{y}(t)\} - [C_{S,D}^{accel}]\{x_{S,D}(t)\}) + [B_C]^T\{\lambda_C(t)\} \tag{2.71}$$

By using the expressions representative of the compatibility and equilibrium conditions (i.e. equations (2.70) and (2.71), respectively), and by dropping $\{\bullet\}$, $[\bullet]$ and (t) for ease of readability, we can set-up the following system of equations.

$$
\begin{cases}
(D_{S,D}^{accel})^{-1}(\ddot{y} - C_{S,D}^{accel}x_{S,D}) + B_C^T\lambda_C = u \\
B_C\ddot{y} = 0
\end{cases}
\tag{2.72}
$$

By performing some mathematical manipulations, the system of equations (2.72) can be rewritten as given hereafter.

$$
\begin{cases}
\lambda_C = (B_C D_{S,D}^{accel} B_C^T)^{-1}(B_C C_{S,D}^{accel}x_S + B_C D_{S,D}^{accel}u) \\
\ddot{y} = (C_{S,D}^{accel} - D_{S,D}^{accel}B_C^T(B_C D_{S,D}^{accel} B_C^T)^{-1}B_C C_{S,D}^{accel})x_{S,D} \\
\quad + (D_{S,D}^{accel} - D_{S,D}^{accel}B_C^T(B_C D_{S,D}^{accel} B_C^T)^{-1}B_C D_{S,D}^{accel})u
\end{cases}
\tag{2.73}
$$

By using equation (2.71) and the bottom equation of the system of equations (2.73), the state equations of the diagonal coupled state-space model (equation (2.69)) can be rewritten as given below.

$$
\begin{aligned}
\dot{x}_{S,D} &= (A_{S,D} - B_{S,D}B_C^T(B_C D_{S,D}^{accel} B_C^T)^{-1}B_C C_{S,D}^{accel})x_{S,D} \\
&\quad + (B_{S,D} - B_{S,D}B_C^T(B_C D_{S,D}^{accel} B_C^T)^{-1}B_C D_{S,D}^{accel})u
\end{aligned}
\tag{2.74}
$$

By using equation (2.74) and the bottom equation of the system of equations (2.73), the coupled state-space model can be defined as follows

$$
\begin{aligned}
\{\dot{\bar{x}}(t)\} &= [\bar{A}]\{\bar{x}(t)\} + [\bar{B}]\{\bar{u}(t)\} \\
\{\ddot{\bar{y}}(t)\} &= [\bar{C}^{accel}]\{\bar{x}(t)\} + [\bar{D}^{accel}]\{\bar{u}(t)\}
\end{aligned}
\tag{2.75}
$$

where,

$$
\begin{aligned}
[\bar{A}] &= A_{S,D} - B_{S,D}B_C^T(B_C D_{S,D}^{accel} B_C^T)^{-1}B_C C_{S,D}^{accel} \\
[\bar{B}] &= B_{S,D} - B_{S,D}B_C^T(B_C D_{S,D}^{accel} B_C^T)^{-1}B_C D_{S,D}^{accel} \\
[\bar{C}^{accel}] &= C_{S,D}^{accel} - D_{S,D}^{accel}B_C^T(B_C D_{S,D}^{accel} B_C^T)^{-1}B_C C_{S,D}^{accel} \\
[\bar{D}^{accel}] &= D_{S,D}^{accel} - D_{S,D}^{accel}B_C^T(B_C D_{S,D}^{accel} B_C^T)^{-1}B_C D_{S,D}^{accel}
\end{aligned}
\tag{2.76}
$$

overbar variables represent vectors/matrices associated with the coupled state-space model.

It is worth mentioning that several system identification algorithms developed to identify state-space models from experimentally acquired data (e.g. from measured FRFs) provide an estimation of displacement state-space models (see, for instance, [46]). Nevertheless, to derive the LM-SSS method we have exploited acceleration models, hence LM-SSS is only capable of coupling acceleration models. Thereby, to apply the LM-SSS equations given in (2.75) and (2.76), the identified displacement state-

space models must be previously double-differentiated to compute the correspondent acceleration models.

By double differentiating a given identified displacement state-space model, we can obtain the correspondent acceleration model as follows [45]

$$\{\dot{x}(t)\} = [A^{accel}]\{x(t)\} + [B^{accel}]\{u(t)\}$$
$$\{\ddot{y}(t)\} = [C^{accel}]\{x(t)\} + [D^{accel}]\{u(t)\}$$

(2.77)

where, matrices $[A^{accel}]$, $[B^{accel}]$, $[C^{accel}]$ and $[D^{accel}]$ can be computed from the state-space matrices of the identified displacement model as:

$$[A^{accel}] = [A], \quad [B^{accel}] = [B]$$
$$[C^{accel}] = \left[C^{disp}AA\right], \quad [D^{accel}] = \left[C^{disp}AB\right] + [D^{disp}]$$

(2.78)

where, superscript *disp* denotes state-space matrices of a displacement state-space model and $[D^{disp}] = [0]$.

Decoupling

To perform decoupling in the state-space domain, the SSS methods proposed in literature (see, for instance, [9], [8], [44]) are still valid. However, the state-space models of the substructures to be decoupled must be represented in negative form [47], [43]. To derive the negative form of a given state-space model, let us consider an acceleration state-space model directly defined from the mass, damping and stiffness matrices of a given mechanical system [41] as follows:

$$\{\dot{x}(t)\} = [A]\{x(t)\} + [B]\{u(t)\}$$
$$\{\ddot{y}(t)\} = [C^{accel}]\{x(t)\} + [D^{accel}]\{u(t)\}$$

(2.79)

where, the state-space matrices are given below.

$$[A] = \begin{bmatrix} -M^{-1}V & -M^{-1}K \\ I & 0 \end{bmatrix}, \quad [B] = \begin{bmatrix} M^{-1} \\ 0 \end{bmatrix}$$
$$[C^{accel}] = \begin{bmatrix} -M^{-1}V & -M^{-1}K \end{bmatrix}, \quad [D^{accel}] = \begin{bmatrix} M^{-1} \end{bmatrix}$$

(2.80)

To compute the negative form of the state-space model given in expression (2.79), we must multiply the matrices $[M]$, $[V]$ and $[K]$ by -1 [43],[47], as given hereafter.

$$[A] = \begin{bmatrix} -(-M)^{-1}(-V) & -(-M)^{-1}(-K) \\ I & 0 \end{bmatrix}, \quad [B] = \begin{bmatrix} -M^{-1} \\ 0 \end{bmatrix}$$
$$[C^{accel}] = [-(-M)^{-1}(-V) \quad -(-M)^{-1}(-K)], \quad [D^{accel}] = \begin{bmatrix} -M^{-1} \end{bmatrix}$$

(2.81)

From the state-space matrices of the model given in expression (2.81), it is evident that to compute the negative form of an acceleration state-space model, we must multiply its input and feedthrough matrices by -1, while its state and output matrices must remain unchanged. Although, the negative form of a state-space model was derived by using an acceleration model directly constructed from the mass, damping and stiffness matrices of a given system, the procedure here presented continues to be valid to transform displacement and velocity state-space models into negative form. Moreover, the state-space models can be established in any domain (for example, in the modal domain), this approach remains valid to transform them into negative form.

After having performed the intended decoupling operations, we must retain from the obtained state-space model the inputs and outputs of the substructure to be identified, while the other inputs and outputs must be eliminated. This can be performed by only keeping the columns of the input and feedthrough matrices associated with the inputs of the component to be identified and by keeping the rows of the output and feedthrough matrices associated with the outputs of the same component.

2.3   Mitigating the limitations of LM-SSS

In this section, approaches to mitigate all the limitations pointed to the LM-SSS method in section 2.2.3 will be presented. To start, in section 2.3.1, the LM-SSS formulation is extended to be capable of directly performing coupling operations with displacement and velocity models. This extension of LM-SSS enables a direct computation of displacement, velocity and acceleration coupled state-space models. Then, a novel coupling form, specially tailored to perform coupling with LM-SSS, is outlined in section 2.3.2, whereas section 2.3.3 presents two novel post-processing procedures to enable the elimination of the redundant states originated from DS operations. Thereby, the performance of coupling with LM-SSS by using state-space models transformed into UCF together with these post-processing procedures makes the computation of minimal-order coupled models possible.

Afterwards, in section 2.3.4 a post-processing procedure to retain a unique set of DOFs from coupled state-space models obtained with LM-SSS is proposed. This development enables a smooth elimination of the redundant DOFs included in the coupled state-space models computed with LM-SSS, avoiding, in this way, the need of manually eliminating them. Finally, in section 2.3.5, the LM-SSS method enhanced with the proposed post-processing procedures is compared with the SSS methods presented in [9] and [8].

2.3.1 Extending LM-SSS to compute displacement and velocity coupled models

The LM-SSS method presented in section 2.2.3 will be here extended to directly compute displacement and velocity coupled state-space models. To start, let us exploit the relations defined in equation (2.78) to rewrite expression (2.76) as follows:

$$
\begin{aligned}
[\bar{A}] &= A_{S,D} - B_{S,D}E(C_{S,D}^{disp}A_{S,D}A_{S,D}) \\
[\bar{B}] &= B_{S,D} - B_{S,D}E(C_{S,D}^{disp}A_{S,D}B_{S,D}) \\
[\bar{C}^{accel}] &= C_{S,D}^{disp}A_{S,D}A_{S,D} - (C_{S,D}^{disp}A_{S,D}B_{S,D})E(C_{S,D}^{disp}A_{S,D}A_{S,D}) \\
[\bar{D}^{accel}] &= C_{S,D}^{disp}A_{S,D}B_{S,D} - (C_{S,D}^{disp}A_{S,D}B_{S,D})E(C_{S,D}^{disp}A_{S,D}B_{S,D})
\end{aligned}
\tag{2.82}
$$

where, $[E]$ is given below.

$$
[E] = B_C^T(B_C(C_{S,D}^{disp}A_{S,D}B_{S,D})B_C^T)^{-1}B_C
\tag{2.83}
$$

By using expressions (2.78), equation (2.82) can be rewritten to compute coupled displacement state-space models as given below.

$$
\begin{aligned}
[\bar{A}] &= A_{S,D} - B_{S,D}E(C_{S,D}^{disp}A_{S,D}A_{S,D}) \\
[\bar{B}] &= B_{S,D} - B_{S,D}E(C_{S,D}^{disp}A_{S,D}B_{S,D}) \\
[\bar{C}^{disp}] &= C_{S,D}^{disp} - (C_{S,D}^{disp}A_{S,D}B_{S,D})E(C_{S,D}^{disp}) \\
[\bar{D}^{disp}] &= C_{S,D}^{disp}A_{S,D}B_{S,D} - (C_{S,D}^{disp}A_{S,D}B_{S,D})E(C_{S,D}^{disp}A_{S,D}B_{S,D})- \\
&\qquad \bar{C}^{disp}\bar{A}\bar{B} = 0
\end{aligned}
\tag{2.84}
$$

By exploiting the relations between the state-space matrices of acceleration and velocity state-space models (see [45]), expression (2.82) can be rewritten to directly calculate coupled velocity state-space models as follows:

$$
\begin{aligned}
[\bar{A}] &= A_{S,D} - B_{S,D}E(C_{S,D}^{disp}A_{S,D}A_{S,D}) \\
[\bar{B}] &= B_{S,D} - B_{S,D}E(C_{S,D}^{disp}A_{S,D}B_{S,D}) \\
[\bar{C}^{vel}] &= C_{S,D}^{disp}A_{S,D} - (C_{S,D}^{disp}A_{S,D}B_{S,D})E(C_{S,D}^{disp}A_{S,D}) \\
[\bar{D}^{vel}] &= C_{S,D}^{disp}B_{S,D} - (C_{S,D}^{disp}A_{S,D}B_{S,D})E(C_{S,D}^{disp}B_{S,D})
\end{aligned}
\tag{2.85}
$$

where, superscript *vel* denotes state-space matrices of velocity state-space models. Note that, if the coupled state-space model obeys Newton's second law $[C_{S,D}^{disp}B_{S,D}] = [0]$ [45],[8], hence $[\bar{D}^{vel}] = [0]$.

2.3.2 Unconstrained Coupling Form

When performing coupling with state-space models that are not defined in the physical domain, these models must be previously transformed into coupling form in order to open the possibility of computing minimal-order coupled state-space models (see section 2.2.3). This is also valid, when performing decoupling operations, because this DS operation also promotes the presence of redundant states in the resultant state-space model.

The transformation of the state vector of a given state-space model representative of the dynamics of a given substructure into coupling form can be defined as follows [8]:

$$\{z(t)\} = [T_{CF}]\{q(t)\} = \begin{Bmatrix} \dot{y}^J(t) \\ y^J(t) \\ x^I(t) \end{Bmatrix} \tag{2.86}$$

where, $[T_{CF}] \in \mathbb{R}^{n \times n}$ is the matrix responsible for transforming a state-space model into coupling form, $\{q(t)\} \in \mathbb{R}^{n \times 1}$ represents a state vector expressed in a given domain and $\{z(t)\} \in \mathbb{R}^{n \times 1}$ represents a state vector transformed into coupling form. Superscripts J and I denote variables related to interface and internal DOFs, respectively.

Matrix $[T_{CF,\alpha}]$ can be constructed as follows:

$$[T_{CF}] = \begin{bmatrix} C^{disp,J}A \\ C^{disp,J} \\ N \end{bmatrix} \tag{2.87}$$

where, the first and second block rows transform the states into the first derivative of the output DOFs and into the output DOFs [45], respectively. The last block row (i.e. $N \in \mathbb{R}^{(n-2n_J) \times n}$) applies a transformation on the internal states and it is included on $[T_{CF}]$ to make sure that the dimension of the state-space matrices is preserved.

Unlike the approach proposed by Sövall and Abrahamsson in [8], when using LM-SSS, all the states are involved (including the internal states) in the DS operations. For this reason, $[N]$ does not have to be computed to make sure that the interface inputs do not contribute for the response of the internal states. Therefore, provided that $[T_{CF}]$ is invertible and full rank, any transformation can be applied on the internal states. Thereby, $[N]$ can be computed as follows:

$$\begin{bmatrix} C^{disp,J}A \\ C^{disp,J} \end{bmatrix} [N]^T = 0 \tag{2.88}$$

By computing $[N]$ as given in expression (2.88), we make sure that $[T_{CF}]$ is always full rank, provided that $[C^{disp}]$ is full row rank. In this way, expression (2.88) concludes the development of a novel coupling form specifically suited to perform coupling with LM-SSS. This coupling form will be from now on denoted Unconstrained Coupling

Form (UCF), because it is simple and it provides almost complete freedom for the transformation of the internal states.

By comparing UCF with the coupling form proposed in [8], UCF has the advantage of not requiring the selection of a subspace from a nullspace. This is an important advantage, because the selection of the subspace used to define the similarity transformation matrix to transform state-space models into the coupling form proposed in [8] is hard to be made and strongly affects the accuracy of the transformation [41].

It is worth mentioning that the input and the output vectors of a given state-space model to be transformed into coupling form must be, previously, partitioned in terms of interface and internal DOFs as given hereafter.

$$\{u(t)\} = \begin{Bmatrix} u^J(t) \\ u^I(t) \end{Bmatrix} \qquad (2.89a) \qquad \{y(t)\} = \begin{Bmatrix} y^J(t) \\ y^I(t) \end{Bmatrix} \qquad (2.89b)$$

Obviously, the rows and columns of the state-space matrices of the model must be sorted in accordance with the input and output vectors.

2.3.3   Minimal-Order Coupled State-Space Models

When coupling state-space models, for each pair of connected DOFs, one interface DOF must be eliminated to avoid the presence of redundant DOFs on the coupled state-space model. Similarly, one state and its correspondent first derivative must be eliminated to make sure that a minimal order coupled model, thus free of redundant states originated from the coupling operation, is obtained [9]. LM-SSS method is unable to directly compute a coupled state-space model free of redundant inputs and outputs and, it is also unable to directly compute minimal-order coupled state-space models. Procedures to remove the redundant inputs and outputs present in the coupled models obtained with LM-SSS are discussed in section 2.3.4. Here, we will focus our attention on the elimination of the redundant states originated from coupling operations by proposing two post-processing procedures to eliminate these states from the coupled models computed with LM-SSS.

To start, let us assume that acceleration state-space models representative of the substructures depicted in figure 2.1 have been coupled by exploiting LM-SSS. Let us further assume that before being coupled, the state-space models of these substructures were transformed into coupling form. Thereby, the obtained coupled state-space model can be represented as follows:

$$\begin{aligned} \{\dot{\bar{z}}(t)\} &= [\bar{A}]\{\bar{z}(t)\} + [\bar{B}]\{\bar{u}(t)\} \\ \{\ddot{\bar{y}}(t)\} &= [\bar{C}^{accel}]\{\bar{z}(t)\} + [\bar{D}^{accel}]\{\bar{u}(t)\} \end{aligned} \qquad (2.90)$$

where, the state vector is given below.

$$\{\bar{z}(t)\} = \left\{ \dot{\bar{y}}_{\alpha}^{J}(t) \quad \bar{y}_{\alpha}^{J}(t) \quad \bar{x}_{\alpha}^{I}(t) \quad \dot{\bar{y}}_{\beta}^{J}(t) \quad \bar{y}_{\beta}^{J}(t) \quad \bar{x}_{\beta}^{I}(t) \right\}^{T} \tag{2.91}$$

Recall that to couple these structures, we must impose compatibility at the interface DOFs of both substructures (see section 2.2.3), thus the following identities hold.

$$\{\bar{y}^{J}(t)\} = \{\bar{y}_{\alpha}^{J}(t)\} = \{\bar{y}_{\beta}^{J}(t)\} \quad (2.92a) \qquad \{\dot{\bar{y}}^{J}(t)\} = \{\dot{\bar{y}}_{\alpha}^{J}(t)\} = \{\dot{\bar{y}}_{\beta}^{J}(t)\} \quad (2.92b)$$

From expressions (2.91), (2.92a) and (2.92b), it is evident that the computed coupled state-space model is a non-minimal order model, because it presents states, whose physical meaning is the same (e.g. $\{\bar{y}_{\alpha}^{J}(t)\}$ and $\{\bar{y}_{\beta}^{J}(t)\}$). However, to compute a minimal order coupled model, we cannot simply remove one state and respective first derivative of each pair of states representing the same physical quantity. This is justified by the fact that these states contribute to the dynamics of the coupled model. Hence, when removing these redundant states we must ensure that their contribution is retrieved by the states that remain in the coupled model.

To properly eliminate the redundant states from the coupled model, we may define a signed Boolean matrix as follows:

$$[B_{T}]\{z(t)\} = \{0\} \tag{2.93}$$

where, from now on matrix $[B_{T}]$ will be referred as state mapping matrix. Exemplifying for the coupled state-space model obtained by coupling the substructures shown in figure 2.1, expression (2.93) would be given as follows:

$$[B_{T}]\{z(t)\} = \begin{bmatrix} \phi I & 0 & 0 & -\phi I & 0 & 0 \\ 0 & \phi I & 0 & 0 & -\phi I & 0 \end{bmatrix} \begin{Bmatrix} \dot{\bar{y}}_{\alpha}^{J}(t) \\ \bar{y}_{\alpha}^{J}(t) \\ \bar{x}_{\alpha}^{I}(t) \\ \dot{\bar{y}}_{\beta}^{J}(t) \\ \bar{y}_{\beta}^{J}(t) \\ \bar{x}_{\beta}^{I}(t) \end{Bmatrix} = \{0\} \tag{2.94}$$

where, $[I] \in \mathbb{R}^{n_o \times n_o}$ denotes an identity matrix and ϕ is a numerical coefficient, whose value can be selected to be either 1 or -1.

At this point, we may set-up a relation between the state vector of the original coupled model and of the minimal-order coupled model as follows:

$$\{z(t)\} = [L_{T}]\{\tilde{z}(t)\}, \forall \{\tilde{z}(t)\} \tag{2.95}$$

where, $\{\tilde{z}\} \in \mathbb{R}^{n_{min} \times 1}$ (with n_{min} being the number of states of the minimal-order coupled model) denotes the state vector of the minimal-order coupled state-space model, while from now on $[L_{T}]$ will be denoted as state Boolean localization matrix. Vector

$\{\tilde{z}(t)\}$ must respect equation (2.93), hence we may define the following relations

$$[B_T]\{z(t)\} = [B_T][L_T]\{\tilde{z}(t)\} = \{0\} \tag{2.96}$$

thus, matrix $[L_T]$ can be computed from the nullspace of $[B_T]$ as given below.

$$[L_T] = null([B_T]) \tag{2.97}$$

It is worth mentioning that a matrix defined in similar way as $[L_T]$ has already been exploited in [41],[42] to translate the SSS method proposed in [8] into the general framework presented in [12].

By using expression (2.95), we may rewrite expression (2.90) as given below.

$$[L_T]\{\dot{\tilde{z}}(t)\} = [\bar{A}][L_T]\{\tilde{z}(t)\} + [\bar{B}]\{u(t)\}$$
$$\{\ddot{y}(t)\} = [\bar{C}^{accel}][L_T]\{\tilde{z}(t)\} + [\bar{D}^{accel}]\{u(t)\} \tag{2.98}$$

By exploiting the Moore-Penrose pseudoinverse of matrix $[L_T]$, a minimal realization of the original coupled state-space model computed with LM-SSS (see expression (2.90)) can be defined as given below.

$$\{\dot{\tilde{z}}(t)\} = [L_T]^{\dagger}[\bar{A}][L_T]\{\tilde{z}(t)\} + [L_T]^{\dagger}[\bar{B}]\{u(t)\}$$
$$\{\ddot{y}(t)\} = [\bar{C}^{accel}][L_T]\{\tilde{z}(t)\} + [\bar{D}^{accel}]\{u(t)\} \tag{2.99}$$

The post-processing procedure just presented requires the calculation of the pseudoinverse of matrix $[L_T]$. Thus, it is important to analyze matrix $[L_T]$ to evaluate if the computation of its pseudoinverse will demand important computational effort and if it may introduce numerical problems associated with ill-conditioned matrix inversions.

$[L_T]$ is a matrix of dimension $n \times n_{min}$, with $n > n_{min}$, whose rank is n_{min}. Thus, the pseudoinverse of $[L_T]$ can be computed as given hereafter [48].

$$[L_T]^{\dagger} = (L_T^T L_T)^{-1} L_T^T \tag{2.100}$$

As $[L_T]$ is a Boolean matrix, it will represent an orthogonal basis for the nullspace of $[B_T]$ [3]. Hence, matrix $[L_T]^T[L_T]$ can be defined as follows:

$$[L_T]^T[L_T] = \begin{bmatrix} v_1^T \\ v_2^T \\ \vdots \end{bmatrix} \begin{bmatrix} v_1 & v_2 & \ldots \end{bmatrix} = \begin{bmatrix} v_1 \bullet v_1 & & \\ & v_2 \bullet v_2 & \\ & & \ddots \end{bmatrix} \tag{2.101}$$

where, $v_i \bullet v_j = 0$, $\forall\ i \neq j$, $\bullet$ represents dot product and v_i represents the ith column of $[L_T]$ matrix.

Observing expression (2.101), it is evident that $[L_T]^T[L_T]$ is a diagonal and invertible matrix [28]. Therefore, the computation of $[L_T]^{\dagger}$ will not introduce numerical problems and it will not require important computational effort.

Alternatively, to eliminate the redundant states from the coupled state-space models, we may exploit a manual post-processing procedure. To implement this manual approach, for each pair of redundant sates we must proceed as follows:

- Sum the columns of $[\bar{A}]$ that are associated with the pair of redundant states under analysis and repeat the same operation on the columns of $[\bar{C}^{accel}]$;

- Eliminate the row and column of $[\bar{A}]$ associated to one of those redundant states;

- Eliminate the same row and column of matrices $[\bar{B}]$ and $[\bar{C}^{accel}]$, respectively;

- Repeat the three first steps for the first derivative of the analyzed pair of redundant states.

By exploiting this manual procedure, a minimal-order coupled state-space model can be determined without using $[L_T]$.

It is worth mentioning that the post-processing procedures here discussed to eliminate the redundant states originated from coupling operations still hold and can be exploited in similar manner to eliminate the redundant states originated from decoupling operations.

2.3.4 Retaining the unique set of interface DOFs

The LM-SSS method is a dual DS formulation, thus, when performing DS operations with this technique the full set of interface DOFs is retained. This happens, because the compatibility and equilibrium conditions (see equations (2.70) and (2.71), respectively) used to formulate LM-SSS do not define a direct relation between the unique set of coupled outputs and inputs and the set of outputs and inputs of the state-space models to be coupled. Therefore, for each pair of connected DOFs, two outputs and inputs, whose physical meaning is the same, will be present in the coupled state-space model. To compute a coupled model composed by a unique set of DOFs, for each pair of repeated outputs and inputs, we can simply eliminate one of the rows of the $[C]$ and $[D]$ matrices associated with one of the repeated outputs and one of the columns of the $[B]$ and $[D]$ matrices associated with one of the repeated inputs [1]. Nevertheless, this manual procedure might get cumbersome, when the coupling operations involve the coupling of several interface DOFs belonging to several different substructures.

To ease the elimination of the redundant outputs and inputs that are present in the coupled state-space model, we may exploit the relations between the full and unique sets of outputs and inputs defined in expressions (2.35) and (2.45), respectively. Note that these conditions have already been used in [27] to retain the unique set of DOFs from the coupled set of FRFs obtained by exploiting LM-FBS (this procedure was also shown in section 2.2.2). Note also that, expressions (2.35) and (2.45) are established in the frequency domain. Nevertheless, they are still valid in the time domain, thus we may express them in the time domain as given below.

$$\{\tilde{u}(t)\} = [L_C]^T\{u(t)\} \qquad (2.102a) \qquad \{y(t)\} = [L_C]\{\tilde{y}(t)\} \qquad (2.102b)$$

where, $\{\tilde{u}(t)\}$ represents the unique set of force inputs and $\{\tilde{y}(t)\}$ represents the unique set of displacements outputs.

Let us now consider the following generic acceleration coupled state-space model determined by exploiting LM-SSS.

$$\begin{aligned}
\{\dot{\bar{x}}(t)\} &= [\bar{A}]\{\bar{x}(t)\} + [\bar{B}]\{\bar{u}(t)\} \\
\{\ddot{\bar{y}}(t)\} &= [\bar{C}^{accel}]\{\bar{x}(t)\} + [\bar{D}^{accel}]\{\bar{u}(t)\}
\end{aligned} \qquad (2.103)$$

As the state-space model given in expression (2.103) is an acceleration model, before retaining its unique set of outputs and inputs, we must compute the second order time derivative of equation (2.102b) as given hereafter.

$$\{\ddot{y}(t)\} = [L_C]\{\ddot{\tilde{y}}(t)\} \qquad (2.104)$$

By exploiting equations (2.102a) and (2.104), expression (2.103) can be rewritten as given below.

$$\begin{aligned}
\{\dot{\bar{x}}(t)\} &= [\bar{A}]\{\bar{x}(t)\} + [\bar{B}]([L_C]^T)^\dagger\{\tilde{u}(t)\} \\
[L_C]\{\ddot{\tilde{y}}(t)\} &= [\bar{C}^{accel}]\{\bar{x}(t)\} + [\bar{D}^{accel}]([L_C]^T)^\dagger\{\tilde{u}(t)\}
\end{aligned} \qquad (2.105)$$

Finally, using the pseudoinverse of matrix $[L_C]$, the state-space model given in expression (2.105) can be rewritten as given below.

$$\begin{aligned}
\{\dot{\bar{x}}(t)\} &= [\bar{A}]\{\bar{x}(t)\} + [\bar{B}]([L_C]^T)^\dagger\{\tilde{u}(t)\} \\
\{\ddot{\tilde{y}}(t)\} &= [L_C]^\dagger[\bar{C}^{accel}]\{\bar{x}(t)\} + [L_C]^\dagger[\bar{D}^{accel}]([L_C]^T)^\dagger\{\tilde{u}(t)\}
\end{aligned} \qquad (2.106)$$

The coupled state-space model given in expression (2.106) represents the state-space model given in expression (2.103) composed by a unique set of interface inputs and outputs. Thus, without presenting redundant inputs and outputs.

Note that, as $[L_C]$ is Boolean, it represents an orthogonal basis of the nullspace of $[B_C]$. For this reason, the computation of $[L_C]^\dagger$ and $([L_C]^T)^\dagger$ will not demand important computational effort, because to calculate those matrices we are only required to invert a diagonal matrix (see section 2.3.3).

It is also worth mentioning, that the procedure here presented continues to be valid to eliminate the redundant inputs and outputs of displacement and velocity coupled state-space models computed with LM-SSS.

2.3.5 Comparison of LM-SSS with state-of-the-art SSS techniques

Here, we will perform a comparison between the LM-SSS method enhanced by the post-processing procedures discussed in this section with the SSS methods proposed by Su and Juang (here, also denoted as classical SSS) in [9] and by Sjövall and Abrahamsson in [8].

When exploiting classical SSS, we make use of a so-called coupling matrix to impose both compatibility and equilibrium conditions. This matrix is constructed by only taking into account the interface DOFs of the components to be coupled. Each row of the coupling matrix corresponds to a coupled DOF, while each of its columns is associated with one interface DOF of the components to be coupled. Each row of the coupling matrix is defined by assigning a unitary value to the terms associated with the matching DOFs that are coupled to obtain the coupled DOF associated with the row under construction, while the other terms must be set to zero.

By using the constructed coupling matrix, we can define relations between the interface outputs of the components to be coupled and the unique set of coupled interface outputs. These relations represent the compatibility conditions. Similarly, the equilibrium conditions can be represented by using the coupling matrix to define relations between the interface inputs of the components to be coupled and the unique set of coupled interface inputs. Thereby, the compatibility and equilibrium conditions can be defined as given hereafter.

$$\{y^J(t)\} = [T_{SJ}]^T\{\tilde{y}^J(t)\}, \quad \{\tilde{u}^J(t)\} = [T_{SJ}]\{u^J(t)\} \tag{2.107}$$

where, $[T_{SJ}] \in \mathbb{R}^{n_J \times 2n_J}$ denotes the coupling matrix used in the classical SSS approach to set-up the coupling conditions.

At this point, the state-space matrices of the models of the substructures to be coupled must be partitioned in terms of internal and interface DOFs. Afterwards, we must concatenate the partitioned state-space matrices in block diagonal form to set-up an uncoupled diagonal state-space model as given hereafter.

$$
\begin{aligned}
\{\dot{x}_S(t)\} &= [A_{S,D}]\{x_S(t)\} + \begin{bmatrix} B_{S,D}^I & B_{S,D}^J \end{bmatrix} \begin{Bmatrix} u^I(t) \\ u^J(t) \end{Bmatrix} \\
\begin{Bmatrix} y^I(t) \\ y^J(t) \end{Bmatrix} &= \begin{bmatrix} C_{S,D}^I \\ C_{S,D}^J \end{bmatrix} \{x_S(t)\} + \begin{bmatrix} D_{S,D}^{II} & D_{S,D}^{IJ} \\ D_{S,D}^{JI} & D_{S,D}^{JJ} \end{bmatrix} \begin{Bmatrix} u^I(t) \\ u^J(t) \end{Bmatrix}
\end{aligned}
\tag{2.108}
$$

The performed concatenating operations to construct the uncoupled diagonal state-space model are exemplified for the construction of $[A_{S,D}]$, $[B_{S,D}^I]$, $[C_{S,D}^I]$ and $[D_{S,D}^{II}]$ in the expression given below.

$$[A_{S,D}] = \begin{bmatrix} A_\alpha & & \\ & A_\beta & \\ & & \ddots \end{bmatrix}, \quad [B_{S,D}^I] = \begin{bmatrix} B_\alpha^I & & \\ & B_\beta^I & \\ & & \ddots \end{bmatrix}$$

$$[C_{S,D}^I] = \begin{bmatrix} C_\alpha^I & & \\ & C_\beta^I & \\ & & \ddots \end{bmatrix}, \quad [D_{S,D}^{II}] = \begin{bmatrix} D_\alpha^{II} & & \\ & D_\beta^{II} & \\ & & \ddots \end{bmatrix} \tag{2.109}$$

By imposing the coupling conditions defined in equations (2.107) in the uncoupled diagonal state-space model (see equation (2.108)) and after performing some mathematical manipulations, we may compute the coupled state-space model as follows:

$$\{\dot{\tilde{x}}(t)\} = [\tilde{A}]\{\tilde{x}(t)\} + \begin{bmatrix} \tilde{B}^I & \tilde{B}^J \end{bmatrix} \begin{Bmatrix} \tilde{u}^I(t) \\ \tilde{u}^J(t) \end{Bmatrix}$$

$$\begin{Bmatrix} \tilde{y}^I(t) \\ \tilde{y}^J(t) \end{Bmatrix} = \begin{bmatrix} \tilde{C}^I \\ \tilde{C}^J \end{bmatrix} \{\tilde{x}(t)\} + \begin{bmatrix} \tilde{D}^{II} & \tilde{D}^{IJ} \\ \tilde{D}^{JI} & \tilde{D}^{JJ} \end{bmatrix} \begin{Bmatrix} \tilde{u}^I(t) \\ \tilde{u}^J(t) \end{Bmatrix} \tag{2.110}$$

where,

$$[\tilde{A}] = A_{S,D} + B_{S,D}^J Q C_{S,D}^J$$

$$[\tilde{B}] = \begin{bmatrix} B_{S,D}^I + B_{S,D}^J Q D_{S,D}^{JI} & B_{S,D}^J (D_{S,D}^{JJ})^{-1} T_{SJ}^T S^{-1} \end{bmatrix}$$

$$[\tilde{C}] = \begin{bmatrix} C_{S,D}^I + D_{S,D}^{IJ} Q C_{S,D}^J \\ S^{-1} T_{SJ} (D_{S,D}^{JJ})^{-1} C_{S,D}^J \end{bmatrix} \tag{2.111}$$

$$[\tilde{D}] = \begin{bmatrix} D_{S,D}^{II} + D_{S,D}^{IJ} Q D_{S,D}^{JI} & D_{S,D}^{IJ} (D_{S,D}^{JJ})^{-1} T_{SJ}^T S^{-1} \\ S^{-1} T_{SJ} (D_{S,D}^{JJ})^{-1} D_{S,D}^{JI} & S^{-1} \end{bmatrix}$$

where, overtilde variables denote vectors/matrices associated with a coupled state-space model composed by unique sets of outputs and inputs, whereas variables $[S]$ and $[Q]$ are given below.

$$[S] = T_{SJ} (D_{S,D}^{JJ})^{-1} T_{SJ}^T \tag{2.112}$$

$$[Q] = (D_{S,D}^{JJ})^{-1} T_{SJ}^T S^{-1} T_{SJ} (D_{S,D}^{JJ})^{-1} - (D_{S,D}^{JJ})^{-1} \tag{2.113}$$

By comparing LM-SSS with classical SSS, it is evident that LM-SSS is simpler to implement, because there is no need of partitioning the state-space matrices in terms of internal and interface DOFs to compute the diagonal coupled state-space model used in LM-SSS (see expression (2.66)). In contrast, to construct the diagonal uncoupled state-space model used in classical SSS, we are required to partition the state-space matrices (see expression (2.110)).

Furthermore, by using classical SSS we are required to compute two matrix inver-

sions, while by exploiting LM-SSS we are only required to perform a single matrix inversion. This might represent an important advantage of LM-SSS over classical SSS, when dealing, for instance, with real-time substructuring applications involving systems presenting time-varying dynamic behaviour and, whose interfaces are characterized by many interface DOFs. When dealing with this kind of applications, state-space models representative of each variation on the dynamics of the substructures to be coupled must be computed and coupled. Thus, these applications require the performance of several coupling operations. Thereby, performing a single matrix inversion rather than two for each coupling operation can represent a dramatic decrease on the computational cost associated with the real-time substructuring application. On top of this, the matrix to be inverted by using LM-SSS is of dimension $n_J \times n_J$ (see expression (2.76)), whereas the matrices to be inverted by exploiting classical SSS are of dimension $n_J \times n_J$ and $2n_J \times 2n_J$ (see expression (2.111)). Therefore, as the number of interface DOFs of the substructures to be coupled increases, more important will be the advantage of using LM-SSS instead of classical SSS.

Observing the coupling conditions defined for the classical SSS method (equations (2.107)), we may notice that they establish relations between the unique set of interface outputs and inputs and the interface outputs and inputs of the components to be coupled. Thus, the coupled state-space model computed by classical SSS (see equation (2.110)) will be composed by unique sets of interface outputs and inputs, hence there is no need to use a post-processing procedure to eliminate redundant interface DOFs. This represents an advantage of classical SSS over LM-SSS.

To analyze the SSS approach proposed in [8], we will consider the coupling of the two substructures shown in figure 2.2. To start, we must transform the state-space models of these substructures into the coupling form presented in [8] (from now on labelled as SACF) as required by the method presented in the same publication. The displacement state-space models of substructure α and β transformed into SACF can be represented as follows

$$
\begin{Bmatrix} \ddot{y}_P^J(t) \\ \dot{y}_P^J(t) \\ \dot{x}_P^I(t) \end{Bmatrix} = \begin{bmatrix} A_P^{vv} & A_P^{vd} & A_P^{vI} \\ I & 0 & 0 \\ 0 & A_P^{Id} & A_P^{II} \end{bmatrix} \begin{Bmatrix} \dot{y}_P^J(t) \\ y_P^J(t) \\ x_P^I(t) \end{Bmatrix} + \begin{bmatrix} B_P^{vv} & B_P^{vI} \\ 0 & 0 \\ 0 & B_P^{II} \end{bmatrix} \begin{Bmatrix} \dot{u}_P^J(t) \\ u_P^I(t) \end{Bmatrix}
$$
$$
\begin{Bmatrix} y_P^J(t) \\ y_P^I(t) \end{Bmatrix} = \begin{bmatrix} 0 & I & 0 \\ C_P^{Iv} & C_P^{Id} & C_P^{II} \end{bmatrix} \begin{Bmatrix} \dot{y}_P^J(t) \\ y_P^J(t) \\ x_P^I(t) \end{Bmatrix}
$$
(2.114)

where, subscript P denotes vectors/matrices associated with substructure P, for this specific case P may either be α or β.

The compatibility and equilibrium conditions can be defined as follows

$$\begin{Bmatrix} y_\alpha^J(t) \\ y_\beta^J(t) \end{Bmatrix} = \begin{bmatrix} I \\ I \end{bmatrix} \{\tilde{y}^J(t)\} \qquad (2.115a) \qquad \{\tilde{u}^J(t)\} = \begin{bmatrix} I & I \end{bmatrix} \begin{Bmatrix} u_\alpha^J(t) \\ u_\beta^J(t) \end{Bmatrix} \qquad (2.115b)$$

where, $[I] \in \mathbb{R}^{n_J \times n_J}$ is an identity matrix.

To compute the coupled state-space model, we must start by summing the first block rows of the state equations of the state-space models of both components (i.e. α and β). Then, by imposing both coupling conditions defined in expressions (2.115) and after making some mathematical manipulations, we can determine the first block row of the coupled state-space model (for details, see [49]). Finally, by correctly placing the remaining state-space matrix terms of the models of the substructures α and β, we may define the coupled state-space model as follows

$$\begin{Bmatrix} \ddot{\tilde{y}}^J(t) \\ \dot{\tilde{y}}^J(t) \\ \dot{x}_\alpha^I(t) \\ \dot{x}_\beta^I(t) \end{Bmatrix} = \begin{bmatrix} \tilde{A}^{vv} & \tilde{A}^{vd} & \tilde{A}_\alpha^{vI} & \tilde{A}_\beta^{vI} \\ I & 0 & 0 & 0 \\ 0 & A_\alpha^{Id} & A_\alpha^{II} & 0 \\ 0 & A_\beta^{Id} & 0 & A_\beta^{II} \end{bmatrix} \begin{Bmatrix} \dot{\tilde{y}}^J(t) \\ \tilde{y}^J(t) \\ x_\alpha^I(t) \\ x_\beta^I(t) \end{Bmatrix} + \begin{bmatrix} \tilde{B}^{vv} & \tilde{B}_\alpha^{vI} & B_\beta^{vI} \\ 0 & 0 & 0 \\ 0 & B_\alpha^{II} & 0 \\ 0 & 0 & B_\beta^{II} \end{bmatrix} \begin{Bmatrix} \tilde{u}^J(t) \\ u_\alpha^I(t) \\ u_\beta^I(t) \end{Bmatrix}$$

$$\begin{Bmatrix} \tilde{y}^J(t) \\ y_\alpha^I(t) \\ y_\beta^I(t) \end{Bmatrix} = \begin{bmatrix} 0 & I & 0 & 0 \\ C_\alpha^{Iv} & C_\alpha^{Id} & C_\alpha^{II} & 0 \\ C_\beta^{Iv} & C_\beta^{Id} & 0 & C_\beta^{II} \end{bmatrix} \begin{Bmatrix} \dot{\tilde{y}}^J(t) \\ \tilde{y}^J(t) \\ x_\alpha^I(t) \\ x_\beta^I(t) \end{Bmatrix} \qquad (2.116)$$

where,

$$\tilde{A}^{vv} = B_\alpha^{vv} \Gamma A_\beta^{vv} + B_\beta^{vv} \Gamma A_\alpha^{vv} \tag{2.117}$$

$$\tilde{A}^{vd} = B_\alpha^{vv} \Gamma A_\beta^{vd} + B_\beta^{vv} \Gamma A_\alpha^{vd} \tag{2.118}$$

$$\tilde{A}_\alpha^{vI} = B_\beta^{vv} \Gamma A_\alpha^{vI} \tag{2.119}$$

$$\tilde{A}_\beta^{vI} = B_\alpha^{vv} \Gamma A_\beta^{vI} \tag{2.120}$$

$$\tilde{B}^{vv} = B_\alpha^{vv} \Gamma B_\beta^{vv} \tag{2.121}$$

$$\tilde{B}_\alpha^{vI} = B_\beta^{vv} \Gamma B_\alpha^{vI} \tag{2.122}$$

$$\tilde{B}_\beta^{vI} = B_\alpha^{vv} \Gamma B_\beta^{vI} \tag{2.123}$$

with $\Gamma = (B_\alpha^{vv} + B_\beta^{vv})^{-1}$.

The coupled state-space model computed with the approach proposed in [8] (see expression 2.116) is a minimal-order coupled model and does not present redundant interface DOFs, because the coupling conditions used to compute it directly define relations between the unique set of coupled outputs and inputs and the outputs and

inputs of the state-space models of the substructures α and β (see equations (2.115)). Therefore, we may conclude that this is an advantage of the method developed by Sjövall and Abrahamsson in [8] over the LM-SSS method that requires the use of post-processing procedures to compute minimal order coupled models and to retain the unique set of coupled outputs and inputs (see sections 2.3.3 and 2.3.4, respectively).

Nevertheless, we may also point some advantages of using LM-SSS instead of the method proposed in [8]. To start, the LM-SSS method enables the coupling of an unlimited number of substructures at same time, while by exploiting the approach proposed in [8], we are limited to couple two substructures at same time. Moreover, it is important to mention that we can perform coupling by using the approach proposed in [8], because the interface inputs of a state-space model transformed into SACF do not contribute for the dynamic response of the internal states (see expression (2.114)). If the interface inputs of the state-space models of the substructures contributed to the response of the internal states, we could not directly insert terms of the state-space matrices of the models to be coupled in the coupled state-space model (see expression (2.116)). In other words, if this condition is not met, the internal states must be involved on the coupling operation and, hence the approach proposed in [8] cannot be applied. Conversely, by using LM-SSS this condition does not need to be met, because all the states of the state-space models are involved on the coupling operation. Thus, when transforming the state-space models to be coupled with LM-SSS into coupling form, the transformation to be applied on the internal states can be arbitrary, provided that the transformation matrix used to transform the model into coupling form is full rank and invertible (see section 2.3.2). This is the reason why LM-SSS can also be used to couple state-space models without being transformed into coupling form. Furthermore, for computing minimal-order coupled models, LM-SSS can be used to couple models transformed into UCF or SACF, while the approach proposed in [8] requires the specific use of SACF. The possibility of using UCF is an important advantage of LM-SSS over the method proposed in [8], because unlike SACF, UCF does not require the selection of a subspace from a nullspace. Note that it was shown in [41] that the selection of the subspace to compute the transformation matrix of SACF is difficult to be performed and strongly affects the accuracy of the transformation into coupling form. Thus, we may conclude that, when compared with the approach presented in [8], LM-SSS has the advantage of being able to couple an unlimited number of substructures at same time and it is simpler to implement, because it does not require the use of state-space models transformed into SACF, whose transformation matrix is difficult to be correctly set-up.

To summarize, we may conclude that the disadvantage of using LM-SSS instead of the classical SSS and the method developed in [8] is the need of using a post-processing procedure to retain the unique set of coupled DOFs. Moreover, when comparing LM-SSS with the approach presented in [8], LM-SSS presents the additional disadvantage of requiring another post-processing procedure to eliminate the redundant states orig-

inated from the DS operations. However, note that the post-processing procedures needed to retain the unique set of DOFs and to eliminate the redundant states are very simple to be implemented, hence these disadvantages do not represent important limitations of LM-SSS.

Conversely, LM-SSS showed to present the advantage of being simpler to implement than the classical SSS and than the method proposed in [8]. On top of this, it requires the computation of less matrix inversions than classical SSS and it enables the coupling of an unlimited number of substructures at same time, while the approach presented in [8] can only couple a maximum of two components at same time. Therefore, we may claim that the use of LM-SSS with the post-processing procedures presented in this section is, indeed, a very promising technique that holds important practical advantages over the other SSS methods.

2.4 Primal state-space assembly formulation

In this section, we will present a primal state-space assembly formulation. This approach will be outlined by assuming the performance of coupling operations with state-space models representative of inverted FRFs, i.e. representative of, for instance, dynamic stiffness and apparent mass. To present this method, let us assume that an unlimited number of components is intended to be coupled and that the primal assembly operation will be performed with state-space models representative of apparent mass. When dealing with analytically characterized substructures for which the mass, stiffness and damping matrices are known, these state-space models can be computed by using expressions (B.3). In an experimental context, state-space models representative of the apparent mass of the substructures under study can be computed from the inverted FRFs or by inverting state-space models estimated from measured FRFs. The most common approach is to estimate state-space models from measured FRFs (see, for example, [46],[40],[10]), yielding, in general, the identification of displacement models. To obtain a state-space model representative of apparent mass, we must double-differentiate the estimated displacement model and then, invert it by following the procedure presented in appendix A.

After having computed state-space models representative of the apparent mass of the components to be coupled, we can set up a diagonal coupled state-space model as follows:

$$
\begin{Bmatrix} \{\dot{x}_\alpha(t)\} \\ \{\dot{x}_\beta(t)\} \\ \vdots \end{Bmatrix} = [A_{S,D}^{apm}] \begin{Bmatrix} \{x_\alpha(t)\} \\ \{x_\beta(t)\} \\ \vdots \end{Bmatrix} + [B_{S,D}^{apm}] \begin{Bmatrix} \{\ddot{y}_\alpha(t)\} \\ \{\ddot{y}_\beta(t)\} \\ \vdots \end{Bmatrix}
$$

$$
\begin{Bmatrix} \{u_\alpha(t)\} \\ \{u_\beta(t)\} \\ \vdots \end{Bmatrix} + \begin{Bmatrix} \{g_\alpha(t)\} \\ \{g_\beta(t)\} \\ \vdots \end{Bmatrix} = [C_{S,D}^{apm}] \begin{Bmatrix} \{x_\alpha(t)\} \\ \{x_\beta(t)\} \\ \vdots \end{Bmatrix} + [D_{S,D}^{apm}] \begin{Bmatrix} \{\ddot{y}_\alpha(t)\} \\ \{\ddot{y}_\beta(t)\} \\ \vdots \end{Bmatrix}
$$

(2.124)

where, superscript *apm* denotes variables of a state-space model representative of apparent mass, matrices $[A_{S,D}^{apm}]$, $[B_{S,D}^{apm}]$, $[C_{S,D}^{apm}]$ and $[D_{S,D}^{apm}]$ are given below.

$$
[A_{S,D}^{apm}] = \begin{bmatrix} A_\alpha^{apm} & & \\ & A_\beta^{apm} & \\ & & \ddots \end{bmatrix}, \quad [B_{S,D}^{apm}] = \begin{bmatrix} B_\alpha^{apm} & & \\ & B_\beta^{apm} & \\ & & \ddots \end{bmatrix}
$$

$$
[C_{S,D}^{apm}] = \begin{bmatrix} C_\alpha^{apm} & & \\ & C_\beta^{apm} & \\ & & \ddots \end{bmatrix}, \quad [D_{S,D}^{apm}] = \begin{bmatrix} D_\alpha^{apm} & & \\ & D_\beta^{apm} & \\ & & \ddots \end{bmatrix}
$$

(2.125)

The state-space model given in expression (2.124) can be represented in a more compact manner as given below.

$$
\{\dot{x}_S(t)\} = [A_{S,D}^{apm}]\{x_S(t)\} + [B_{S,D}^{apm}]\{\ddot{y}(t)\}
$$
$$
\{u(t)\} + \{g(t)\} = [C_{S,D}^{apm}]\{x_S(t)\} + [D_{S,D}^{apm}]\{\ddot{y}(t)\}
$$

(2.126)

By exploiting the Boolean localization matrix $[L_C]$ (see section 2.2.2), we may define both compatibility and equilibrium conditions as follows

$$
\{y(t)\} = [L_C]\{\tilde{y}(t)\} \qquad (2.127a) \qquad\qquad [L_C]^T\{g(t)\} = \{0\} \qquad (2.127b)
$$

where, $\{\tilde{y}(t)\}$ represents the coupled output vector composed by the unique set of coupled displacements.

Recall that in primal formulation, the compatibility conditions are imposed by retaining the unique set of coupled DOFs, thus this condition can be mathematically established by equation (2.127a). The equilibrium conditions are imposed by forcing the mutual cancellation of the connecting forces. Thereby, these conditions are given by equation (2.127b) [12].

As we are deriving the primal state-space assembly formulation by using state-space models representative of apparent mass (whose inputs are accelerations), the compatibility conditions must be defined in terms of accelerations as well. Hence,

expression (2.127a) must be double-differentiated as given hereafter.

$$\{\ddot{y}(t)\} = [L_C]\{\ddot{\tilde{y}}(t)\} \qquad (2.128)$$

By exploiting expression (2.128), expression (2.126) can be rewritten as given below.

$$\{\dot{x}_S(t)\} = [A_{S,D}^{apm}]\{x_S(t)\} + [B_{S,D}^{apm}][L_C]\{\ddot{\tilde{y}}(t)\}$$
$$(\{u(t)\} + \{g(t)\}) = [C_{S,D}^{apm}]\{x_S(t)\} + [D_{S,D}^{apm}][L_C]\{\ddot{\tilde{y}}(t)\} \qquad (2.129)$$

Pre-multiplying the output equations of the state-space models given in expression (2.129) by $[L_C]^T$ and by imposing the equilibrium conditions (see expression (2.127b)), we may rewrite expression (2.129) as given below.

$$\{\dot{x}_S(t)\} = [A_{S,D}^{apm}]\{x_S(t)\} + [B_{S,D}^{apm}][L_C]\{\ddot{\tilde{y}}(t)\}$$
$$[L_C^T]\{u(t)\} = [L_C]^T[C_{S,D}^{apm}]\{x_S(t)\} + [L_C]^T[D_{S,D}^{apm}][L_C]\{\ddot{\tilde{y}}(t)\} \qquad (2.130)$$

The primally assembled state-space model given in expression (2.130) can be rewritten as follows:

$$\{\dot{\tilde{x}}(t)\} = [\tilde{A}^{apm}]\{\tilde{x}(t)\} + [\tilde{B}^{apm}]\{\ddot{\tilde{y}}(t)\}$$
$$\{\tilde{u}(t)\} = [\tilde{C}^{apm}]\{\tilde{x}(t)\} + [\tilde{D}^{apm}]\{\ddot{\tilde{y}}(t)\} \qquad (2.131)$$

where, $\{\tilde{u}(t)\}$ represents the unique set of coupled inputs, while matrices $[\tilde{A}]$, $[\tilde{B}]$, $[\tilde{C}]$ and $[\tilde{D}]$ must be calculated as given hereafter.

$$[\tilde{A}^{apm}] = [A_{S,D}^{apm}], \quad [\tilde{B}^{apm}] = [B_{S,D}^{apm}][L_C],$$
$$[\tilde{C}^{apm}] = [L_C]^T[C_{S,D}^{apm}], \quad [\tilde{D}^{apm}] = [L_C]^T[D_{S,D}^{apm}][L_C] \qquad (2.132)$$

It is worth mentioning that we can also exploit expressions (2.132) to perform primal disassembly. Nevertheless, the state-space models of the structures to be disassembled must be previously transformed into negative form, by following the procedure presented in appendix B.

Note also that primal assembly/disassembly operations can be implemented with state-space models transformed into coupling form (see, [8] and section 2.3.2). To transform the state-space models involved in these operations into coupling form, we can follow two different strategies. We can transform directly the state-space models representative of inverted FRFs (i.e. representative, for instant, of dynamic stiffness and apparent mass) into coupling form or, in alternative we can transform a model representative of accelerance and then invert it. To eliminate the redundant states originated from both primal assembly and disassembly operations, the post-processing procedures discussed in 2.3.3 continue to be valid.

As final note, it is worth mentioning that in general when the components are ex-

perimentally characterized, the use of dual formulations is preferred. This is justified by the fact that to perform DS operations with dual formulations we are only required to invert quantities related to the interface DOFs. In contrast, when exploiting primal formulations, we are often demanded to invert all data, because accelerance is the quantity usually measured from experimental tests (this was also discussed in section 2.2.2). Nonetheless, primal formulations might be interesting for specific applications. For example, when working with numerically characterized structures, it might be of interest to identify a state-space model of a massless component from the state-space model of the assembly where it is included. The exploitation of the dual SSS formulation (i.e. LM-SSS) to identify state-space models representative of massless components leads to ill-condition numerical problems, because matrix $B_C(C_{S,D}^{disp}A_{S,D}B_{S,D})B_C^T$ becomes singular (see expression (2.82)). Conversely, the primal disassembly approach does not involve the performance of matrix inversions, hence the identification of a model representative of massless components can be successfully performed (see expressions (2.131) and (2.132)).

2.5 State-Space Substructuring via compatibility relaxation

In this section, the LM-SSS formulation will be extended to include the dynamics of CEs into coupling operations via compatibility relaxation. By using the SSS methods presented in literature (see for, example, [9],[8],[41],[42],[44]) to include CEs into coupling SSS operations, we are forced to treat them as others substructures to be coupled. When dealing with CEs that are analytically or numerically modelled, this approach does not impose important disadvantages. However, when dealing with CEs experimentally characterized, the possibility of including them via compatibility relaxation presents important advantages [2].

To experimentally characterize the dynamics of a CE (e.g. a rubber mount), it is common practice to test it with fixtures attached to its ends. Thus, to experimentally characterize this component, we are required to decouple the dynamics of the fixtures from the assembly, where it is included (i.e. fixtures attached to the ends of the CE) [17],[33]. Hence, we are required to know the dynamics of the complete assembly and of the fixtures used to test the CE. If these mechanical components are to be characterized experimentally, this requirement imposes the performance of several experimental modal characterization tests.

The decoupling operations required to identify the dynamics of the CE can be implemented by either using the LM-SSS method or the primal state-space assembly formulation presented in sections 2.2.3 and 2.4, respectively. However, by performing these decoupling operations, we will end-up with a state-space model representative of the CE that is composed by $n_{fmf} + 2n_f - 2n_J$ states (assuming that the CE was tested

with two fixtures attached to its ends and that the redundant states originated from the decoupling operations are eliminated). Variables n_f and n_{fmf} denote the number of states of the state-space model representative of one of the fixtures used to test the CE and of the state-space model representative of the fixtures attached to the CE, respectively.

The state-space models identified from experimentally acquired data are usually composed by a number of states that is substantially higher than the number of its outputs and inputs [41]. For this reason, the performance of decoupling operations might represent an important increment of states on the identified model of the CE. This increment of states is due to the double inclusion of the dynamics of the substructures to be decoupled. Indeed, the dynamics of the substructures to be decoupled were already included on the model representative of the complete assembly, then by performing decoupling the dynamics of these components is reintroduced. Hence, the identified model will be spoiled by pairs of spurious modes. In a real case scenario, there is generally no a-priori knowledge on the dynamics of the substructure to be identified. Thus, the identification and consequent elimination of these pairs of spurious modes is hard or even impossible to be performed [47].

Representing the dynamics of CEs by using state-space models contaminated by spurious states presents two important disadvantages. On the one hand, by including the dynamics of the CEs into coupling operations through these identified models, we will end-up with coupled models spoiled by spurious states. On the other hand, the computational effort required to perform calculations (e.g. time-domain simulations) with these coupled models and with the identified models of the CEs will be substantially higher. These disadvantages will be more noticeable as the number of spurious states included on the identified models of the CEs increases. Hence, as the number of state-space models to be decoupled to identify the CEs increases and as these models are composed by a higher number of states, more significant will be the disadvantages of identifying models representative of CEs by performing decoupling operations.

Conversely, by extending the LM-SSS formulation to include the dynamics of the CEs via compatibility relaxation, we have the possibility of embed the dynamics of the CEs into the coupling operations by merely using models representative of their diagonal dynamic stiffness terms [34],[50]. For this reason, there is no need of performing decoupling operations to obtain the state-space models needed to include the dynamics of the CEs into the coupling operations. In [51], it was proven that the off diagonal terms of the dynamic stiffness of a mechanical system composed by two components connected by a CE are the off diagonal terms of the CE as well. This means that the off diagonal terms of the CE can be identified directly from the experimental modal characterization of the assembly where it is included. From these off diagonal terms, we may exploit the inverse substructuring (IS) approach [52],[53],[51],[54] (in some publications also tagged as in-situ characterization) to obtain the correspondent diagonal dynamic stiffness terms. IS assumes that the CEs are massless and that no

cross couplings between their DOFs exist. In other words, each DOF on one side of the CE associated with a determined direction is only coupled with the DOF on the other side associated with the exact same direction. If the CEs under analysis verify the assumptions underlying IS, we can compute the diagonal dynamic stiffness terms of these components by simply multiplying their off diagonal ones by -1 [55],[54],[33]. Thereby, in this section we will also present the state-space realization of IS (see [2]) to identify the state-space models required by the LM-SSS formulation to include the dynamics of the CEs via compatibility relaxation without performing decoupling operations.

In this way, it is straightforward to conclude that by extending the formulation of LM-SSS to include CEs via compatibility relaxation, we may benefit from important advantages. On the one hand, we avoid the use of decoupling operations making it possible to identify models free of spurious states representative of the dynamics of the CEs. Thus, the coupled state-space models computed by including the dynamics of the CEs via compatibility relaxation will also be free of spurious states. On the other hand, we are no longer required to know the dynamics of the fixtures used to test the CEs. Hence, the CEs can be tested on the structure where they are included (i.e. in-situ), avoiding the need of performing dismounting and mounting operations. On top of this, we are not demanded to perform extra experimental modal characterization tests to characterize the dynamics of the substructures to which the CEs are connected.

In this section, we will start by extending the LM-SSS formulation to include the dynamics of CEs via compatibility relaxation (section 2.5.1). Then, in section 2.5.2 two post-processing procedures to eliminate the extra states originated from the coupling operations performed with LM-SSS via compatibility relaxation will be outlined. Afterwards, in section 2.5.3 we will present how to determine analytically and numerically state-space models representative of CEs to be included in the LM-SSS formulation via compatibility relaxation, while in section 2.5.4 the state-space realization of IS is presented to enable the experimental determination of the same state-space models.

2.5.1 Including CEs into LM-SSS via compatibility relaxation

Here, the LM-SSS formulation (see section 2.2.3) will be extended to enable the inclusion of CEs into the coupling operations via compatibility relaxation. To develop this variant of LM-SSS, let us assume that it is intended to couple an unlimited number of components connected by an unlimited number of CEs. Let us further assume that these CEs respect the assumptions underlying IS, i.e. that they are massless and that no cross couplings between their DOFs exist. If these conditions are met, expression (2.56) holds. Moreover, the frequency domain compatibility conditions defined in equation (2.57) are also valid in the time domain, hence we may rewrite them in state-space model form as follows

$$\{\dot{x}_M(t)\} = [A_{M,D}]\{x_M(t)\} + [B_{M,D}]\{\lambda_C(t)\}$$
$$[B_C]\{y(t)\} = [C_{M,D}^{disp}]\{x_M(t)\}$$

(2.133)

where, the defined state-space model is representative of the inverted diagonal dynamic stiffness terms of the CEs to be included in the coupling operation, subscript M denotes state vectors and state-space matrices of state-space models representative of the dynamics of CEs, while matrices $[A_{M,D}]$, $[B_{M,D}]$ and $[C_{M,D}^{disp}]$ are given below.

$$[A_{M,D}] = \begin{bmatrix} A_{M_1} & & \\ & A_{M_2} & \\ & & \ddots \end{bmatrix}, \quad [B_{M,D}] = \begin{bmatrix} B_{M_1} & & \\ & B_{M_2} & \\ & & \ddots \end{bmatrix}$$

$$[C_{M,D}^{disp}] = \begin{bmatrix} C_{M_1}^{disp} & & \\ & C_{M_2}^{disp} & \\ & & \ddots \end{bmatrix}$$

(2.134)

The output equations of the state-space model given in expression (2.133) represents the compatibility conditions in terms of relative displacement between the interfaces of the connected substructures. Yet, to develop the LM-SSS formulation with compatibility relaxation we must define the compatibility conditions in terms of the relative acceleration between the interfaces of the substructures to be coupled. Thus, we must double-differentiate the state-space model given in expression (2.133) as follows (see [45]):

$$\{\dot{x}_M(t)\} = [A_M]\{x_M(t)\} + [B_{M,D}]\{\lambda_C(t)\}$$
$$[B_C]\{\ddot{y}(t)\} = \left[C_{M,D}^{accel}\right]\{x_M(t)\} + \left[D_{M,D}^{accel}\right]\{\lambda_C(t)\}$$

(2.135)

where, the established state-space model is representative of the inverted diagonal apparent mass terms of the CEs, whereas $\left[C_{M,D}^{accel}\right]$ and $\left[D_{M,D}^{accel}\right]$ are given hereafter.

$$\left[C_{M,D}^{accel}\right] = \left[C_{M,D}^{disp}A_{M,D}A_{M,D}\right], \quad \left[D_{M,D}^{accel}\right] = \left[C_{M,D}^{disp}A_{M,D}B_{M,D}\right]$$

(2.136)

As the CEs are assumed to be massless, expression (2.1) continues to be valid. Hence, the local equilibrium conditions defined in expression (2.71) still hold as well. Thus, by using this expression and the compatibility conditions established by the output equations of the model given in expression (2.135), we may define the following system of equations:

$$\begin{cases} (D_{S,D}^{accel})^{-1}(\ddot{y} - C_{S,D}^{accel}x_S) + B_C^T\lambda_C = u \\ B_C\ddot{y} = C_{M,D}^{accel}x_M + D_{M,D}^{accel}\lambda_C \end{cases}$$

(2.137)

after performing some mathematical manipulations, the system of equations (2.137),

can be rewritten as follows:

$$\begin{cases} \lambda_C = E_{CR}(-C_{M,D}^{accel}x_M + B_C C_{S,D}^{accel}x_S + B_C D_{S,D}^{accel}u) \\ \ddot{y} = (C_{S,D}^{accel} - D_{S,D}^{accel}B_C^T E_{CR}B_C C_{S,D}^{accel})x_S + D_{S,D}^{accel}B_C^T E_{CR}C_{M,D}^{accel}x_M \\ \quad + (D_{S,D}^{accel} - D_{S,D}^{accel}B_C^T E_{CR}B_C D_{S,D}^{accel})u \end{cases} \tag{2.138}$$

where, matrix $[E_{CR}]$ is given below.

$$[E_{CR}] = (B_C D_{S,D}^{accel}B_C^T + D_{M,D}^{accel})^{-1} \tag{2.139}$$

By using together expression (2.71) and the bottom equation of the system of equations (2.138), the state equation of the diagonal coupled state-space model (equation (2.69)) can be rewritten as in expression (2.140).

$$\dot{x}_S = (A_{S,D} - B_{S,D}B_C^T E_{CR}B_C C_{S,D}^{accel})x_S + B_{S,D}B^T E_{CR}C_{M,D}^{accel}x_M \\ + (B_{S,D} - B_{S,D}B_C^T E_{CR}B_C D_{S,D}^{accel})u \tag{2.140}$$

From the upper equation of the system of equations (2.138), the state equation of the state-space model given in expression (2.135) can be rewritten as given hereafter.

$$\dot{x}_M = B_{M,D}E_{CR}B_C C_{S,D}^{accel}x_S + (A_{M,D} - B_{M,D}E_{CR}C_{M,D}^{accel})x_M \\ + B_{M,D}E_{CR}B_C D_{S,D}^{accel}u \tag{2.141}$$

By using equations (2.140), (2.141) and the bottom equations of the system of equations (2.138), we may compute the coupled state-space model as follows:

$$\begin{cases} \dot{\tilde{x}}_S(t) \\ \dot{\tilde{x}}_M(t) \end{cases} = [\tilde{A}]\begin{cases} \tilde{x}_S(t) \\ \tilde{x}_M(t) \end{cases} + [\tilde{B}]\{\tilde{u}(t)\}$$
$$\{\ddot{\tilde{y}}(t)\} = [\tilde{C}^{accel}]\begin{cases} \tilde{x}_S(t) \\ \tilde{x}_M(t) \end{cases} + [\tilde{D}^{accel}]\{\tilde{u}(t)\} \tag{2.142}$$

with,

$$[\tilde{A}] = \begin{bmatrix} \tilde{A}_{SS} & \tilde{A}_{SM} \\ \tilde{A}_{MS} & \tilde{A}_{MM} \end{bmatrix}, \quad [\tilde{B}] = \begin{bmatrix} \tilde{B}_S \\ \tilde{B}_M \end{bmatrix}$$
$$[\tilde{C}^{accel}] = \begin{bmatrix} \tilde{C}_S^{accel} & \tilde{C}_M^{accel} \end{bmatrix}, \quad [\tilde{D}^{accel}] = \begin{bmatrix} \tilde{D}_S^{accel} \end{bmatrix} \tag{2.143}$$

where, the coupled state-space matrices can be computed by following the expressions given below.

$$[\tilde{A}_{SS}] = A_{S,D} - B_{S,D}B_C^T E_{CR} B_C C_{S,D}^{accel}$$
$$[\tilde{A}_{SM}] = B_{S,D}B_C^T E_{CR} C_{M,D}^{accel}$$
$$[\tilde{A}_{MS}] = B_{M,D} E_{CR} B_C C_{S,D}^{accel}$$
$$[\tilde{A}_{MM}] = A_{M,D} - B_{M,D} E_{CR} C_{M,D}^{accel}$$
$$[\tilde{B}_S] = B_{S,D} - B_{S,D}B_C^T E_{CR} B_C D_{S,D}^{accel} \qquad (2.144)$$
$$[\tilde{B}_M] = B_{M,D} E_{CR} B_C D_{S,D}^{accel}$$
$$[\tilde{C}_S^{accel}] = C_{S,D}^{accel} - D_{S,D}^{accel} B_C^T E_{CR} B_C C_{S,D}^{accel}$$
$$[\tilde{C}_M^{accel}] = D_{S,D}^{accel} B_C^T E_{CR} C_{M,D}^{accel}$$
$$[\tilde{D}_S^{accel}] = D_{S,D}^{accel} - D_{S,D}^{accel} B_C^T E_{CR} B_C D_{S,D}^{accel}$$

Note that, the used compatibility conditions to develop the coupling approach here presented do not impose null relative acceleration between the interfaces of the coupled substructures (see expression (2.135)). Thus, the output and input vectors of the coupled state-space models (see expression (2.142)) obtained with this approach, will be composed by the unique sets of coupled outputs and inputs, respectively. Hence, there is no need to eliminate outputs and inputs from the computed coupled state-space models.

Note also that the assumptions underlying the coupling approach here presented are the same as the ones underlying IS method [17]. Thus, the CEs to be included in coupling operations via compatibility relaxation, must respect the assumptions underlying IS. When dealing with CEs that are not suitable to be characterized by IS, we must include them into the coupling operations by treating them as a regular substructure to be coupled, for example by exploiting LM-SSS (see section 2.2.3).

As final note, it is also worth mentioning that by exploiting expressions (2.143) and (2.144), we can compute acceleration coupled state-space models that embed the dynamics of CEs via compatibility relaxation. Furthermore, by simply adjusting the expressions used to compute the output and feedthrough matrices (see expressions (2.144)), we can also obtain displacement and velocity coupled state-space models (see appendix C).

2.5.2   Minimal-order coupled state-space models

The coupled models obtained by exploiting LM-SSS via compatibility relaxation (see section 2.5.1) are not minimal-order coupled models. Thus, here we will present two post-processing procedures to compute minimal-order coupled models from the coupled models obtained by exploiting LM-SSS with compatibility relaxation.

To start, let us assume that the components depicted in figure 2.3 were coupled by using LM-SSS with compatibility relaxation. In addition, let us assume that the state-space models representative of the inverted diagonal apparent mass terms of the CE were previously transformed into coupling form and, that the acceleration state-space

models representative of substructures α and β were also previously transformed into coupling form. In this scenario, by exploiting LM-SSS with compatibility relaxation and by dropping $\{\bullet\}$ and (t) for ease of readability, the state vector of the coupled state-space model would be given as follows:

$$\{\tilde{z}_{\alpha M \beta}\} = \left\{ \dot{\tilde{y}}_{\alpha}^{J} \quad \tilde{y}_{\alpha}^{J} \quad \tilde{x}_{\alpha}^{I} \quad \dot{\tilde{y}}_{\beta}^{J} \quad \tilde{y}_{\beta}^{J} \quad \tilde{x}_{\beta}^{I} \quad [B_C]\dot{\tilde{y}} \quad [B_C]\tilde{y} \quad \tilde{x}_{M}^{I} \right\}^{T} \tag{2.145}$$

where, subscript $\alpha M \beta$ denotes a variable associated with the assembled structure depicted in figure 2.3, while $\{\tilde{y}\}$ is given below.

$$\{\tilde{y}\} = \left\{ \tilde{y}_{\alpha}^{I} \quad \tilde{y}_{\alpha}^{J} \quad \tilde{y}_{\beta}^{J} \quad \tilde{y}_{\beta}^{I} \right\}^{T} \tag{2.146}$$

By observing the coupled state vector given in expression (2.145), it is evident that the coupled model is not composed by states, whose physical meaning is the same. Indeed, this happens, because LM-SSS with compatibility relaxation includes the dynamics of the CEs by using state-space models, whose outputs are representative of the relative motion between the interfaces of the substructures connected by the CEs (see expression (2.135)). Hence, when these models are transformed into coupling form, they will be composed by states, whose physical meaning is the relative displacement and the relative velocity between the interfaces of the connected substructures. Although these states cannot be classified as redundant, because they present different physical meaning, their contribution to the dynamics of the coupled model can be retrieved by the states of the coupled model representative of the displacement and velocity of the interface DOFs of the connected substructures. Thus, these states can be classified as extra states and, hence can be eliminated.

To eliminate these extra states, the post-processing procedure presented in section 2.3.3 that makes use of a state Boolean localization matrix continues to be valid. Nevertheless, the construction of the state mapping matrix $[B_T]$ used to compute the required state Boolean localization matrix $[L_T]$ is now dependent on the mapping matrix $[B_C]$ used to perform coupling with LM-SSS via compatibility relaxation (see section 2.5.1). To demonstrate how matrix $[B_T]$ must be set-up, let us assume that $[B_C]$ is constructed as follows:

$$[B_C]\{\tilde{y}\} = \begin{bmatrix} 0 & I_{\alpha}^{J} & I_{\beta}^{J} & 0 \end{bmatrix} \begin{Bmatrix} \tilde{y}_{\alpha}^{I} \\ \tilde{y}_{\alpha}^{J} \\ \tilde{y}_{\beta}^{J} \\ \tilde{y}_{\beta}^{I} \end{Bmatrix} = \{0\} \tag{2.147}$$

where, I_{α}^{J} and I_{β}^{J} are given as follows:

$$[I_{\alpha}^{J}] = \phi[I] \tag{2.148a} \qquad\qquad [I_{\beta}^{J}] = -\phi[I] \tag{2.148b}$$

where, $[I] \in \mathbb{R}^{n_J \times n_J}$ is an identity matrix, while ϕ is a numeric coefficient, which can be selected to be either -1 or 1. Variable ϕ is responsible for adjusting the post-processing procedures here presented in accordance with the computation of $[B_C]$.

By exploiting expressions (2.147), (2.148a) and (2.148b), $[B_T]$ can be set-up in accordance with $[B_C]$ by following the expression given hereafter.

$$[B_T]\{\tilde{z}_{\alpha M \beta}\} = \begin{bmatrix} I_\beta^J & 0 & 0 & I_\alpha^J & 0 & 0 & I & 0 & 0 \\ 0 & I_\beta^J & 0 & 0 & I_\alpha^J & 0 & 0 & I & 0 \end{bmatrix} \begin{Bmatrix} \dot{\tilde{y}}_\alpha^J \\ \tilde{y}_\alpha^J \\ \tilde{x}_\alpha^I \\ \dot{\tilde{y}}_\beta^J \\ \tilde{y}_\beta^J \\ \tilde{x}_\beta^I \\ \phi\left(\dot{\tilde{y}}_\alpha^J - \dot{\tilde{y}}_\beta^J\right) \\ \phi\left(\tilde{y}_\alpha^J - \tilde{y}_\beta^J\right) \\ \tilde{x}_M^I \end{Bmatrix} = \left\{0\right\} \quad (2.149)$$

After having set-up $[B_T]$, $[L_T]$ can be directly computed from the nullspace of $[B_T]$ (see expression (2.97)). Then, by applying the post-processing procedure presented in section 2.3.3, the minimal-order coupled state-space model can be computed. The state vector of this model is represented below.

$$\{\tilde{z}_{\alpha M \beta}\} = \left\{ \dot{\tilde{y}}_\alpha^J \quad \tilde{y}_\alpha^J \quad \tilde{x}_\alpha^I \quad \dot{\tilde{y}}_\beta^J \quad \tilde{y}_\beta^J \quad \tilde{x}_\beta^I \quad \tilde{x}_M^I \right\}^T \tag{2.150}$$

Note that, the post-processing procedure just discussed to eliminate the extra states originated from the performance of coupling operations with LM-SSS via compatibility relaxation are still valid, when these coupled models are originated from coupling operations involving an unlimited number of substructures and CEs.

In contrast, the manual post-processing procedure presented in section 2.3.3 cannot be used to compute minimal-order coupled models from the coupled models obtained with LM-SSS via compatibility relaxation. Nonetheless, a manual post-processing procedure can also be defined to eliminate the extra states originated from coupling operations performed with this formulation. This manual post-processing procedure is given below and must be applied for each pair of coupled interface outputs.

1. Add the column of $[\tilde{A}]$ associated with the difference between the coupled interface outputs previously multiplied by ϕ to the column that is associated with the coupled interface output of the first substructure state-space model introduced in the diagonal coupled model (see equation (2.66));

2. Add the column of $[\tilde{A}]$ that is associated with the difference between the coupled interface outputs previously multiplied by $-\phi$ to the column that is associated

with the coupled interface output of the second substructure state-space model introduced in the diagonal coupled model (see equation (2.66));

3. Repeat the procedures outlined in the first and second bullets for matrix $[\tilde{C}]$;

4. Eliminate the row and column of matrix $[\tilde{A}]$ associated with the difference between the coupled interface outputs;

5. Eliminate the same row and column of matrices $[\tilde{B}]$ and $[\tilde{C}]$, respectively;

6. Repeat the procedure for the first derivative of the analyzed pair of coupled interface DOFs.

2.5.3 Analytical and Numerical determination of state-space models representative of inverted diagonal apparent mass terms of CEs

In case that a given CE is analytically or numerically characterized, its stiffness, damping and mass matrices are usually known. Thereby, to identify a state-space model representative of its diagonal apparent mass terms, we may start by retaining from their stiffness, damping and mass matrices the coefficients associated with the set of diagonal apparent mass terms intended to be identified. Afterwards, we must construct a state-space model representative of the set of diagonal apparent mass terms to be identified by exploiting expressions (B.3). Lastly, by inverting this model, the intended state-space model representative of the inverted set of diagonal apparent mass terms can be obtained.

It is worth mentioning that, if the CE under study is massless, the feedthrough matrix of the model representative of its diagonal apparent mass terms will be null. Thus, the inversion of this state-space model cannot be performed without facing ill-conditioned numerical problems (see expressions (A.5)). To surpass this difficulty, we can sum to the feedthrough matrix of this model an identity matrix multiplied by a small residue. The value of this residue must be as small as possible, because its only intent is to prevent ill-conditioned numerical problems, when inverting the feedthrough matrix of the model representative of the set of diagonal apparent mass terms to be identified. It is evident that summing this matrix is equivalent to couple small virtual masses to the edges of the CE under analysis.

2.5.4 State-Space realization of IS

Performing direct excitation of an isolated CE is, in general, unfeasible. Thus, these components are commonly tested with fixtures attached to its edges (see for example, [51],[56],[33]). For this reason, to estimate state-space models representative of the inverted diagonal apparent mass terms of a given CE, we will extend IS method into the state-space domain.

In this way, let us consider the generic test set-up used to experimentally characterize the dynamics of CEs depicted in figure 2.5.
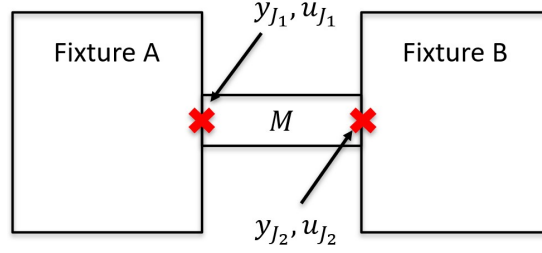
Figure 2.5: Typical measurement set up to characterize the dynamic behaviour of a connecting element [2].

In addition, we will assume that state-space models representative of the apparent mass of the CE M and of the fixtures A and B are available. In this scenario, by exploiting the primal state-space assembly formulation (see section 2.4), we can set-up the following coupled state-space model representative of the apparent mass of the assembly shown in figure 2.5:

$$
\begin{aligned}
\begin{Bmatrix} \dot{\tilde{x}}_{F_A}(t) \\ \dot{\tilde{x}}_M(t) \\ \dot{\tilde{x}}_{F_B}(t) \end{Bmatrix} &= \left[\tilde{A}^{apm}_{F_A M F_B} \right] \begin{Bmatrix} \tilde{x}_{F_A}(t) \\ \tilde{x}_M(t) \\ \tilde{x}_{F_B}(t) \end{Bmatrix} + \left[\tilde{B}^{apm}_{F_A M F_B} \right] \begin{Bmatrix} \ddot{\tilde{y}}_{J_1}(t) \\ \ddot{\tilde{y}}_{J_2}(t) \end{Bmatrix} \\
\begin{Bmatrix} \tilde{u}_{J_1}(t) \\ \tilde{u}_{J_2}(t) \end{Bmatrix} &= \left[\tilde{C}^{apm}_{F_A M F_B} \right] \begin{Bmatrix} \tilde{x}_{F_A}(t) \\ \tilde{x}_M(t) \\ \tilde{x}_{F_B}(t) \end{Bmatrix} + \left[\tilde{D}^{apm}_{F_A M F_B} \right] \begin{Bmatrix} \ddot{\tilde{y}}_{J_1}(t) \\ \ddot{\tilde{y}}_{J_2}(t) \end{Bmatrix}
\end{aligned}
\tag{2.151}
$$

where, matrices $[\tilde{A}^{apm}_{F_A M F_B}]$, $[\tilde{B}^{apm}_{F_A M F_B}]$, $[\tilde{C}^{apm}_{F_A M F_B}]$ and $[\tilde{D}^{apm}_{F_A M F_B}]$ are given as follows:

$$
\begin{aligned}
[\tilde{A}^{apm}_{F_A M F_B}] &= \begin{bmatrix} A^{apm}_{F_A} & 0 & 0 \\ 0 & A^{apm}_{M} & 0 \\ 0 & 0 & A^{apm}_{F_B} \end{bmatrix} \\
[\tilde{B}^{apm}_{F_A M F_B}] &= \begin{bmatrix} \tilde{B}^{apm}_{F_A M F_B, J_1} & \tilde{B}^{apm}_{F_A M F_B, J_2} \end{bmatrix} = \begin{bmatrix} B^{apm}_{F_A, J_1} & 0 \\ B^{apm}_{M, J_1} & B^{apm}_{M, J_2} \\ 0 & B^{apm}_{F_B, J_2} \end{bmatrix} \\
[\tilde{C}^{apm}_{F_A M F_B}] &= \begin{bmatrix} \tilde{C}^{apm}_{F_A M F_B, J_1} \\ \tilde{C}^{apm}_{F_A M F_B, J_2} \end{bmatrix} = \begin{bmatrix} C^{apm}_{F_A, J_1} & C^{apm}_{M, J_1} & 0 \\ 0 & C^{apm}_{M, J_2} & C^{apm}_{F_B, J_2} \end{bmatrix} \\
[\tilde{D}^{apm}_{F_A M F_B}] &= \begin{bmatrix} \tilde{D}^{apm}_{F_A M F_B, J_1 J_1} & \tilde{D}^{apm}_{F_A M F_B, J_1 J_2} \\ \tilde{D}^{apm}_{F_A M F_B, J_2 J_1} & \tilde{D}^{apm}_{F_A M F_B, J_2 J_2} \end{bmatrix} \\
&= \begin{bmatrix} D^{apm}_{F_A, J_1 J_1} + D^{apm}_{M, J_1 J_1} & D^{apm}_{M, J_1 J_2} \\ D^{apm}_{M, J_2 J_1} & D^{apm}_{F_B, J_2 J_2} + D^{apm}_{M, J_2 J_2} \end{bmatrix}
\end{aligned}
\tag{2.152}
$$

where, subscripts J_1 and J_2 denote outputs or/and inputs associated with the inter-

face DOFs of fixtures A and B, respectively, subscripts F_A and F_B denote variables associated with fixtures A and B (see figure 2.5), respectively, while subscript $F_A M F_B$ denotes variables associated with the coupled model representative of the apparent mass of the assembled structure composed by the fixtures A and B connected by the CE M.

By applying a Fourier transformation on the state-space model given in expression (2.151) and by dropping $[\bullet]$, $\{\bullet\}$ and $(j\omega)$ for ease of readability, we arrive to the following expression:

$$
\begin{aligned}
j\omega \tilde{X}_{F_A M F_B} &= \tilde{A}^{apm}_{F_A M F_B} \tilde{X}_{F_A M F_B} + \tilde{B}^{apm}_{F_A M F_B}(-\omega^2 \tilde{Y}_{F_A M F_B}) \\
\tilde{U}_{F_A M F_B} &= \tilde{C}^{apm}_{F_A M F_B} \tilde{X}_{F_A M F_B} + \tilde{D}^{apm}_{F_A M F_B}(-\omega^2 \tilde{Y}_{F_A M F_B})
\end{aligned}
\tag{2.153}
$$

after making some mathematical manipulations, we may define the following expression:

$$
\tilde{Z}^A = \frac{\tilde{U}_{F_A M F_B}}{-\omega^2 \tilde{Y}_{F_A M F_B}} = \tilde{C}^{apm}_{F_A M F_B}(j\omega I - \tilde{A}^{apm}_{F_A M F_B})^{-1}\tilde{B}^{apm}_{F_A M F_B} + \tilde{D}^{apm}_{F_A M F_B}
\tag{2.154}
$$

where, $[\tilde{Z}^A(j\omega)]$ represents an apparent mass matrix.

By exploiting expression (2.151) and after making some mathematical manipulations, equation (2.154) can be rewritten as follows:

$$
[\tilde{Z}^A_{F_A M F_B}(j\omega)] = \begin{bmatrix} \tilde{Z}^A_{F_A M F_B, J_1 J_1}(j\omega) & \tilde{Z}^A_{F_A M F_B, J_1 J_2}(j\omega) \\ \tilde{Z}^A_{F_A M F_B, J_2 J_1}(j\omega) & \tilde{Z}^A_{F_A M F_B, J_2 J_2}(j\omega) \end{bmatrix}
\tag{2.155}
$$

where, by dropping again $[\bullet]$, $\{\bullet\}$ and $(j\omega)$, we have:

$$
\begin{aligned}
\tilde{Z}^A_{F_A M F_B, J_1 J_1} &= \tilde{C}^{apm}_{F_A M F_B, J_1}(j\omega I - \tilde{A}^{apm}_{F_A M F_B})^{-1}\tilde{B}^{apm}_{F_A M F_B, J_1} + \tilde{D}^{apm}_{F_A M F_B, J_1 J_1} \\
\tilde{Z}^A_{F_A M F_B, J_1 J_2} &= \tilde{C}^{apm}_{F_A M F_B, J_1}(j\omega I - \tilde{A}^{apm}_{F_A M F_B})^{-1}\tilde{B}^{apm}_{F_A M F_B, J_2} + \tilde{D}^{apm}_{F_A M F_B, J_1 J_2} \\
\tilde{Z}^A_{F_A M F_B, J_2 J_1} &= \tilde{C}^{apm}_{F_A M F_B, J_2}(j\omega I - \tilde{A}^{apm}_{F_A M F_B})^{-1}\tilde{B}^{apm}_{F_A M F_B, J_1} + \tilde{D}^{apm}_{F_A M F_B, J_2 J_1} \\
\tilde{Z}^A_{F_A M F_B, J_2 J_2} &= \tilde{C}^{apm}_{F_A M F_B, J_2}(j\omega I - \tilde{A}^{apm}_{F_A M F_B})^{-1}\tilde{B}^{apm}_{F_A M F_B, J_2} + \tilde{D}^{apm}_{F_A M F_B, J_2 J_2}.
\end{aligned}
\tag{2.156}
$$

From expressions (2.156) and (2.152) and having in mind that $[\tilde{A}^{apm}_{F_A M F_B}]$ is a block diagonal matrix, it is straightforward to conclude that the off diagonal apparent mass terms of the assembled structure can be identified from the state-space model representative of the CE. Hence, those terms are also the off diagonal apparent mass terms of the CE as pointed out in [51]. This means that it is possible to identify state-space models representative of the off diagonal apparent mass terms of the CE directly from the state-space model representative of the apparent mass of the assembled structure. To perform this identification, we must retain from the model of the assembly the outputs and inputs associated with the off diagonal terms of interest. The rest of the outputs and inputs must be eliminated. This can be done by only keeping the rows of

$[\tilde{C}^{apm}_{F_A M F_B}]$ and $[\tilde{D}^{apm}_{F_A M F_B}]$ associated with the outputs of the off diagonal apparent mass terms to be identified and by solely keeping the columns of $[\tilde{B}^{apm}_{F_A M F_B}]$ and $[\tilde{D}^{apm}_{F_A M F_B}]$ associated with the inputs of the off diagonal apparent mass terms to be identified.

If the assumptions underlying IS are verified for the CE under study, the diagonal apparent mass terms can be obtained by multiplying the off diagonal terms by -1 (see quation (2.56)). Thus, to compute a state-space model representative of the diagonal apparent mass terms of the CE, we must transform the identified state-space model representative of the off diagonal terms of these elements into negative form (see appendix B). By inverting the resultant state-space model, we are able to compute the intended state-space model representative of the inverted diagonal apparent mass terms of the CE.

Chapter 3

On the computation of stable coupled models

3.1 Introduction

In this section, we will focus our attention on the computation of accurate stable coupled models through SSS. To compute these models, we must start by making sure that the state-space models involved in the coupling operations verify all the required criteria to be suitable for being exploited in DS operations. Each of these state-space models is responsible for characterizing the dynamics of one substructure involved on the coupling operations. Thus, they must accurately represent the dynamic behaviour of the substructures involved in these operations. On top of this, each of these state-space models must be stable (i.e. their poles must be pure imaginary or present negative real part), reciprocal (when representing the dynamics of reciprocal substructures), verify the Newton's second law, passive and must present outputs and inputs placed at the interfaces of the substructures involved in the DS operations [46].

When estimated analytically or numerically, the state-space models generally fulfill all the criteria outlined above. Thus, it is in general straightforward to compute stable coupled models by coupling them. In contrast, by estimating state-space models from experimentally acquired data (for example, from measured FRFs), it is usually difficult to compute state-space models respecting the mentioned criteria. For this reason, in this section we will only focus our attention on state-space models experimentally identified.

To experimentally identify a state-space model representative of the dynamics of a given mechanical system, it is common to exploit system identification algorithms with data collected from the experimental modal characterization of that given mechanical system. Many different system identification algorithms have been proposed in literature. Examples of these algorithms are the approaches, commonly, clustered under the label subspace methods (see, for example, [57], [58], [59], [60]). This kind of methods is capable of directly estimating state-space models from experimentally

acquired data (either from time-domain or frequency-domain data depending on the exploited subspace method). Other system identification approaches, specially, targeting structural dynamics applications can be found in literature as well. These methods are usually tagged as Experimental Modal Analysis (EMA) methods and provide an estimation for the modal parameters of the substructures under analysis [21]. These parameters can then, be used to set-up state-space models (see, for instance, [40], [10]). A classical EMA technique is the Rational Fractional Polynomial method presented in [61], which was then, extended to deal with systems presenting multiple inputs in [62]. After the publication of these techniques many other methods were published (e.g. [63], [64], [65]). One of the most used and well-known EMA approaches is the PolyMAX (Polyreference least-squares complex frequency-domain) method, which was proposed in [66], [22]. This method makes use of the polyreference Least-Squares Complex Frequency-domain (pLSCF) method to construct the so-called stabilization diagram from which the poles and modal participation factors can be estimated. Then, the Least-Squares Frequency-domain (LSFD) method (see, appendix D) is applied with the poles, the modal participation factors and the reference FRFs to estimate the mode shapes and the upper and lower residual matrices in a linear-least squares sense. To improve the quality of the modal parameters estimated by PolyMAX, the Maximum Likelihood Modal Model method (ML-MM) was developed in a series of papers [67], [68], [69], [70]. ML-MM is an iterative method based on solving a non-linear optimization problem. At each iteration, this method optimizes the modal parameters in two different steps. Firstly, the poles and modal participation factors are updated by exploiting the Gauss-Newton optimization. Afterwards, the remaining modal parameters (i.e. mode shapes, upper and lower residual matrices) are computed by using LSFD with the optimized poles and modal participation factors and with the reference FRFs. These optimized modal parameters are then used in the next iteration. The described optimization loop runs until convergence is attained or the defined maximum number of iterations is reached. Interesting overviews on the EMA techniques can be found in [71], [72], [21], [73], [74].

Here, to experimentally identify state-space models, we will start by exploiting PolyMAX to estimate modal parameters from sets of experimentally acquired FRFs. Afterwards, if the estimated modal parameters are not of enough quality, the ML-MM method will be exploited to improve them. Finally, by following the procedures presented in [40], the state-space models will be constructed from the estimated modal parameters. Note that, we have decided to exploit this methodology, because in [40] it turned out to be accurate on experimentally estimating state-space models to be used on real industrial applications. Furthermore, both PolyMAX and ML-MM approaches are well established techniques that have already demonstrated to be accurate on estimating modal parameters from challenging experimentally acquired data sets (see, for instance, [22], [70], [75]).

When using PolyMAX and ML-MM approaches to estimate modal parameters form

measured FRFs, we make sure that the identified poles are stable. Thus, we are sure that the state-space models constructed from these modal parameters will be stable as well. Moreover, if the substructure under analysis verifies reciprocity, we may construct a reciprocal state-space model by estimating reciprocal modal parameters as reported in [70].

The identification of state-space models verifying Newton's second law is also mandatory, otherwise mismatches between the accelerance FRFs of the modal model (constructed from the identified modal parameters) and the accelerance FRFs of the identified state-space model will be observed [10]. On top of this, state-space models that do not respect Newton's second law cannot be properly transformed into coupling form [8], making the elimination of the redundant states originated from DS operations impracticable, when the state-space models involved in these operations are not defined in the physical domain (common situation in practice). Bylin et al. in [76] proposed an iterative methodology that re-computes the input and output matrices of state-space models to force them to obey Newton's second law. Nevertheless, this approach makes use of linear least-squares constraints. Therefore, the resultant state-space models only respect Newton's second law in a weak sense. Hence, as discussed in [46], the resultant state-space models do not strictly verify this physical law and, consequently, they are not suitable for being included in SSS operations. In alternative, the method proposed by Liljerehn in [5] to force state-space models to respect Newton's second law can be exploited. This approach has already showed in [46], [10] to be reliable to, strictly, force models estimated from experimentally acquired data to verify Newton's second law. Nevertheless, this method holds the disadvantage of imposing Newton's second law by means of undamped residual compensation modes (RCMs). This is, indeed, not recommended, because the performance of time-domain simulations with state-space models composed by undamped modes may lead to numerical instabilities [40]. Hence, the approach presented in [5] is only suitable to impose Newton's second law on state-space models that will not be exploited in time-domain simulations. To overcome this limitation, a novel approach to force state-space models to respect Newton's second law without using undamped RCMs will be proposed in this section.

Additionally, the estimated state-space models to be used in SSS must be passive. If this requirement is not met the coupled state-space models resultant from SSS operations will also be non-passive and most likely unstable. Thus, it is common that by exploiting SSS approaches with experimentally identified models, we end-up with coupled state-space models that cannot be used for performing stable time-domain simulations. This strongly limits the applications of SSS methods.

Several approaches to impose passivity on state-space models are available in literature. These techniques can be roughly divided into two groups: optimal algorithms and sub-optimal algorithms. The group of the optimal algorithms includes approaches that impose passivity on the estimated state-space models by forcing them to respect the Positive or Bounded real lemmas (see [77]). In addition, to make sure that the FRFs

of the passive model match as close as possible the FRFs of the originally identified model, the optimal approaches make also use of least-squares constraints. Even though these methods lead in general to the computation of accurate passive models, they are characterized for demanding very high computational effort. In [78], [79], [80], it is possible to find examples of this kind of approaches. In contrast, the sub-optimal algorithms require less computational effort than the optimal approaches. Yet, the passive models computed by using these approaches are in general not as accurate as the passive models computed by exploiting optimal algorithms. A sub-optimal approach that makes use of a constrained iterative scheme that is based on Hamiltonian eigenvalue extraction and perturbation can be found in [81]. An interesting overview of different approaches to impose passivity on state-space models can be found in [82].

Nevertheless, the algorithms listed above are not suitable to deal with some structural dynamics applications, because they either yield passive models with limited accuracy or they require very high computational effort. Indeed, the determination of passive models associated with high computation costs may unable the exploitation of SSS in many practical applications. One may think, for instance, on applications involving the characterization and the performance of time-domain simulations of assembled systems presenting time-varying dynamic behaviour. To characterize this kind of substructures, it is usual practice to exploit Linear Parameter-Varying (LPV) models (see, [83], [84], [85], [86]). To construct these models, we must use a set of state-space models representative of the dynamics of the assembled system for some pre-selected fixed operating conditions. Thereby, assuming that a LPV model is set-up from, for example, 5 coupled state-space models, we are required to force $5 \times n_{sub}$ state-space models to be passive, where n_{sub} represents the number of substructures to be coupled to compute a coupled model representative of a given fixed operating condition. Therefore, it is straightforward to conclude that to deal with this type of applications, there is the need for direct methods that are capable of computing reliable passive state-space models without demanding high computational effort.

In an attempt of computing accurate passive models, while avoiding high computational costs, Liljerehn and Abrahamsson in [4] proposed a direct method to impose passivity on velocity state-space models. This approach was developed with the aim of targeting structural dynamics applications involving SSS, which are also the applications that we are targeting in this document. To impose passivity on velocity state-space models, this method relies on the application of a minimal adjustment on the elements of both input and output state-space matrices associated with each mode of the model to ensure that the direct elements of the FRFs of each of these modes are positive real. This approach was successfully applied in [4] to impose passivity on a state-space model estimated from experimentally acquired FRFs. Furthermore, in the same publication it was demonstrated that a passive stable coupled model could be obtained by coupling the model forced to be passive with a passive model computed from information extracted from a Finite Element model. Nonetheless, both models involved

in the coupling operation were representative of simple substructures. Moreover, imposing passivity by forcing the direct elements of the FRFs of all the modes included in a given state-space model to present positive real part, represents a too strict passivity requirement [43]. Hence, this approach might lead to relevant mismatches between the FRFs of the computed passive model and the FRFs of the originally identified state-space model, specially, when dealing with identified models representative of complex substructures and composed by a high number of modes. More importantly, to exploit this method we must select the frequency band for which the elements of the FRFs of each mode will be investigated and forced to be positive real. Therefore, there is no warranty that the computed passive state-space model will verify passivity for frequencies outside of the selected frequency band and for frequencies in between consecutive frequency points. Thereby, we run the risk of obtaining state-space models that are not globally passive, i.e. that are not passive for the entire frequency axis. The computation of models that are not globally passive is not acceptable, because the coupled state-space models originated from DS operations involving this kind of models are, in general, unstable.

To overcome the difficulties associated with imposing passivity on state-space models, a procedure to directly impose stability on unstable coupled models will be here outlined. With this approach, we aim at enabling the direct calculation of stable coupled models without strictly relying on iterative algorithms. Moreover, we intend to come up with a methodology that enables the computation of accurate stable models even when performing SSS operations with state-space models representative of complex substructures and presenting high model order.

Before being suitable to be exploited in SSS operations, the identified state-space models have to present outputs and inputs collocated at the interface of the components under analysis. Yet, in practice there are many substructures for which the placement of sensors and/or actuators at their interfaces is infeasible. For this reason, it is sometimes not possible to estimate state-space models, whose outputs and inputs are placed at the interface of the experimentally characterized components. To surpass this difficulty, it is common to exploit the so-called Virtual Point Transformation (VPT) approach (see, [87], [27], [88]). By exploiting VPT we have the possibility of transforming the outputs and inputs of the measured FRFs into the desired locations (i.e. into the defined virtual points), provided that the components can be assumed to present rigid local behaviour in the frequency band of interest. Thereby, enabling the computation of the FRFs at the intended locations. This set of FRFs can then be used to construct the intended state-space models. In alternative, we may think on directly applying VPT on the state-space models to transform their outputs and inputs into the defined virtual points. To make this approach possible, the VPT method will be extended into the state-space model domain.

In the following, we will start by presenting in section 3.2 a state-of-the-art approach to define state-space models from estimated modal parameters. Then, in section 3.3 a

novel procedure to impose Newton's second law on state-space models without relying on undamped RCMs is presented, whereas the state-space realization of the VPT approach is outlined in section 3.4. Finally, in section 3.5 a novel procedure to impose stability on unstable coupled state-space models is presented.

3.2 State-of-the-art method to experimentally estimate state-space models

The purpose of this section is to explain in detail a state-of-the-art approach to construct complete state-space models by using modal parameters estimated from experimentally acquired FRFs. We will start by presenting how to set-up a state-space model from the modal parameters associated with the in-band poles (section 3.2.1). Then, in section 3.2.2 we will show how to construct state-space models representative of the contribution of both the upper and lower out-of-band modes. Finally, in section 3.2.3 we will present how to compute complete state-space models by using state-space models constructed from the in-band and out-of-band modes.

3.2.1 In-band modes

Let us assume that the modal parameters of an experimentally characterized substructure were estimated from their measured FRFs. From these identified modal parameters, we may set-up a modal model representative of the displacement FRFs of the characterized substructure as follows:

$$[H(j\omega)] = \sum_{r=1}^{n_{ib}} \left(\frac{\{\psi_{ib,r}\}\{l_{ib,r}\}}{j\omega - \lambda_{ib,r}} + \frac{\{\psi_{ib,r}\}^*\{l_{ib,r}\}^*}{j\omega - \lambda_{ib,r}^*} \right) + \frac{[LR]}{(j\omega)^2} + [UR] \qquad (3.1)$$

where, $[H(j\omega)] \in \mathbb{C}^{n_o \times n_i}$ represents a FRF matrix composed by n_o outputs and n_i inputs, n_{ib} represents the number of identified modes, subscript $[\bullet]^*$ denotes the complex conjugate of a vector/matrix, $\{\psi_r\} \in \mathbb{C}^{n_o \times 1}$ is the rth mode shape, $\{l_r\} \in \mathbb{C}^{1 \times n_i}$ is the rth modal participation factor, λ_r is the rth pole, while $[LR] \in \mathbb{R}^{n_o \times n_i}$ and $[UR] \in \mathbb{R}^{n_o \times n_i}$ are the lower and upper residuals matrices, whose role is modelling the contribution of the lower and upper out-of-band modes in the frequency band of interest, respectively. Finally, subscript ib denotes vectors/matrices associated with the in-band modes.

The modal model given in expression (3.1) can be rewritten in matrix form as follows:

$$[H(j\omega)] = [\Psi_{ib} \quad \Psi_{ib}^*] \left[j\omega[I] - \begin{bmatrix} \Lambda_{ib} & 0 \\ 0 & \Lambda_{ib}^* \end{bmatrix} \right]^{-1} \begin{bmatrix} L_{ib} \\ L_{ib}^* \end{bmatrix} + \frac{[LR]}{(j\omega)^2} + [UR] \qquad (3.2)$$

where, $[\Lambda] \in \mathbb{C}^{n_{ib} \times n_{ib}}$ is a diagonal matrix composed by the system poles, $[L] \in \mathbb{C}^{n_{ib} \times n_i}$ is a matrix including as rows the modal participation factors and their complex conju-

gates and $[\Psi] \in \mathbb{C}^{n_o \times n_{ib}}$ is a matrix including as columns the mode shape vectors and their complex conjugates.

From expression (3.2), we may define a state-space model associated with the in-band modes as follows (see [45]):

$$\{\dot{x}_{ib}(t)\} = [A_{ib}]\{x_{ib}(t)\} + [B_{ib}]\{u_{ib}(t)\}$$
$$\{y_{ib}(t)\} = [C_{ib}^{disp}]\{x_{ib}(t)\} \tag{3.3}$$

where, matrices $[A_{ib}]$, $[B_{ib}]$ and $[C_{ib}^{disp}]$ are given hereafter.

$$[A_{ib}] = \begin{bmatrix} \Lambda_{ib} & 0 \\ 0 & \Lambda_{ib}^* \end{bmatrix}, \quad [B_{ib}] = \begin{bmatrix} L_{ib} \\ L_{ib}^* \end{bmatrix}, \quad [C_{ib}^{disp}] = [\Psi_{ib} \quad \Psi_{ib}^*] \tag{3.4}$$

3.2.2 Out-of-band modes

To construct a complete state-space model, the inclusion of the contribution of the out-of band modes is mandatory. For this reason, in the following we will demonstrate how to set-up state-space models representative of the contribution of both upper and lower out-of-band modes. These models can then be concatenated with the state-space model constructed from the in-band modal parameters (see expression (3.3)) to set-up the intended complete state-space model.

Upper out-of-band modes

To include the contribution of the upper out-of-band modes, which is given by the upper residual matrix (see expression (3.3)), we must start by performing the singular value decomposition (SVD) (see, [89]) of matrix $[UR]$ as follows:

$$[UR] = [P_{UR}][\sigma_{UR}][W_{UR}]^T = \sum_{r=1}^{n_{UR}} \{P_{UR,r}\}\sigma_{UR,rr}\{W_{UR,r}\}^T \tag{3.5}$$

where, subscript UR denotes vectors/matrices associated with the upper out-of-band modes, while $n_{UR} = min(n_i, n_o)$. $[P_{UR}] \in \mathbb{R}^{n_o \times n_{UR}}$ and $[W_{UR}] \in \mathbb{R}^{n_{UR} \times n_i}$ are the matrices composed by the left and right eigenvectors of matrix $[UR]$, respectively, whereas $[\sigma_{UR}] \in \mathbb{R}^{n_{UR} \times n_{UR}}$ is a diagonal matrix composed by the singular values of $[UR]$ [21]. Note also that, $\{P_{UR,r}\} \in \mathbb{R}^{n_o \times 1}$ represents the rth column of $[P_{UR}]$, $\sigma_{UR,rr}$ denotes the rth element on the diagonal of $[\sigma_{UR}]$ and $\{W_{UR,r}\} \in \mathbb{R}^{1 \times n_i}$ represents the rth row of $[W_{UR}]$. By exploiting the SVD of $[UR]$, we may define residual compensation modes (RCMs) tailored to model the contribution of the upper out-of-band modes. The modal parameters associated with these RCMs can be computed as follows:

$$\lambda_{UR,r} = -\xi_{UR,r}\omega_{UR,r} \pm j\omega_{UR,r}\sqrt{1 - \xi_{UR,r}^2} \tag{3.6}$$

$$\{l_{UR,r}\} = -\frac{j}{2}\sqrt{\sigma_{UR,rr}}\{W_{UR,r}\}^T \tag{3.7}$$

$$\{\psi_{UR,r}\} = \frac{\omega_{UR,r}}{\sqrt{1-\xi_{UR,r}^2}}\sqrt{\sigma_{UR,rr}}\{P_{UR,r}\} \tag{3.8}$$

where, $\omega_{UR,r}$ and $\xi_{UR,r}$ are the selected natural frequency and damping ratio of the rth mode of the computed RCMs, respectively.

By using expressions (3.6), (3.7) and (3.8),we may define a proportionally damped modal model (i.e. modal model, whose residue matrices are pure imaginary [90]) that approximates the contribution of the upper out-of-band modes as hereafter.

$$[UR] \approx [H_{UR}(j\omega)] = \sum_{r=1}^{n_{UR}} \left(\frac{2j\omega_{UR,r}\sqrt{1-\xi_{UR,r}^2}}{(j\omega)^2 + 2j\omega\xi_{UR,r}\omega_{UR,r} + \omega_{UR,r}^2}\{\psi_{UR,r}\}\{l_{UR,r}\} \right) \tag{3.9}$$

Substituting expressions (3.7) and (3.8) in equation (3.9), it is evident that equations (3.9) and (3.5) match for $\omega = 0$ rad s^{-1}. However, for other frequencies the same match is no longer verified and, hence expression (3.9) represents no more than an approximation of expression (3.5).

To understand the effect of selecting different values for the natural frequencies and damping rations of the RCMs on the quality of the match between expressions (3.5) and (3.9), let us start by assuming that the natural frequencies and the damping ratios of all the RCMs are selected to be the same (which is usual in practice). In this way, by exploiting expression (3.9), we may define the following identity for $\omega = 0$ rad s^{-1}:

$$[UR] = [H_{UR}(0)] = \frac{\sum_{r=1}^{n_{UR}} \left(2j\omega_{UR}\sqrt{1-\xi_{UR}^2}\{\psi_{UR,r}\}\{l_{UR,r}\} \right)}{\omega_{UR}^2} \tag{3.10}$$

which is equivalent to the expression given hereafter.

$$\sum_{r=1}^{n_{UR}} \left(2j\omega_{UR}\sqrt{1-\xi_{UR}^2}\{\psi_{UR,r}\}\{l_{UR,r}\} \right) = \omega_{UR}^2[UR] \tag{3.11}$$

By observing equations (3.9) and (3.11), it is evident that as the value selected for ω_{UR} increases, the more accurate will be the proportionally damped modal model (see expression (3.9)) to model the contribution of the upper out-of-band modes. Moreover, we can also conclude that the accuracy of this modal model will increase as the value selected for ξ_{UR} is selected to be lower.

At this point, we can exploit the RCMs computed from the SVD of $[UR]$ to define a state-space model representative of the contribution of the upper out-of-band modes as follows:

$$\{\dot{x}_{UR}(t)\} = [A_{UR}]\{x_{UR}(t)\} + [B_{UR}]\{u_{UR}(t)\}$$
$$\{\dot{y}_{UR}(t)\} = [C_{UR}^{disp}]\{x_{UR}(t)\}$$

(3.12)

with,

$$[A_{UR}] = \begin{bmatrix} \Lambda_{UR} & 0 \\ 0 & \Lambda_{UR}^* \end{bmatrix}, \quad [B_{UR}] = \begin{bmatrix} L_{UR} \\ L_{UR}^* \end{bmatrix}$$
$$[C_{UR}^{disp}] = \begin{bmatrix} \Psi_{UR} & \Psi_{UR}^* \end{bmatrix}$$

(3.13)

where, $[\Lambda_{UR}]$, $[L_{UR}]$ and $[\Psi_{UR}]$ are given below.

$$[\Lambda_{UR}] = \begin{bmatrix} \lambda_{UR,1} & & \\ & \lambda_{UR,2} & \\ & & \ddots \end{bmatrix}, \quad [L_{UR}] = \begin{bmatrix} l_{UR,1} \\ l_{UR,2} \\ \vdots \end{bmatrix}, \quad [\Psi_{UR}] = \begin{bmatrix} \psi_{UR,1} \\ \psi_{UR,2} \\ \vdots \end{bmatrix}^T$$

(3.14)

As discussed above, the proportionally damped modal model given in expression (3.9) will be more accurate to approximate the contribution of the upper out-of-band modes as the value selected for ω_{UR} increases and as the value selected for ξ_{UR} decreases. Obviously, the same conclusions hold for the accuracy of the state-space model given in expression (3.12), because it was set-up from the modal parameters used to define the proportionally damped modal model given in expression (3.9).

Nevertheless, if the state-space model under construction is to be discretized, for instance, to perform time-domain simulations, the value selected for ω_{UR} must not be extremely high, because to properly discretize a state-space model, we must use a sampling frequency that is at least twice the value of the highest natural frequency of the modes included in the state-space model [40]. Thus, if an extremely high value is selected for ω_{UR}, we will be forced to discretize the constructed state-space model by using an even higher sampling frequency. This would definitely lead to a substantial increment of the computational effort associated with the performance of calculations with the discretized model. Hence, it would make the constructed model less appealing to be exploited in practice. Moreover, the RCMs computed from the SVD of $[UR]$ must not be undamped (i.e. the value selected for ξ_{UR} must not be zero), because the performance of time simulations with state-space models composed by undamped modes may give rise to numerical instabilities [40].

As a rule of thumb, it was proposed in [10] that the value selected for ω_{UR} must respect $\omega_{UR} \geq 5 \times \omega_{max}$ (where, ω_{max} denotes the maximum frequency of interest). However, this value represents a lower limit for the selection of ω_{UR}. In fact, there are many cases for which the natural frequency of the RCMs computed from $[UR]$ must be selected to be higher than $5 \times \omega_{max}$. In practice, we must select a value for ω_{UR} that ensures that the FRFs of the state-space model given in expression (3.12) well match

the elements of $[UR]$ in the frequency band of interest (see expression (3.1))).

To avoid numerical instabilities associated with the performance of time-domain simulations with state-space models composed by undamped or slightly damped modes, a default value of 0.4 was recommended for ξ_{UR} in [40]. Yet, the authors have noticed that in the computation of many state-space models to be exploited in time-domain simulations, it is not necessary to select such a high value for ξ_{UR}. Thus, as a rule of thumb, we recommend that the value of ξ_{UR} must obey $0.1 \leq \xi_{UR} < 1$. In this way, when constructing the state-space model, we must start by selecting the value of ξ_{UR} to be 0.1. If the performance of time-domain simulations with the constructed model leads to numerical instabilities, we must reconstruct the model by selecting a higher value for ξ_{UR}. When an appropriate value for ξ_{UR} is found, we must re-check the quality of the match between the FRFs of the state-space model computed from the RCMs representative of the contribution of the upper out-of-band modes with the elements of $[UR]$ in the frequency band of interest. If this match turns out to not be of sufficient quality, the state-space model must be reconstructed by selecting a higher value for ω_{UR}. It is worth noting, that as we are using a modal model (which, is only made of pairs of complex conjugate poles) to define the modal parameters of the RCMs calculated from the SVD of $[UR]$, the value of ξ_{UR} has to remain below 1.

Lower out-of-band modes

To include the contribution of the lower out-of-band modes, tailored RCMs representative of the contribution of these modes in the frequency band of interest must be defined. However, the contribution of the lower out-of-band modes is modelled by matrix $\frac{[LR]}{(j\omega)^2}$ (see expression (3.3)), thus it is not evident, from which matrix these RCMs must be computed. In an attempt to solve this question, let us assume that the contribution of the lower out-of-band modes is approximated by a generic set of RCMs. Additionally, let us further assume that by using this generic set of RCMs, we can define the following proportionally damped modal model:

$$\frac{[LR]}{(j\omega)^2} \approx [H_{LR}(j\omega)] = \sum_{r=1}^{n_{LR}} \left(\frac{2j\omega_{LR,r}\sqrt{1-\xi_{LR,r}^2}}{(j\omega)^2 + 2j\omega\xi_{LR,r}\omega_{LR,r} + \omega_{LR,r}^2} \{\psi_{LR,r}\}\{l_{LR,r}\} \right) \quad (3.15)$$

where, subscript LR denotes vectors/matrices associated with the lower out-of-band modes, whereas $n_{LR} = min(n_i, n_o)$.

From the observation of equation (3.15), it is straightforward to conclude that the generic proportionally damped modal model will accurately approximate the contribution of the lower out-of-band modes (i.e. $\frac{[LR]}{(j\omega)^2}$), in case that its numerator is equal to $[LR]$ and if the values of the natural frequencies of the RCMs used to compute this modal model are small when compared with ω_{min} (where, ω_{min} denotes the mini-

mum frequency of interest). From now on, we will once again assume that the natural frequencies and damping ratios associated with the RCMs are selected to be equal (common approach in practice). In this way, for $\omega = 0 \; rads^{-1}$, expression (3.15) can be rewritten as given hereafter.

$$[H_{LR}(0)] = \frac{\sum_{r=1}^{n_{LR}} \left(2j\omega_{LR}\sqrt{1 - \xi_{LR}^2}\{\psi_{LR,r}\}\{l_{LR,r}\} \right)}{\omega_{LR}^2} \tag{3.16}$$

By observing expression (3.16), it is evident that the numerator of the proportionally damped modal model will be equal to $[LR]$, if $[H_{LR}(0)] = \frac{[LR]}{\omega_{LR}^2}$. Thus, to compute RCMs capable of modelling the contribution of the lower out-of-band modes, we must perform the SVD of $\frac{[LR]}{\omega_{LR}^2}$ as follows:

$$\frac{[LR]}{\omega_{LR}^2} = [P_{LR}][\sigma_{LR}][W_{LR}]^T = \sum_{r=1}^{n_{LR}} \{P_{LR,r}\}\sigma_{LR,rr}\{W_{LR,r}\}^T \tag{3.17}$$

where, $[P_{LR}] \in \mathbb{R}^{n_o \times n_{LR}}$ and $[W_{LR}] \in \mathbb{R}^{n_{LR} \times n_i}$ are the matrices composed by the left and right eigenvectors of matrix $\frac{[LR]}{\omega_{LR}^2}$, respectively, whereas $[\sigma_{LR}] \in \mathbb{R}^{n_{LR} \times n_{LR}}$ is a diagonal matrix composed by the singular values of $\frac{[LR]}{\omega_{LR}^2}$ [21]. Note also that, $\{P_{LR,r}\} \in \mathbb{R}^{n_o \times 1}$ represents the rth column of $[P_{LR}]$, $\sigma_{LR,rr}$ denotes the rth element on the diagonal of $[\sigma_{LR}]$ and $\{W_{LR,r}\} \in \mathbb{R}^{1 \times n_i}$ represents the rth row of $[W_{LR}]$.

From expression (3.17), the modal parameters associated with the RCMs responsible for modelling the contribution of the lower out-of-band modes can be calculated as given below.

$$\lambda_{LR,r} = -\xi_{LR}\omega_{LR} + j\omega_{LR}\sqrt{1 - \xi_{LR}^2} \tag{3.18}$$

$$\{l_{LR,r}\} = -\frac{j}{2}\sqrt{\sigma_{LR,rr}}\{W_{LR,r}\}^T \tag{3.19}$$

$$\{\psi_{LR,r}\} = \frac{\omega_{LR}}{\sqrt{1 - \xi_{LR}^2}}\sqrt{\sigma_{LR,rr}}\{P_{LR,r}\} \tag{3.20}$$

By exploiting the modal parameters associated with the RCMs computed from the SVD of $\frac{[LR]}{\omega_{LR}^2}$ (see expressions (3.18), (3.19) and (3.20)), we may define a state-space model representative of the contribution of the lower out-of-band modes as follows:

$$\begin{aligned} \{\dot{x}_{LR}(t)\} &= [A_{LR}]\{x_{LR}(t)\} + [B_{LR}]\{u_{LR}(t)\} \\ \{y_{LR}(t)\} &= [C_{LR}^{disp}]\{x_{LR}(t)\} \end{aligned} \tag{3.21}$$

with,

$$[A_{LR}] = \begin{bmatrix} \Lambda_{LR} & 0 \\ 0 & \Lambda_{LR}^* \end{bmatrix}, \quad [B_{LR}] = \begin{bmatrix} L_{LR} \\ L_{LR}^* \end{bmatrix}$$
$$[C_{LR}^{disp}] = \begin{bmatrix} \Psi_{LR} & \Psi_{LR}^* \end{bmatrix} \tag{3.22}$$

where, matrices $[\Lambda_{LR}]$, $[L_{LR}]$ and $[\Psi_{LR}]$ are given below.

$$[\Lambda_{LR}] = \begin{bmatrix} \lambda_{LR,1} & & \\ & \lambda_{LR,2} & \\ & & \ddots \end{bmatrix}, \quad [L_{LR}] = \begin{bmatrix} l_{LR,1} \\ l_{LR,2} \\ \vdots \end{bmatrix}, \quad [\Psi_{LR}] = \begin{bmatrix} \psi_{LR,1} \\ \psi_{LR,2} \\ \vdots \end{bmatrix}^T \tag{3.23}$$

From equations (3.15), it is evident that the RCMs computed from $\frac{[LR]}{\omega^2}$ will be more accurate to approximate the contribution of the lower out-of-band modes as the values for their natural frequencies and damping ratios are selected to be lower. Thus, the same applies for the state-space model defined in expression (3.21) from this set of RCMs.

As decreasing the value selected for the natural frequencies associated with the RCMs computed from $\frac{[LR]}{\omega^2}$ is not linked with any negative consequence, this value can be selected with freedom. In contrast, the value selected for the damping ratios of these RCMs must follow the rule of thumb proposed to define the damping ratios of the RCMs responsible for modelling the contribution of the upper out-of-band modes. To assess the accuracy of the RCMs responsible for modelling the contribution of $\frac{[LR]}{(j\omega)^2}$, we must compare the FRFs of the state-space model given in expression (3.21) with $\frac{[LR]}{(j\omega)^2}$ (which represents the contribution of the lower out-of-band modes, see expression (3.1)) in the frequency band of interest. If relevant mismatches are observed, these RCMs must be re-computed by choosing a lower value for their natural frequencies.

3.2.3   Complete state-space model

To construct a complete state-space model, we must concatenate the state-space models representative of the in-band modes and of the upper and lower out-of-band modes (expressions (3.3), (3.12) and (3.21), respectively). In this way, the complete state-space model can be set-up as follows:

$$\{\dot{x}_{full}(t)\} = [A_{full}]\{x_{full}(t)\} + [B_{full}]\{u_{full}(t)\}$$
$$\{y_{full}(t)\} = \begin{bmatrix} C_{full}^{disp} \end{bmatrix} \{x_{full}(t)\} \tag{3.24}$$

with,

$$[A_{full}] = \begin{bmatrix} \Lambda_{full} & 0 \\ 0 & \Lambda_{full}^* \end{bmatrix}, \quad [B_{full}] = \begin{bmatrix} L_{full} \\ L_{full}^* \end{bmatrix}, \quad [C_{full}^{disp}] = \begin{bmatrix} \Psi_{full} & \Psi_{full}^* \end{bmatrix} \tag{3.25}$$

where, matrices $[\Lambda_{full}]$, $[L_{full}]$ and $[\Psi_{full}]$ are given below.

$$[\Lambda_{full}] = \begin{bmatrix} \Lambda_{i_b} & 0 & 0 \\ 0 & \Lambda_{LR} & 0 \\ 0 & 0 & \Lambda_{UR} \end{bmatrix}, \quad [L_{full}] = \begin{bmatrix} L_{i_b} \\ L_{LR} \\ L_{UR} \end{bmatrix}, \quad [\Psi_{full}] = [\Psi_{i_b} \quad \Psi_{LR} \quad \Psi_{UR}] \quad (3.26)$$

Note that the complete state-space model given in expression (3.24) can be transformed into block-diagonal form by applying a similarity transformation as presented in [91],[39]. When a state-space model is transformed into real block-diagonal form, its state-space matrices become real-valued matrices. Thereby, we have the possibility of decreasing the numerical complexity of the calculations to be performed with the complete state-space model.

3.3   Imposing Newton's second law

The aim of this section is to present a novel approach to impose Newton's second law on state-space models without relying on the use of undamped RCMs. In section 3.3.1, we will start by explaining in detail the negative consequences of computing state-space models violating Newton's second law. Afterwards, in section 3.3.2 a novel approach to force state-space models to respect Newton's second law without using undamped RCMs is presented. Finally, a comparison between the proposed novel approach and a state-of-the-art procedure to impose Newton's second law on state-space models is given in section 3.3.3.

3.3.1   Negative effects of violating Newton's second law

Newton's second law states that there is a direct relation between force and acceleration, but there are no direct relations between force and displacement or velocity. For this reason, the feedthrough matrices of displacement and velocity state-space models (i.e. $[D^{disp}]$ and $[D^{vel}]$, respectively) must be null. This requirement is always met for displacement state-space models, because the feedthrough matrix of this kind of models is by definition null. In contrast, the feedthrough matrix of a velocity state-space model will not necessarily be null. To better understand the reason why the feedthrough matrices of velocity models might not be null, let us consider the expression to calculate the displacement FRFs of a generic state-space model as given below (see [45]).

$$[H(j\omega)] = [C^{disp}](j\omega[I] - [A])^{-1}[B] \quad (3.27)$$

To get to a mathematical expression to calculate the mobility FRFs of a given state-space model, we must differentiate equation (3.27) as follows:

$$[H^{vel}(j\omega)] = j\omega[H(j\omega)] = [C^{vel}](j\omega[I] - [A^{vel}])^{-1}[B^{vel}] + [D^{vel}] \quad (3.28)$$

with,

$$[A^{vel}] = [A], \quad [B^{vel}] = [B], [C^{vel}] = [C^{disp}][A], \quad [D^{vel}] = [C^{disp}][B] \qquad (3.29)$$

where, superscript *vel* denotes vectors/matrices associated to a velocity state-space model.

By observing expressions (3.28) and (3.29), it is evident that there is no guarantee that the feedthrough matrix of velocity state-space models is always null. Hence, the state-space models estimated from experimentally acquired data may violate Newton's second law. The computation of state-space models that violate Newton's second law presents two practical disadvantages. On the one hand, models not verifying Newton's second law cannot be properly transformed into coupling form [8]. This unables the computation of minimal-order coupled state-space models, when performing coupling operations with state-space models that are not represented in the physical domain (common situation in practice) (see section 2.2.3). On the other hand, the accelerance FRFs of a state-space model violating Newton's second law cannot be properly computed, which leads to a mismatch between these FRFs and the accelerance FRFs of the modal model used to construct the state-space model (see section 3.2). To better explain the second pointed disadvantage of estimating models that do not obey Newton's second law, let us differentiate expression (3.28) to obtain the accelerance FRFs of a generic state-space model as follows:

$$[H^{accel}(j\omega)] = (j\omega)^2[H(j\omega)] = [C^{accel}](j\omega[I] - [A])^{-1}[B] + [D^{accel}] \\ + j\omega[C^{disp}][B] \qquad (3.30)$$

where, $[C^{accel}]$ and $[D^{accel}]$ are given below.

$$[C^{accel}] = [C^{disp}][A][A], \quad [D^{accel}] = [C^{disp}][A][B] \qquad (3.31)$$

From the observation of expressions (3.30) and (3.31), it is clear that the term $j\omega[C^{disp}][B]$ is not included on any state-space matrix of the acceleration state-space model. If the state-space model violates Newton's second law, $[C^{disp}][B]$ will not be null. Hence, a mismatch between the accelerance FRFs of the state-space model and of the modal model used to construct it will be observed.

3.3.2   Novel approach

To present a novel approach to impose Newton's second law without relying on the use of undamped RCMs, let us assume that a complete state-space model representative of a given substructure was set-up by following the procedures discussed in section 3.2. In this way, by using expression (3.28), we may compute the mobility FRFs of this

model as follows

$$[H_{full}^{vel}(j\omega)] = [C_{full}^{vel}](j\omega[I] - [A_{full}])^{-1}[B_{full}] + [D_{full}^{vel}] \tag{3.32}$$

where, matrices $[C_{full}^{vel}]$ and $[D_{full}^{vel}]$ are given below.

$$[C_{full}^{vel}] = [C_{full}^{disp}][A_{full}], \quad [D_{full}^{vel}] = [C_{full}^{disp}][B_{full}] \tag{3.33}$$

The product $[C_{full}^{disp}][B_{full}]$ can be represented as follows:

$$[C_{full}^{disp}][B_{full}] = [C_{ib}^{disp}][B_{ib}] + [C_{LR}^{disp}][B_{LR}] + [C_{UR}^{disp}][B_{UR}] \tag{3.34}$$

or, alternatively, by using expressions (3.24), (3.25) and (3.26), we may define the product $[C_{full}^{disp}][B_{full}]$ as given below.

$$\begin{aligned}[C_{full}^{disp}][B_{full}] = &[\Psi_{ib}L_{ib} + \Psi_{LR}L_{LR} + \Psi_{UR}L_{UR} \\ &+ \Psi_{ib}^{*}L_{ib}^{*} + \Psi_{LR}^{*}L_{LR}^{*} + \Psi_{UR}^{*}L_{UR}^{*}]\end{aligned} \tag{3.35}$$

By computing the column-row expansion (see [28]) of each matrix product present in expression (3.35), we may establish the following expression.

$$\begin{aligned}[C_{full}^{disp}][B_{full}] = \Bigg[&\sum_{r=1}^{n_{ib}}(\psi_{ib,r}l_{ib,r}) + \sum_{r=1}^{n_{LR}}(\psi_{LR,r}l_{LR,r}) + \sum_{r=1}^{n_{UR}}(\psi_{UR,r}l_{UR,r}) \\ &+ \sum_{r=1}^{n_{ib}}(\psi_{ib,r}^{*}l_{ib,r}^{*}) + \sum_{r=1}^{n_{LR}}(\psi_{LR,r}^{*}l_{LR,r}^{*}) + \sum_{r=1}^{n_{UR}}(\psi_{UR,r}^{*}l_{UR,r}^{*})\Bigg]\end{aligned} \tag{3.36}$$

By observing expression (3.36), it is clear that by estimating the in-band modal parameters by assuming a proportionally damped modal model (for example, by following the approach reported in [70], which involves the use of the constrained version of LSFD presented in appendix E), we can ensure that $[C_{ib}^{disp}][B_{ib}] = [0]$, because the residue matrices (i.e. $\{\psi_{ib,r}\}\{l_{ib,r}\}$) of a proportionally damped modal model are pure imaginary [90]. For this reason, $[C_{LR}^{disp}][B_{LR}] = [0]$ and $[C_{UR}^{disp}][B_{UR}] = [0]$ is always verified, because the modal parameters of the RCMs responsible for modelling the contribution of both upper and lower out-of-band modes are defined by using proportionally damped modal models (see section 3.2.2). Thus, it is straightforward to conclude that $[C_{full}^{disp}][B_{full}] = [C_{ib}^{disp}][B_{ib}]$ (see expression (3.34)). Therefore, from now on, to force the complete state-space models to respect Newton's second law, we will restrict our attention to $[C_{ib}^{disp}][B_{ib}]$. Note also that, matrix $[C_{ib}^{disp}][B_{ib}]$ will always be real, even when the modal parameters are determined without assuming a proportionally damped modal model.

Although the computation of state-space models respecting Newton's second law by

using modal parameters estimated by assuming a proportionally damped modal model is possible, we must keep in mind that most of the real mechanical systems do not present proportional damping. Thus, it is expected that the use of modal parameters estimated without assuming a proportionally damped modal model lead to the computation of state-space models presenting better accuracy. Hence, it continues to be of interest to investigate how to properly force state-space models to verify Newton's second law.

To correctly force a complete displacement state-space model (see expression (3.24)) to respect Newton's second law, we must make sure that the matrix resultant from the product of its output and input matrices is a null matrix. On top of this, we must also guarantee that the correspondent velocity state-space model properly includes the contribution of $[C_{ib}^{disp}][B_{ib}]$. Recall that to include the contribution of the upper out-of-band modes, we must make sure that $[UR]$ is properly included in the displacement state-space model (see expression (3.1)), whereas to properly impose Newton's second law we are demanded to ensure that the contribution of $[C_{ib}^{disp}][B_{ib}]$ is properly included in the complete velocity state-space model. Thus, it is evident that both problems are similar. This suggests that to impose Newton's second law, we can follow an approach similar to the one exploited in section 3.2.2 to include the contribution of $[UR]$ in the displacement state-space models. Thereby, we must start by computing the SVD of $[C_{ib}^{disp}][B_{ib}]$ as follows:

$$[C_{ib}^{disp}][B_{ib}] = [P_{CB}][\sigma_{CB}][W_{CB}]^T = \sum_{r=1}^{n_{CB}} \{P_{CB,r}\}\sigma_{CB,rr}\{W_{CB,r}\}^T \qquad (3.37)$$

where, $[P_{CB}] \in \mathbb{R}^{n_o \times n_{CB}}$ and $[W_{CB}] \in \mathbb{R}^{n_{CB} \times n_i}$ are the matrices composed by the left and right singular vectors of matrix $[C_{ib}^{disp}][B_{ib}]$, respectively, while $[\sigma_{CB}] \in \mathbb{R}^{n_{CB} \times n_{CB}}$ is a diagonal matrix composed by the singular values of $[C_{ib}^{disp}][B_{ib}]$. Subscript CB denotes vectors/matrices associated with $[C_{ib}^{disp}][B_{ib}]$, whereas $n_{CB} = min(n_i, n_o)$. Note also that, $\{P_{CB,r}\} \in \mathbb{R}^{n_o \times 1}$ represents the rth column of $[P_{CB}]$, $\sigma_{CB,rr}$ denotes the rth element on the diagonal of $[\sigma_{CB}]$ and $\{W_{CB,r}\} \in \mathbb{R}^{1 \times n_i}$ represents the rth row of $[W_{CB}]$.

By using expression (3.37), we may define a set of RCMs, whose modal parameters are given as follows:

$$\lambda_{CB,r} = -\xi_{CB,r}\omega_{CB,r} + j\omega_{CB,r}\sqrt{1 - \xi_{CB,r}^2} \qquad (3.38)$$

$$\{l_{CB,r}\} = -\frac{j}{2}\sqrt{\sigma_{CB,rr}}\{W_{CB,r}\}^T \qquad (3.39)$$

$$\{\psi_{CB,r}\} = \frac{\omega_{CB,r}}{\sqrt{1 - \xi_{CB,r}^2}}\sqrt{\sigma_{CB,rr}}\{P_{CB,r}\} \qquad (3.40)$$

where, $\omega_{CB,r}$ and $\xi_{CB,r}$ are the selected natural frequency and damping ratio of the rth

mode of the RCMs computed from the SVD of matrix $[C_{ib}^{disp}][B_{ib}]$, respectively. From now on, we will assume that the natural frequencies and damping ratios of all the RCMs computed from the SVD of $[C_{ib}^{disp}][B_{ib}]$ are selected to be equal, i.e. $\omega_{CB} = \omega_{CB,r}$ and $\xi_{CB} = \xi_{CB,r}$ (which is the common choice in practice to set-up the RCMs responsible for modelling the out-of-band modes (see section 3.2.2)).

By exploiting the modal parameters of the RCMs defined from matrix $[C_{ib}^{disp}][B_{ib}]$ (see equations (3.38), (3.40) and (3.39)), a state-space model can be defined as follows

$$
\begin{aligned}
\{\dot{x}_{CB}(t)\} &= [A_{CB}]\{x_{CB}(t)\} + [B_{CB}]\{u_{CB}(t)\} \\
\{\dot{y}_{CB}(t)\} &= [C_{CB}^{vel}]\{x_{CB}(t)\} + [D_{CB}^{vel}]\{u_{CB}(t)\}
\end{aligned}
\tag{3.41}
$$

where, matrices $[A_{CB}]$, $[B_{CB}]$, $[C_{CB}^{vel}]$ and $[D_{CB}^{vel}]$ are given as follows (see expressions (3.28) and (3.29)):

$$
[A_{CB}] = \begin{bmatrix} \Lambda_{CB} & 0 \\ 0 & \Lambda_{CB}^* \end{bmatrix}, \quad [B_{CB}] = \begin{bmatrix} L_{CB} \\ L_{CB}^* \end{bmatrix}
$$
$$
[C_{CB}^{vel}] = \begin{bmatrix} \Psi_{CB} & \Psi_{CB}^* \end{bmatrix}, \quad [D_{CB}^{vel}] = [C_{CB}^{vel}][A_{CB}]^{-1}[B_{CB}]
\tag{3.42}
$$

while, $[\Lambda_{CB}]$, $[L_{CB}]$ and $[\Psi_{CB}]$ are given hereafter.

$$
[\Lambda_{CB}] = \begin{bmatrix} \lambda_{CB,1} & & \\ & \lambda_{CB,2} & \\ & & \ddots \end{bmatrix}, \quad [L_{CB}] = \begin{bmatrix} l_{CB,1} \\ l_{CB,2} \\ \vdots \end{bmatrix}, \quad [\Psi_{CB}] = \begin{bmatrix} \psi_{CB,1} \\ \psi_{CB,2} \\ \vdots \end{bmatrix}^T
\tag{3.43}
$$

By using the state-space model defined in expression (3.41), we have the possibility of imposing Newton's second law on the complete velocity state-space model, while properly including the contribution of $[C_{ib}^{disp}][B_{ib}]$. Nevertheless, it would be better to have the possibility of directly imposing Newton's second law on the complete displacement state-space model, while making sure that $[C_{ib}^{disp}][B_{ib}]$ is properly included into the correspondent complete velocity model. This would be advantageous, because from the complete displacement state-space model, we can easily compute the correspondent complete velocity and complete acceleration state-space models (see expressions (3.29) and 3.31). In contrast, to compute the complete displacement state-space model from the complete velocity model, we are forced to perform matrix inversions (see expressions (3.29)). Thus, to be able to directly impose Newton's second law on the complete displacement state-space model, we must compute the displacement state-space model associated with the velocity model given in expression (3.41) as follows:

$$
\begin{aligned}
\{\dot{x}_{CB}(t)\} &= [A_{CB}]\{x_{CB}(t)\} + [B_{CB}]\{u_{CB}(t)\} \\
\{y_{CB}(t)\} &= [C_{CB}^{disp}]\{x_{CB}(t)\} + [D_{CB}^{disp}]\{u_{CB}(t)\}
\end{aligned}
\tag{3.44}
$$

where, $[C_{CB}^{disp}]$ and $[D_{CB}^{disp}]$ are given as hereafter.

$$[C_{CB}^{disp}] = [C_{CB}^{vel}][A_{CB}]^{-1}, \quad [D_{CB}^{disp}] = [0] \tag{3.45}$$

Analyzing expression (3.45), we may notice that to compute the displacement state-space model associated with the velocity model given in expression (3.41), we are required to invert matrix $[A_{CB}]$. Nevertheless, this matrix is diagonal and it is of dimension $2n_{CB} \times 2n_{CB}$, thus the computation of its inverse will, in general, not demand a high computational effort. On top of this, as the natural frequencies and damping ratios of all the RCMs are often assumed to be equal, $[A_{CB}]$ is expected to present a low condition number. Therefore, the inversion of $[A_{CB}]$ will, in general, not introduce numerical problems associated with ill-conditioned matrix inversions. Moreover, the performance of this matrix inversion is definitely preferable than computing the complete displacement state-space model from the velocity complete model, which would require the inversion of a matrix of dimension $2(n_{ib}+n_{UR}+n_{LR}+n_{CB}) \times 2(n_{ib}+n_{UR}+n_{LR}+n_{CB})$.

By exploiting the state-space model defined in expression (3.45), we may establish a complete displacement state-space model that respects Newton's second law as follows:

$$\{\dot{x}_{full}^{INL}(t)\} = [A_{full}^{INL}]\{x_{full}^{INL}(t)\} + [B_{full}^{INL}]\{u_{full}^{INL}(t)\}$$
$$\{y_{full}^{INL}(t)\} = [C_{full}^{INL,disp}]\{x_{full}^{INL}(t)\} \tag{3.46}$$

with,

$$[A_{full}^{INL}] = \begin{bmatrix} A_{full} & 0 \\ 0 & A_{CB} \end{bmatrix}, \quad [B_{full}^{INL}] = \begin{bmatrix} B_{full} \\ B_{CB} \end{bmatrix}, \quad [C_{full}^{INL,disp}] = \begin{bmatrix} C_{full}^{disp} & C_{CB}^{disp} \end{bmatrix} \tag{3.47}$$

while, superscript INL denotes variables associated with a state-space model that was forced to respect Newton's second law. Note that, in appendix F it is mathematically proven that the RCMs here proposed are, indeed, capable of properly imposing Newton's second law on displacement state-space models. It is also worth mentioning, that the state-space model given in expression (3.46) can be transformed into block-diagonal form by applying a similarity transformation as presented in [91], [39].

At this point, it is important to analyze how the accuracy of the RCMs depends on the selected values for their natural frequencies and damping rations. To perform this study, we must define and analyze the expression that enables the computation of the FRFs of the velocity model given in expression (3.41). All the steps to get to this expression are presented in appendix F. Thus, let us recall the intended expression (i.e. expression (F.9)) as given below.

$$[H_{CB}^{vel}(j\omega)] = \frac{\omega_{CB}^2[C_{ib}^{disp}][B_{ib}]}{-\omega^2 + 2j\omega\xi_{CB}\omega_{CB} + \omega_{CB}^2} - [C_{ib}^{disp}][B_{ib}] \tag{3.48}$$

Equation (3.48) presents two different right-hand side terms. The role of the first term is to include the contribution of $[C_{ib}^{disp}][B_{ib}]$ into the complete velocity state-space

model, whereas the second term has the function of ensuring that $[C_{full}^{INL,disp}][B_{full}^{INL}] = [0]$ is verified. Therefore, the velocity model computed from the RCMs responsible for imposing Newton's second law (see expression (3.48)) will be more accurate as its FRFs are closer to be null. Furthermore, expression (3.48) shows that the RCMs responsible for imposing Newton's second law will always make sure that $[C_{full}^{INL,disp}][B_{full}^{INL}]$ is very close to be a null matrix (not being a null matrix due to small numerical errors), not mattering the selected values for the natural frequencies and damping ratios of these RCMs. Nevertheless, the accuracy of the first right-hand side term is dependent on the values selected for the natural frequencies and damping ratios of the RCMs responsible for imposing Newton's second law. By analyzing this term, it is evident that as the value selected for the natural frequencies of the RCMs increases and as the value selected for the damping ratios of the RCMs decreases, the value of the first right-hand side term of expression (3.48) will be closer to $[C_{ib}^{disp}][B_{ib}]$. Thus, the contribution of $[C_{ib}^{disp}][B_{ib}]$ will be included on the complete velocity state-space model with greater accuracy and hence, more precise will be the RCMs to impose Newton's second law.

To select the value of the natural frequencies of these RCMs (i.e. ω_{CB}), we propose, as a rule of thumb, that this value must respect $10 \times \omega_{max} \leq \omega_{CB}$. Therefore, we must start by comstructing the RCMs to impose Newton's second law by defining $\omega_{CB} = 10 \times \omega_{max}$. Then, to evaluate the accuracy of the constructed RCMs, we must compute the first term of the right-hand side of equation (3.48) and compare it with the elements of $[C_{ib}^{disp}][B_{ib}]$ in the frequency band of interest. If this match turns out to be of good quality, it means that the RCMs responsible for imposing Newton's second law were correctly set-up. Otherwise, these RCMs must be re-computed by selecting a higher value for their natural frequencies.

To define the value of the damping ratios of these RCMs (i.e. ξ_{CB}), we suggest, as a rule of thumb, that this value must obey $0.1 \leq \xi_{CB} < 1$ (ξ_{CB} must remain below 1, because the modal parameters of the RCMs are defined by using a modal model). Even though, we mentioned above that the RCMs will be more accurate as the value for their damping ratios is selected to be lower, it is not a good practice to include undamped or slightly damped modes on state-space models. Indeed, the inclusion of this kind of modes may give rise to instabilities, when performing time-domain simulations with the constructed models [40]. Thus, we must start by computing the RCMs responsible for imposing Newton's second law by using $\xi_{CB} = 0.1$. If numerical instabilities are found, when simulating the constructed model in time-domain, the state-space model must be re-computed by using RCMs set-up with a higher value for ξ_{CB}. When an appropriate value for ξ_{CB} is found, we must re-evaluate the quality of the match between the first term on the right-hand side of equation (3.48) and $[C_{ib}^{disp}][B_{ib}]$ in the frequency band of interest. If the match turns out to not be of sufficient quality, the RCMs must be re-constructed by selecting a higher value for their natural frequencies.

3.3.3   Comparing the novel approach with a state-of-the-art method

In this section, we will compare the approach proposed in section 3.3.2 to force state-space models to verify Newton's second law with the state-of-the-art approach presented in [5]. An evident difference between both approaches is that unlike the novel approach here presented, the method proposed in [5] does not make use of pairs of complex conjugate RCMs. For this reason, the procedure proposed in [5] holds the advantage of requiring the use of a lower number of RCMs than the approach proposed in section 3.3.2. Nevertheless, the RCMs used in the technique presented in [5] are undamped, while by exploiting the approach here presented we can use damped RCMs. This represents a very important advantage of using the approach here presented, because the performance of time-domain simulations with models composed by undamped modes may lead to numerical instabilities. On top of this, it is possible to prove that the procedure developed in section 3.3.2 provides the possibility of properly forcing state-space models to obey Newton's second law by using RCMs presenting lower natural frequencies. This represents another very important practical advantage, if the computed state-space models are to be discretized. This is justified by the fact that to properly discretize a state-space model, we must use a sampling frequency that is at least twice the value of the highest natural frequency of the modes included in the state-space model to be discretized (see [40]). Thereby, by using the novel approach to compute state-space models respecting Newton's second law, we generally have the possibility of discretizing these models by using lower sampling frequencies, which substantially decreases the computational effort required to perform calculations with them.

To mathematically prove the second pointed advantage to the method developed in section 3.3.2, let us assume that we intend to impose Newton's second law on a SISO (Single Input Single Output) state-space model. In this way, by exploiting the approach proposed in [5] and by recalling that $[C_{ib}^{disp}][B_{ib}]$ is real (see section 3.3), the following displacement state-space model representative of the RCMs proposed in [5] can be defined:

$$\{\dot{x}_{CB,AL}(t)\} = [A_{CB,AL}]\{x_{CB,AL}(t)\} + [B_{CB,AL}]\{u_{CB,AL}(t)\}$$
$$\{y_{CB,AL}(t)\} = [C_{CB,AL}^{disp}]\{x_{CB,AL}(t)\} \tag{3.49}$$

with,

$$[A_{CB,AL}] = [j\omega_{CB,AL}]\,,\ [B_{CB,AL}] = \left[-\sqrt{\sigma_{CB}}W_{CB}^T\right]\,,\ [C_{CB,AL}^{disp}] = [P_{CB}\sqrt{\sigma_{CB}}] \tag{3.50}$$

where, subscript AL denotes matrices/vectors associated with the state-space model representative of the RCMs proposed in [5] to impose impose Newton's second law. Thereby, we may compute the FRFs of the correspondent velocity state-space model

as given below.

$$[H_{CB,AL}^{vel}(j\omega)] = \frac{\omega_{CB,AL}P_{CB}\sigma_{CB}W_{CB}^T}{-\omega + \omega_{CB,AL}} - P_{CB}\sigma_{CB}W_{CB}^T \qquad (3.51)$$

By computing the FRFs of the velocity state-space model constructed from the RCMs proposed in section 3.3.2 (see expression (3.41)) and by assuming $\xi_{CB} = 0$, we obtain the following expression.

$$[H_{CB}^{vel}(j\omega)] = \frac{\omega_{CB}^2 P_{CB}\sigma_{CB}W_{CB}^T}{-\omega^2 + \omega_{CB}^2} - P_{CB}\sigma_{CB}W_{CB}^T \qquad (3.52)$$

Analyzing expression (3.52), it is evident that the first right-hand side term of this expression is responsible for including the contribution of $[C_{ib}^{disp}][B_{ib}]$ into the complete velocity state-space model, whereas the second term has the role of imposing $[C_{full}^{INL,disp}][B_{full}^{INL}] = [0]$. Having in mind that $\omega_{CB} > \omega_{max}$, by comparing expressions (3.51) and (3.52), we may conclude that we are required to use a lower value of ω_{CB} to force the first right-hand side term of expression (3.52) to be, approximately, equal to $[C_{ib}^{disp}][B_{ib}]$ than to force the first right-hand side term of equation (3.51) to present the same value. Thus, proving that by exploiting the approach proposed in 3.3.2, we have the advantage of properly imposing Newton's second law by using RCMs presenting lower natural frequencies. Note that, this conclusion still applies for Multiple Input Multiple Output (MIMO) state-space models.

3.4 State-Space realization of the VPT approach

Let us assume that an experimental modal characterization of a given mechanical system, whose interface is not feasible to place actuators and/or sensors, is conducted. Then, from the collected sets of FRFs and by following the procedures outlined in sections 3.2 and 3.3.2, the state-space model given below can be identified.

$$\begin{aligned} \{\dot{x}(t)\} &= [A]\{x(t)\} + [B]\{u(t)\} \\ \{y(t)\} &= [C^{disp}]\{x(t)\} \end{aligned} \qquad (3.53)$$

Let us now further assume that we intend to perform DS operations with the experimentally characterized component. Hence, we are required to compute a state-space model representative of this component, whose outputs and inputs are placed on its interface. In this way, by assuming that the substructure under analysis behaves as a rigid body in the frequency range of interest, we may start by applying VPT (see [87]) to transform the outputs and inputs of the FRFs of the state-space model given in expression (3.53) into the defined virtual points (VPs) (i.e. into the intended locations, in this case into the interface of the substructure under analysis). Thus, by exploiting equation (3.27) to compute the FRFs of the state-space model given in expression (3.53) and by applying the VPT approach, we may obtain the intended set of FRFs as

follows:

$$[H_{VP}(j\omega)] = \frac{\{Y_{VP}(j\omega)\}}{\{U_{VP}(j\omega)\}} = [T_y]([C^{disp}](j\omega[I] - [A])^{-1}[B])[T_u]^T \tag{3.54}$$

where, subscript VP denotes vectors/matrices computed by exploiting VPT, whereas matrices $[T_y]$ and $[T_u]^T$ are given below:

$$[T_y] = (R_y^T R_y)^{-1} R_y^T \qquad (3.55a) \qquad\qquad [T_u]^T = R_u (R_u^T R_u)^{-1} \qquad (3.55b)$$

while, $[R_y]$ and $[R_u]$ represent, respectively, the output and input Interface Deformation Mode (IDM) matrices. These matrices must be constructed as reported in [87].

By observing expression (3.54), it is straightforward that we can directly apply the VPT approach on the state-space matrices of the state-space model given in expression (3.53). Thereby, we can transform the outputs and inputs of this model into the interface of the component under study, yielding the following state-space model:

$$\begin{aligned} \{\dot{x}(t)\} &= [A]\{x(t)\} + [B_{VP}]\{u_{VP}(t)\} \\ \{y_{VP}(t)\} &= [C_{VP}^{disp}]\{x(t)\} \end{aligned} \tag{3.56}$$

where, matrices $[B_{VP}]$ and $[C_{VP}^{disp}]$ are given hereafter.

$$[B_{VP}] = [B][T_u]^T \qquad (3.57a) \qquad\qquad [C_{VP}^{disp}] = [T_y][C^{disp}] \qquad (3.57b)$$

Note that, the state-space model given in expression (3.56) could have been obtained from the set of FRFs computed with VPT (see expression (3.54)) by applying the procedures presented in sections 3.2 and 3.3. However, if a mistake on the construction of $[R_y]$ and/or $[R_u]$ matrices is noticed after the estimation of the intended model, we are required to repeat the full identification procedure. In contrast, by directly applying VPT on the state-space matrices of the state-space model representative of the measured FRFs (from now on this approach will be denoted as VPT-SS), possible errors on the construction of $[R_y]$ and/or $[R_u]$ matrices can be easily fixed, because we are only required to re-apply VPT by using the corrected transformation matrices (see equations (3.55a) and (3.55b)) on the state-space model representative of the measured sets of FRFs.

3.5 Imposing stability on coupled state-space models

The coupled state-space models obtained by exploiting SSS techniques are many times unstable (i.e. state-space model composed by poles presenting positive real part), in special, when they are originated from coupling operations involving non-passive state-space models. For this reason, in general the SSS methods cannot be exploited

to compute coupled state-space models to be used in time-domain simulations. This tremendously limits the applications of SSS methods. To come up with an approach to properly force coupled state-space models to be stable, let us start by transforming a given displacement coupled model into complex diagonal form as follows (see [39]):

$$\{\dot{\bar{x}}_{or,cdf}(t)\} = [\bar{A}_{or,cdf}]\{\bar{x}_{or,cdf}(t)\} + [\bar{B}_{or,cdf}]\{\bar{u}_{or,cdf}(t)\}$$
$$\{\bar{y}_{or,cdf}(t)\} = [\bar{C}_{or,cdf}^{disp}]\{\bar{x}_{or,cdf}(t)\} \tag{3.58}$$

where, subscript *or* denotes matrices/vectors of an unstable coupled state-space model directly obtained from coupling operations (from now on denoted as original unstable coupled state-space model), subscript *cdf* denotes matrices/vectors of a state-space model transformed into complex diagonal form, while $[\bar{A}_{or,cdf}]$, $[\bar{B}_{or,cdf}]$ and $[\bar{C}_{or,cdf}^{disp}]$ are given as follows:

$$[A_{or,cdf}] = [T_{or,cdf}]^{-1}[\bar{A}_{or}][T_{or,cdf}], \quad [B_{or,cdf}] = [T_{or,cdf}]^{-1}[\bar{B}_{or}]$$
$$[C_{or,cdf}^{disp}] = [\bar{C}_{or}^{disp}][T_{or,cdf}] \tag{3.59}$$

$[T_{or,cdf}]$ is a modal matrix composed by the eigenvectors of $[\bar{A}_{or}]$ and can be determined by solving the following eigenvalue problem [39]:

$$[\bar{A}_{or}][T_{or,cdf}] = [T_{or,cdf}][\Lambda_{or}] \tag{3.60}$$

where, $[\Lambda_{or}]$ is a diagonal matrix composed by the eigenvalues of $[\bar{A}_{or}]$ (which are also the poles of the coupled system).

At this point, it is worth to recall the generic expression to compute the poles of a given mechanical system as follows:

$$\lambda, \lambda^* = -\xi_n \omega_n \pm j\omega_n \sqrt{1 - \xi_n^2} \tag{3.61}$$

where, ω_n and ξ_n denote the natural frequency and the damping ratio associated with a given pole. From the observation of equation (3.61), it is evident that an unstable pole (i.e. presenting real positive part) can be interpreted as a nonphysical pole that presents a negative damping ratio. Therefore, we will divide the original unstable coupled model into two different models, one composed by the stable poles (from now on denoted as stable state-space model) and the other one composed by the nonphysical unstable poles (from now on tagged as unstable state-space model).

To set-up the stable state-space model, we must start by searching in the diagonal of $[A_{or,cdf}]$ the stable poles. Then, by setting up a diagonal matrix with these stable poles, we can compute the state matrix of the stable model (i.e. $[A_{st}]$). Afterwards, the input matrix of the stable model (i.e. $[B_{st}]$) can be computed from the rows of $[B_{or,cdf}]$ associated with the stable poles, whereas the output matrix of the stable model (i.e. $[C_{st}^{disp}]$) can be defined by using the columns of $[C_{or,cdf}^{disp}]$ associated with the stable poles. To construct the unstable state-space model, the same methodology must be followed,

however in place of looking for the stable poles included in the diagonal of $[A_{or,cdf}]$, we have to search for the unstable ones.

To impose stability on the defined unstable state-space model, we must firstly solve the system of equations given below to determine the natural frequency and the damping ratio associated with each unstable pole:

$$\begin{cases} -\xi_{ut,r}\omega_{ut,r} = \Re(\lambda_{ut,r}) \\ \omega_{ut,r}\sqrt{1 - \xi_{ut,r}^2} = |\Im(\lambda_{ut,r})| \\ \omega_{ut,r} \geq 0 \end{cases} \tag{3.62}$$

where, subscript ut denotes variables associated with the unstable state-space model, $|\bullet|$ represents the absolute value of a variable, while $\Re$ and $\Im$ denote, respectively, the real and imaginary parts of a variable.

Analyzing the system of equations (3.62) and by taking into account that all the poles of the unstable model are unstable, it is evident that all the determined damping rations will be negative. Thereby, to impose stability on the unstable model, we must start by multiplying all the determined damping ratios by -1. Afterwards, the poles of the unstable model must be re-constructed by following equation (3.61) and introduced in the diagonal of $[A_{ut}]$. Thus, making it possible to compute a stabilized version of the unstable model. Nevertheless, the FRFs of this stabilized model are expected to be significantly different from the FRFs of the unstable model. This is expected, because by multiplying the damping ratios calculated with the system of equations (3.62) by -1 to obtain the stabilized model, the FRFs of the unstable model are altered. To compensate the difference between the FRFs of the stabilized and unstable models, we will exploit the Least-Squares Frequency Domain estimator (see, for example, [66]).

By using LSFD, we have the possibility of computing the mode shapes and the lower and upper residual matrices in a linear least-squares sense, provided that the reference FRFs, the poles and the modal participation factors are available in advance. Therefore, to exploit this estimator, the mode shapes of the stabilized state-space model will be assumed to be unknown.

To implement LSFD, we must start by defining the modal model in matrix form (see equation (3.1)) as follows:

$$\left[\hat{H}(j\omega)\right] = \begin{bmatrix} [\Upsilon] & [LR] & [UR] \end{bmatrix} \left[\hat{A}(L,\lambda,j\omega)\right] \tag{3.63}$$

matrices $\left[\hat{H}(j\omega)\right] \in \mathbb{R}^{n_o \times 2n_i n_f}$, $[\Upsilon] \in \mathbb{R}^{n_o \times 2n_m}$ and $\left[\hat{A}(L,\lambda,j\omega)\right] \in \mathbb{R}^{(2n_m+2n_i) \times 2n_i n_f}$ (being n_m and n_f the number of modes and frequency lines, respectively) are given below:

$$\left[\hat{H}(j\omega)\right] = \begin{bmatrix} \Re([H_{target}(j\omega)]_1 & \ldots & [H_{target}(j\omega)]_{n_f}) \\ \Im([H_{target}(j\omega)]_1 & \ldots & [H_{target}(j\omega)]_{n_f}) \end{bmatrix}^T \tag{3.64}$$

$$[\Upsilon] = \begin{bmatrix} \Re([\Psi]) & \Im([\Psi]) \end{bmatrix} \tag{3.65}$$

$$\left[\hat{A}(L, \lambda, j\omega) \right] = \begin{bmatrix} \hat{A}_\Re(L, \lambda, j\omega) & \hat{A}_\Im(L, \lambda, j\omega) \end{bmatrix} \tag{3.66}$$

where, $[H_{target}(j\omega)]$ represents the displacement FRF matrices that the stabilized state-space model must present, whereas $\left[\hat{A}_\Re(L, \lambda, j\omega) \right]$ and $\left[\hat{A}_\Im(L, \lambda, j\omega) \right]$ are given hereafter.

$$\left[\hat{A}_\Re(L, \lambda, j\omega) \right] = \begin{bmatrix} [\hat{a}_\Re(L, \lambda, j\omega)]_1 & \dots & [\hat{a}_\Re(L, \lambda, j\omega)]_{n_f} \\ \left[\hat{b}_\Re(\omega) \right]_1 & \dots & \left[\hat{b}_\Re(\omega) \right]_{n_f} \end{bmatrix} \tag{3.67}$$

$$\left[\hat{A}_\Im(L, \lambda, j\omega) \right] = \begin{bmatrix} [\hat{a}_\Im(L, \lambda, j\omega)]_1 & \dots & [\hat{a}_\Im(L, \lambda, j\omega)]_{n_f} \\ [0] & \dots & [0] \end{bmatrix} \tag{3.68}$$

while, $[\hat{a}_\Re(L, \lambda, j\omega)]$, $[\hat{a}_\Im(L, \lambda, j\omega)]$ and $\left[\hat{b}_\Re(\omega) \right]$ must be computed as follows:

$$[\hat{a}_\Re(L, \lambda, j\omega)]_1 = \begin{bmatrix} \Re(\frac{l_1}{j\omega_1 - \lambda_1}) + \Re(\frac{l_1^*}{j\omega_1 - \lambda_1^*}) \\ \vdots \\ \Re(\frac{l_{n_m}}{j\omega_1 - \lambda_{n_m}}) + \Re(\frac{l_{n_m}^*}{j\omega_1 - \lambda_{n_m}^*}) \\ -\Im(\frac{l_1}{j\omega_1 - \lambda_1}) + \Im(\frac{l_1^*}{j\omega_1 - \lambda_1^*}) \\ \vdots \\ -\Im(\frac{l_{n_m}}{j\omega_1 - \lambda_{n_m}}) + \Im(\frac{l_{n_m}^*}{j\omega_1 - \lambda_{n_m}^*}) \end{bmatrix} \tag{3.69}$$

$$[\hat{a}_\Im(L, \lambda, j\omega)]_1 = \begin{bmatrix} \Im(\frac{l_1}{j\omega_1 - \lambda_1}) + \Im(\frac{l_1^*}{j\omega_1 - \lambda_1^*}) \\ \vdots \\ \Im(\frac{l_{n_m}}{j\omega_1 - \lambda_{n_m}}) + \Im(\frac{l_{n_m}^*}{j\omega_1 - \lambda_{n_m}^*}) \\ \Re(\frac{l_1}{j\omega_1 - \lambda_1}) - \Re(\frac{l_1^*}{j\omega_1 - \lambda_1^*}) \\ \vdots \\ \Re(\frac{l_{n_m}}{j\omega_1 - \lambda_{n_m}}) - \Re(\frac{l_{n_m}^*}{j\omega_1 - \lambda_{n_m}^*}) \end{bmatrix} \tag{3.70}$$

$$\left[\hat{b}_\Re(\omega) \right]_1 = \begin{bmatrix} \frac{[I]}{-\omega_1^2} \\ [I] \end{bmatrix} \tag{3.71}$$

where $[I] \in \mathbb{R}^{n_i \times n_i}$ is an identity matrix. In appendix D, a mathematical proof for the construction of matrix $\left[\hat{A}(L, \lambda, j\omega) \right]$ is presented and it is also shown how $\left[\hat{A}(L, \lambda, j\omega) \right]$ must be computed, when exploiting LSFD with mobility or acceleration reference FRFs. Even though in general it leads to less accurate results, LSFD can also be used by assuming that both upper and lower residual matrices are null. This is also presented in appendix D.

By using expression (3.63), the mode shapes, the lower and the upper residual

matrices can be estimated in a linear least-squares sense as given below.

$$\begin{bmatrix} [\Upsilon] & [LR] & [UR] \end{bmatrix} = \begin{bmatrix} \hat{H}(j\omega) \end{bmatrix} \begin{bmatrix} \hat{A}(L, \lambda, j\omega) \end{bmatrix}^{\dagger} \tag{3.72}$$

Note that the poles of a given mechanical system can be real (when $\xi_n \geq 1$) or appear as complex conjugate pairs (see [39]). However, the LSFD estimator relies on the modal model. This means that LSFD is unable to re-estimate the mode shapes associated with real poles. To overcome this difficulty, we must divide the stabilized model into two different models, being one of them composed by the real poles and the other one composed by the pairs of complex conjugate poles. These two models can be defined from the stabilized state-space model by following the described methodology to construct the stable and unstable models from the original unstable coupled state-space model.

After having partitioned the stabilized model, we have to identify the modal parameters of the model composed by the pairs of complex conjugate poles. To extract the modal parameters from this model, we must start by identifying from the diagonal of its state matrix, one pole of each pair of complex conjugate poles, the associated row of its input matrix, which represents the correspondent modal participation factor and the correspondent column of its output matrix representative of the correspondent mode shape. As final step before exploiting LSFD, we have to establish the FRFs that the state-space model composed by the pairs of complex conjugate poles must present (target FRFs). We aim that the FRFs of the stabilized state-space model perfectly match the FRFs of the unstable model. Thus, having in mind that the modal parameters of the state-space model containing the real poles will not be optimized, we must define the target FRFs as follows:

$$[H_{target}(j\omega)] = [H_{ut}(j\omega)] - [H_{rp}^{stbz}(j\omega)] \tag{3.73}$$

where, $[H_{ut}(j\omega)]$ and $[H_{rp}^{stbz}(j\omega)]$ denote the FRFs of the unstable model and of the model composed by the real poles constructed from the stabilized state-space model, respectively.

After exploiting LSFD, we end-up with a set of modal parameters (i.e. poles, modal participation factors, mode shapes, lower and upper residual matrices) that can be used to construct an optimized model composed by the pairs of complex conjugate poles identified from the stabilized model (see section 3.2). Before constructing this optimized model, we must compare the FRFs of the modal model that can be computed with the optimized modal parameters with the target FRFs (see equation (3.73)). If this comparison turns out to not be a match of enough quality, we have to further optimize the modal parameters of the model composed by the pairs of complex conjugate poles by, for example, exploiting ML-MM (see [67], [68], [69], [70]). After being satisfied with the quality of the optimized modal parameters, we are ready to use these parameters to set-up an optimized state-space model composed by the pairs of complex conjugate

poles by following the procedures discussed in section 3.2. Afterwards, by concatenating in block-diagonal form the stable model, the stabilized model composed by the real poles and the optimized model, we may define the intended stable coupled state-space model as follows:

$$
\{\dot{\bar{x}}_{or}^{stbz}(t)\} = \begin{bmatrix} \bar{A}_{st} & & \\ & \bar{A}_{pcp}^{op,stbz} & \\ & & \bar{A}_{rp}^{stbz} \end{bmatrix} \{\bar{x}_{or}^{stbz}(t)\} + \begin{bmatrix} \bar{B}_{st} \\ \bar{B}_{pcp}^{op,stbz} \\ \bar{B}_{rp}^{stbz} \end{bmatrix} \{\bar{u}_{or}^{stbz}(t)\}
$$
$$
\{\bar{y}_{or}^{stbz}(t)\} = \begin{bmatrix} \bar{C}_{st}^{disp} & \bar{C}_{pcp}^{op,stbz,disp} & \bar{C}_{rp}^{stbz,disp} \end{bmatrix} \{\bar{x}_{or}^{stbz}(t)\}
$$

(3.74)

where, subscripts st denote matrices/vectors associated with the stable coupled state-space model computed from the original unstable coupled model, whereas subscripts rp and pcp denote matrices/vectors associated with the state-space models composed by the real poles and by the pairs of complex conjugate poles identified from the stabilized model, respectively. Superscript $stbz$ denotes matrices/vectors related to state-space models that were forced to be stable, while superscript op denotes matrices/vectors related to a state-space model constructed with the optimized modal parameters.

In the event that the stable coupled state-space model given in expression (3.74) does not obey Newton's second law, it must be forced to verify this physical law by exploiting the approach proposed in section 3.3.2.

Note that the stable coupled state-space models computed by exploiting the procedures here proposed, might be composed by more states than the original unstable coupled models. This increment on the number of states of the stable coupled model may result from the use of RCMs to incorporate the contribution of the lower and upper residual matrices associated with the optimized modal parameters (in case that LSFD is used without assuming that $[UR]$ and $[LR]$ are null matrices) and, if demanded, due to the inclusion of an extra set of RCMs to impose Newton's second law. Thereby, the inclusion of these sets of RCMs may represent at most an increment of $6 \times min(n_o, n_i)$ states.

It is also worth mentioning that the approach here proposed to impose stability on coupled state-space models still holds and, can be applied in similar way to impose stability on unstable models computed from decoupling operations.

Chapter 4

Numerical and experimental validation

In this section, numerical and experimental substructuring cases will be analyzed. In section 4.1, numerical substructuring cases are exploited to validate: the novel technique to force state-space models to obey Newton's second law introduced in section 3.3.2, the post-processing procedures proposed in section 2.3 to mitigate the limitations of LM-SSS method, the primal state-space assembly formulation derived in section 2.4, the LM-SSS via compatibility relaxation method presented in section 2.5.1, the post-processing procedures presented in section 2.5.2 to compute minimal-order coupled models with LM-SSS via compatibility relaxation and the state-space realization of the IS method introduced in section 2.5.4. Then, in section 4.2.3 an experimental substructuring case is used to experimentally validate: the approaches numerically validated in section 4.1 and the methodology presented in section 3.5 to impose stability on unstable coupled state-space models.

4.1 Numerical Validation

In section 4.1.1, we will start by analyzing an assembled structure composed by two substructures rigidly coupled to validate the approaches outlined in section 2.3. Then, in section 4.1.2 an assembly composed by the same two substructures connected by two mounts is used to validate the approaches presented in sections 2.4 and 2.5.

4.1.1 Numerical validation of LM-SSS enhanced with post-processing procedures

In this section, the LM-SSS (see section 2.2.3) method enhanced with the post-processing procedures presented in section 2.3 will be numerically validated. To perform this numerical validation, we will analyze the components depicted in figure 4.1.

When coupled, the components shown in figure 4.1 give rise to the assembled struc-
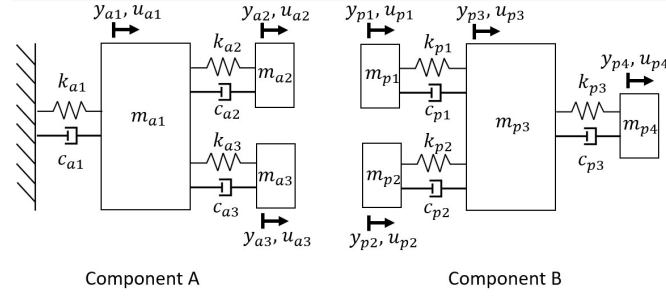
Figure 4.1: Uncoupled components [3].

ture depicted in figure 4.2. The value of the physical parameters denoted in figures 4.1 and 4.2 are listed in table 4.1.
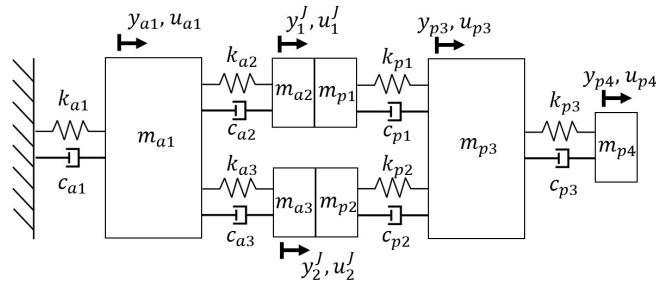
Figure 4.2: Assembled system [3].

Table 4.1: Physical parameter values of the analytical assembled structure composed by the substructures A and B rigidly connected [3].

i	m_i (kg)	c_i (Nsm^{-1})	k_i (Nm^{-1})
a1	10	30	1.5×10^5
a2	3	50	5×10^5
a3	3	50	4.5×10^5
p1	5	50	1×10^5
p2	7	50	1.5×10^5
p3	10	10	5×10^3
p4	1	–	–

In the following, we will start by estimating state-space models from the FRFs of components A and B perturbed by artificial noise, these models will be then transformed into SACF and UCF. Afterwards, the identified state-space models are coupled by exploiting LM-SSS. Three coupled state-space models are determined: a non minimal-order coupled model obtained by exploiting LM-SSS with the untransformed identified models and two minimal-order coupled models obtained by using LM-SSS to couple the identified state-space models transformed into SACF and UCF together with the post-processing procedures outlined in section 2.3.3 to eliminate the redundant states originated from the coupling operations. Finally, LM-SSS is exploited to

decouple the component A from the three computed coupled state-space models to identify three different state-space models representative of component B. These three state-space models of component B are obtained by the following approaches: decoupling from the non minimal-order coupled model the identified state-space model of component A and by exploiting LM-SSS together with the post-processing procedures presented in section 2.3.3 to decouple from the minimal-order coupled models obtained by coupling the estimated models transformed into SACF and UCF the identified state-space model of component A transformed into SACF and UCF, respectively, leading to the computation of two models representative of component B free of the redundant states originated from the decoupling operations.

Identified State-Space Models

To start, we must determine an exact state-space model representative of the components and of the assembled structure shown in figures 4.1 and 4.2, respectively. These state-space models were directly computed from the stiffness, damping and mass matrices of the systems under analysis. Both stiffness and mass matrices were defined by exploiting the Lagrange equations (see, for instance, [92]), whereas, for the sake of simplicity, the damping matrix of each mechanical system was defined from the respective stiffness matrix by replacing the stiffness terms with the damping ones.

However, to perform a more robust numerical validation, the exact state-space models will not be used to perform DS operations. The models to be coupled will instead be estimated from the FRFs of the mechanical systems under study perturbed with artificial noise. These artificially perturbed FRFs will be computed as follows (see [8]):

$$H_{P,ij}(\omega_{k_f}) = H_{P,ij}(\omega_{k_f}) + \gamma_{ij,k_f} + j\theta_{ij,k_f} \tag{4.1}$$

where, subscript P denotes the FRFs of a given substructure P, whereas subscripts i, j and k_f denote, respectively, the output, input and the discrete frequency of the FRF term to be perturbed. Variables γ and θ denote Gaussian distributed independent stochastic variables with zero mean and a standard deviation, in this case, assumed to be 5×10^{-3} m s^{-2} N^{-1}. It is worth noticing that by following this approach to perturb the FRFs, we are only adding artificial noise on the response (output) part of the FRFs.

To estimate state-space models directly from the perturbed FRFs, we started by computing modal parameters from these FRFs with the Simcenter Testlab$^{\circledR}$ implementation of both PolyMAX [66], [22] and Maximum Likelihood Modal Model method (ML-MM) [67], [68], [69], [74]. State-space models were constructed with the estimated modal parameters by following the procedures discussed in section 3.2. Then, these models were forced to obey Newton's second law by exploiting the approach discussed in section 3.3.2, leading to the computation of state-space models representative of components A and B composed by 24 and 30 states, respectively. Note that, to con-

struct both state-space models, the RCMs responsible for including the contribution of the upper out-of-band modes were set-up by selecting a natural frequency of 5×10^2 Hz, while the RCMs responsible for including the contribution of the lower out-of-band modes were defined by selecting a natural frequency of 1×10^{-1} Hz. In addition, the RCMs responsible for imposing Newton's second law were set-up by selecting a natural frequency of 1×10^3 Hz. Furthermore, as time-domain simulations are not intended to be performed with the state-space models computed in this section, all sets of RCMs were defined to be undamped.

In figure 4.3, it is shown the comparison between an accelerance FRF of the exact state-space model of component A with the same artificially perturbed FRF and with the same FRF of the estimated state-space model, whereas the same comparison is shown in figure 4.4 for an accelerance FRF of component B.

Figure 4.3: Comparison of the accelerance FRF, whose output is the DOF a3 and the input is the DOF a1, of the exact state-space model representative of component A with: a) the same FRF artificially perturbed; b) the same FRF of the estimated state-space model.

After having estimated the state-space models from the artificially perturbed FRFs, these models were transformed into SACF (see [8]) and into UCF (see section 2.3.2). Figures 4.5 shows the comparison of an accelerance FRF of the identified state-space model representative of component A with the same FRF of the same state-space model transformed into SACF and UCF. The same comparison is shown in figure 4.6 for an accelerance FRF of the identified state-space model representative of component B.

By observing figures 4.3 and 4.4, we may conclude that the state-space models representative of both components A and B estimated from the artificially perturbed FRFs are very well-matching the correspondent exact FRFs. Thus, it is evident that these models were successfully identified. Moreover, from the analysis of figures 4.5 and 4.6, it is straightforward to conclude that both identified state-space models were successfully transformed into SACF and UCF, because the FRFs of the transformed

Figure 4.4: Comparison of the accelerance FRF, whose output is the DOF p1 and the input is the DOF p3, of the exact state-space model representative of component B with: a) the same FRF artificially perturbed; b) the same FRF of the estimated state-space model.

models perfectly match the correspondent FRFs of the unstransformed state-space models.

Coupling Results

To compute a coupled state-space model representative of the assembled structure depicted in figure 4.2, we started by exploiting LM-SSS to couple the state-space models identified in section 4.1.1. This coupling operation lead to the computation of a non minimal-order coupled model presenting 54 states. Then, to retain the unique set of outputs and inputs from the computed coupled model, the post-processing procedure discussed in section 2.3.4 was applied. The same coupling operation was done by using LM-FBS to couple the FRFs of the identified state-space models. In figure 4.7, it is shown the comparison between an accelerance FRF of the exact state-space model of the assembled structure with the same FRF obtained by using LM-FBS and with the same FRF of the coupled model obtained with LM-SSS.

By observing figure 4.7, we may conclude that the coupled FRF obtained with LM-FBS and the FRF of the coupled model obtained with LM-SSS are very well-matching the correspondent FRF of the exact state-space model of the assembled structure. Moreover, the FRF of the coupled model computed with LM-SSS is perfectly matching the coupled FRF obtained with LM-FBS. This demonstrates that both methods lead to the same coupling result, when the FRFs involved on the coupling operation with LM-FBS are the FRFs of the state-space models coupled with LM-SSS.

At this point, to assess the accuracy of LM-SSS to compute minimal-order coupled models, the coupling operation described above was performed with the identified state-
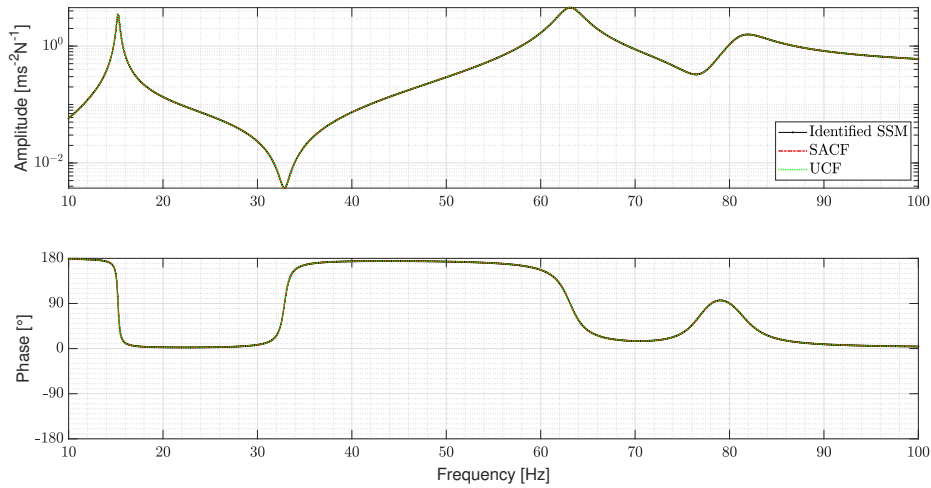
Figure 4.5: Comparison of the accelerance FRF, whose output and input is the DOF a2, of the estimated state-space model representative of component A with the same FRF of the same state-space model transformed into SACF and UCF.

space models transformed into SACF and UCF (see section 4.1.1). Then, from the obtained coupled state-space models, minimal-order coupled state-space models were computed by eliminating the extra states originated from the coupling operation. For ease of implementation, the elimination of these redundant states was performed by exploiting the post-processing procedure presented in section 2.3.3 that relies on the use of a state Boolean localization matrix. As expected, it was found that both computed minimal-order coupled models were composed by 50 states. Finally, the post-processing procedure outlined in section 2.3.4 was used to retain the unique set of outputs and inputs from the computed minimal-order coupled models. In figure 4.8, it is depicted the comparison of an accelerance FRF of the computed non minimal-order coupled model with the same FRF of the minimal-order coupled models obtained by coupling state-space models previously transformed into SACF and UCF.

By analyzing figure 4.8, we conclude that the accelerance FRFs of the non minimal-order coupled model and of the minimal-order coupled models obtained by coupling state-space models previously transformed into SACF and UCF are perfectly matching. Thus, it is evident that by exploiting LM-SSS to couple identified models previously transformed into UCF together with the post-processing procedures presented in section 2.3.3, it is possible to compute accurate minimal-order coupled models.

Decoupling Results

To evaluate the performance of LM-SSS to implement decoupling operations, we will start by identifying a state-space model representative of component B by decoupling with LM-SSS the estimated state-space model of component A (see section 4.1.1) from the non minimal-order coupled state-space model of the assembled structure computed
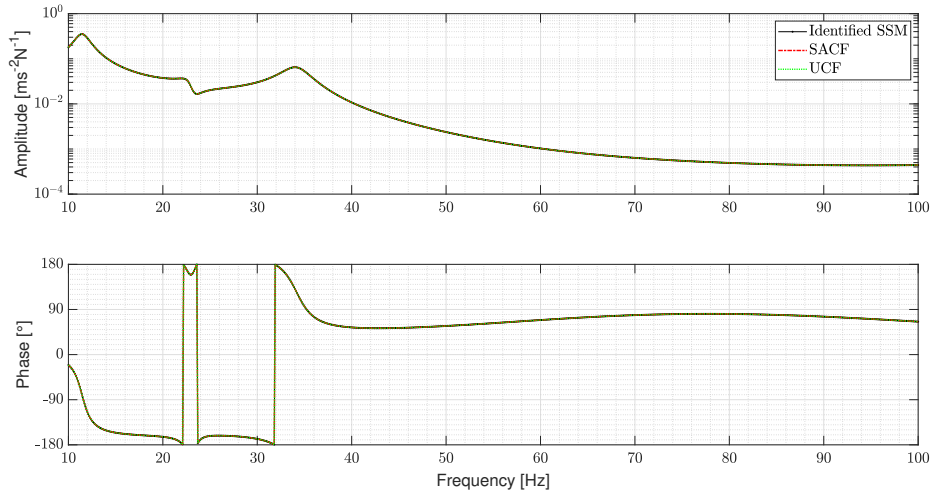
Figure 4.6: Comparison of the accelerance FRF, whose output is the DOF p4 and the input is the DOF p1, of the estimated state-space model representative of component B with the same FRF of the same state-space model transformed into SACF and UCF.

in section 4.1.1. The same decoupling operation will also be performed by exploiting LM-FBS to decouple the FRFs of the estimated state-space model of component A from the FRFs of the non minimal-order coupled model.

In figure 4.9, it is depicted the comparison between an accelerance FRF of the exact state-space model of component B with the same accelerance FRF of component B obtained by performing decoupling with LM-FBS and with the same FRF of the identified state-space model of component B computed by performing decoupling with LM-SSS.

From the observation of figure 4.9, it is possible to conclude that the FRF of component B identified by performing decoupling with LM-FBS and the same FRF of the state-space model identified by performing decoupling with LM-SSS are very well-matching with the same FRF of the exact state-space model of component B. On top of this, we may realize that the FRF of component B identified by performing decoupling with LM-FBS perfectly matches the FRF of the identified model of component B obtained by implementing decoupling with LM-SSS. This clearly indicates that by performing decoupling with LM-FBS and with LM-SSS, the same coupling results are obtained, provided that the FRFs involved on the decoupling operation with the LM-FBS method are the FRFs of the state-space models involved on the decoupling operation performed with LM-SSS.

It is now important to show that LM-SSS is also capable of decoupling state-space models previously transformed into coupling form and that the redundant states originated from decoupling operations can be correctly eliminated by exploiting the post-processing procedures presented in section 2.3.3. In this way, the state-space model of component B will be re-estimated by decoupling the identified state-space model
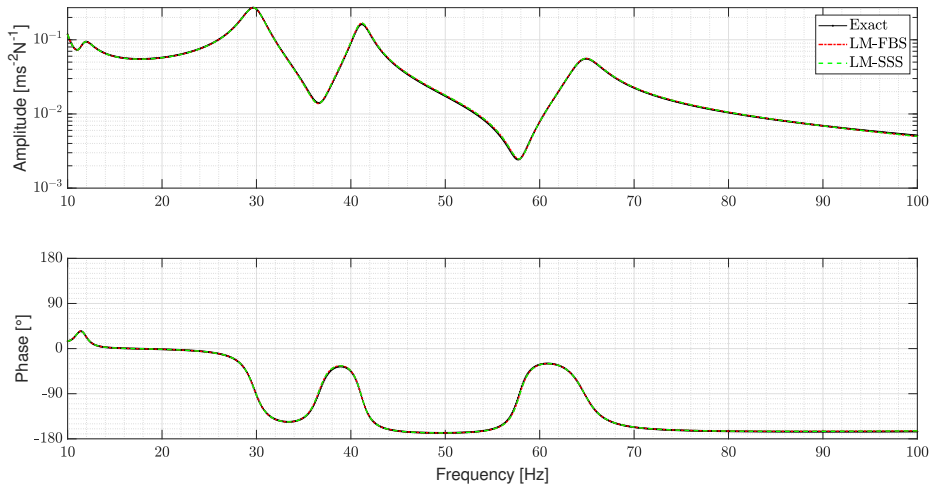
Figure 4.7: Comparison of the accelerance FRF, whose output is the DOF 2 and the input is the DOF p3, of the exact state-space model of the assembled structure with the same FRF obtained by using LM-FBS and with the same FRF of the non minimal-order coupled model computed by exploiting LM-SSS.

of component A previously transformed into SACF and UCF from the minimal-order coupled models (which are directly obtained in coupling form) determined in section 4.1.1 by using state-space models transformed into SACF and UCF, respectively. Then, the post-processing procedure presented in section 2.3.3 that relies on the use of a state Boolean localization matrix will be exploited to erase the redundant states originated from the coupling operation.

Figure 4.10 shows a comparison of an accelerance FRF of the state-space model representative of component B identified by directly using the estimtaed state-space models (see section 4.1.1) with the same FRFs of the identified state-space models computed by performing decoupling operations with models previously transformed into SACF and UCF.

Figure 4.10 clearly demonstrates that the FRFs of the three identified models are perfectly matching. Thus, validating the use of LM-SSS to perform decoupling operations with identified state-space models previously transformed into UCF together with the post-processing procedures described in section 2.3.3 to erase the redundant states originated from decoupling operations.

At this point, we must reflect on the number of states of the state-space models of component B identified through decoupling with LM-SSS. By directly exploiting the state-space models estimated in section 4.1.1, we were able to identify a state-space model representative of component B composed by 78 states, whereas by using the same state-space models previously transformed into SACF and UCF, we were able to compute two state-space models representative of component B composed by 70 states. Note that, the models of component B identified through decoupling with LM-SSS are composed by a number of states substantially higher than the state-space model
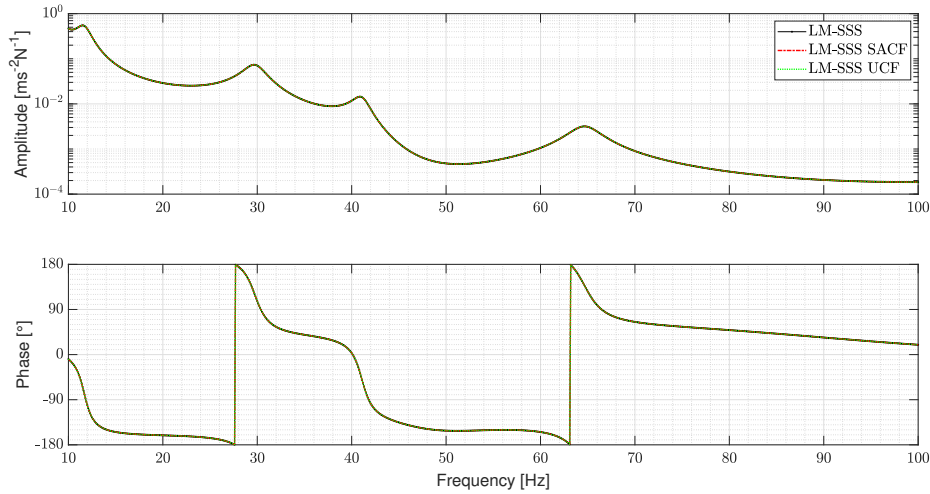
Figure 4.8: Comparison of the accelerance FRF, whose output is the DOF 1 and the input is the DOF p4, of the non minimal-order coupled model with the same FRFs of the minimal-order coupled models obtained by coupling identified state-space models prevoiously transformed into SACF and UCF.

directly estimated from the artificially perturbed FRFs of component B (see section 4.1.1). Thus, we may conclude that all the state-space models estimated through decoupling operations are non minimal-order models.

The high number of states composing the models identified through decoupling can be explained by the introduction of the dynamics of component A to decouple it from the assembled structure, which leads to the identification of models representative of component B including the dynamics of the component A twice. This double inclusion of the dynamics of component A leads to the presence of pairs of spurious modes on the identified models of component B [47]. The elimination of these spurious modes is usually hard to be performed, because it is difficult to distinguish spurious modes from physical ones, when there is no previous knowledge regarding the dynamics of the component to be identified (which is the common situation in practice). Therefore, when possible, we suggest to avoid decoupling operations, by exploiting system identification algorithms to estimate state-space models directly from data collected during the experimental modal characterization of the components or, by numerically modelling the components to construct state-space models representative of their dynamic behaviour.

4.1.2 Numerical validation of LM-SSS via compatibility relaxation

In this section, the LM-SSS via compatibility relaxation method outlined in section 2.5.1, the state-space realization of IS presented in section 2.5.4 and the primal state-space assembly formulation presented in section 2.4 will be numerically validated. To perform these numerical validations, we will analyze an assembled structure, which is composed by the components A and B analyzed in section 4.1.1 connected by two
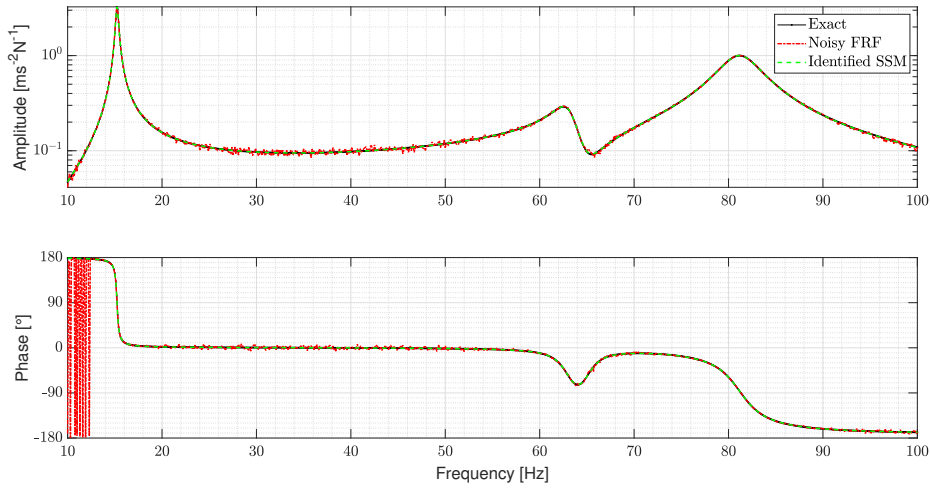
Figure 4.9: Comparison of the accelerance FRF, whose output is the DOF p2 and the input
is the DOF p3, of the exact state-space model of component B with the same
coupled FRF obtained by performing decoupling with LM-FBS and with the same
FRF of the identified state-space model of component B computed by performing
decoupling with LM-SSS.

mounts that respect the underlying assumptions of IS (see section 2.5) (see figure 4.11).
The assembled structure can be observed in figure 4.12, while the value of the physical
parameters indicated in figures 4.11 and 4.12 is given in table 4.2. Note that, the
mounts are assumed to present two fixtures attached to their edges (see figure 4.11),
because this is the common set-up used in practice to test CEs (see section 2.5.4).
Moreover, by assuming that the mounts present fixtures attached to their edges, we
have the possibility of numerically validate the state-space realization of the IS method
to identify the diagonal apparent mass terms of these mounts from the state-space
models representative of the mounts with attached fixtures to their edges.

Table 4.2: Physical parameter values of the analytical assembled structure composed by sub-
structures A and B connected by the mounts m1 and m2 [2].

i	m_i (kg)	c_i (N s m^{-1})	k_i (N m^{-1})
a1	10	30	1.5×10^5
a2	3	50	5×10^5
a3	3	50	4.5×10^5
p1	5	50	1×10^5
p2	7	50	1.5×10^5
p3	10	10	5×10^3
p4	1	-	-
m1	-	20	1×10^5
m2	-	20	2×10^5
T	2	-	-
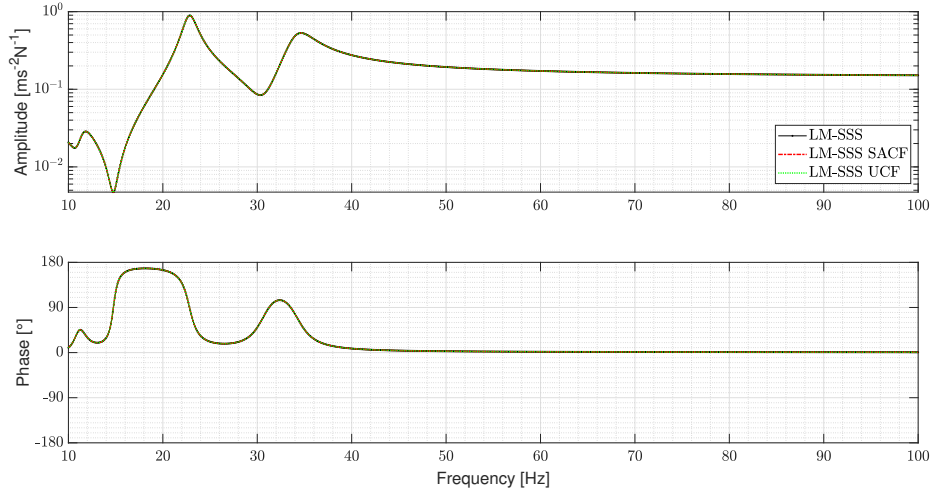
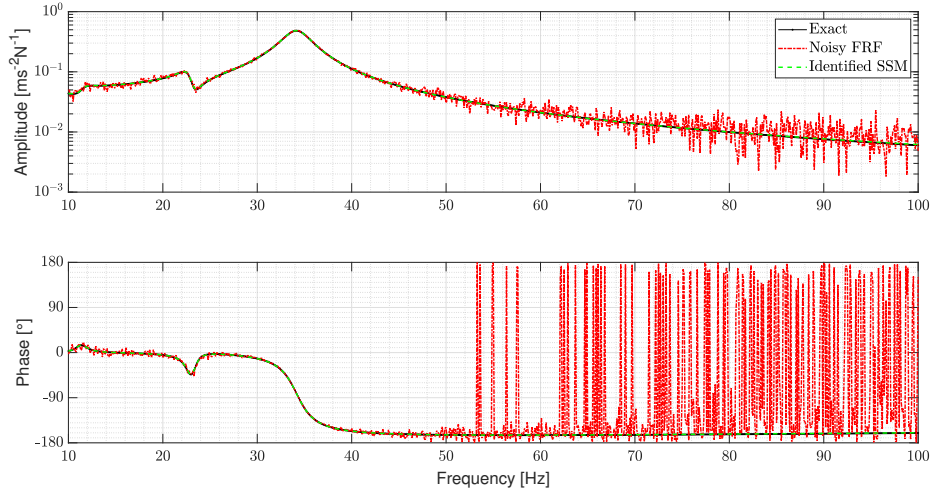**Figure 4.10:** Comparison of the accelerance FRF, whose output and input is the DOF $p2$, of the state-space model representative of component B identified by directly applying decoupling with LM-SSS on the unstransformed estimated state-space models with the same FRFs of the identified state-space models computed by performing decoupling operations with models previously transformed into SACF and UCF.
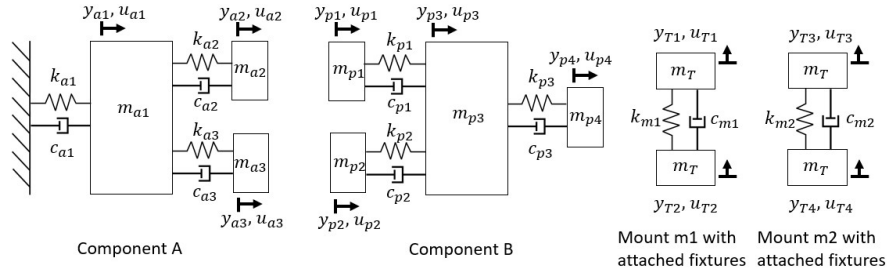
Figure 4.11: Isolated components [2].

In the following, we will start by estimating state-space models from the FRFs of the components and mounts with attached fixtures perturbed with artificial noise, these models are then transformed into UCF (which was already numerically validated in section 4.1.1). Afterwards, LM-SSS via compatibility relaxation is exploited to couple the components and mounts depicted in figure 4.11. By exploiting this method, two different coupled models are calculated: a non minimal-order coupled model obtained by coupling the untransformed identified models and a minimal-order coupled model computed by coupling the identified models transformed into UCF and by exploiting the post-processing procedures presented in section 2.5.2 to eliminate the extra states originated from the coupling operation. The same coupling operation is then, performed with LM-SSS by treating the mounts as regular substructures to be coupled. To implement this coupling operation, primal disassembly (see section 2.4) is firstly exploited to identify state-space models representative of the mounts without fixtures attached to their edges. Subsequently, two coupled state-space models are computed
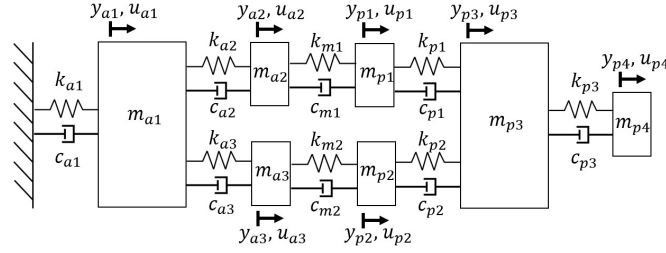
Figure 4.12: Assembled structure [2].

by coupling with LM-SSS the identified state-space models of the mounts with the identified models of components A and B. One of the computed coupled models is a non minimal-order coupled model obtained by exploiting LM-SSS with the untransformed identified state-space models, while the other is a minimal-order coupled model obtained by coupling the identified state-space models transformed into UCF and by exploiting the post-processing procedures presented in section 2.3.3. Afterwards, the FRFs of both models are compared with the FRFs of the non minimal-order coupled state-space model obtained with LM-SSS via compatibility relaxation. Finally, the obtained coupling results are discussed.

Identification of State-Space Models

The exact state-space models of the components, mounts and assembled structure were computed by exploiting the same methodology used to define the exact state-space models of the numerical structures analyzed in section 4.1.1.

To perform a more robust numerical validation, the state-space models representative of the substructures and mounts with attached fixtures (see figure 4.11) to be involved in DS operations will be computed from the FRFs of these mechanical systems perturbed with artificial noise. The perturbation of these FRFs will be performed as reported in section 4.1.1. For this reason, the state-space models representative of components A and B estimated in section 4.1.1 will be here exploited. Thus, we are only required to estimate state-space models representative of the mounts m1 and m2 with fixtures attached to their edges.

By exploiting once again the Simcenter Testlab® implementation of both PolyMAX [66], [22] and Maximum Likelihood Modal Model method (ML-MM) [67], [68], [69], [74], modal parameters were estimated from the artificially perturbed FRFs of mounts m1 and m2 with fixtures attached to their edges. By using the estimated modal parameters and by following the procedures discussed in section 3.2, state-space models representative of the mounts m1 and m2 with fixtures attached to their edges were set-up. Then, the constructed state-space models were forced to verify Newton's second law by exploiting the approach presented in section 3.3.2, leading to the computation of state-space models representative of the mounts m1 and m2 with fixtures attached to their edges composed by 14 states. It is worth mentioning that to construct both

state-space models, the RCMs used to model the contribution of the upper out-of-band modes were defined by selecting a natural frequency of 5×10^2 Hz, whereas the RCMs responsible for including the contribution of the lower out-of-band modes were set-up by selecting a natural frequency of 1×10^{-1} Hz. In addition, the RCMs responsible for imposing Newton's second law were defined by selecting a natural frequency of 1×10^3 Hz. Moreover, as time-domain simulations will not be performed with the state-space models here computed, the damping ratio of all the sets of RCMs was selected to be zero.

Afterwards, the estimated state-space models were double-differentiated and inverted (see appendix A). From the resultant models, state-space models representative of an off diagonal apparent mass term of mounts m1 and m2 can be obtained by retaining from these inverted models, the output and input associated with the off diagonal term of interest, while the other outputs and inputs must be eliminated (see section 2.5.4). For the mount m1, we have decided to retain the off diagonal term associated with the output y_{T1} and the input u_{T2}, whereas the off diagonal term of mount m2 associated with the output y_{T3} and u_{T4} was retained. To obtain state-space models representative of the diagonal apparent mass terms of the mounts under analysis the state-space realization of IS must be exploited (see section 2.5.4). Thereby, we have the possibility of determining models representative of the diagonal apparent mass terms of the mounts by transforming into negative form (by following the approach presented in appendix 3.3.1) the identified state-space models representative of an off diagonal term of each mount. Then, the computed state-space models representative of the diagonal terms of the mounts must be inverted to compute the state-space models required to include the dynamics of mounts m1 and m2 in the LM-SSS formulation via compatibility relaxation (see section 2.5.1). In addition, diagonal apparent mass terms of mounts m1 and m2 were identified from the accelerance noisy FRFs of the mounts with fixtures attached to their edges. This was done by inverting the noisy accelerance FRFs of mount m1 with attached fixtures and by retaining the off diagonal apparent mass term associated with the output y_{T1} and with the input u_{T2}. The identified off diagonal term was then, multiplied by -1 to estimate the intended diagonal apparent mass term of mount m1. To estimate the diagonal apparent mass term of mount m2, the same methodology was applied, however, the retained off diagonal term was the one associated with the output y_{T3} and with the input is u_{T4}.

In figure 4.13, it is possible to observe the comparison of the exact inverted diagonal apparent mass term of mount m1 with the same term identified from the accelerance noisy FRFs of mount m1 with attached fixtures and from the acceleration state-space model representative of mount m1 with fixtures attached to its edges. The same comparison is reported for mount m2 in figure 4.14.

Figures 4.3 and 4.4, clearly demonstrate that accurate inverted state-space models representative of the diagonal apparent mass terms of CEs respecting the assumptions underlying IS (see section 2.5) can be identified from state-space models representative
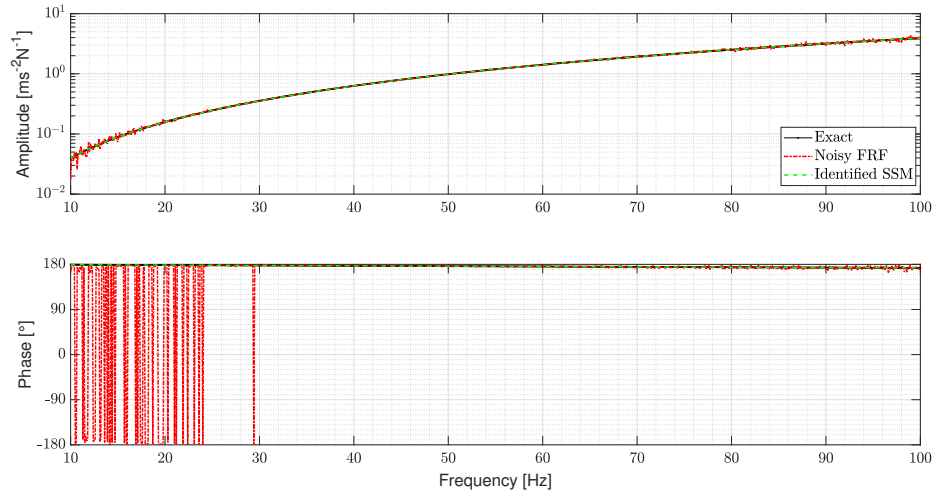
Figure 4.13: Comparison of the exact inverted diagonal apparent mass term of mount m1
with the same term identified from the accelerance noisy FRFs of mount m1 with
attached fixtures and from the acceleration state-space model representative of
mount m1 with fixtures attached to its edges.

of the assemblies, where they are included, by using the state-space realization of IS
(see section 2.5.4).

Coupling by Relaxing the Compatibility Conditions

To compute a non minimal-order coupled state-space model representative of the as-
sembled structure depicted in figure 4.12, the LM-SSS formulation via compatibility re-
laxation will be exploited (see section 2.5.1) with the state-space models representative
of the components A and B (identified in section 4.1.1) and with the inverted models
representative of the diagonal apparent mass terms of the mounts m1 and m2 identified
in section 4.1.2. In addition, a coupled state-space model will also be computed by ex-
ploiting the LM-SSS via compatibility relaxation with the same identified state-space
models previously transformed into UCF (which was already numerically validated in
section 4.1.1). From this coupled model, a minimal-order coupled state-space model
will then be computed by exploiting the post-processing procedure presented in section
2.3.3 that relies on the use of a state Boolean localization matrix to eliminate the extra
states originated from the performed coupling operation. The performance of these
coupling operations leads to the computation of a non minimal-order coupled state-
space model presenting 82 states and to the calculation of a minimal-order coupled
model composed by 78 states. Moreover, the same coupling operation was performed
by exploiting the LM-FBS formulation via compatibility relaxation (see section 2.2.2)
with the FRFs of the state-space models representative of the components A and B
and of the diagonal apparent mass terms of the mounts m1 and m2.

Note that we have obtained the state-space models representative of the inverted
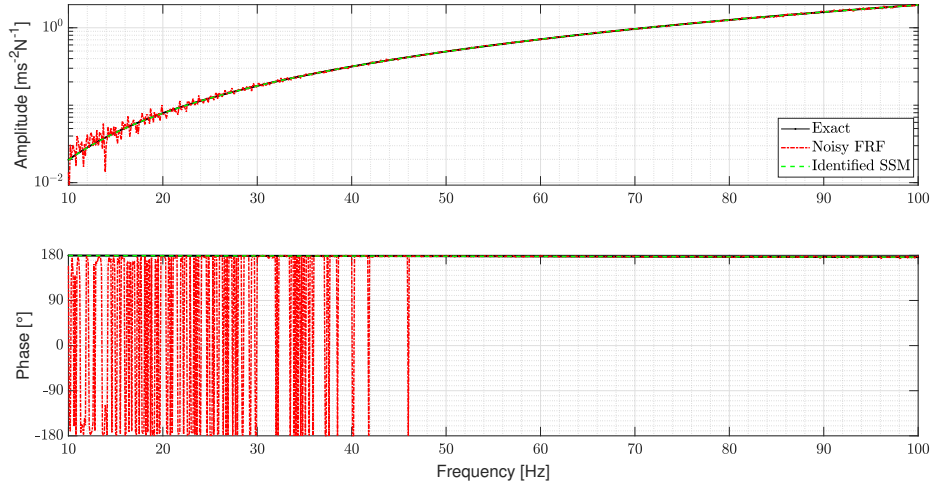
Figure 4.14: Comparison of the exact inverted diagonal apparent mass term of mount m2 with the same term identified from the acceleration noisy FRFs of mount m2 with attached fixtures and from the acceleration state-space model representative of mount m2 with fixtures attached to its edges.

diagonal apparent mass terms of the mounts transformed into UCF from the state-space models representative of the mounts with attached fixtures transformed into UCF by exploiting the state-space realization of IS presented in section 2.5.4. The intended state-space models were obtained in this way, because to transform the state-space models representative of the inverted diagonal apparent mass terms of the mounts into coupling form, we are required to know their displacement output matrices (see section 2.3.2). However, these matrices are not known, being only available their acceleration output matrices. As to compute the displacement output matrix of a given state-space model from the acceleration one, we are required to perform the inversion of its state matrix (see expressions (3.30) and (3.31)), the direct transformation of the state-space models representative of the inverted diagonal apparent mass terms of the mounts into UCF is not recommended. This is the reason why, we decided to compute the intended models from the state-space models representative of the mounts with attached fixtures, whose displacement output matrices are available, transformed into UCF.

In figure 4.15, it is shown the comparison of an acceleration FRF of the exact state-space model representative of the assembled structure with the same coupled FRF obtained with LM-FBS via compatibility relaxation and with the same FRFs of the non minimal-order and of the minimal-order coupled models computed with LM-SSS via compatibility relaxation.

By analyzing figure 4.15, it is evident that the acceleration FRF of the coupled models obtained with LM-SSS via compatibility relaxation and the coupled acceleration FRF obtained through LM-FBS via compatibility relaxation are very well matching the same acceleration FRF of the exact state-space model of the assembled structure. Thus, we may claim that LM-SSS via compatibility relaxation is, indeed, accurate to
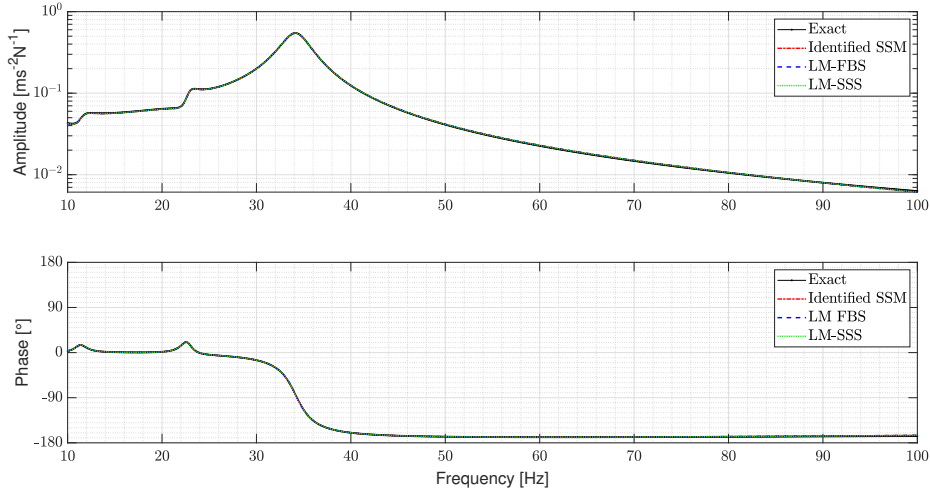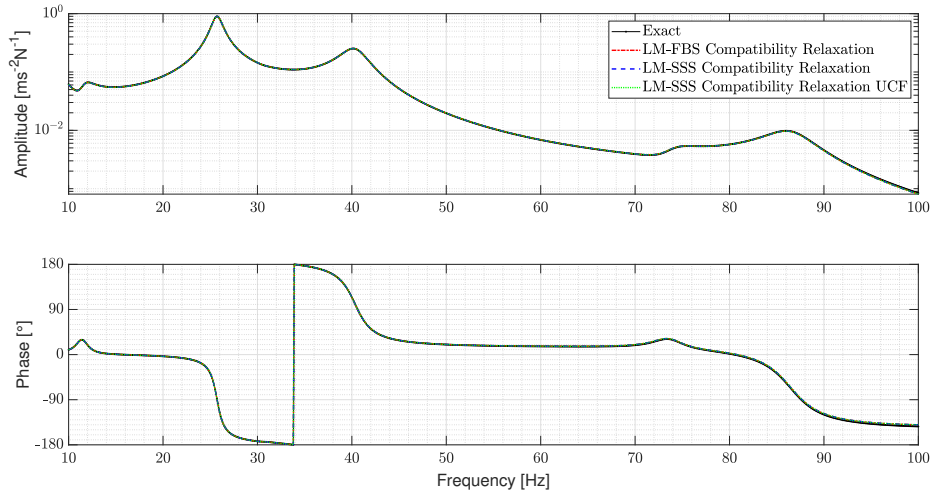
Figure 4.15: Comparison of the accelerance FRF, whose output is the DOF p3 and the input is the DOF a1, of the exact state-space model of the assembled structure with the same coupled FRF computed with LM-FBS via compatibility relaxation and with the same FRFs of the non minimal-order and of the minimal-order coupled models obtained by exploiting LM-SSS via compatibility relaxation.

compute coupled models representative of substructures connected by CEs respecting the assumptions underlying IS.

By further observing figure 4.15, we may conclude that the FRFs of the coupled models are perfectly matching the coupled accelerance FRFs obtained by LM-FBS via compatibility relaxation. Therefore, it is evident that both LM-SSS via compatibility relaxation and LM-FBS via compatibility relaxation lead to the same coupling results, provided that the FRFs involved on the coupling operation with LM-FBS via compatibility relaxation are the FRFs of the state-space models coupled with LM-SSS via compatibility relaxation. On top of this, as the FRFs of the non minimal-order and minimal order coupled models are perfectly matching, it is straightforward to infer that the post-processing procedures described in section 2.5.2 are valid to eliminate the extra states originated from the performance of coupling operations with LM-SSS via compatibility relaxation.

Coupling by treating the Mounts as Regular Components

In this section, we will start by using the primal state-space assembly formulation outlined in section 2.4 to decouple the fixtures attached to the edges of mounts m1 and m2 to compute state-space models representative of these mounts without fixtures attached to their edges (see figure 4.11). As the fixtures to be decoupled do not present stiffness (see Table 4.2), they will not present any flexible mode. For this reason, there is no point on estimating modal parameters from the FRFs of the fixtures to compute state-space models representative of their dynamics. Thus, the state-space models representative of the fixtures will be directly estimated from their mass matrices.

Figure 4.16 compares the apparent mass term, whose output is the DOF T2 and the input is the DOF T1, of the exact state-space model of mount m1 with the same off diagonal apparent mass term obtained by the following methodologies: i) identified from the inverted noisy accelerance FRFs, by performing primal disassembly with ii) the untransformed state-space models representative of the fixtures and of the mount m1 with the fixtures attached to its edges and with iii) the same state-space models previously transformed into UCF and by using the post-processing procedure presented in section 2.3.3 that relies on the use of a state Boolean localization matrix, leading to the computation of a minimal-order model free of the redundant states originated from the primal disassembly operation. The same comparison is performed in figure 4.17 for the off diagonal apparent mass term of the mount m2, whose output is the DOF T3 and the input is the DOF T4.
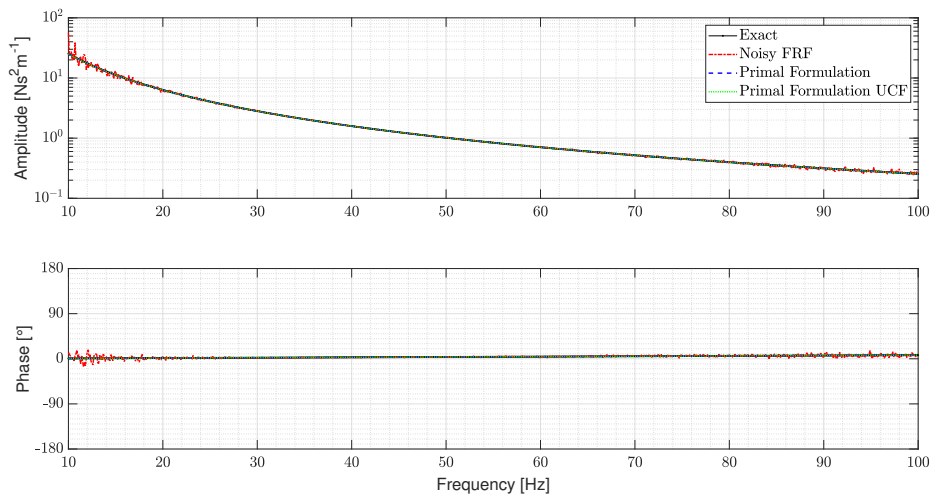
Figure 4.16: Comparison of the apparent mass term, whose output is the DOF T1 and the input is the DOF T2, of the exact state-space model of mount m1 with the same off diagonal apparent mass term computed by the following approaches: i) identified from the inverted noisy accelerance FRFs, by performing primal disassembly with ii) the unstansformed state-space models and with iii) the same state-space models previously transformed into UCF and by exploiting the post-processing procedure presented in section 2.3.3 that relies on the use of a state Boolean localization matrix.

From the analysis of figures 4.16 and 4.17, it is clear that the apparent mass terms of the state-space models identified through primal disassembly are very well-matching the same term of the correspondent exact state-space models. Moreover, it is straightforward that the FRFs of the state-space models identified through primal disassembly by using the untransformed models are perfectly matched by the FRFs of the minimal-order models obtained with primal disassembly. Thus, we may claim that the primal state-space assembly formulation presented in section 2.4 and the strategy discussed in the same section to remove the redundant states originated from the performance of primal assembly/disassembly operations are numerically validated. Note that, the
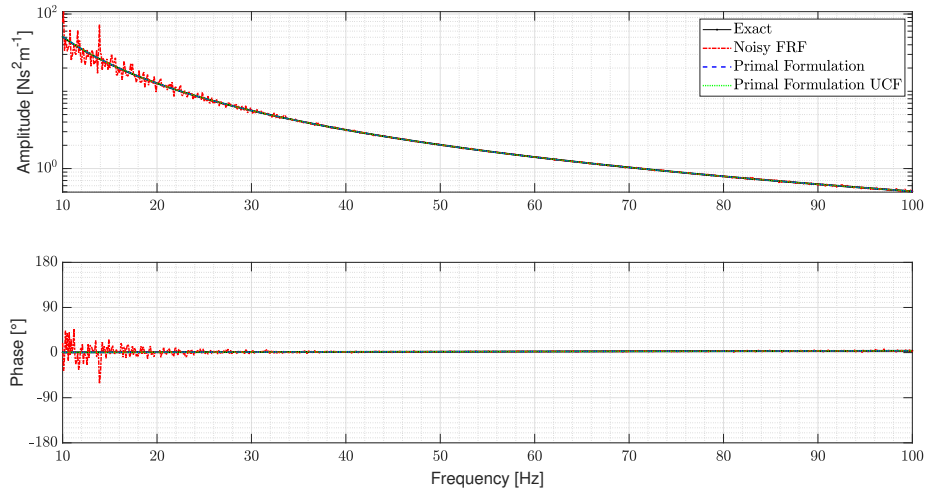
Figure 4.17: Comparison of the apparent mass term, whose output is the DOF T3 and the
input is the DOF T4, of the exact state-space model of mount m2 with the
same off diagonal apparent mass term computed by the following approaches:
i) identified from the inverted noisy accelerance FRFs, by performing primal
disassembly with ii) the unstansformed state-space models and with iii) the
same state-space models previously transformed into UCF and by exploiting the
post-processing procedure presented in section 2.3.3 that relies on the use of a
state Boolean localization matrix.

state-space model identified by exploiting primal disassembly is composed by 18 states,
whereas the minimal-order model computed with the same approach presents 14 states.

At this point, the state-space models of mounts m1 and m2 identified through primal
disassembly will be inverted and coupled with the state-space models of substructures
A and B by exploiting LM-SSS. This coupling operation will lead to the computation of
a non minimal-order coupled model. Additionally, the same coupling operation will be
conducted by using the same models previously transformed into coupling form and by
exploiting the post-processing procedure presented in section 2.3.3 that relies on the use
of a state Boolean localization matrix, enabling the computation of a minimal order-
coupled model representative of the assembled structure given in figure 4.12. After
performing these coupling operations, it was found that the non minimal-order coupled
state-space model was composed by 90 states, while the minimal-order coupled model
presented 74 states.

In figure 4.18, an accelerance FRF of the exact model of the assembled structure
under analysis is compared with the same FRF of the coupled state-space models com-
puted by the following methodologies: i) non minimal-order coupled model computed
with LM-SSS via compatibility relaxation, ii) non minimal-order coupled model com-
puted by using LM-SSS and iii) minimal-order coupled model computed with LM-SSS.
By performing this comparison, we intend to prove that, if the CEs obey the assump-
tions underlying IS, all the approaches used to compute the coupled state-space model
lead to the calculation of coupled models presenting the same FRFs. Note that, the

inverted non minimal-order and minimal-order coupled state-space models that could have been computed by exploiting the primal state-space assembly formulation would also present the same FRFs.
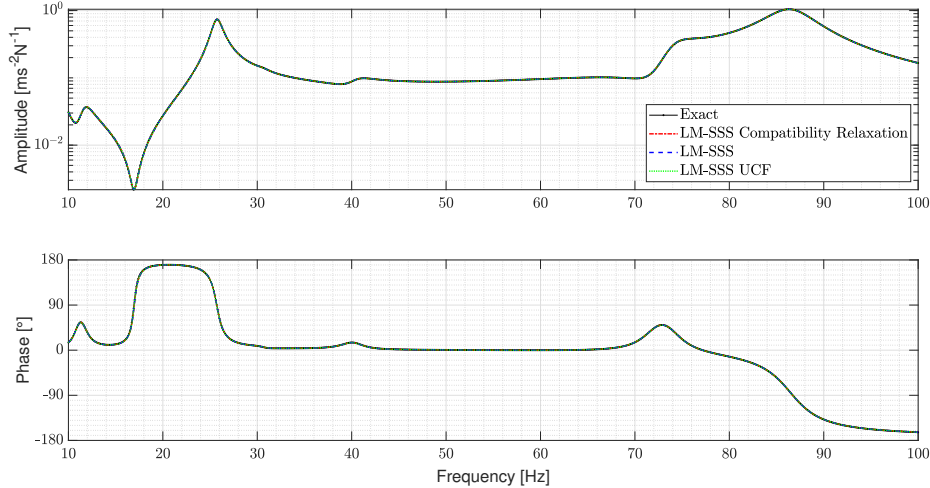
Figure 4.18: Comparison of the accelerance FRF, whose output is the DOF a3 and the input is the DOF a1, of the exact state-space model of the assembled structure with the same FRF of the following coupled state-space models: i) non minimal-order coupled model computed by exploiting LM-SSS via compatibility relaxation, ii) non minimal-order coupled model obtained with LM-SSS and iii) minimal-order coupled model computed with LM-SSS.

Results and discussion

By analyzing the results reported in this section, it is clear that by performing decoupling/disassembly operations or by using the state-space realization of IS (see section 2.5.4), we can accurately identify state-space models representative of the dynamics of both m1 and m2 mounts. However, it was found that the state-space models identified through the state-space realization of IS (made of 14 states) were composed by a lower number of states than the state-space models obtained through primal disassembly (composed by 18 states). The state-space models obtained by exploiting primal disassembly present more states due to the performed disassembly operations to remove the dynamics of the fixtures attached to the mounts (see section section 2.5).

Nevertheless, the minimal-order models representative of the mounts obtained with primal disassembly (made of 14 states) are composed by the same number of states as the models identified with the state-space realization of IS. Indeed, the state-space models obtained by both strategies present the same number of states, because the models of the masses are solely composed by a single interface DOF and were analytically computed. Hence, these models only present two states (i.e. twice the number of their DOFs). Thus, having in mind that the post-processing procedures exploited to compute minimal-order models (see section 2.3.3) remove from the state-space mod-

els originated from primal assembly/disassembly operations a number of states that is twice the value of the coupled interface DOFs, it is evident that all the introduced states to perform the disassembly operation are eliminated.

Turning our attention to the computed coupled state-space models, we may realize that the non minimal-order coupled models computed by exploiting LM-SSS via compatibility relaxation and by using LM-SSS present, respectively, 82 and 90 states. As expected, due to the performance of decoupling operations to estimate the state-space models of the mounts m1 and m2 to be included in the coupling operation with LM-SSS, the coupled model obtained by using this approach presents more states than the coupled model computed through LM-SSS via compatibility relaxation. In contrast, the minimal-order coupled state-space model computed with LM-SSS presents 74 states, while the minimal-order coupled model computed with LM-SSS via compatibility relaxation is composed by 78 states. The minimal-order coupled model computed through LM-SSS via compatibility relaxation presents a larger number of states, because the compatibility conditions are defined by calculating the relative motion between the interface DOFs of components A and B. Thus, the extra states to be eliminated to compute the minimal-order coupled model are the ones representative of the relative displacement between these interface DOFs and the respective first-order derivatives (see section 2.5.2). This renders the elimination of 4 states. Conversely, by exploiting LM-SSS, we impose that the interface DOFs of each mount must present the same physical motion as the interface DOFs of the components A and B to which the mount is connected. Therefore, per each pair of matching interface DOFs, the computed coupled model will present a pair of states presenting the same physical meaning. The same is valid for the states representative of the respective first-order derivatives (see section 2.3.3). Hence, to compute the minimal-order coupled model we are required to eliminate 8 states. As we eliminate more states from the coupled state-space model computed with LM-SSS, the minimal-order coupled model obtained with this method presents less states than the minimal-order coupled model computed with LM-SSS via compatibility relaxation.

It is now straightforward to infer that the minimal-order coupled state-space model calculated by exploiting LM-SSS is the most interesting one, because it is composed by the lowest number of states, while presenting the same FRFs as the other computed coupled state-space models. However, it is worth mentioning that this model is the most interesting, because we are dealing with an analytical substructuring case. Indeed, in an experimental scenario, the fixtures could not generally be represented by an analytically determined state-space model. Thus, we would very likely be required to identify state-space models representative of the dynamics of the fixtures by exploiting system identification algorithms (see section 3.1), which in general lead to the estimation of state-space models presenting a number of states higher than twice the number of the outputs (which is the number of states of analytically computed state-space models) of the structures under study. Hence, the performance of decoupling operations with these

estimated state-space models would lead to the identification of models representative of the CEs spoiled by spurious states. For this reason, the coupled state-space models obtained with LM-SSS are expected to be composed by a number of states significantly higher than the number of states of the coupled model obtained with LM-SSS via compatibility relaxation. This is verified for the experimental substructuring case to be analyzed in section 4.2.

4.2   Experimental Validation

In this section, the approaches presented in sections 2.3, 2.4, 2.5, 3.3.2, 3.4 and 3.5 are experimentally validated. To start, in section 4.2.1 the components/assemblies to be studied are presented and the conducted experimental tests to characterize them are described. Then, in section 4.2.2 state-space models representative of the experimentally characterized components/assemblies are computed in accordance with the procedures presented in sections 3.2 and 3.3.2. Afterwards, in section 4.2.3 the performance of decoupling/coupling operations with LM-SSS and the use of the post-processing procedures presented in section 2.3.3 to eliminate the redundant states originated from these DS operations is experimentally validated. In section 4.2.4, the quality of the state-space models computed by exploiting primal state-space disassembly (see section 2.4) is evaluated and the accuracy of the post-processing procedures outlined in section 2.3.3 to eliminate the redundant states originated from primal disassembly operations is assessed, while the state-space realization of IS (see section 2.5.4) is experimentally validated. Then, in section 4.2.5 the use of the primal state-space assembly formulation together with the tailored post-processing procedures presented in section 2.3.3 is experimentally validated to compute minimal-order coupled models. Additionally, in the same section, the use of LM-SSS via compatibility relaxation with the tailored post-processing procedures outlined in section 2.5.2 to eliminate the extra states originated from this coupling operation is experimentally validated. Finally, the approach proposed in section 3.5 to impose stability on coupled state-space models is experimentally validated in section 4.2.6.

4.2.1   Testing Campaign

To experimentally validate the techniques presented in sections 2.3, 2.4, 2.5, 3.3.2, 3.4 and 3.5, the following mechanical systems were experimentally characterized:

- Two aluminum crosses (from now on tagged as aluminum cross A and B);

- Two steel crosses (from now on tagged as steel cross A and B);

- Assembly A composed by the two aluminum crosses linked by a rubber mount;

- Assembly B composed by the two steel crosses linked by a rubber mount.

To perform the intended experimental validations, we will be required to perform DS operations with the state-space models representative of the dynamics of the experimentally characterized mechanical systems. For this reason, we are required to estimate state-space models, whose outputs and inputs are located at the interfaces of the crosses/assemblies under analysis. Nevertheless, the instrumentation of sensors and the performance of excitation at the interfaces of these components is infeasible. Thus, to surpass this difficulty, the crosses were produced to behave as rigid bodies in the frequency band of interest, which was defined to be from 2×10^1 Hz to 5×10^2 Hz. Thereby, we can compute the intended state-space models by exploiting VPT-SS (see section 3.4) with the state-space models identified from FRFs collected from experimental tests performed on the crosses/assemblies by applying excitation and by placing sensors at accessible locations.

The test set-ups used to experimentally characterize the crosses and assemblies are depicted in figures 4.19a and 4.19b, respectively. The experimental modal characterization tests were performed by using the roving hammer approach. Each cross, either isolated or included in the assembly, was excited at sixteen different locations with an instrumented hammer (PCB Model 086C03), while the responses of each cross were measured by using three accelerometers (PCB Model TLD356A32) as shown in figure 4.20.
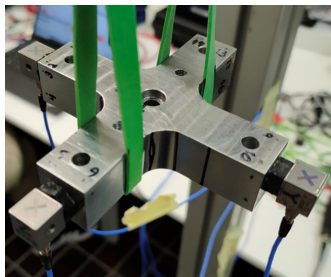
(a) Crosses.
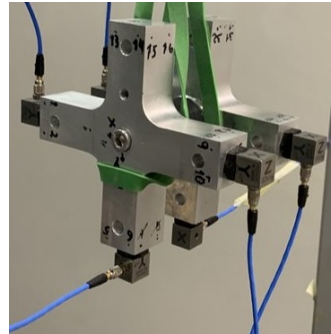
(b) Assemblies.

Figure 4.19: Test set-ups used to perform the experimental modal characterization of the isolated crosses and assemblies [3].

To demonstrate that the aluminum and steel crosses can be assumed to behave as rigid bodies in the frequency band of interest, Finite Element (FE) analysis of both components were conducted in COMSOL Multiphysics® to determine their first flexible eigenfrequencies. In figure 4.21a, the mesh used to analyze the aluminum cross is shown, while figure 4.21b depicts the first flexible eigenmode of this component. From the performance of these FE analysis, it was found that the first flexible modes of the aluminum and steel crosses presented eigenfrequencies of 5.187×10^3 Hz and 5.950×10^3 Hz, respectively. Thus, we can conclude that these components can be assumed to behave as rigid bodies in the frequency band of interest (i.e. from 2×10^1 Hz to 5×10^2 Hz). Moreover, it is worth noting that the fixtures attached to the
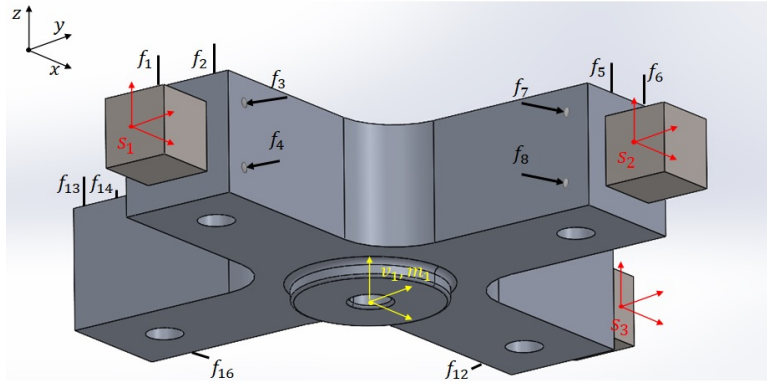
Figure 4.20: Locations of measurement accelerometers (red), hammer impact directions (black arrows) and virtual point (yellow) [3].

rubber mount were designed with a cross shape to enable an accurate excitation of the rotational DOFs of the rubber mount. In this way, it is possible to perform a reliable six DOFs characterization of each isolated cross and to make a reliable twelve DOFs characterization of both assemblies A and B (see [33],[56]).
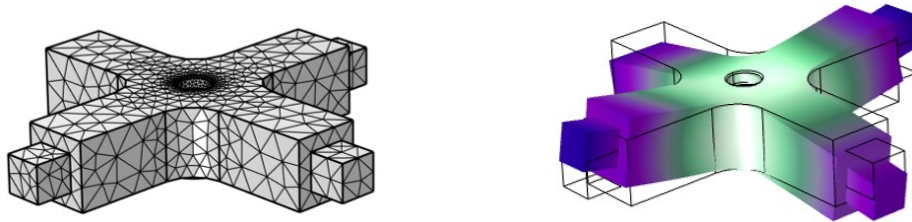
(a) Mesh used to analyze the aluminum cross. **(b)** First flexible eigenmode of the aluminum cross.

Figure 4.21: Finite element model analysis performed on the aluminum cross.

4.2.2 State-space models identification

Here, we will estimate state-space models representative of the aluminum and steel crosses alone and of the assemblies A and B (see section 4.2.1). To estimate these models, we will start by exploiting the Simcenter Testlab® implementation of both PolyMAX and ML-MM methods to identify modal parameters from the measured FRFs of each mechanical components and assemblies. It is worth mentioning, that these modal parameters will not be identified by assuming a proportional damped modal model. Thereby, we have the chance of evaluating in practice the suitability of the RCMs proposed in section 3.3.2 to impose Newton's second law on state-space models. In addition, we circumvent the use of a modal model that is likely to not be the most adequate to describe the dynamic behaviour of the mechanical systems under study, in special the dynamics of the assemblies A and B, which are composed by a rubber mount.

From the identified modal parameters, state-space models representative of the systems under study were set-up by following the procedures reported in section 3.2.1.

To include the contribution of the lower and upper out-of-band modes in the frequency band of interest, sets of RCMs were set-up as reported in section 3.2.2 and inserted into the state-space models. On top of this, a set of RCMs defined by following the approach presented in section 3.3.2 was included into the constructed state-space models to force them to respect Newton's second law. The sets of RCMs inserted in each constructed state-space model to include the contribution of the lower out-of-band models were set-up by selecting $\omega_{LR} = 1 \times 10^{-1}$ Hz and $\xi_{LR} = 1 \times 10^{-1}$, whereas the sets of RCMs included in each of the constructed state-space models to account for the contribution of the upper out-of-band modes and to impose Newton's second law were defined by selecting $\omega_{UR} = \omega_{CB} = 1.5 \times 10^4$ Hz and $\xi_{UR} = \xi_{CB} = 1 \times 10^{-1}$ (see, sections 3.2.2 and 3.3.2). After including these sets of RCMs on the state-space models computed from the identified modal parameters, complete state-space models describing the dynamics of the mechanical systems under analysis and respecting Newton's second law were obtained. Nevertheless, as these models are to be exploited in DS operations, they must contain inputs and outputs collocated at the interface of the mechanical systems. To fulfill this requirement, the VPT-SS method (see, section 3.4) was used to transform the positions of the inputs and outputs of the estimated state-space models into the interface of the respective mechanical systems.

Subsequently, the approach proposed in [4] was implemented to compute passive models from the state-space models resultant from the application of VPT-SS. This method requires the user to define the frequency band for which the FRFs of the modes included in the state-space models are going to be monitored and imposed to be positive real. However, no recommendations on how to properly define this frequency band are reported in [4]. Here, to make sure that the dynamics of all the modes included in the state-space models is well monitored, this frequency band was selected to range from 1×10^{-2} Hz to 1.8×10^4 Hz. On top of this, in an attempt to circumvent possible passivity violations for frequencies in between successive frequency points included in the selected frequency band, these points were defined to be spaced by 1×10^{-2} Hz. It is worth mentioning that, we have decided to exploit this approach to compute passive models for two reasons. Firstly, it was developed by targeting applications involving SSS. Secondly, it is a direct approach that does not rely on the use of iterative algorithms and, hence, does not demand high computational effort. Thus, obtaining coupled models by coupling state-space models forced to be passive by using the technique proposed in [4] is the strategy that shares more similarities with the approach that we proposed in section 3.5 to compute stable coupled state-space models.

In figures 4.22, 4.23, 4.24 and 4.25 interface FRFs of each of the components/assemblies under analysis computed by exploiting VPT on the measured FRFs are compared: i) with the same FRFs of the respective estimated state-space model, ii) with the same FRFs of the respective estimated state-space model transformed into UCF and iii) with the same FRFs of the passive state-space model computed from the respective identi-

fied model by using the method outlined in [4]. It is worth mentioning that from now on, the virtual point responses of the crosses aluminum and steel A will be denoted v_1, whereas the virtual point loads of the same components will be tagged m_1. Furthermore, the virtual point responses of the crosses aluminum and steel B will be denoted v_2, while the virtual point loads of the same crosses will be tagged m_2

From the analysis of figures 4.22, 4.23, 4.24 and 4.25, we may conclude that the identified state-space models accurately describe the dynamics of the systems under analysis. On top of this, it was found that all the estimated state-space models obey Newton's second law. In fact, the $[C_{full}^{INL,disp}][B_{full}^{INL}]$ matrix of the model describing the dynamics of assembly A is the one presenting the term with the highest maximum value. The absolute value of this term is, approximately, 1×10^{-12}. Thus, it is evident that the approaches presented in section 3.2 are accurate to compute state-space models from experimentally acquired FRFs and that the method discussed in section 3.3.2 is reliable to impose Newton's second law on these models. Moreover, it is also clear that the FRFs of the estimated state-space models and of the same models transformed into UCF are perfectly matching. Hence, we may conclude that state-space models estimated from measured FRFs can be accurately transform into UCF.

Focusing our analysis on the computed passive models, it is straightforward to conclude that they poorly represent the dynamics of the mechanical systems under study. Indeed, as discussed in section 3, the method proposed in [4] was already expected to lead to the computation of low quality passive models. The poor accuracy of these models is directly linked to the adjustments made on the terms of the output and input matrices of the respective identified state-space models to force them to obey passivity. As the mismatches between the FRFs of the estimated and passive models resultant from these adjustments are not compensated in a later stage, they tend to sum up leading to the significant deviations between the FRFs of both models observed in figures 4.22, 4.23, 4.24 and 4.25. Moreover, the computed passive models were found to violate passivity for frequency values not included in the chosen frequency band. Thus, these models are not globally passive. In fact, the enforcement of passivity by solely considering the frequency points included in a selected frequency band, commonly, leads to the computation of models that obey passivity for the considered frequency points, but that do not necessarily verify this criteria for other frequency values (see, [78]). On top of this, the computed passive models violate Newton's second law. This is linked to the fact that the method proposed in [4] does not use any constraint to guarantee that the adjustments performed on the output and input matrices of the state-space models do not promote the computation of passive models violating Newton's second law. As a result of the lack of global passivity and of the poor quality of the models defined by exploiting the method outlined in [4], these models will not be exploited to conduct the DS operations reported in the following sections.

At this point, it is important to report that the models representative of the dynamics of the aluminum crosses A and B are composed, respectively, by 204 and 210 states.

(a)

(b)
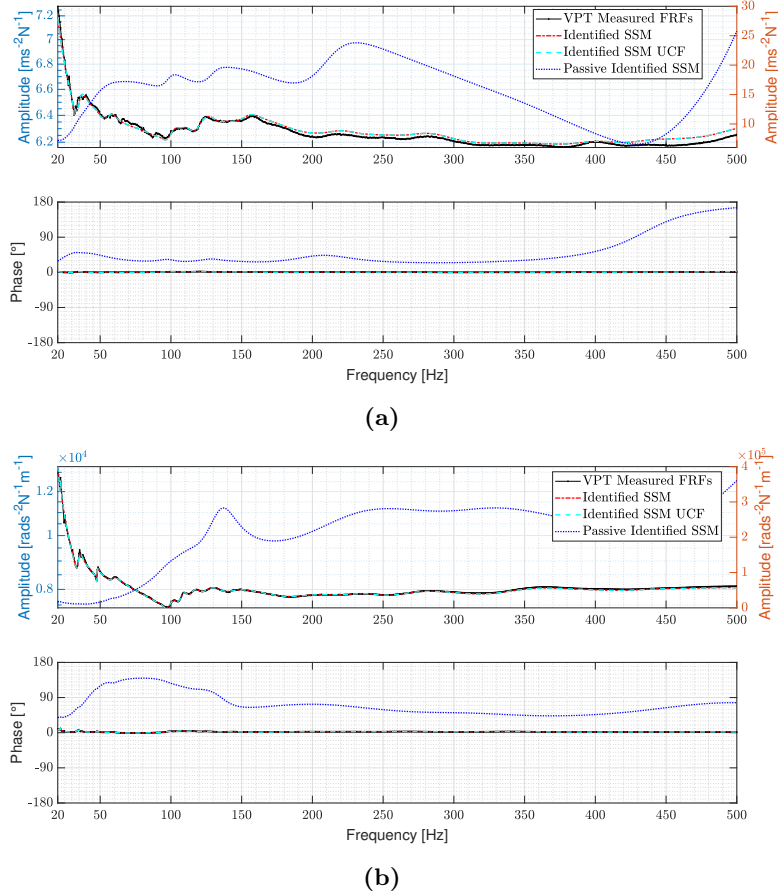
Figure 4.22: Comparison of some accelerance interface FRFs (black solid line) (the left y axis must be used to interpret the amplitude of these FRFs) with the same accelerance FRFs of the: i) respective estimated state-space model (red dash-dotted line) (the left y axis must be used to interpret the amplitude of these FRFs), ii) of the respective estimated state-space model transformed into UCF (cyan dashed line) (the left y axis must be used to interpret the amplitude of these FRFs) and iii) of the passive model obtained by using the technique outlined in [4] (blue dotted line) (the right y axis must be used to interpret the amplitude of these FRFs): a) FRF of the aluminum cross A, whose output and input are v_1^y and m_1^y, respectively; b) FRF of the aluminum cross B, whose output and input are $v_2^{R_x}$ and $m_2^{R_x}$, respectively.

(a)

(b)
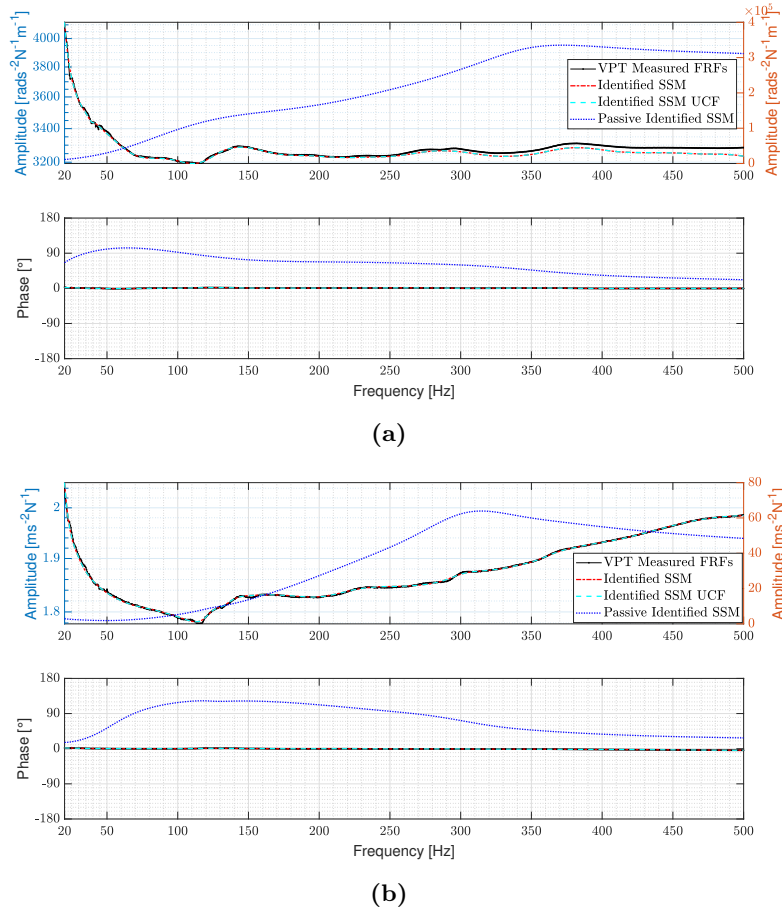
Figure 4.23: Comparison of some accelerance interface FRFs (black solid line) (the left y axis must be used to interpret the amplitude of these FRFs) with the same accelerance FRFs of the: i) respective estimated state-space model (red dash-dotted line) (the left y axis must be used to interpret the amplitude of these FRFs), ii) of the respective estimated state-space model transformed into UCF (cyan dashed line) (the left y axis must be used to interpret the amplitude of these FRFs) and iii) of the passive model obtained by using the technique outlined in [4] (blue dotted line) (the right y axis must be used to interpret the amplitude of these FRFs): a) FRF of the steel cross A, whose output and input are $v_1^{R_x}$ and $m_1^{R_x}$, respectively; b) FRF of the steel cross B, whose output and input are v_2^{z} and m_2^{z}, respectively.

(a)

(b)
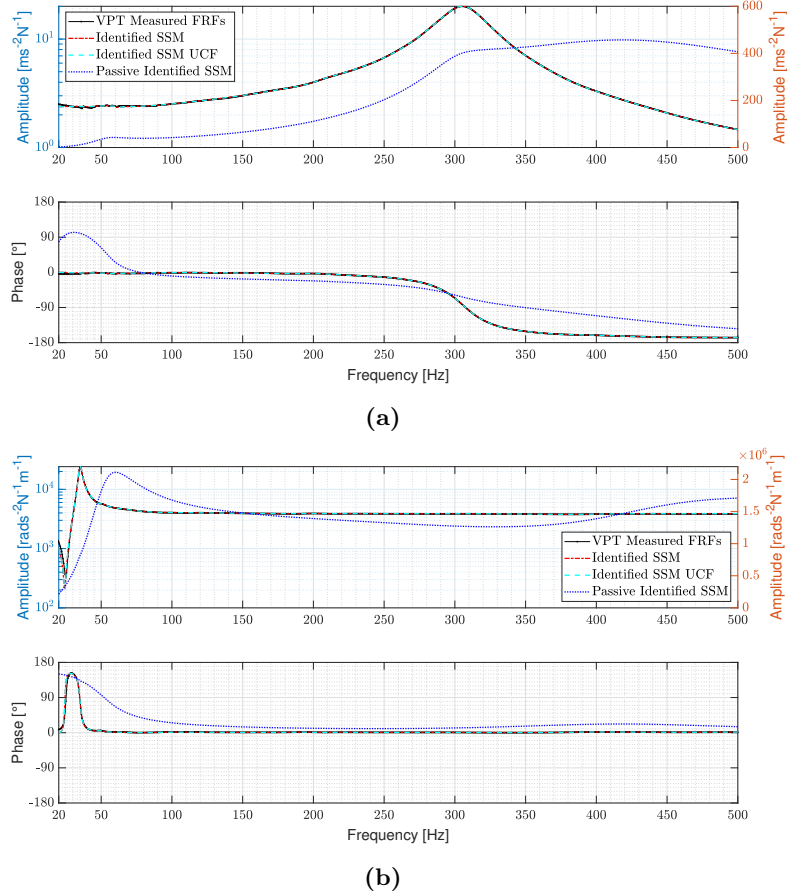
Figure 4.24: Comparison of some accelerance interface FRFs (black solid line) (the left y axis must be used to interpret the amplitude of these FRFs) with the same accelerance FRFs of the: i) respective estimated state-space model (red dash-dotted line) (the left y axis must be used to interpret the amplitude of these FRFs), ii) of the respective estimated state-space model transformed into UCF (cyan dashed line) (the left y axis must be used to interpret the amplitude of these FRFs) and iii) of the passive model obtained by using the technique outlined in [4] (blue dotted line) (the right y axis must be used to interpret the amplitude of these FRFs): a) FRF of assembly A, whose output and input are v_2^z and m_1^z, respectively; b) FRF of assembly A, whose output and input are $v_1^{R_z}$ and $m_1^{R_z}$, respectively.
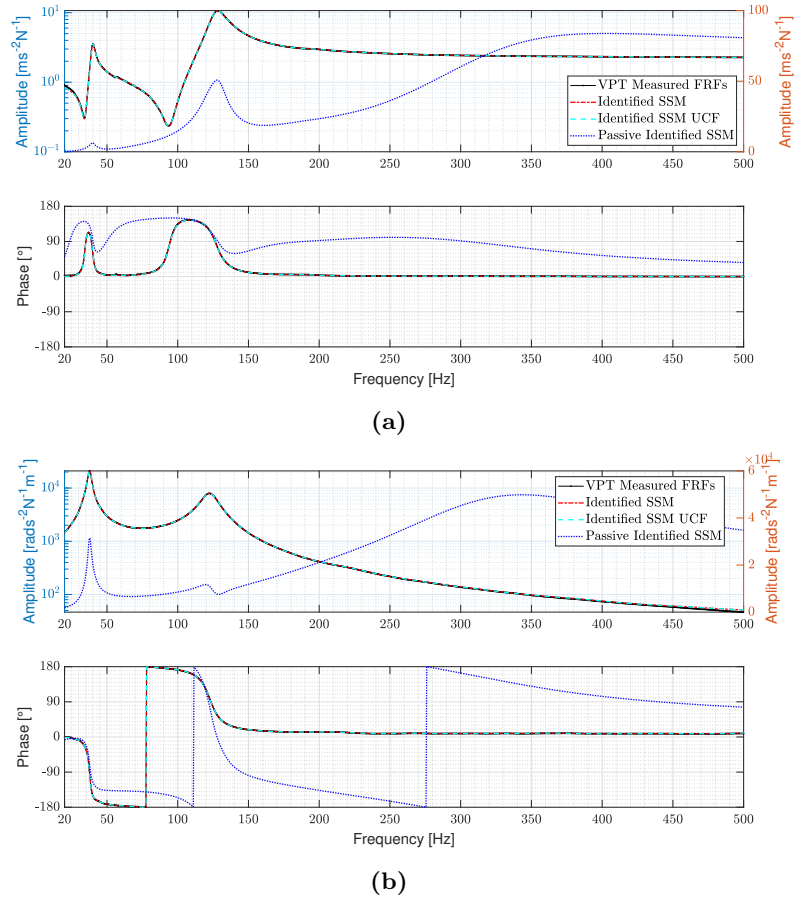
Figure 4.25: Comparison of some accelerance interface FRFs (black solid line) (the left y axis must be used to interpret the amplitude of these FRFs) with the same accelerance FRFs of the: i) respective estimated state-space model (red dash-dotted line) (the left y axis must be used to interpret the amplitude of these FRFs), ii) of the respective estimated state-space model transformed into UCF (cyan dashed line) (the left y axis must be used to interpret the amplitude of these FRFs) and iii) of the passive model obtained by using the technique outlined in [4] (blue dotted line) (the right y axis must be used to interpret the amplitude of these FRFs): a) FRF of assembly B, whose output and input are v_1^y and m_1^y, respectively; b) FRF of assembly B, whose output and input are $v_1^{R_y}$ and $m_2^{R_y}$, respectively.

The estimated state-space models describing the dynamic behaviour of the steel crosses A and B are made of 206 and 192 states, respectively, while the models representative of assemblies A and B are composed by 260 and 272 states, respectively. Naturally, in the frequency band of interest, the mechanical systems under study present a significant lower number of modes. However, to compute state-space models presenting FRFs matching as closely as possible the correspondent reference FRFs (i.e. FRFs obtained by applying VPT on the measured FRFs), we decided to compute the estimated models by using a significant number of modes. On top of this, we would expect the identified models describing the dynamics of the aluminium crosses A and B to be composed by the same number of states (the same was, naturally, foreseen for the models representative of crosses steel A and B). Yet, the identified state-space models representative of these crosses were identified from different sets of FRFs. As these sets of FRFs were experimentally acquired they did not match. This can be explained, for instance, due to slight differences on the mechanical properties of the crosses. For this reason, the estimated state-space models representative of the crosses aluminum A and B are not equal neither made of the same number of states (the same holds for the models representative of the steel crosses A and B).

When comparing the approach presented in section 3.3.2 to impose Newton's second law with the technique proposed by Liljerehn in [5], it is obvious that the approach outlined in section 3.3.2 presents the relevant advantage of not making use of undamped RCMs. Additionally, in section 3.3, we proved mathematically that by exploiting the method presented in section 3.3.2, the state-space models can be accurately forced to verify Newton's second law by using RCMs presenting lower natural frequencies than by using the approach outlined in [5]. To show this advantage in practice, we defined two extra models representative of assembly A by using the previously identified modal parameters and by following the procedures presented in section 3.2. To compute these models, the RCMs responsible for including the contribution of the lower and upper out-of-band modes were set-up by selecting $\omega_{LR} = 1 \times 10^{-1}$ Hz, $\omega_{UR} = 1.5 \times 10^4$ Hz and $\xi_{LR} = \xi_{UR} = 1 \times 10^{-1}$. Then, one of these models was imposed to respect Newton's second law by exploiting the method proposed in [5] (from now on, this model will be tagged state-space model A), while the other one was forced to verify this physical law by exploiting the approach discussed in section 3.3.2 (from now on, this model will be denoted state-space model B). The RCMs used to impose Newton's second law on both state-space models A and B were set-up by defining $\omega_{CB} = 5 \times 10^3$ Hz and $\xi_{CB} = 0$.

Figure 4.26 clearly shows that the FRFs of the state-space model B are better matching the interface FRFs of assembly A than the FRFs of the state-space model A. As expected, this is more evident for higher frequencies (see, expressions (3.51) and (3.52))). Therefore, it is straightforward to conclude that by following the method presented in section 3.3.2, Newton's second law can be accurately imposed by using RCMs presenting lower natural frequencies than by exploiting the approach outlined in [5].

(a)

(b)
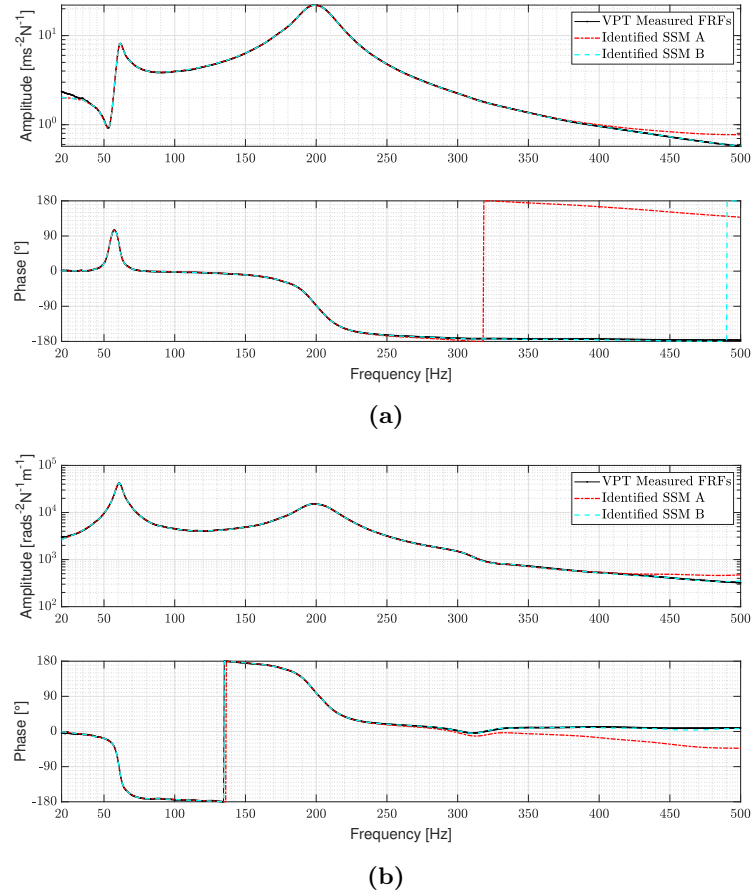
Figure 4.26: Comparison of two accelerance interface FRFs of assembly A with the same accelerance FRFs of state-space model A (forced to obey Newton's second law by using the method presented in [5]) (red dash-dotted line) and of state-space model B (forced to verify Newton's second law by exploiting the method discussed in section 3.3.2) (cyan dashed line): a) FRF of the assembly A, whose output and input are, respectively, v_2^y and m_1^y; b) FRF of the assembly A, whose output and input are, respectively, $v_2^{R_x}$ and $m_1^{R_x}$.

4.2.3   Experimental validation of LM-SSS enhanced with post-processing procedures

To identify state-space models representative of the rubber mount, we will start by decoupling the two aluminum crosses from assembly A by exploiting LM-SSS. Two different state-space models will be computed. One of them will be obtained by using the untransformed estimated displacement state-space models leading to the computation of a displacement non minimal-order model, while the other will be computed by exploiting the same models previously transformed into UCF together with the post-processing procedures presented in section 2.3.3 enabling the computation of a displacement minimal-order model. Unfortunately, the FRFs of the rubber mount are not known. For this reason, the FRFs of the rubber mount identified by performing decoupling with LM-FBS will be considered as reference to assess the quality of the FRFs of the models computed through LM-SSS decoupling. In figure 4.27, it is shown the comparison of two dynamic stiffness terms of the rubber mount obtained by the following approaches: i) by inverting and multiplying by $-\omega^2$ the accelerance FRFs obtained by exploiting LM-FBS to decouple the accelerance interface FRFs of the aluminum crosses (computed by applying VPT on the respective sets of experimentally acquired FRFs) from the accelerance interface FRFs of assembly A determined by applying VPT on the respective set of measured FRFs; ii) by inverting the FRFs of the displacement non minimal-order state-space model computed by decoupling with LM-SSS the untransformed displacement state-space models representative of the aluminum crosses from the untransformed displacement state-space model of assembly A and iii) by inverting the FRFs of the displacement minimal-order state-space model calculated by implementing the decoupling operation performed in ii) by using the displacement state-space models transformed into UCF (i.e. the state-space models representative of both aluminum crosses and assembly A) and by exploiting the post-processing procedure presented in section 2.3.3 that relies on the use of a state Boolean localization matrix to eliminate the redundant states originated from the decoupling operation.

From the observation of figure 4.27, it is clear that the dynamic stiffness terms of the rubber mount identified by using LM-FBS are very well matched by the correspondent dynamic stiffness terms of both non minimal-order and minimal-order state-space models computed by performing decoupling with LM-SSS. On top of this, for low frequencies, the identified dynamic stiffness terms are, roughly, given by a straight line as expected (see, [33]). This observation further validates the identified rubber mount dynamic stiffness terms. It is worth mentioning that, as expected, the non minimal-order and minimal-order rubber mount models obtained by implementing decoupling with LM-SSS are composed by 674 and 650 states, respectively.

At this point, the identified rubber mount state-space models will be coupled with both steel crosses by exploiting LM-SSS. Figure 4.28 compares two interface accelerance FRFs of assembly B obtained by exploiting VPT on its measured FRFs with

(a)

(b)
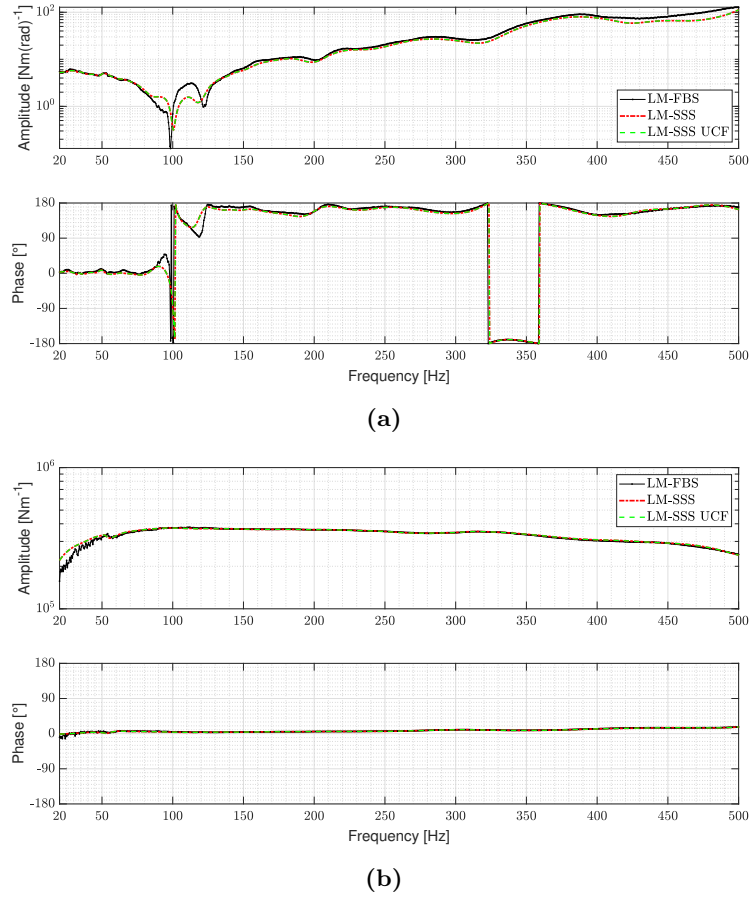
Figure 4.27: Comparison of two dynamic stiffness terms obtained by the following approaches: i) by inverting and multiplying by $-\omega^2$ the accelerance FRFs obtained by exploiting LM-FBS to decouple the accelerance interface FRFs of the aluminum crosses from the accelerance interface FRFs of assembly A; ii) by inverting the FRFs of the displacement non minimal-order state-space model computed by LM-SSS decoupling and iii) by inverting the FRFs of the displacement minimal-order state-space model calculated by implementing decoupling with LM-SSS: a) dynamic stiffness term of the rubber mount, whose output is v_1^{Rz} and the input is m_1^{Rz}; b) dynamic stiffness term of the rubber mount, whose output is v_2^z and the input is m_2^z.

the same accelerance interface FRFs computed by the following methodologies: i) by using LM-FBS to couple the identified accelerance rubber mount FRFs with the accelerance interface FRFs of the steel crosses (computed by using VPT with the respective measured FRFs); ii) by multiplying by $-\omega^2$ the FRFs of the displacement non minimal-order coupled state-space model computed by applying LM-SSS to couple the identified displacement non minimal-order state-space model of the rubber mount with the estimated displacement state-space models representative of the steel crosses and iii) by multiplying by $-\omega^2$ the FRFs of the displacement minimal-order coupled model obtained by exploiting LM-SSS to couple the identified displacement minimal-order rubber mount model (already identified in UCF) with the estimated displacement state-space models representative of the steel crosses transformed into UCF and by exploiting the approach relying on the use of a state Boolean localization matrix (presented in section 2.3.3) to eliminate the redundant states originated from the coupling operation. Note that, to retain a unique set of outputs and inputs from the coupled models computed with strategies ii) and iii), the post-processing procedure discussed in section 2.3.4 was applied.

Analyzing figure 4.28, we may conclude that the accelerance interface FRFs of assembly B are very well-matched by the accelerance coupled FRFs obtained with LM-FBS and by the accelerance FRFs computed from the displacement coupled state-space models computed with LM-SSS. Thus, it is clear that LM-SSS can be used to perform accurate coupling operations with state-space models defined from experimentally acquired data. Moreover, we may also claim that by using LM-SSS to perform DS operations with state-space models transformed into UCF together with the post-processing procedures outlined in section 2.3.3, reliable minimal-order state-space models can be computed, even when working with models directly estimated from experimentally acquired data. It is worth mentioning that, as expected, the non minimal-order and minimal-order coupled models computed with LM-SSS are composed by 1072 and 1024 states, respectively.

The coupling operation here performed was re-implemented by exploiting the approach proposed by Su and Juang in [9] (here also labelled as classical SSS). It turned out that the FRFs of the acceleration coupled state-space model computed with classical SSS perfectly match the accelerance FRFs computed from the displacement coupled models obtained with LM-SSS. As discussed in section 2.3.5, the LM-SSS method holds the advantage of being more computationally efficient, because it just requires the performance of a matrix inversion to compute the coupled state-space model, while classical SSS demands the performance of two different matrix inversions. Thus, to demonstrate the benefit of using LM-SSS in place of classical SSS in terms of computation time, we measured the time required to compute the two matrix inversions involved in classical SSS and the time used to compute the matrix inversion involved in LM-SSS. To give statistical consistency to the measured time results, the matrix inversions involved in classical SSS and LM-SSS were repeated 1×10^4 times. It was concluded that, the ma-

(a)

(b)
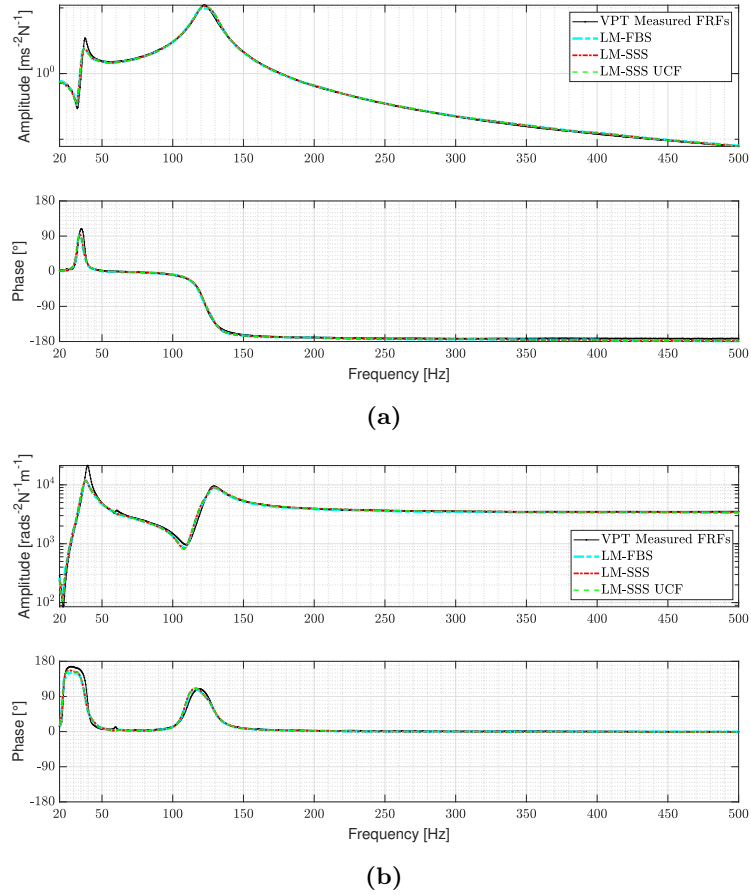
Figure 4.28: Comparison of two accelerance interface FRFs obtained by exploiting VPT on its measured FRFs with the same accelerance interface FRFs computed by the following methodologies: i) by using LM-FBS to couple the identified rubber mount FRFs with the interface FRFs of the steel crosses; ii) by multiplying by $-\omega^2$ the FRFs of the displacement non minimal-order coupled state-space model computed with LM-SSS and iii) by multiplying by $-\omega^2$ the FRFs of the displacement minimal-order coupled model obtained by exploiting LM-SSS: a) accelerance FRF of the assembly B, whose output is v_1^x and the input is m_2^x; b) accelerance FRF of the assembly B, whose output is $v_2^{R_x}$ and the input is $m_2^{R_x}$.

trix inversions involved in classical SSS are performed in $2.12 \times 10^{-5}s$ (average value), whereas the matrix inversion involved in LM-SSS takes place in $5.49 \times 10^{-6}s$ (average value). Thus, it is clear that the performance of the matrix inversion involved in LM-SSS is, approximately, four times faster than the performance of the matrix inversions involved in classical SSS. This analysis was performed on an Intel(R) Core(TM) i7-8550U CPU and 8 GB RAM machine. The reported improvement in terms of computational time by using LM-SSS is not relevant for the coupling operation here performed. Nevertheless, when dealing with some applications demanding the performance of several coupling operations, e.g. real-time substructuring applications involving mechanical components presenting time-varying dynamics (see section 2.3.5), the use of LM-SSS might substantially decrease the computational cost associated with the application. Moreover, the benefit of exploiting LM-SSS in terms of computational time is expected to be more important as the number of interface DOFs of the substructures involved in the coupling operations increases (see section 2.3.5).

4.2.4 Experimental validation of primal state-space disassembly and of the state-space realization of IS

Here, state-space models representative of the rubber mount will be identified by exploiting primal disassembly (see section 2.4) and the state-space realization of IS (see section 5.3.3). To assess the accuracy of these identified models, the rubber mount dynamic stiffness obtained by LM-FBS and by applying IS on the apparent mass of assembly A, will be considered as reference. In [33], these approaches have already shown to be reliable to characterize the dynamics of a rubber mount. Furthermore, the rubber mount dynamic stiffness of the displacement non minimal-order state-space model obtained by using LM-SSS decoupling (which was already experimentally validated in section 4.2.3) will also be exploited to evaluate the accuracy of the rubber mount state-space models to be identified in this section.

In figure 4.29, it is shown the comparison of two rubber mount dynamic stiffness terms identified by using the following strategies: i) by inverting and multiplying by $-\omega^2$ the accelerance FRFs computed by using LM-FBS to decouple the accelerance interface FRFs of both aluminum crosses from the accelerance FRFs of assembly A (see section 4.2.3); ii) by multiplying by $-\omega^2$ the rubber mount diagonal apparent mass terms obtained by exploiting IS with the off diagonal apparent mass terms of assembly A, whose outputs and inputs are the interface DOFs of the aluminum crosses A and B, respectively; iii) by inverting the FRFs of the displacement non minimal-order rubber mount state-space model obtained with LM-SSS (see section 4.2.3); iv) by multiplying by $-\omega^2$ the apparent mass of the non minimal-order state-space model computed by primarily disassembling the inverted acceleration models representative of the aluminum crosses from the inverted acceleration model of assembly A and v) by multiplying by $-\omega^2$ the apparent mass of the state-space model representative of

the rubber mount diagonal apparent mass terms computed by exploiting the state-space realization of IS (see section 5.3.3) with the state-space model representative of the rubber mount off diagonal terms, whose outputs and inputs are, respectively, the interface DOFs of aluminum crosses A and B, identified from the inverted acceleration model of assembly A.

From the analysis of figure 4.29, it is straightforward that the dynamic stiffness terms of the state-space model obtained by using primal disassembly are very well matching the dynamic stiffness terms obtained through the performance of decoupling with LM-FBS. Moreover, as expected the dynamic stiffness terms of the state-space models obtained by applying LM-SSS decoupling and primal disassembly are perfectly matching. These observations demonstrate that the primal state-space assembly formulation presented in section 2.4 is reliable to perform disassembly operations with state-space models estimated from experimentally acquired data.

Further observing figure 4.29, it is clear that the dynamic stiffness terms obtained by applying IS on the apparent mass of assembly A and by exploiting the state-space realization of IS on the state-space model representative of the apparent mass of assembly A are very well-matching. This demonstrates that the state-space realization of IS is accurate even when working with models estimated from experimentally acquired data.

Additionally, in figure 4.29 it is evident that the dynamic stiffness terms computed through decoupling/disassembly operations (i.e. through strategies i, iii and iv) and the dynamic stiffness terms computed by applying IS (i.e. strategies ii and v) are well matching at low frequencies. Yet, as the frequency increases, more relevant deviations between the results obtained by both approaches are observed. As the IS approach assumes that the rubber mount is massless, the more pronounced deviations observed at higher frequencies are expected. Indeed, the observed deviations indicate that for higher frequencies, the massless assumption is no longer valid to properly characterize the dynamics of the rubber mount.

To validate the post-processing procedures outlined in section 2.3.3 to eliminate the redundant states originated from primal disassembly operations, a minimal-order rubber mount state-space model was computed by using the state-space models previously transformed into UCF (i.e. state-space models of both aluminum crosses and assembly A) together with the post-processing procedure that relies on the use of a state Boolean localization matrix. In addition, the state-space realization of IS was applied on the inverted acceleration state-space model of assembly A transformed into UCF to identify the diagonal apparent mass terms of the rubber mount. Figure 4.30 compares the dynamic stiffness terms of the rubber mount determined by the following approaches: by multiplying by $-\omega^2$ the apparent mass of the non minimal-order state-space model computed by primal state-space disassembly (solution iv); by multiplying by $-\omega^2$ the minimal-order model obtained by exploiting primal disassembly with the state-space models previously transformed into UCF (i.e. state-space models of both aluminum

(a)

(b)
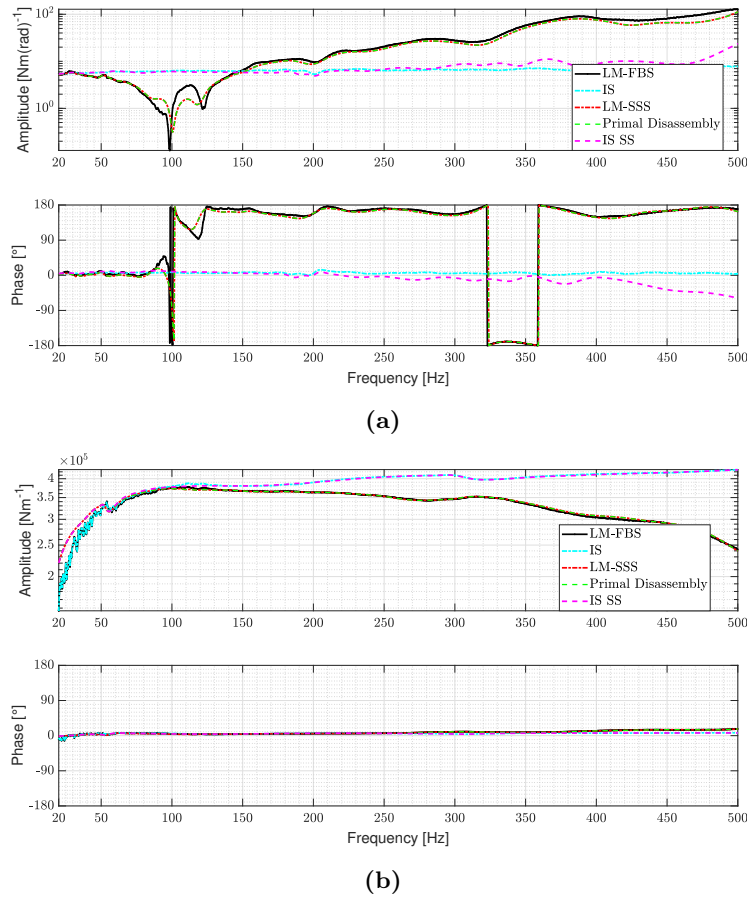
Figure 4.29: Comparison of some rubber mount dynamic stiffness terms obtained by exploit-
ing the following strategies: i) LM-FBS decoupling, ii) IS on the apparent mass of
assembly A, iii) dynamic stiffness of the displacement non minimal-order state-
space model computed with LM-SSS decoupling, iv) dynamic stiffness of the
state-space model obtained with primal disassembly and v) dynamic stiffness of
the model obtained by applying the state-space realization of IS on the state-
space model representative of the apparent mass of assembly A: a) rubber mount
dynamic stiffness term, whose output and input are, respectively, $v_1^{R_z}$ and $m_1^{R_z}$;
b) rubber mount dynamic stiffness term, whose output and input are, respec-
tively, v_2^z and m_2^z.

crosses and assembly A) with the post-processing procedure that relies on the use of a state Boolean localization matrix (see section 2.3.3) (solution vi); by multiplying by $-\omega^2$ the apparent mass of the state-space model representative of the rubber mount diagonal apparent mass terms computed by exploiting the state-space realization of IS (solution v) and by multiplying by $-\omega^2$ the apparent mass of the state-space model representative of the rubber mount diagonal apparent mass terms transformed into UCF computed by using the state-space realization of IS (see section 5.3.3) with the state-space model representative of the rubber mount off diagonal terms, whose outputs and inputs are, respectively, the interface DOFs of aluminum crosses A and B, identified from the inverted acceleration model of assembly A previously transformed into UCF (solution vii).

Analyzing figure 4.30, we may conclude that the dynamic stiffness terms of the non minimal-order and minimal-order state-space models obtained by using primal disassembly are perfectly matching. Thus, it is obvious that the post-processing procedures outlined in section 2.3.3 are accurate to eliminate the redundant states originated from primal disassembly operations involving models estimated from experimentally acquired data. On top of this, it is clear that the FRFs of the state-space models representative of the rubber mount diagonal apparent mass terms obtained by applying IS on the inverted untrnsformed acceleration model of assembly A and on the inverted acceleration model of assembly A previously transformed into UCF perfectly match. Hence, proving that the state-space realization of IS can be applied on state-space models previously transformed into UCF.

Analyzing the computed rubber mount state-space models, it is possible to conclude that by exploiting strategies iii) and iv), rubber mount state-space models made of 674 states were computed, whereas with strategy vi), it was possible to compute a state-space model representative of the mount composed by 650 states. In contrast, by following strategies v) and vii), state-space models representative of the diagonal apparent mass terms of the rubber mount composed by 260 states were obtained. It is straightforward to conclude that the strategies iii), iv) and vi) lead to the computation of rubber mount models made of a substantially higher number of states, when compared with the state-space models computed by following strategies v) and vii). The strategies involving decoupling or primal disassembly operations lead to the computation of rubber mount models composed by more states, because of the inclusion of the dynamics of both aluminum crosses A and B to decouple them from assembly A. These DS operations lead to the determination of state-space models that include the dynamics of the decoupled/disassembled components twice (see section 2.5). Hence, these state-space models include pairs of spurious modes, whose identification and elimination is difficult, when the dynamics of the component to be identified is unknown (usual scenario in practice).

Therefore, we may conclude that by performing decoupling with LM-SSS or by exploiting primal state-space disassembly, we have the advantage of not performing any

(a)

(b)
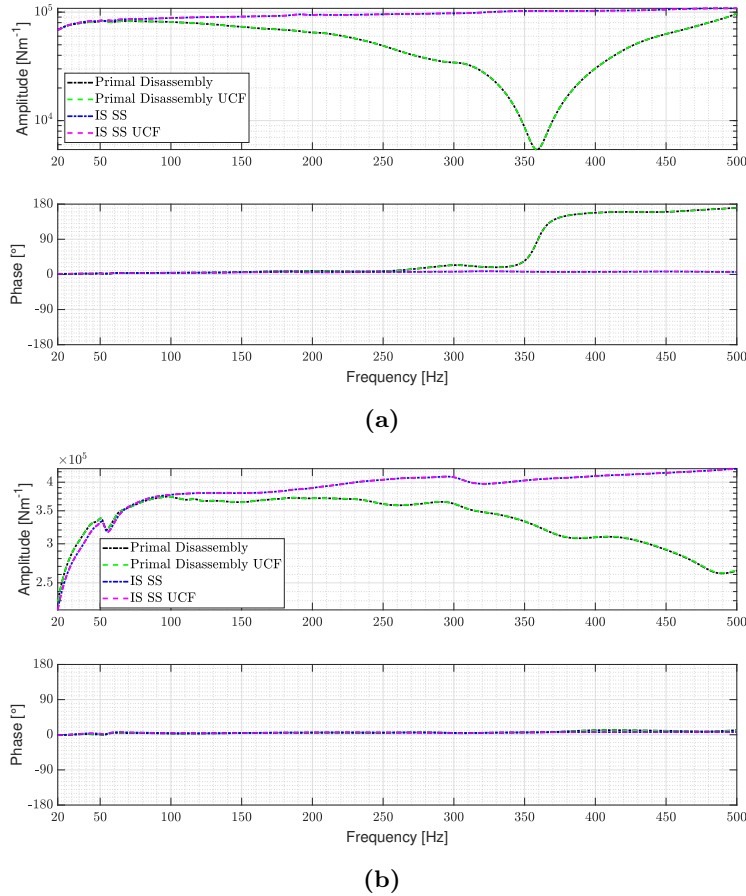
Figure 4.30: Comparison of the rubber mount dynamic stiffness terms obtained by the following approaches: dynamic stiffness of the non minimal-order model computed with primal state-space disassembly (solution iv); dynamic stiffness of the minimal-order model computed with primal state-space disassembly (solution vi), dynamic stiffness of the model obtained by applying the state-space realization of IS on the inverted acceleration state-space model of assembly A (approach v) and the dynamic stiffness of the model obtained by applying the state-space realization of IS on the inverted acceleration state-space model of assembly A previously transformed into UCF (approach vii): a) rubber mount dynamic stiffness term, whose output and input are, respectively, v_1^x and m_1^x; b) rubber mount dynamic stiffness term, whose output and input are, respectively, v_1^z and m_1^z.

assumption regarding the dynamics of the CE. Thus, these strategies hold to identify the dynamics of any component/CE. Conversely, IS can only be applied to identify components verifying its underlying assumptions (i.e. the components must be massless and must not present cross couplings between their DOFs (see section 2.5)). Nevertheless, IS has the advantage of enabling the experimental characterization of CEs included in assemblies without requiring dismounting and mounting operations and knowledge regarding the dynamics of the structures to which the CE is connected, hence, avoiding the performance of additional experimental tests to characterize the structures to which the CE is linked. Moreover, the characterization of CEs through IS avoids the performance of decoupling/disassembly operations, enabling the identification of state-space models made of a lower number of states. Thus, the advantage of using IS will be more pronounced as the number of substructures to be decoupled/disassembled enlarges and as the state-space models that represent their dynamics are made of a higher number of states. On top of this, as the state-space models computed by IS are generally composed by a lower number of states, the computational cost associated with the performance of calculations with them will generally be significantly lower. For this reason, these models are more suitable to be exploited, for example, in real-time applications.

4.2.5   Experimental validation of primal state-space assembly and LM-SSS via compatibility relaxation

In this section, state-space models representative of assembly B, will be obtained by coupling the rubber mount state-space models identified in section 4.2.4 with the identified state-space models representative of both steel crosses (see section 4.2.2). Figures 4.31 and 4.32 report the comparison of some interface acceleration FRFs of assembly B computed by applying VPT on the experimentally acquired FRFs with the acceleration FRFs obtained by the following approaches: a) by using LM-FBS to couple the interface acceleration FRFs of both steel crosses with the rubber mount acceleration FRFs obtained with LM-FBS decoupling; b) by exploiting LM-FBS via compatibility relaxation (see section 2.2.2) to couple the interface acceleration FRFs of both steel crosses with the inverted rubber mount diagonal apparent mass terms determined by applying IS on the inverted interface acceleration FRFs of assembly A; c) by multiplying by $-\omega^2$ the FRFs of the displacement non minimal-order coupled state-space model obtained by using LM-SSS to couple the rubber mount displacement non minimal-order model obtained with LM-SSS decoupling with the displacement state-space models of both steel crosses; d) acceleration FRFs of the inverted coupled model calculated by exploiting primal state-space assembly to couple the non minimal-order state-space model representative of the rubber mount identified by primal disassembly with the inverted acceleration state-space models of both steel crosses and e) FRFs of the acceleration non minimal-order coupled model computed by using LM-SSS via compatibility relaxation (see section 2.5) to couple the inverted model representative of

the diagonal rubber mount apparent mass terms obtained through the application of the state-space realization of IS on the inverted model of assembly A with the acceleration state-space models of both steel crosses.

By analyzing figures 4.31 and 4.32, it is clear that the coupled accelerance FRFs obtained with LM-FBS (methodology a), the accelerance FRFs computed from the displacement non minimal-order model obtained with LM-SSS (methodology c) and of the inverted non minimal-order model computed with primal assembly (methodology d) are very well matching with the interface accelerance FRFs of assembly B. On top of this, it is obvious that the accelerance FRFs of the coupled model obtained with LM-SSS are perfectly matching the same FRFs of the inverted coupled model obtained by primal state-space assembly (see section 2.4). Hence, we may claim that the primal state-space assembly formulation presented in section 2.4 is reliable to couple state-space models estimated from experimentally acquired data.

By focusing our attention on figure 4.31a, it is clear that the axial (z axis direction represented in figure 4.20) driving point interface FRF of assembly B is well matched by the same FRF of the non minimal-order coupled state-space model obtained with LM-SSS via compatibility relaxation (methodology e). The same is also verified in figure 4.31b for the driving point FRF associated with the rotation DOF around the axial direction. The good quality of the FRFs of the non minimal-order coupled model obtained with LM-SSS via compatibility relaxation is probably justified by the fact that the weight of the rubber mount (approximately, 27 g) is substantially lower than the weight of each steel cross (approximately, 560 g). Moreover, cross couplings between the z direction and the rotations around the x and y axis (see figure 4.20 to observe the orientation of the axis) are not expected (see [33]). The same holds for the cross couplings between the rotation around the z axis and the x and y directions. Hence, the IS assumptions do not significantly deteriorate the coupled results related with both z axis and rotation around z. In contrast, figures 4.32a and 4.32b show that the FRFs of the coupled model obtained with LM-SSS via compatibility relaxation associated with both x and y directions are poorly matching the same interface FRFs of assembly B. The poor quality of the FRFs of the coupled model obtained with LM-SSS via compatibility relaxation are due to the existence of significant cross couplings between the rotations around one of the radial directions (i.e. x or y directions, see figure 4.20) and the displacement on the other radial direction (see [33]). These important cross couplings are ignored when computing the coupled model with LM-SSS via compatibility relaxation, because the dynamics of the rubber mount is included with a state-space model identified by using the state-space realization of IS (see section 2.5.4).

Further observing figures 4.31a and 4.31b, we may conclude that the coupled FRFs computed by exploiting LM-FBS via compatibility relaxation are very well matched by the FRFs of the non minimal-order coupled model obtained with LM-SSS via compatibility relaxation. Indeed, both sets of FRFs are not perfectly matching, because the FRFs of the identified state-space models do not perfectly match the correspondent
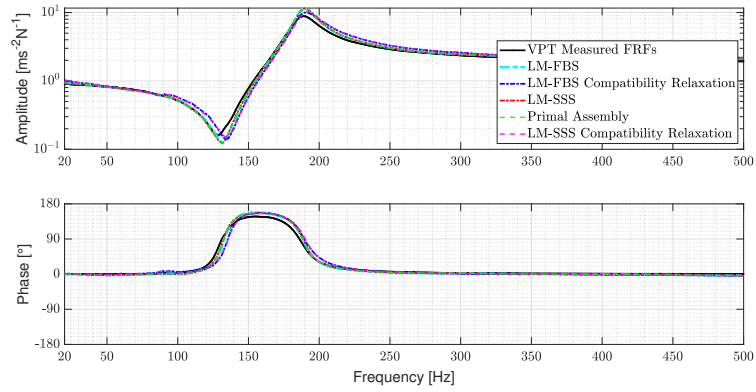
(a)
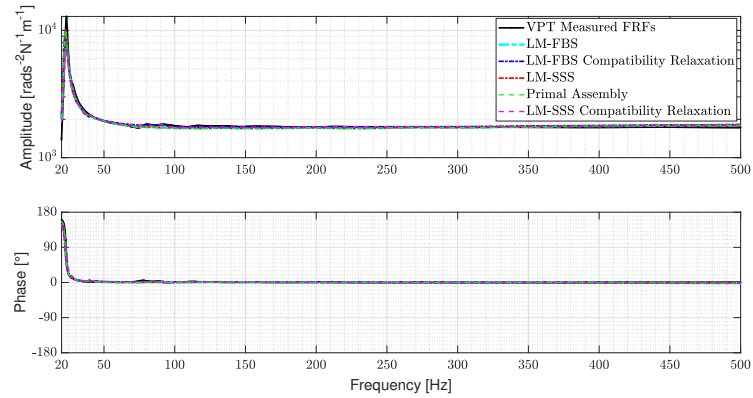
(b)

Figure 4.31: Comparison of two interface accelerance FRFs of assembly B with the coupled accelerance FRFs computed by exploiting the following approaches: LM-FBS (methodology a), LM-FBS via compatibility relaxation (methodology b), LM-SSS (methodology c), primal state-space assembly (methodology d) and LM-SSS via compatibility relaxation (methodology e): a) accelerance FRF of assembly B, whose output and input are, respectively, v_2^z and m_2^z; b) accelerance FRF of assembly B, whose output and input are, respectively, $v_2^{R_z}$ and $m_2^{R_z}$.

(a)

(b)
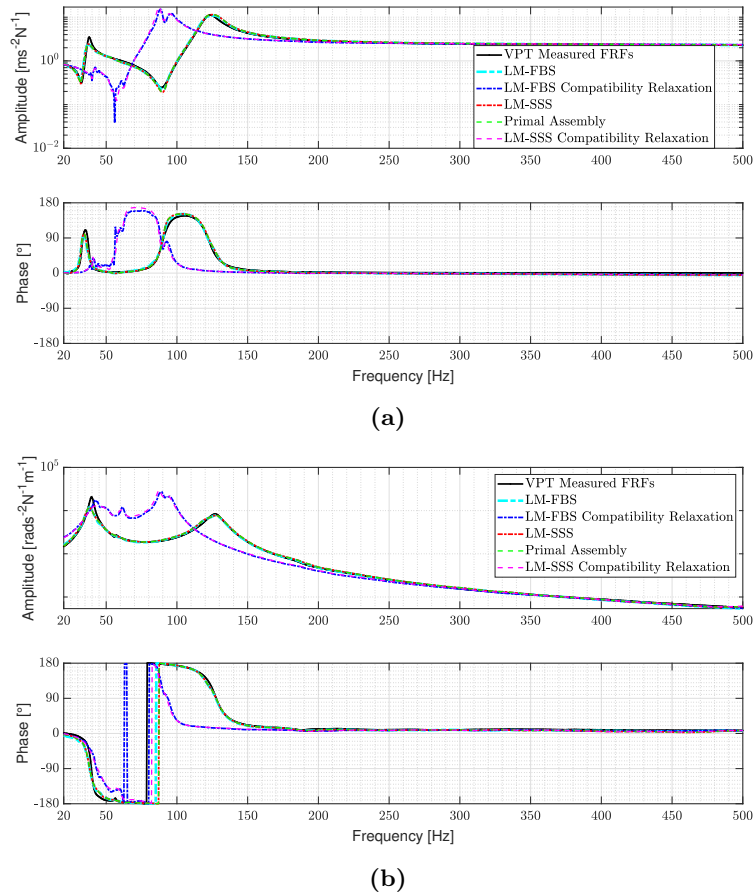
Figure 4.32: Comparison of two interface accelerance FRFs of assembly B with the coupled accelerance FRFs computed by exploiting the following approaches: LM-FBS (methodology a), LM-FBS via compatibility relaxation (methodology b), LM-SSS (methodology c), primal state-space assembly (methodology d) and LM-SSS via compatibility relaxation (methodology e): a) accelerance FRF of assembly B, whose output and input are, respectively, v_1^x and m_1^x; b) accelerance FRF of assembly B, whose output and input are, respectively, $v_2^{R_x}$ and $m_1^{R_x}$.

measured FRFs (see section 4.2.2). For this reason, it is clear that LM-SSS via compatibility relaxation (see section 2.5.1) is an accurate approach to include the dynamics of CEs into LM-SSS formulation even when dealing with state-space models estimated from measured FRFs.

It is now important to assess the quality of the minimal-order coupled state-space models computed by using primal state-space assembly and LM-SSS via compatibility relaxation, when coupling substructures and CEs characterized by state-space models estimated from measured FRFs. In figures 4.33, it is compared the accelerance FRFs of coupled state-space models obtained by exploiting different methodologies: inverted non minimal-order coupled model obtained by exploiting primal state-space assembly (methodology d); inverted minimal-order coupled model obtained by using primal state-space assembly and the post-processing procedure presented in section 2.3.3 that makes use of a state Boolean localization matrix with the inverted state-space models of both steel crosses transformed into UCF and with the minimal-order rubber mount state-space model (already computed in UCF) identified by using primal state-space disassembly (see section 4.2.4) (methodology f); non minimal-order coupled state-space model obtained by exploiting LM-SSS via compatibility relaxation (methodology e) and the minimal-order coupled state-space model obtained by exploiting LM-SSS via compatibility relaxation with the inverted model of the rubber mount diagonal apparent mass terms computed from the inverted acceleration model of assembly A transformed into UCF (see section 4.2.4) with the state-space models of both steel crosses transformed into UCF and by exploiting the post-processing procedure presented in section 2.5.2 that makes use of a state Boolean localization matrix (methodology g).

From figures 4.33, it is possible to conclude that the FRFs of both inverted non minimal-order and inverted minimal-order coupled state-space models obtained by exploiting the primal state-space assembly formulation are perfectly matching. Therefore, we may claim that the use of the primal state-space assembly formulation with the post-processing procedures outlined in section 2.3.3 represents a reliable methodology to compute minimal-order coupled state-space models even when working with state-space models estimated from measured FRFs.

In addition, by analyzing figures 4.33, it is clear that the accelerance FRFs of the non minimal-order and minimal-order coupled state-space models computed by LM-SSS via compatibility relaxation are perfectly matching. Thus, it is evident that the use of LM-SSS via compatibility relaxation together with the post-processing procedures presented in section 2.5.2 is an accurate approach to obtain minimal-order coupled state-space models even when coupling substructures and CEs characterized by state-space models estimated from measured FRFs.

At this point, it is interesting to compare the number of states of the coupled state-space models determined in this section. By following methodologies c) and d), coupled state-space models composed by 1072 states were computed, whereas by exploiting methodology f) a coupled state-space model made of 1024 states was deter-

(a)

(b)
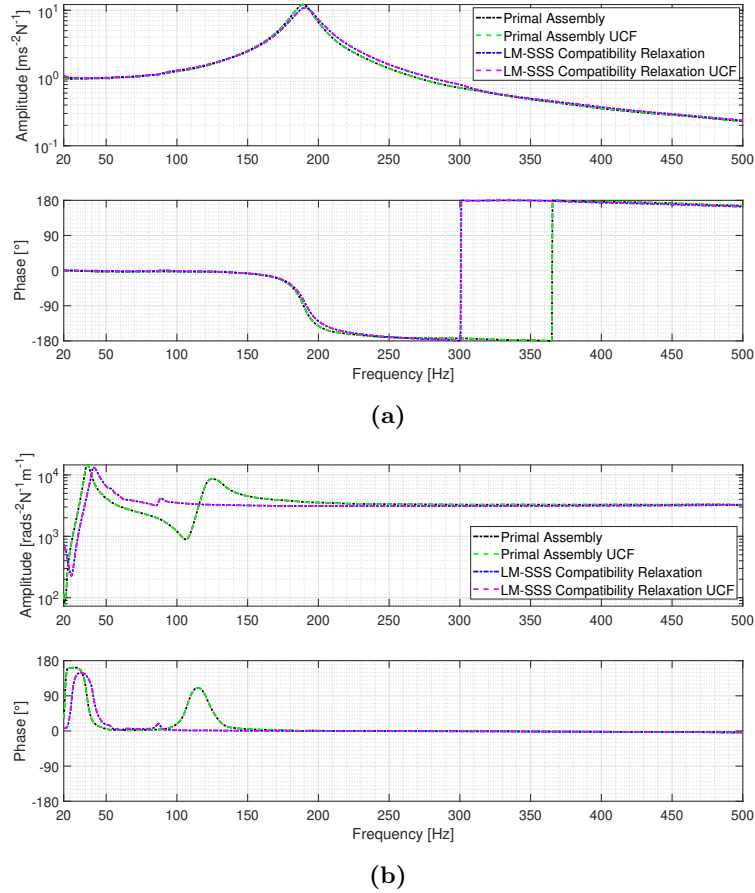
Figure 4.33: Comparison of the accelerance FRFs of the coupled state-space models computed by the following methodologies: non minimal-order coupled state-space model computed by using the primal state-space assembly formulation (methodology d), minimal-order coupled state-space model determined by exploiting the primal state-space assembly formulation (methodology f), non minimal-order coupled state-space model computed through LM-SSS via compatibility relaxation (methodology e) and the minimal-order coupled state-space model obtained by using LM-SSS via compatibility relaxation (methodology g): a) accelerance FRF of assembly B, whose output and input are, respectively, v_1^z and m_2^z; b) accelerance FRF of assembly B, whose output and input are, respectively, $v_2^{R_y}$ and $m_2^{R_y}$.

mined. Methodologies e) and g) lead to the calculation of coupled models made of, respectively, 658 and 646 states. The methodologies c), d) and f), lead to the computation of coupled state-space models composed by a substantially higher number of states, because by following these methodologies the dynamics of the rubber mount is included by using state-space models identified by performing decoupling/disassembly operations (see section 2.5). Thus, we may infer that by including CEs into the coupling operations by treating them as regular substructures, we have the advantage of not making any assumption regarding their dynamic behavior. Thereby, the application of this strategy is not limited in terms of frequency range and it is valid to characterize any CE and substructure. Nevertheless, in general this strategy leads to the determination of coupled state-space models made of spurious states and hence, made of a larger number of states.

Conversely, by performing coupling with LM-SSS via compatibility relaxation, the CEs are characterized by IS. Thus, LM-SSS via compatibility relaxation can only be successfully applied to compute coupled state-space models representative of assembled structures composed by CEs respecting the underlying assumptions of IS (see section 2.5). Therefore, this coupling formulation can only be applied on CEs that do not present important cross couplings between their DOFs and up to frequencies for which the mass of the CEs does not significantly contribute to their dynamic behaviour. However, if the mass of the substructures linked by a given CE is significantly higher than the mass of the CE, the violation of the massless assumption will in general not lead to an important deterioration of the quality of the coupled results [33]. Furthermore, the use of LM-SSS via compatibility relaxation opens the possibility of calculating coupled state-space models free of spurious states and hence, it generally leads to the determination of coupled models made of a substantially lower number of states. Thus, the coupled models obtained through LM-SSS via compatibility relaxation are interesting, when the coupled state-space models are to be exploited in time-domain analysis. Thereby, when analyzing CEs suitable to be characterized by IS or when the coupled models obtained by LM-SSS via compatibility relaxation are reliable, there is no point on using decoupling/disassembly operations to compute state-space models representative of the CEs.

4.2.6 Imposing stability on coupled state-space models

In this section, the displacement minimal-order coupled state-space model representative of assembly B computed in section 4.2.3 will be imposed to be stable by following the approach discussed in section 3.5. Even though all the coupled state-space models computed in sections 4.2.3, 4.2.4 and 4.2.5 are unstable, we have decided to impose stability solely on this model, because the approach proposed in section 3.5 can only be applied on displacement models. Indeed, by exploiting the primal state-space assembly formulation (see section 2.4), it is not possible to directly compute displacement

coupled models, because the coupling operation is performed with inverted state-space models. As reported in appendix A, the inversion of a given state-space model requires the inversion of its feedthrough matrix. Yet, the feedthrough matrix of both displacement and velocity models is null (see section 3.3.1). Hence, we are required to use inverted acceleration state-space models to perform assembling operations with the primal state-space assembly formulation. By inverting the resultant models, one will always compute acceleration coupled state-space models. For the same reason, the state-space realization of IS (see section 2.5.4) can only be applied on inverted acceleration state-space models. Thus, by inverting the models identified with this approach, we will always obtain a state-space model representative of the inverted diagonal apparent mass terms of the CEs and not of their inverted diagonal dynamic stiffness terms. This is the reason why in section 4.2.5, we were only capable of computing acceleration coupled state-space models with LM-SSS via compatibility relaxation. To surpass these difficulties, one could think of exploiting expression (2.78) to compute displacement coupled models from these acceleration coupled models computed with the primal state-space assembly formulation and LM-SSS via compatibility relaxation. However, the computation of a given displacement model from the respective acceleration one is not recommended, because this operation involves the inversion of the state matrix of the model, which may introduce numerical problems associated with the performance of ill-conditioned matrix inversions. For this reason, stability will only be imposed on the displacement minimal-order coupled state-space model computed with LM-SSS in section 4.2.3.

In this way, to impose stability on this displacement coupled model, we started by computing two state-space models from this model, one made of its stable poles (composed by 959 states) and the other one made of its unstable poles (made of 65 states). Subsequently, by following the approach presented in section 3.5, a stabilized model was computed from the state-space model made of the unstable poles. From this stabilized model, two additional models were constructed, one containing its real poles (composed by 3 states) and the other composed by its pairs of complex conjugate poles (made of 62 states).

In accordance with section 3.5, the LSFD estimator was, then, used to improve the quality of the modal parameters of the state-space model constructed from the pairs of complex conjugate poles of the stabilized model. Note that the LSFD estimator was exploited by using as reference the accelerance target FRFs (see, appendix D) computed by subtracting the accelerance FRFs of the state-space model composed by the real poles of the stabilized model from the accelerance FRFs of the state-space model composed by the unstable poles of the minimal-order coupled model computed with LM-SSS (see section 4.2.3). Figures 4.34 and 4.35 present the comparison of the displacement target FRFs calculated by dividing the correpondent accelerance FRFs by $-\omega^2$ with the same displacement FRFs of the: i) state-space model composed by the pairs of complex conjugate poles of the stabilized model and ii) of the modal model

defined from the modal parameters improved with LSFD.

By analyzing figures 4.34 and 4.35, it is clear that the displacement FRFs of the state-space model composed by the pairs of complex conjugate poles of the stabilized model are poorly matching the respective target FRFs. As discussed in section 3.5, this observation was expected, because the pairs of complex conjugate poles composing the state-space model computed from the stabilized model were forced to be stable by multiplying their real part by -1, leading to a significant modification of their FRFs. Thereby, due to the poor quality of the state-space model composed by the pairs of complex conjugate poles of the stabilized model, it will not be used to compute a stable state-space model represnetative of the unstable minimal-order coupled model computed with LM-SSS in section 4.2.3.

Conversely, by observing figures 4.34 and 4.35, it is evident that the target FRFs are very well-matched by the FRFs of the modal model constructed from the modal parameters refined with LSFD. It is important to mention, that we have decided to exploit the LSFD estimator with accelerance target FRFs, because LSFD estimates the modal parameters by solving a linear least-squares problem. Thus, the modal model defined from the modal parameters estimated with this estimator will better approximate the reference FRFs at frequencies for which their amplitudes are higher. By observing figures 4.34 and 4.35, it is evident that the amplitude of the displacement target FRFs at lower frequencies is significantly higher than at higher frequencies. Thus, the displacement FRFs of the modal model computed from the modal parameters estimated with LSFD by taking as reference the displacement target FRFs would not well match these FRFs at higher frequencies. In contrast, the acceleration target FRFs present less pronounced differences in terms of their amplitude at lower and higher frequencies. This is the reason why, by exploiting LSFD with accelerance target FRFs, the accelerance FRFs of the modal model constructed from the estimated modal parameters well match the accelerance target FRFs in the full frequency band of interest. Naturally, in this situation, the displacement target FRFs are also well approximated by the displacement FRFs of the modal model defined from the modal parameters estimated with LSFD as can be observed in figures 4.34 and 4.35.

After having optimized the modal parameters of the model composed by the pairs of complex conjugate poles of the stabilized state-space model, we can set-up a stable coupled model (from now on denoted as SSM LSFD) representative of the unstable displacement minimal-order coupled model computed with LM-SSS in section 4.2.3. To define the SSM LSFD model, we must use the model composed by the stable poles of the minimal-order coupled model computed with LM-SSS, the model composed by the real poles of the stabilized model and the complete state-space model computed from the modal parameters refined with LSFD (see, section 3.5). Note that to define a complete state-space model from the modal parameters obtained with LSFD, we have computed sets of RCMs to include the contribution of both lower and upper out-of-band modes. These sets of RCMs were set-up by following the procedures described in section

(a)

(b)
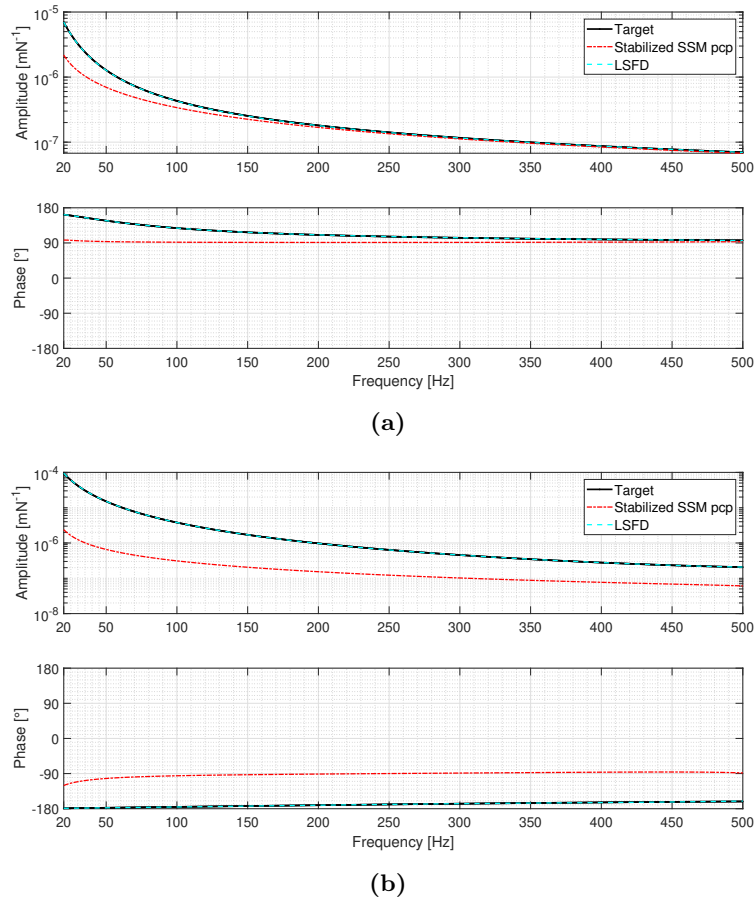
Figure 4.34: Comparison of two displacement target FRFs with: i) the displacement FRFs of
the model containing the pairs of complex conjugate poles of the stabilized state-
space model and ii) with the displacement FRFs of the modal model constructed
from the modal parameters refined with LSFD: a) displacement target FRF,
whose output and input are, respectively, v_1^x and m_2^x; b) displacement target
FRF, whose output and input are, respectively, v_1^z and m_1^z.
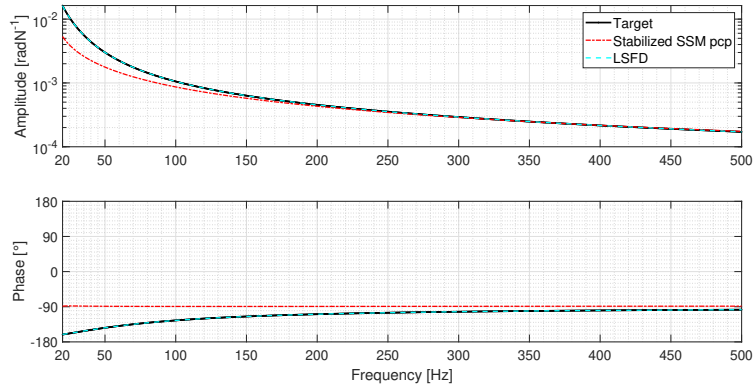
(a)
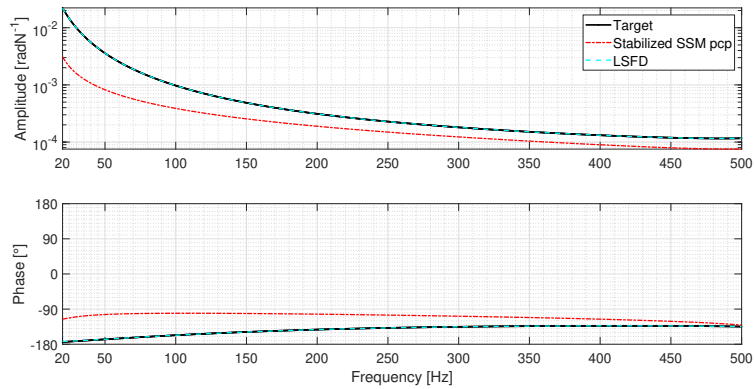
(b)

Figure 4.35: Comparison of two displacement target FRFs with: i) the displacement FRFs of the model containing the pairs of complex conjugate poles of the stabilized state-space model and ii) with the displacement FRFs of the modal model constructed from the modal parameters refined with LSFD: a) displacement target FRF, whose output and input are, respectively, $v_2^{R_z}$ and $m_1^{R_z}$; b) displacement target FRF, whose output and input are, respectively, $v_2^{R_y}$ and $m_2^{R_y}$.

3.2.2 and by selecting $\omega_{LR} = 1 \times 10^{-2}$ Hz, $\omega_{UR} = 7.5 \times 10^4$ Hz and $\xi_{LR} = \xi_{UR} = 1 \times 10^{-1}$. To impose Newton's second law on the SSM LSFD model, a set of RCMs was defined as reported in section 3.3.2. The natural frequencies of these RCMs were selected to be 7.5×10^4 Hz, while their damping ratios were chosen to be 1×10^{-1}. Thereby, leading to the computation of a displacement stable coupled model (denoted SSM LSFD model) composed by 1096 states representative of the unstable displacement minimal-order coupled model computed with LM-SSS.

To assess the accuracy of the defined sets of RCMs, we will compute the set of FRFs that the SSM LSFD model would present if these sets of RCMs were able to perfectly model the contribution of the out-of-band modes estimated with LSFD and to perfectly impose Newton's second law on the SSM LSFD model. This set of FRFs is given by the sum of the displacement FRFs of the model composed by the stable poles of the unstable minimal-order coupled model obtained with LM-SSS, with the displacement FRFs of the model composed by the real poles of the stabilized state-space model and with the displacement FRFs of the modal model constructed from the modal parameters estimated with LSFD (from now on, this set of FRFs will be labelled FRFs LSFD). Figures 4.36 and 4.37 compare some acceleration FRFs computed from the unstable displacement minimal-order coupled model determined with LM-SSS, with the same acceleration FRFs obtained by multiplying the set FRFs LSFD by $-\omega^2$ and with the same acceleration FRFs of the state-space model obtained by double-differentiating SSM LSFD (see expression (2.78)).

Figures 4.36 and 4.37 clearly show that the FRFs of the unstable minimal-order coupled model computed with LM-SSS are very well-matched by the FRFs LSFD. It is also evident that the FRFs of SSM LSFD well match these two sets of FRFs. Nevertheless, at higher frequencies, the FRFs of SSM LSFD plotted in figures 4.36a and 4.37a deviate from the same FRFs of the set FRFs LSFD and of the unstable coupled model. These deviations are triggered by two distinct factors. Firstly, the FRFs of the state-space model defined from the RCMs responsible for modelling the dynamic participation of the upper out-of-band modes (see expression (3.12)) estimated with LSFD do not approximate the elements of the upper residual matrix so closely at higher frequencies (see, section 3.2.2). Secondly, the FRFs of the velocity model constructed from the defined RCMs to force the SSM LSFD model to verify Newton's second law (see, expression (3.41)) do not present zero amplitude. In fact, the amplitude of these FRFs increases with frequency (see section 3.3.2). On top of this, as the FRFs plotted in figures 4.36a and 4.37a present low amplitudes at higher frequencies, small inaccuracies on the performance of the defined sets of RCMs will promote pronounced mismatches between the FRFs of SSM LSFD and of the set FRFs LSFD. The same mismatches are not observed for the FRFs plotted in figures 4.36b and 4.37b, because their amplitude is relevant at higher frequencies.

To mitigate the deviations observed between the acceleration FRFs of SSM LSFD and the acceleration FRFs of FRFs LSFD, we could simply re-compute the RCMs used
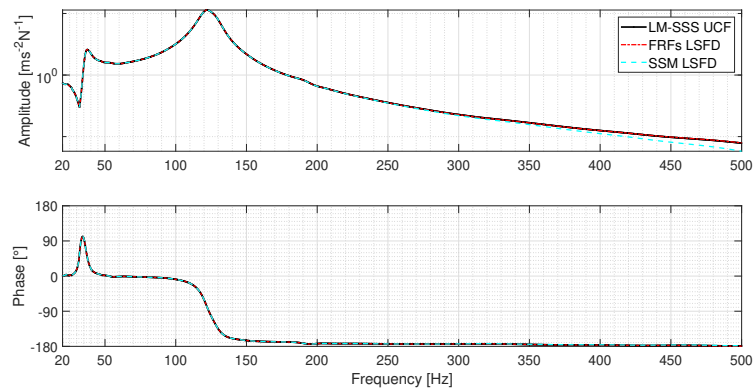
(a)
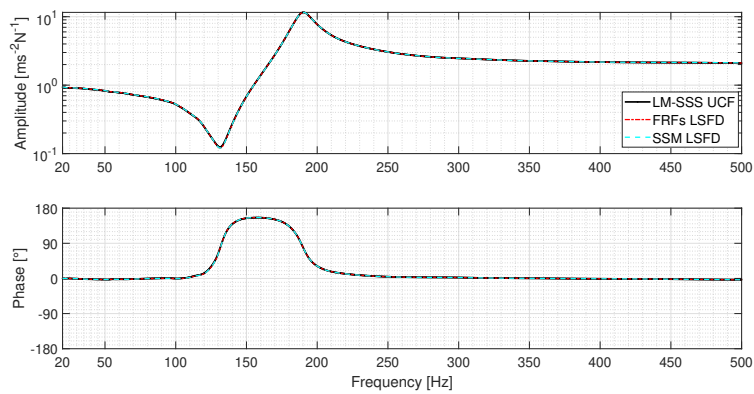
(b)

Figure 4.36: Comparison of two accelerance FRFs computed from the unstable displacement minimal-order coupled model determined with LM-SSS in section 4.2.3 with the same accelerance FRFs of the set FRFs LSFD and with the same accelerance FRFs computed from SSM LSFD: a) FRF of assembly B, whose output and input are v_2^x and m_1^x, respectively; b) FRF of assembly B, whose output and input are v_2^z and m_2^z, respectively.
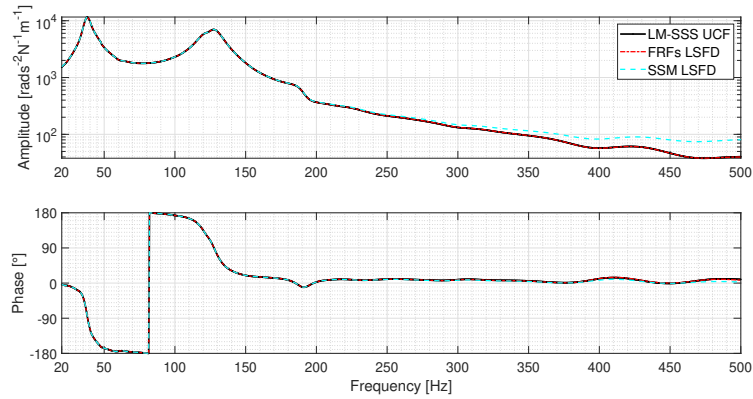
(a)
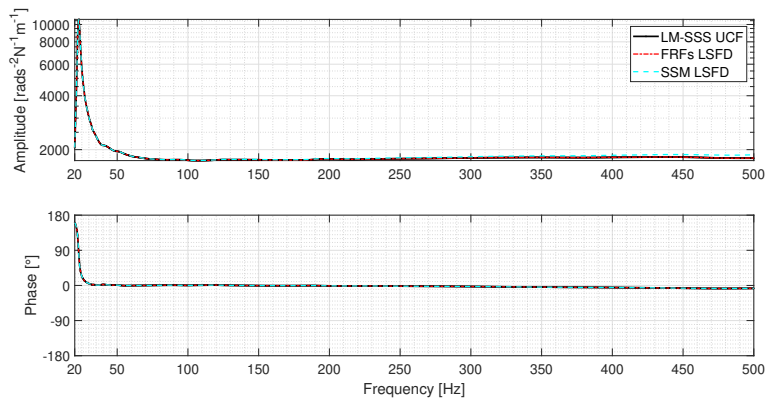
(b)

Figure 4.37: Comparison of two accelerance FRFs computed from the unstable displacement minimal-order coupled model determined with LM-SSS in section 4.2.3 with the same accelerance FRFs of the set FRFs LSFD and with the same accelerance FRFs computed from SSM LSFD: a) FRF of assembly B, whose output and input are $v_1^{R_x}$ and $m_2^{R_x}$, respectively; b) FRF of assembly B, whose output and input are $v_1^{R_z}$ and $m_1^{R_z}$, respectively.

to include the contribution of the upper residual matrix computed by LSFD and to force the SSM LSFD to obey Newton's second law by choosing lower damping ratios or/and by choosing higher natural frequencies (see, sections 3.2.2 and 3.3.2). However, we aim at constructing a stable coupled model representative of the unstable minimal-order coupled model computed with LM-SSS that is adequate for performing time-domain simulations. Thus, these RCMs must not be defined to be undamped or to hold a damping ratio very close to be null, otherwise numerical instabilities might be faced, when performing time-domain simulations with the constructed model [40]. The reconstruction of these RCMs by selecting much higher values for their natural frequencies is also not advised, because to properly discretize the constructed state-space model, we would be demanded to use a significantly higher sampling frequency (see, section 3.2). In this way, to get to an appropriate trade-off between the precision of the constructed SSM LSFD model and its adequacy to be used in time-domain simulations, the RCMs used to set-up SSM LSFD were defined as reported above.

At this point, it is important to demonstrate the benefits of determining a stable coupled model instead of an unstable one. Thereby, a time-domain output simulation will be performed by exploiting the identified state-space model representative of the dynamics of assembly B (see, section 4.2.2), the double-differentiated unstable displacement minimal-order coupled model computed with LM-SSS in section 4.2.3 and the model resultant from the double-differentiation of SSM LSFD. To carry-out this time-domain simulation, we will discretize the three state-space models by using the first-order-hold method (see [93]) and a sampling frequency of 1×10^6 Hz, which is higher than the highest natural frequency of the modes composing the three state-space models to be exploited to perform the intended time-domain simulation (which is 7.5×10^4 Hz). Moreover, the input m_2^z of these discretized models will be fed with a 1 second faded in/out sine sweep signal ranging from 2×10^1 Hz to 5×10^2 Hz to properly excite frequencies included in the frequency band of interest (i.e. between 2×10^1 Hz and 5×10^2 Hz). In figure 4.38, the responses of the outputs v_1^z and v_2^z calculated by using each of the three discretized state-space models are compared.

Analyzing figure 4.38, it is straightforward to conclude that the unstable minimal-order coupled model computed with LM-SSS in section 4.2.3 is not adequate to perform time-domain simulations. To be capable of performing a proper comparison between the output responses computed by using the estimated acceleration model representative of assembly B with the responses simulated with the model resultant from the double-differentiation of SSM LSFD, we have plotted in figure 4.39 the responses of the outputs v_1^z and v_2^z calculated with these models without showing the responses of these ouputs determined with the unstable minimal-order coupled model computed with LM-SSS. Note that the real time-domain response of the assembly B is, unfortunately, not available. Thus, to evaluate the accuracy of the time-domain responses computed with the double-differentiated SSM LSFD model, we will take as reference the time-domain responses simulated with the identified model representative of assembly B.

(a)

(b)
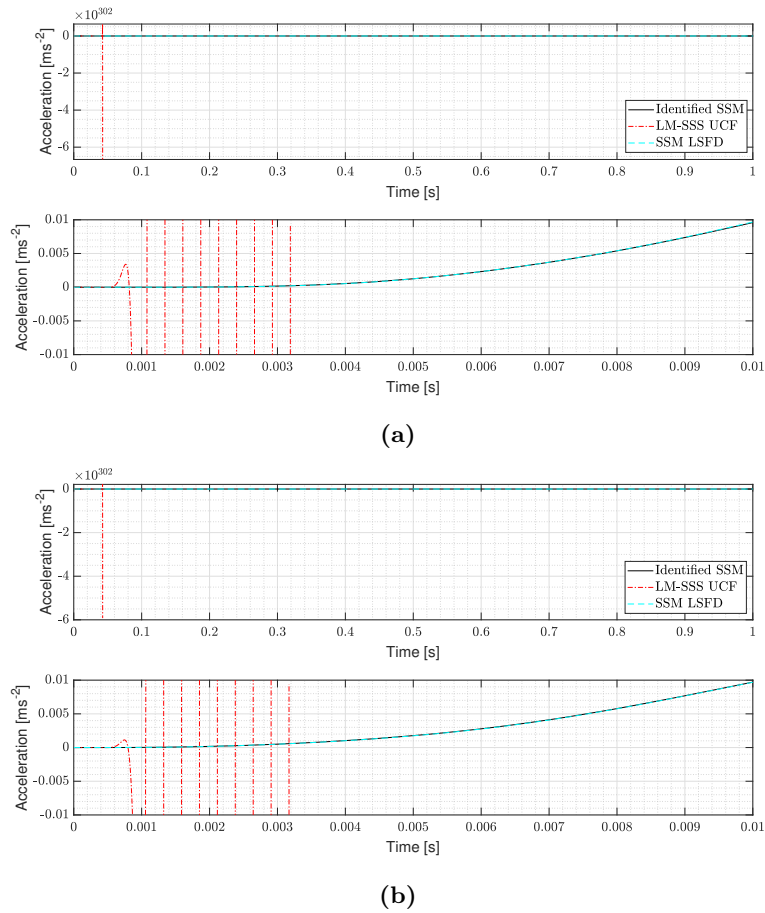
Figure 4.38: Comparison of the time-domain responses of outputs v_1^z and v_2^z computed by exploiting: the acceleration model representative of assembly B estimated in section 4.2.2, by using the double-differentiated unstable displacement minimal-order coupled state-space model computed with LM-SSS in section 4.2.3 and by exploiting the double-differentiated SSM LSFD model: a) Time-domain response of the output v_1^z; b) Time-domain response of the output v_2^z.
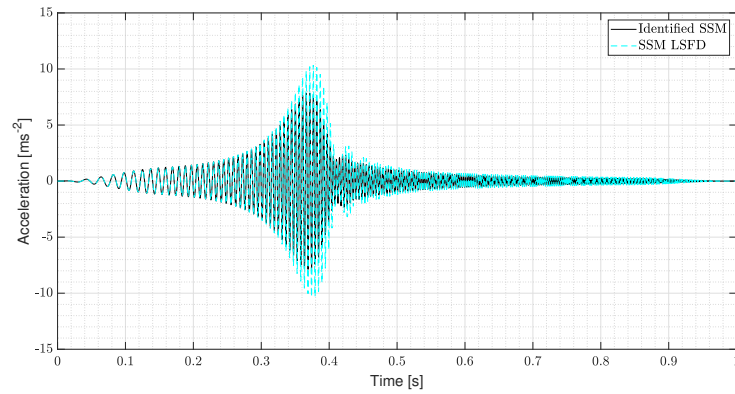
(a)
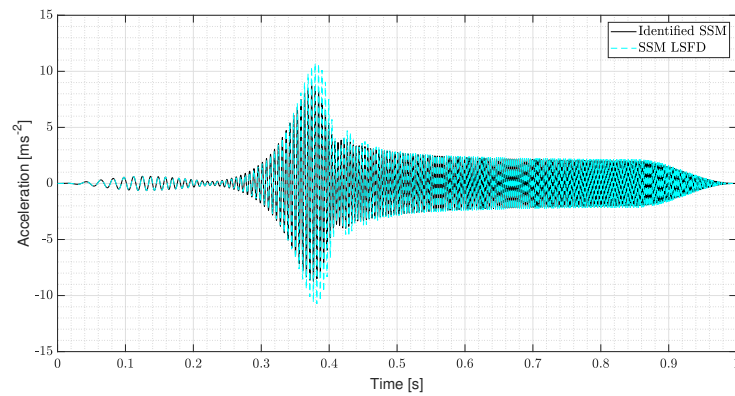
(b)

Figure 4.39: Comparison of the time-domain responses of outputs v_1^z and v_2^z computed by exploiting: the acceleration model representative of assembly B estimated in section 4.2.2 and by using the double-differentiated SSM LSFD model: a) Time-domain response of the output v_1^z; b) Time-domain response of the output v_2^z.

From the analysis of figure 4.39, we can conclude that the model directly estimated from the measured FRFs of assembly B and the SSM LSFD model are stable and adequate to conduct time-domain simulations. Moreover, it is evident that the responses simulated with the estimated state-space model (which are taken as the reference responses) are well-matched by the responses simulated with SSM LSFD. However, it is also visible that SSM LSFD model is clearly overestimating the time-domain responses computed with the identified model of assembly B in the time interval between 0.35 s and 0.4 s. To figure out the reason why SSM LSFD is not simulating so accurately the responses of the system in this time interval, we have plotted in figure 4.40 the accelerance interface FRF of assembly B, whose output and input are $v_2^{\ddot{z}}$ and $m_2^{\ddot{z}}$, respectively, with the same accelerance FRF of the estimated model of assembly B, with the same accelerance FRF computed from the unstable minimal-order coupled model computed with LM-SSS and with the same accelerance FRF of the double-differentiated SSM LSFD model.

Figure 4.40 clearly demonstrates that the interface FRFs of assembly B are very well-matched by the FRFs of the unstable coupled model computed with LM-SSS and by the FRFs of the double-differentiated SSM LSFD model. Nevertheless, for frequencies surrounding the resonance of this FRF, i.e. in between, approximately, 1.80×10^2 Hz and 2.10×10^2 Hz, we can clearly observe that the interface FRF of the coupled models presents higher amplitude than the corresponding interface FRF of assembly B. Yet, the interface FRF of the estimated model does not overestimate this interface FRF of assembly B. Interestingly, in the time interval corresponding to the observed mismatches between the responses computed with the identified model of assembly B and the double-differentiated SSM LSFD model, the frequencies being excited are included in the frequency interval for which the SSM LSFD model overeestimates the interface FRF of assembly B (see Figure 4.39b). Thereby, it is evident that SSM LSFD overestimates the time-domain responses obtained with the identified model of assembly B, because of the deviations observed between the interface FRFs of assembly B and of the unstable minimal-order coupled model computed with LM-SSS. In this way, we may conclude that the methodology discussed in section 3.5 is robust enough to determine high quality stable coupled state-space models from unstable displacement coupled models resultant from many DS operations performed with models estimated from measured FRFs.

Unfortunately, as accurate passive models could not be computed from the identified models (see section 4.2.2), it was not possible to perform a comparison between the exactness of the stable coupled models computed by performing DS operations with passive models and by exploiting the methodology presented in section 3.5. However, it continuous to be possible to perform a well-argued prediction of the exactness of the stable coupled model (obtained by using passive models) that could have been computed, in case that accurate passive models could have been set-up from the models estimated in section 4.2.2. To perform this prediction, we must have in mind that
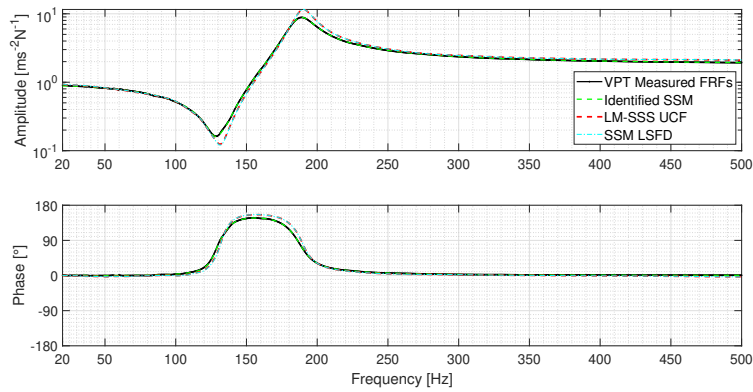
Figure 4.40: Comparison of the accelerance interface FRF of assembly B, whose output and input are, respectively, v_1^z and m_1^z, with: the same accelerance FRF of the estimated state-space model representative of assembly B (see section 4.2.2), with the same accelerance FRF determined from the unstable displacement minimal-order coupled state-space model obtained with LM-SSS in section 4.2.2 and with the same accelerance FRF of the double-differentiated SSM LSFD model.

passivity is generally imposed on velocity state-space models by forcing them to obey different passivity criteria (such as, the Positive Real Lemma (see [77])). In addition, the methods reported in literature to impose passivity on state-space models make use of constraints to compute passive models, whose velocity FRFs match as closely as possible the FRFs of the originally non passive models (see, for instance [78]). Therefore, if the best passive models could be computed, they would present the same FRFs as the original non passive model. Yet, in practice the FRFs of the passive model will not perfectly match the FRFs of the original non passive model, at least small mismatches between both sets of FRFs will always be observed.

Moreover, the methods reported in literature to force state-space models to be passive do not make use of any constraint to ensure that the determined passive model verifies Newton's second law. Thereby, the passive models computed by exploiting these methods are expected to violate Newton's second law. For this reason, RCMs to force the computed passive models to obey this physical law would have to be set-up and introduced into these models. Despite the introduction of these RCMs on the passive models, the computation of stable coupled models by performing DS operations with passive models will in general continue to lead to the computation of stable models composed by a lower number of states than the models that would be computed by using the methodology discussed in section 3.5. Thus, this is definitely a benefit of performing DS operations with passive models in place of using the methodology presented in section 3.5. Nonetheless, hinging on how many DS operations are made at the same interface DOFs, on how many substructures are involved on those operations and on how many internal DOFs each model presents, the stable coupled models resultant from the performance of DS operations with passive models may be made of a number of states equal or even higher than the stable coupled models obtained by exploiting the

approach discussed in section 3.5. For the experimental substructuring case analyzed in this section, to force the passive models representative of each aluminum and steel crosses to verify Newton's second law, we would be required to introduce 12 extra states, whereas to force the passive model of assembly A to obey Newton's second law, 24 additional states would have to be introduced on this model (see section 3.3.2). Thus, the stable coupled model that would be computed by performing DS operations with passive models would present the same number of states as the SSM LSFD model, here determined by following the methodology presented in section 3.5.

On top of this, the stable coupled model computed by performing DS operations with passive models is very likely to present less accuracy than the SSM LSFD model. First of all, the passive models will in general be less accurate than the original non-passive models. Secondly, the used RCMs to force the passive models to verify Newton's second law might promote an additional loss on the accuracy of these models (see, section 3.3.2). Thirdly, it is very likely that by implementing DS operations with the defined passive models, we get to stable coupled models, whose FRFs present more significant deviations from the unstable coupled model than the deviations observed between the FRFs of the passive models and the respective original non passive models. Therefore, we may conclude that the determination of stable coupled models from passive state-space models involves the performance of three procedures that degradate the correctness of the coupling results (i.e. forcing models to obey passivity, imposing Newton's second law on the passive models and the implementation of DS operations). The degradation of accuracy associated with forcing the passive models to verify Newton's second law can be easily attenuated by increasing the selected value for the natural frequencies of the RCMs responsible for imposing this physical law. Yet, the degradation of accuracy associated with the other two procedures cannot be attenuated. In contrast, the method discussed in section 3.5 to determine stable coupled models involves the performance of only two procedures that foster the deterioration of the accuracy of the coupled results. These procedures are the application of LSFD to make the FRFs of the model composed by the pairs of complex conjugate poles of the stabilized model to match as closely as possible the target FRFs and the exploitation of sets of RCMs to introduce the contribution of the out-of-band modes estimated by LSFD and to force the complete stable coupled model to obey Newton's second law. The deterioration of the accuracy of the coupled results due to the application of these two procedures can be easily reduced. Indeed, the loss of accuracy associated with the use of LSFD can be attenuated by further improving the quality of the estimated modal parameters by exploiting ML-MM algorithm (see, for instance, [74]). The loss of accuracy resultant from the use of RCMs to define the complete stable coupled state-space model can also be simply attenuated by tuning the value selected for their natural frequencies (see, sections 3.2.2 and 3.3.2). The benefit of computing stable coupled state-space models from passive models is that, it leads, in general, to the computation of a coupled model that is passive as well (see [4]). Thereby, this coupled model would be more physically

consistent than the SSM LSFD model, which violates passivity. However, it is quite common in practice to describe the dynamics of real structures by making use of non passive models. As an example, we may think on the FRFs collected during the performance of experimental modal characterization tests that are often not passive due, for instance, to slight inaccuracies in the test set-up.

Having in mind the reasons elaborated above, the stable coupled models defined by exploiting the methodology presented in section 3.5 are likely to be more accurate than the stable coupled models obtained by performing DS operations with models imposed to be passive. On top of this, the approach discussed in section 3.5 presents some practical benefits, when compared with the computation of stable coupled models by exploiting state-space models forced to be passive. To start, the methodology presented in section 3.5 demonstrated to be capable of determining accurate stable coupled models originated from the performance of DS operations involving models composed by a high number of states without making use of iterative algorithms. In addition, this approach must be applied on displacement models, while the strategies exploited to enforce passivity take, in general, action over velocity models. In this way, in case that we aim at determining a displacement stable coupled model, we are forced to follow one of two different strategies. On the one hand, we can obtain the displacement coupled model directly from the velocity coupled model (see, expression (3.45)) determined by performing DS operations with passive velocity models representative of the components. On the other hand, we may think on determining the intended displacement coupled model by using the displacement models of the components directly obtained from the respective passive velocity state-space models. Nevertheless, these two strategies hold the drawback of demanding the performance of matrix inversions to compute displacement models from the velocity ones. On top of this, to compute stable coupled models, we are solely demanded to apply the methodology presented in section 3.5 on the unstable state-space model originated from all the implemented DS operations. This benefit is more significant for DS operations involving a higher number of state-space models.

Chapter 5

Novel applications of LPV models in TPA

5.1 Introduction

In this section, we will focus our attention on the TPA techniques commonly clustered under the labels classical and component-based. Due to their wide popularity, the matrix-inverse and the in-situ methods of the classical and component-based TPA methods (see, for instance, [94]), respectively, will be the analyzed techniques. In particular, we aim at using these methods to tackle applications in time-domain involving mechanical systems, whose dynamics is continuously changing over time.

The performance of TPA analysis in time-domain is, indeed, advantageous to deal with applications involving transient phenomena, for example, to perform the characterization of injector noise and to perform ride comfort analysis while driving over bumps. There are many methods available in literature that can be used to compute connecting and equivalent forces in time-domain (see, for example, [95], [96], [97]). Nonetheless, the determination of time-domain forces in the context of applications involving mechanical systems, whose dynamics changes continuously over time, has received little attention. Yet, there are many structures made of components, whose dynamic behaviour may present time-variations due to different external factors (for example, rubber mounts, whose dynamics is dependent on temperature, on the applied static pre-load, etc [33]).

Therefore, to tackle this kind of applications, we will propose the use of the state-space formulation. In fact, the use of state-space models to deal with these problems seems promising, because these models are specially targeted to deal with problems posed in time-domain. Moreover, there are many approaches reported in literature based on the state-space formulation that are capable of characterizing systems presenting time-domain variations on their dynamics. On top of this, the state-space models are also known to be very well suited to perform real-time simulations.

Thereby, in this section we aim at proposing an approach to compute time-domain

connecting and equivalent forces by using the matrix-inverse classical TPA and the in-situ component-based TPA methods, respectively, when dealing with mechanical systems, whose dynamic behaviour is time-dependent. As first step, this approach makes use of local interpolating LPV models (see, for instance, [83]) to characterize the dynamics of the substructures at each time-sample. Then, if the component-based TPA method is to be exploited, the use of LM-SSS enhanced by post-processing procedures (see sections 2.2.3 and 2.3) is proposed, in case that one is interested on coupling at each time sample the state-space models of the substructures to compute models representative of the dynamics of the assemblies at each time-sample (for example, in case that the experimental modal characterization of the assembled structure is not convenient to be performed). Finally, the time-domain connecting forces of the assemblies and the time-domain equivalent forces of the sources are computed by exploiting, respectively, the state-space realizations of the matrix-inverse classical TPA and of the in-situ component-based TPA methods.

In the following, we will start by presenting in section 5.2 the strategy that will be here used to construct interpolating LPV models. In the same section, this methodology is numerically and experimentally validated. Then, in section 5.3, the state-space realizations of the matrix-inverse classical TPA and of the in-situ component-based TPA methods are presented. Finally, in section 5.4 a numerical case is analyzed to validate the use of the state-space realization of the matrix-inverse classical TPA and of the in-situ component-based TPA methods together with LPV models to compute time-domain connecting and equivalent forces, respectively, when dealing with mechanical systems presenting time-varying dynamics.

5.2   Linear Parameter-Varying models

During the last decades, the Linear Parameter-Varying (LPV) models have received significant attention. These models are used to characterize systems, whose dynamic behaviour is dependent on a single or multiple time-varying parameters, commonly denominated as scheduling parameters [83]. Indeed, the LPV models have been successfully exploited to characterize real systems, whose dynamics is dependent on the value of one or more scheduling parameters, in several different areas [98], for instance, in automotive and aerospace applications (see [99] and [100], respectively), to model computing systems (see [101]), to characterize mechatronic systems (see [102]) and to model thermal and fluid processes (see [103] and [104], respectively).

However, the use of LPV models in structural dynamics applications is not common. Yet, many structural dynamics applications involving the characterization of mechanical components presenting time-varying dynamic behaviour would benefit from the exploitation of LPV models. Actually, there are several mechanical structures that when operating under normal conditions promote significant changes on the dynamics of some of their components. An example of these components are the rubber mounts,

whose dynamics is known to depend on several external factors, e.g. on the applied static pre-load and on the temperature at which they are submitted (see [105], [106], [33]). In this way, LPV models can be exploited to either characterize the time-varying behaviour of complete assemblies or to characterize the time-varying dynamic behaviour of isolated components, whose time-varying dynamics can be, subsequently, embedded on the complete assembly by exploiting SSS techniques (see, for instance, [8], [1], [3], [2]).

The methodologies presented in literature to construct LPV models are usually divided in two main classes: the class of the global approaches and the class of the local approaches [83]. In the global methodologies, the LPV models are constructed from data collected during the excitation of the target systems, while the value of the scheduling parameters characterizing their dynamics is continuously changing (see, for instance, [107], [108]). In contrast, the local methodologies rely on experimentally characterizing the dynamics of the target structure submitted to a pre-selected set of different fixed operating conditions associated with constant values of the scheduling parameters. Subsequently, by using the data collected from these experimental tests, a set of Linear Time-Invariant (LTI) state-space models can be estimated. These LTI models are then, interpolated to compute state-space models representative of the dynamics of the target structure for intermediate operating conditions characterized by values of the scheduling parameters in between the values of the scheduling parameters associated with the estimated LTI models (see, for instance, [109], [85]). This interpolation is implemented through an interpolating LPV model defined from the computed LTI models.

The global approaches hold the disadvantage of not being able to characterize the time-varying dynamic behaviour of mechanical systems that cannot be persistently excited, while their dynamics is continuously changing (see, for instance the vibro-acoustic system studied in [110] and the flight applications tackled in [111]). Conversely, in the local approaches the LPV model is defined by using LTI models identified from data collected during the experimental modal characterization of the target structure submitted to pre-selected fixed operating conditions. Thus, well-known system identification algorithms (see section 3) can be used to determine the intended LTI models. Moreover, these approaches hold the advantage of being able to interpolate either continuous or discrete state-space models.

Nevertheless, the local approaches present the important disadvantage of not including information regarding the variation of the scheduling parameters characterizing the dynamics of the target structures, because these approaches construct interpolating LPV models by using LTI models representative of the dynamics of the target structures for fixed operating conditions. For this reason, the computed LPV models are less suited to characterize mechanical components, whose dynamics change significantly with the value of the scheduling parameters and/or in case that the values of these scheduling parameters exhibit fast time-variations. On top of this, the local methodologies are only

applicable to analyze structures that can be tested, while the values of the scheduling parameters characterizing their dynamics is kept constant. Although, there are several structures that can be experimentally characterized in this fashion, there are some applications involving the characterization of structures, whose dynamics is governed by scheduling parameters presenting persist time-variations on their values. To deal with this kind of applications, one must exploit the global methodologies. Even though the local approaches present some disadvantages, many structural dynamics applications involving the characterization of components presenting time-varying dynamics can be tackled by exploiting these approaches. For this reason, in this section we will focus our attention on the construction of LPV models by using local approaches.

To estimate state-space models from experimentally acquired data, it is common to exploit system identification algorithms (see section 3.1). However, by computing state-space models with these algorithms, it is usual to end-up with state-space models that are not represented with respect to the same unique state-space realization. Thus, to properly interpolate a set of estimated LTI state-space models, we must start by coherently represent these models with respect to the same state-space realization. Several different approaches to coherently represent sets of identified LTI models have been reported in literature. For instance, in [112], a set of estimated SISO LTI models is made coherent by transforming each of the estimated state-space models into controllable form, while in [84], the computation of similarity transformation matrices from the observability and controllability matrices of identified LTI models is suggested to transform these models into the same coherent state-space realization. However, by following these approaches we may run into numerical ill-conditioned problems, because both observability and controllability matrices are known to be ill-conditioned for medium and high-order state-space models [113]. Another proposed approach to make a set of state-space models coherent can be found in [114]. This procedure relies on the transformation of LTI state-space models identified by exploiting subspace algorithms (see, for example, [59], [57]) into internally balanced realizations (see, for example, [115], [116]). Nevertheless, the internally balanced realization is not unique, which may lead to problems during the interpolation of the identified LTI models (see, [83], [102]). Furthermore, the transformation of each of the identified LTI models into the internally balanced realization is based on the correspondent controllability and observability Gramians (see, [115], [116]) hence, these models must be observable and controllable. In [83], a set of SISO LTI models is made coherent by representing each of the estimated LTI models as a series connection of low-order sub-models. This technique was then, generalized in [102] to deal with MIMO LTI state-space models. Nonetheless, the approaches proposed in [83] and [102] hold the important disadvantage of requiring a manual sorting of the poles and zeros of each LTI model. Thereby, demanding experience, intuition and interaction from the user.

More recently, in [117], [118], [119], it was discussed and proven that a given set of estimated LTI state-space models does not contain sufficient information to define

similarity transformations capable of making them coherent. For this reason, we are left with two different strategies to make a given set of LTI models coherent. The first strategy is to assume particular global structural assumptions for the state-space matrices of the estimated LTI models. For instance, by transforming the LTI models into a state-space realization for which some elements of the state, input or output matrices of all the LTI models are equal (e.g. by transforming them into the controllable canonical form, see [118]). As second strategy, one may compute a set of coherent state-space models by exploiting adequate input-output data sequences. These data sequences must include time instants for which the target structure is submitted to several jumps between the fixed operating conditions associated with the estimated LTI models. From these data sequences, similarity matrices that enable the transformation of the identified LTI models into the same unique state-space representation can be computed. This strategy was firstly introduced in the framework of piecewise linear systems in [120], while variants of this method in the context of local LPV model identification can be found in [117], [85].

After having computed a coherent set of LTI models, the state-space matrices of these models can be directly interpolated by performing for instance, a linear interpolation of each of their elements (see [121]). Alternatively, one can exploit the coherently represented set of LTI models to compute an interpolating LPV model. A possible approach to define a LPV model is to represent each element of each state-space matrix as a sum of unknown variables multiplied by shape functions dependent on the correspondent values of the scheduling parameters. Polynomial and sinusoidal functions are examples of types of shape functions that can be used to define LPV models (see [121]). The unknown variables of the defined LPV model can then be determined by fitting in a linear least-squares sense the state-space matrices associated with the selected fixed operating conditions (expressed as a sum of the unknown variables multiplied by the shape functions) with the estimated LTI models. Yet, other approaches to construct interpolating LPV models have been presented in literature. For example, the computation of affine LPV models, whose associated unknown variables are determined by solving a nonlinear least-squares problem, is proposed in [83].

Here, to coherently represent a given set of estimated LTI state-space models, we will start by transforming each of the LTI state-space models into complex diagonal form. Thereby, transforming the state matrix of each of these LTI models into a diagonal matrix composed by its poles (see, for instance, [39]). Then, the poles of each LTI model will be sorted in terms of ascending damped natural frequency. In this way, the poles can be automatically sorted without requiring interaction from the user. Finally, to obtain a coherent representation of the set of identified models, a global structural assumption will be performed.

Here, the LPV models will be defined by exploiting the approach presented in [102]. This approach defines LPV models by assuming that they present an homogeneous polynomial dependency on the parameterized values of the scheduling parameters in

a multisimplex Λ. By following this methodology, the unknown variables associated with the LPV modeld under computation are found by solving a linear least-squares problem.

The strategy exploited in this document to compute interpolating LPV models is presented in section 5.2.1. Afterwards, in sections 5.2.2 and 5.2.3, the presented approach to compute LPV models is numerically and experimentally validated, respectively.

5.2.1 Constructing Linear Parameter-Varying models

In this section, a local approach to compute LPV models will be discussed. The construction of LPV models by using local approaches can be divided into three different steps. As first step, we must identify a set of LTI state-space models that accurately characterize the dynamics of the mechanical system under analysis, when submitted to different pre-selected fixed operating conditions. Then, we must guarantee that the identified set of estimated states-space models is coherently represented. Finally, we must construct an interpolating LPV model by using the identified coherent set of state-space models. Here, the construction of LPV models will be presented by exploiting displacement LTI state-space models. Indeed, the use of displacement state-space models is beneficial, because the feedthrough matrices of these models are by definition null. Thus, by using displacement models, we have the possibility to decrease the amount of variables to be calculated in order to define the LPV models. Hence, reducing not only the computational cost associated with the construction of the LPV models, but also the computational cost associated with the use of the constructed LPV models to calculate interpolated state-space models.

To start, we must discuss how to properly select the fixed operating conditions for which LTI models must be identified. There are no rigorous procedures to select fixed operating conditions that enable the computation of a set of LTI models suitable to define an accurate LPV model. However, there are some guidelines that one must follow to properly select these fixed operating conditions. As first guideline, the selected fixed operating conditions must ensure that there is no need of performing extrapolation. This means that if the value of a given scheduling parameter ranges from a minimum value of $\underline{\beta}$ to a maximum value of $\hat{\beta}$, we must select one fixed operating condition associated with a value of that scheduling parameter slightly lower or equal to $\underline{\beta}$ and another one associated with a value of that scheduling parameter slightly higher or equal to $\hat{\beta}$. It is also recommended to select fixed operating conditions associated with equidistant values of the scheduling parameters. Furthermore, the number of selected fixed operating conditions must be large enough to well capture the influence of the scheduling parameters over the dynamics of the system under analysis. Additionally, we must ensure that between consecutive fixed operating conditions, the dynamics of the system under analysis do not change abruptly. At same time, the number of

selected fixed operating conditions must be as small as possible to decrease the number of LTI models to be estimated (see [102]). This is specially important to reduce the number of experimental tests required to be performed, when each of the LTI state-space models is estimated from the experimental modal characterization of the target structure submitted to the associated fixed operating condition.

After having selected the fixed operating conditions, LTI state-space models representative of the dynamics of the target structure submitted to those conditions must be estimated. If these LTI models are analytically computed from the mechanical properties of the mechanical system under analysis, they will represent a coherent set of state-space models. Nonetheless, when the state-space models are to be identified from experimentally acquired data, we are generally required to exploit system identification algorithms (see section 3.1) to compute them. By computing state-space models by using system identification algorithms, it is common to end-up with state-space models that are not represented with respect to the same unique state-space realization. To coherently represent the identified set of state-space models, we may start by transforming each of the estimated state-space models into complex diagonal form as follows (see, section 3.5):

$$\{\dot{x}_{cdf}^i(t)\} = [A_{cdf}^i]\{x_{cdf}^i(t)\} + [B_{cdf}^i]\{u_{cdf}^i(t)\}$$
$$\{y_{cdf}^i(t)\} = [C_{cdf}^{i,disp}]\{x_{cdf}^i(t)\}$$

(5.1)

where,

$$[A_{cdf}^i] = [\Lambda^i] = [T_{cdf}^i]^{-1}[A^i][T_{cdf}^i], \quad [B_{cdf}^i] = [T_{cdf}^i]^{-1}[B^i]$$
$$[C_{cdf}^{i,disp}] = [C^{i,disp}][T_{cdf}^i]$$

(5.2)

while, superscript i denotes variables/vectors/matrices associated with the estimated state-space model representative of the system under study submitted to the ith fixed operating condition, $[\Lambda^i]$ is a diagonal matrix including the eigenvalues of $[A^i]$ (which are also the poles of the state-space model [39]) and matrix $[T_{cdf}^i]$ is a modal matrix composed by the eigenvectors of $[A^i]$ that can be calculated by solving the eigenvalue problem given hereafter.

$$[A^i][T_{cdf}^i] = [T_{cdf}^i][\Lambda^i].$$

(5.3)

With the identified state-space models represented in complex diagonal form, we have the possibility of coherently sort their poles. Thereby, the poles of each state-space model will be sorted in ascending damped natural frequency to take into account the values of their natural frequencies and damping ratios. The damped natural frequency of a given pole can be calculated as follows:

$$\omega_{d,r} = \omega_{n,r}\sqrt{1 - (\xi_{n,r})^2}$$

(5.4)

where, $\omega_{d,r}$ and $\omega_{n,r}$ denote, respectively, the damped natural frequency and the natural frequency of the rth pole, whereas $\xi_{n,r}$ represents the damping ratio of the rth pole. It is worth mentioning that, when sorting pairs of complex conjugate poles, ties in terms of the value of their damped natural frequencies are broken by firstly placing the pole, whose imaginary part is positive, and by placing subsequently the pole, whose imaginary part is negative. Obviously, when sorting each of the poles of each of the estimated state-space models, the associated row of the input matrix and the associated column of the output matrix must be sorted accordingly.

However, as the representation of a given state-space model in complex diagonal form is not unique with respect to the scaling of both output and input matrices, to compute the intended set of coherent state-space models, we also have to coherently scale both input and output matrices of each of the estimated state-space models (see [121], [84]). These matrices can be coherently scaled in accordance with the following expressions:

$$[B^i_{cdf,sc}] = [\Theta^i]^{-1}[B^i_{cdf}] \tag{5.5}$$

$$[C^{i,disp}_{cdf,sc}] = [C^{i,disp}_{cdf}][\Theta^i] \tag{5.6}$$

where, subscript sc denotes a coherently scaled state-space matrix, whereas $[\Theta]$ represents the scaling matrix responsible for scaling both input and output matrices of a given state-space model. To coherently scale the input and output matrices of each of the estimated state-space models, we may, for example, normalize each row of $[B^i_{cdf}]$ with respect to one of its elements [121]. Therefore, by presuming that the normalization of each row of $[B^i_{cdf}]$ is to be performed with respect to its first element, $[\Theta^i]$ must be defined as hereafter:

$$[\Theta^i] = \begin{bmatrix} B^i_{11,cdf} & & \\ & B^i_{21,cdf} & \\ & & \ddots \end{bmatrix} \tag{5.7}$$

where, the first and second subscripts represent, respectively, the number of the row and column associated with the element of $[B^i_{cdf}]$. Note that by scaling both input and output matrices of a given state-space model in accordance with expressions (5.5) and (5.6) and by exploiting the diagonal scaling matrix defined in expression (5.7), the input-output properties of the state-space model remain unaltered. To prove this statement, let us compute the FRFs of the coherently scaled model associated with the fixed operating condition i as hereafter.

$$
\begin{aligned}
[H^i_{cdf,sc}(j\omega)] &= [C^{i,disp}_{cdf}][\Theta^i](j\omega[I] - [\Lambda^i])^{-1}[\Theta^i]^{-1}[B^i_{cdf}] \\
&= [C^{i,disp}_{cdf}](j\omega[I] - [\Lambda^i])^{-1}[B^i_{cdf}]
\end{aligned}
\tag{5.8}
$$

By analyzing equation (5.8) and by remembering that $[\Theta^i]$ and $[\Lambda^i]$ are diagonal matrices, it is clear that by scaling the input and output matrices of the estimated LTI models in accordance with expressions (5.5) and (5.6), respectively, the input-output properties of the LTI state-space models are not perturbed.

At the end of this scaling process, we obtain a coherent representation of the set of estimated state-space models. Thus, we can now exploit this coherent set of models to compute an interpolating LPV model. The computation of this LPV model will be performed by following the methodology proposed in [102]. Moreover, for the sake of simplicity, we will assume that the dynamics of the target system depends on a single scheduling parameter. Nevertheless, the approach presented in [102] continues to be valid to compute LPV models representative of systems, whose dynamics depends on multiple scheduling parameters.

The methodology presented in [102] presumes that the interpolating LPV model to be set-up presents an homogeneous polynomial dependency on the parameterized values of the scheduling parameter in a multisimplex Λ. Therefore, as first step to implement this approach, we must define the dimension of the multisimplex Λ in which the values of the scheduling parameter will be parameterized. Here, the dimension of the multisimplex Λ will be selected to be $\Xi = 2$, which is a commonly chosen dimension (see [102]). In this way, it is possible to parameterize the value of a given scheduling parameter β associated with a given fixed operating condition l as hereafter.

$$
\Delta_{\beta,1} = \frac{\beta^l - \underline{\beta}}{\hat{\beta} - \underline{\beta}}, \quad \Delta_{\beta,2} = 1 - \Delta_{\beta,1}
\tag{5.9}
$$

By using the parameterized values of the scheduling parameter, we may represent the interpolated state-space matrices associated with the fixed operating condition l computed by exploiting the LPV model under construction as follows:

$$diag[A(\alpha^l)] = \sum_{a=1}^{J_\Xi(\chi)} \alpha_a^l \{\breve{A}^a\} \qquad (5.10a)$$

$$[B(\alpha^l)] = \sum_{a=1}^{J_\Xi(\chi)} \alpha_a^l [\breve{B}^a] \qquad (5.10b)$$

$$[C^{disp}(\alpha^l)] = \sum_{a=1}^{J_\Xi(\chi)} \alpha_a^l [\breve{C}^a] \qquad (5.10c)$$

where, $diag[\bullet]$ is a column vector containing the diagonal elements of matrix $[\bullet]$, whereas α_a^l represents the element placed on the ath column of $\{\alpha^l\}$, which can be defined as follows:

$$\{\alpha^l\} = \begin{bmatrix} \Delta_{\beta,1}^\chi \Delta_{\beta,2}^0 & \Delta_{\beta,1}^{\chi-1}\Delta_{\beta,2}^1 & \dots & \Delta_{\beta,1}^0\Delta_{\beta,2}^\chi \end{bmatrix} \qquad (5.11)$$

where, χ denotes the degree of the homogeneous polynomial dependency of the LPV model under construction on the parameterized value of the scheduling parameter in a multisimplex Λ (see equation (5.9)). The number of columns of the vector $\{\alpha^l\}$ is represented by variable $J_\Xi(\chi)$, whose value can be calculated as hereafter.

$$J_\Xi(\chi) = \frac{(\Xi + \chi - 1)!}{\chi!(\Xi - 1)!} \qquad (5.12)$$

To define the interpolating LPV model, we must determine the unknown vectors $\{\breve{A}^a\} \in \mathbb{C}^{n \times 1}$ and the unknown matrices $[\breve{B}^a] \in \mathbb{C}^{n \times n_i}$ and $[\breve{C}^a] \in \mathbb{C}^{n_o \times n}$ (see expression (5.10)). To calculate these vectors/matrices, we must formulate a linear-least squares problem by defining expression (5.10) for the selected fixed operating conditions and by using the state-space matrices of the estimated LTI models. This linear-least squares problem can be established as follows:

$$[a]\{p\} = \{b\} \qquad (5.13)$$

with,

$$[a] = \begin{bmatrix} \alpha^1 \otimes I_{A,A} \\ \vdots \\ \alpha^m \otimes I_{A,A} \\ & \alpha^1 \otimes I_{B,B} \\ & \vdots \\ & \alpha^m \otimes I_{B,B} \\ & & \alpha^1 \otimes I_{C,C} \\ & & \vdots \\ & & \alpha^m \otimes I_{C,C} \end{bmatrix} \qquad (5.14a)$$

$$\{p\} = \left\{ \{p_A\}^T \quad \{p_B\}^T \quad \{p_C\}^T \right\}^T \qquad (5.14b)$$

$$\{b\} = \left\{ \{b_A\}^T \quad \{b_B\}^T \quad \{b_C\}^T \right\}^T \qquad (5.14c)$$

while,

$$\{p_A\} = \left\{ \{\breve{A}^1\}^T \quad \dots \quad \{\breve{A}^{J_{\equiv}(\chi)}\}^T \right\}^T$$

$$\{p_B\} = \left\{ (vec[\breve{B}^1])^T \quad \dots \quad (vec[\breve{B}^{J_{\equiv}(\chi)}])^T \right\}^T$$

$$\{p_C\} = \left\{ (vec[\breve{C}^1])^T \quad \dots \quad (vec[\breve{C}^{J_{\equiv}(\chi)}])^T \right\}^T$$

$$\{b_A\} = \left\{ (diag[A^1_{cdf}])^T \quad \dots \quad (diag[A^m_{cdf}])^T \right\}^T \qquad (5.15)$$

$$\{b_B\} = \left\{ (vec[B^1_{cdf,sc}])^T \quad \dots \quad (vec[B^m_{cdf,sc}])^T \right\}^T$$

$$\{b_C\} = \left\{ (vec[C^{1,disp}_{cdf,sc}])^T \quad \dots \quad (vec[C^{m,disp}_{cdf,sc}])^T \right\}^T$$

where, $\otimes$ denotes the Kronecker matrix product (see, for instance, [122]), $[I_{A,A}] \in R^{n \times n}$, $[I_{B,B}] \in R^{(n \times n_i) \times (n \times n_i)}$ and $[I_{C,C}] \in R^{(n \times n_o) \times (n \times n_o)}$ are identity matrices, $vec[\bullet]$ is the vector obtained by stacking all columns of matrix $[\bullet]$ and m is the number of state-space models included in the set of estimated state-space models. It is worth mentioning that in expression (5.10) and in the construction of $\{b\}$ (see expression (5.15)) we have only considered the diagonal elements of the state matrices of the estimated LTI models, because these models were transformed into complex diagonal form and hence, present diagonal state matrices. In fact, constructing LPV models by exploiting LTI state-space models transformed into complex diagonal form is advantageous, because instead of being required to define the LPV model by determining unknown matrices composed by n^2 elements to calculate the state matrices of the interpolated models, we

are only required to determine unknown vectors composed by n elements (see expression (5.10a)). Thereby, we have the possibility of reducing the computational cost associated with the computation of the LPV models and with the computation of interpolated state-space models by using the defined LPV models.

By observing expression (5.13), it is evident that the unknown vector $\{q\}$ can be determined in a linear least-squares sense as follows:

$$\{p\} = [a]^{\dagger}\{b\} \tag{5.16}$$

the error vector associated with the determination of $\{q\}$ is given hereafter.

$$\{E(p)\} = \begin{bmatrix} diag[A_{cdf}^1] - \sum_{a=1}^{J_\Xi(\chi)} \alpha_a^1 \{\breve{A}^a\} \\ \vdots \\ diag[A_{cdf}^m] - \sum_{a=1}^{J_\Xi(\chi)} \alpha_a^m \{\breve{A}^a\} \\ vec[B_{cdf,sc}^1] - \sum_{a=1}^{J_\Xi(\chi)} \alpha_a^1 vec[\breve{B}^a] \\ \vdots \\ vec[B_{cdf,sc}^m] - \sum_{a=1}^{J_\Xi(\chi)} \alpha_a^m vec[\breve{B}^a] \\ vec[C_{cdf,sc}^{1,disp}] - \sum_{a=1}^{J_\Xi(\chi)} \alpha_a^1 vec[\breve{C}^a] \\ \vdots \\ vec[C_{cdf,sc}^{m,disp}] - \sum_{a=1}^{J_\Xi(\chi)} \alpha_a^m vec[\breve{C}^a] \end{bmatrix} \tag{5.17}$$

As final note, it is important to mention that if the estimated LTI models are solely composed by pairs of complex conjugate poles (for instance, in case the LTI models are identified by using the approaches presented in sections 3.2 and 3.3.2), the number of variables to be determined by solving the linear-least squares problem given in equation (5.14) can be halved. Hence, the number of variables to be calculated to compute interpolated state-space models with the constructed LPV models can also be halved.

5.2.2   Numerical Validation

Here, LPV models representative of the three components (from now on, denoted as components A, B, and C) depicted in figure 5.1 will be computed by exploiting the procedures presented in section 5.2.1. The values of the physical parameters indicated in figure 5.1 are reported in table 5.1.

By analyzing figure 5.1 and table 5.1, we may conclude that one damping and one stiffness parameters associated with substructures A, B and C exhibit a non-linear variation with respect to the value of n_1, n_2 and n_3, respectively. The value of these parameters over time is represented by the curves reported in figure 5.2. A sampling frequency of 2×10^4 Hz was used to discretize each of these curves. Then, state-space models representative of each of the components under study at each time sample were computed directly from their mechanical properties. For the sake of simplicity, the
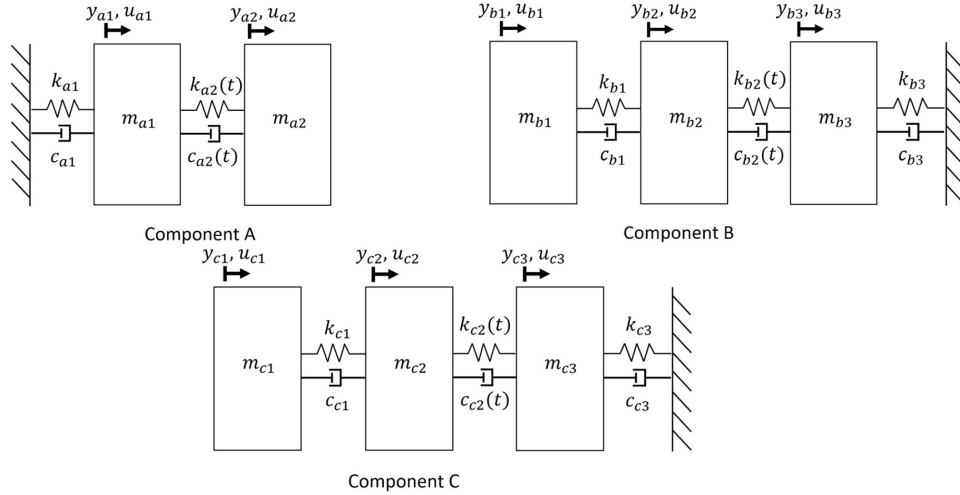
Figure 5.1: Components [6].

Table 5.1: Physical parameter values of components A, B and C [6].

i	m_i (kg)	c_i (N s m^{-1})	k_i (N m^{-1})
$a1$	6	10	4×10^3
$a2$	4	$(5)^{n_1(t)}$	$(2 \times 10^3)^{n_1(t)}$
$b1$	5	20	1×10^3
$b2$	3	$(15)^{n_2(t)}$	$(3.5 \times 10^3)^{n_2(t)}$
$b3$	1.5	5	4×10^3
$c1$	7	10	5×10^3
$c2$	3.5	$(20)^{n_3(t)}$	$(7.5 \times 10^3)^{n_3(t)}$
$c3$	5	12	1×10^3

damping matrix of each of the components at each time sample was defined from the respective stiffness matrix by replacing the stiffness terms with the damping ones.

At this point, three LPV models representative of the three components under study (see figure 5.1) will be constructed by following the procedures presented in section 5.2.1. To define each of these LPV models, four LTI state-space models representative of each of the substructures under study submitted to four different pre-selected fixed operating conditions were used. The values of the time-dependent parameters associated with the selected fixed operating conditions to define each of the LPV models are reported in table 5.2. These conditions were chosen to avoid the need of performing extrapolation and to make sure that between consecutive fixed operating conditions, the dynamics of the systems under analysis do not change abruptly (see section 5.2.1). The state-space models associated with the selected fixed operating conditions were directly set-up by using the mechanical properties of the components under study. Then, to ensure that the obtained sets of state-space models were not represented with respect
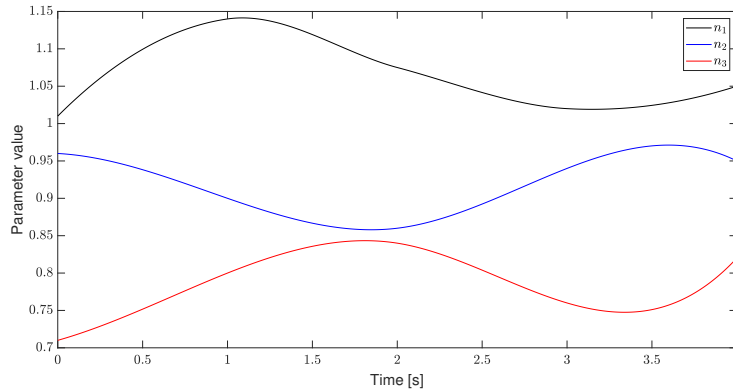
Figure 5.2: Value of parameters n_1, n_2 and n_3 over time.

to the same unique state-space representation (hence, that did not represented coherent sets of models), each of the computed models was transformed into complex diagonal form. Afterwards, the procedures presented in section 5.2.1 were applied to compute sets of coherent state-space models from the estimated sets of LTI models associated with each of the components under analysis. Note that to compute the coherent sets of models, we have normalized the first column of the input matrix of each state-space model (see section 5.2.1).

Table 5.2: Values of the time-varying parameters associated with the selected fixed operating conditions to compute the LPV models representative of components A, B and C, where FOC stands for fixed operating condition [6].

Parameter	FOC 1	FOC 2	FOC 3	FOC 4
n_1	1	1.05	1.1	1.15
n_2	0.85	0.9	0.95	1
n_3	0.7	0.75	0.8	0.85

In figures 5.3, 5.4 and 5.5, it is compared two displacement FRFs of the analytically determined state-space models with the same displacement FRFs of the correspondent coherent state-space models used to compute the LPV models representative of the dynamics of substructures A, B and C, respectively.

By analyzing figures 5.3, 5.4 and 5.5, it is clear that by following the procedures presented in section 5.2.1, we can make a set of state-space models coherent without perturbing their FRFs. Hence, the input-output properties of the models remain unchanged as well.

Finally, by following the procedures outlined in section 5.2.1 and by exploiting the constructed sets of coherent state-space models, LPV models representative of the three components under study were obtained. To construct each of these models, we have parameterized the values of the associated time-varying parameter in a multi-simplex Λ of dimension two. Furthermore, to define the degree of the homogeneous

(a)

(b)
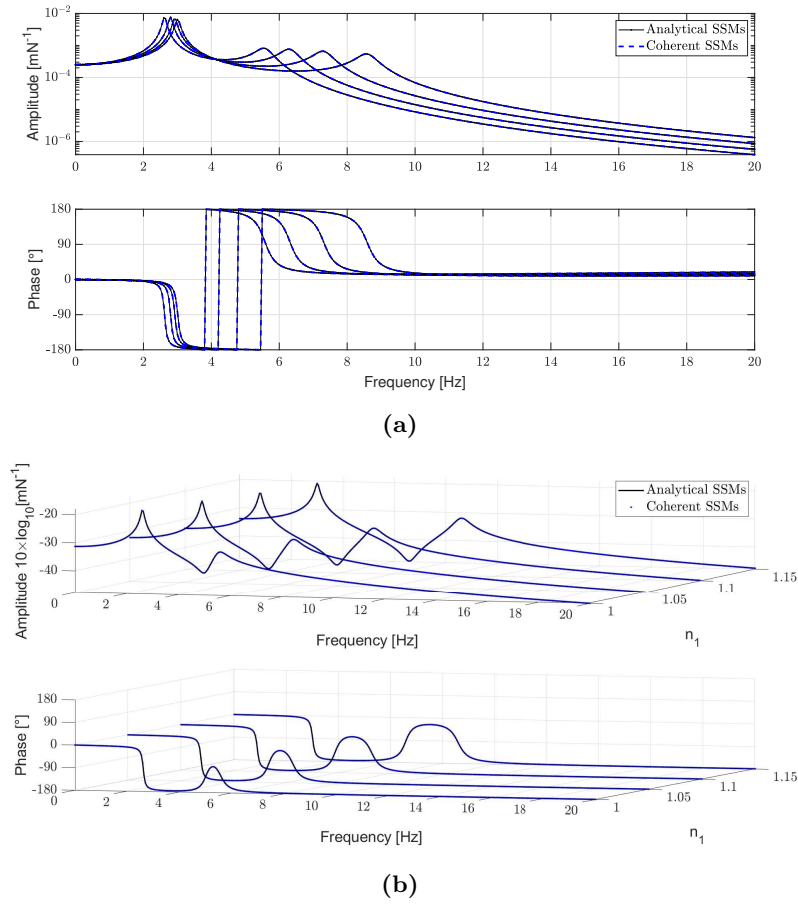
Figure 5.3: Comparison of two displacement FRFs of the set of analytically determined mod-
els with the same FRFs of the coherent set of state-space models to be exploited
to define a LPV model representative of component A: a) displacement FRF,
whose output and input are the DOFs a_1 and a_2, respectively; b) driving point
displacement FRF, whose output and input is the DOF a_2.

polynomial dependency of the LPV models on the parameterized values of the asso-
ciated time-varying parameter, we have computed each of those models by assuming
polynomial dependencies of degrees ranging from 1 to 4. It was found that the error
vectors associated with the solved linear least-squares problems (see expression (5.17))
to calculate the LPV models by selecting a dependency of degree three presented the
lowest 2-norms. For this reason, the three LPV models were constructed by assuming
an homogeneous polynomial dependency of degree three on the parameterized values
of the associated time-varying parameter.

To validate the computed LPV models, they were exploited to compute interpolated
state-space models associated with the fixed operating conditions given in table 5.3.
Figures 5.6, 5.7 and 5.8 report the comparison of two displacement FRFs of the analyt-
ically determined state-space models with the same FRFs of the interpolated models
computed by exploiting the constructed LPV models representative of components A,
B and C, respectively.

(a)

(b)
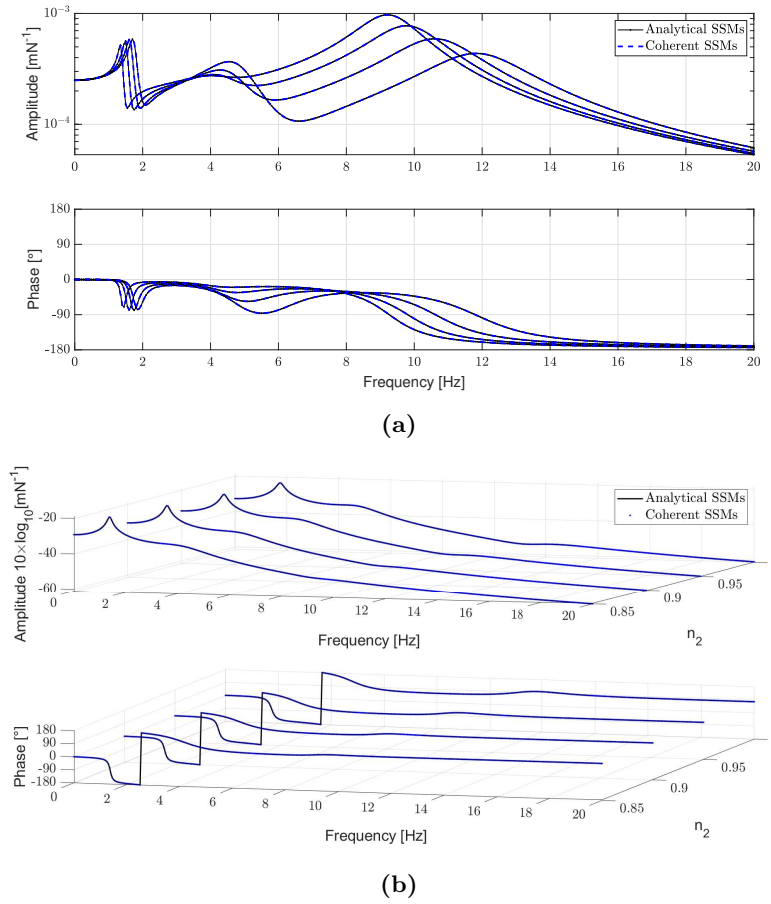
Figure 5.4: Comparison of two displacement FRFs of the set of analytically determined models with the same FRFs of the coherent set of state-space models to be exploited to define a LPV model representative of component B: a) driving point displacement FRF, whose output and input is the DOF b_3; b) displacement FRF, whose output and input are the DOFs b_1 and b_2, respectively.

Table 5.3: Values of the time-varying parameters associated with the fixed operating conditions used to validate the computed LPV models representative of components A, B and C, where FOC stands for fixed operating condition [6].

Parameter	FOC 1	FOC 2	FOC 3	FOC 4
n_1	1.025	1.075	1.115	1.135
n_2	0.875	0.915	0.935	0.97
n_3	0.715	0.735	0.775	0.825

From the observation of figures 5.6, 5.7 and 5.8, it is clear that the FRFs of the analytical models are very well-matched by the same FRFs of the correspondent interpolated state-space models. Thus, we may conclude that the computed LPV models are indeed, accurate to model the dynamics of the substructures A, B and C, provided that they are subjected to operating conditions associated with values of n_1 between

(a)

(b)
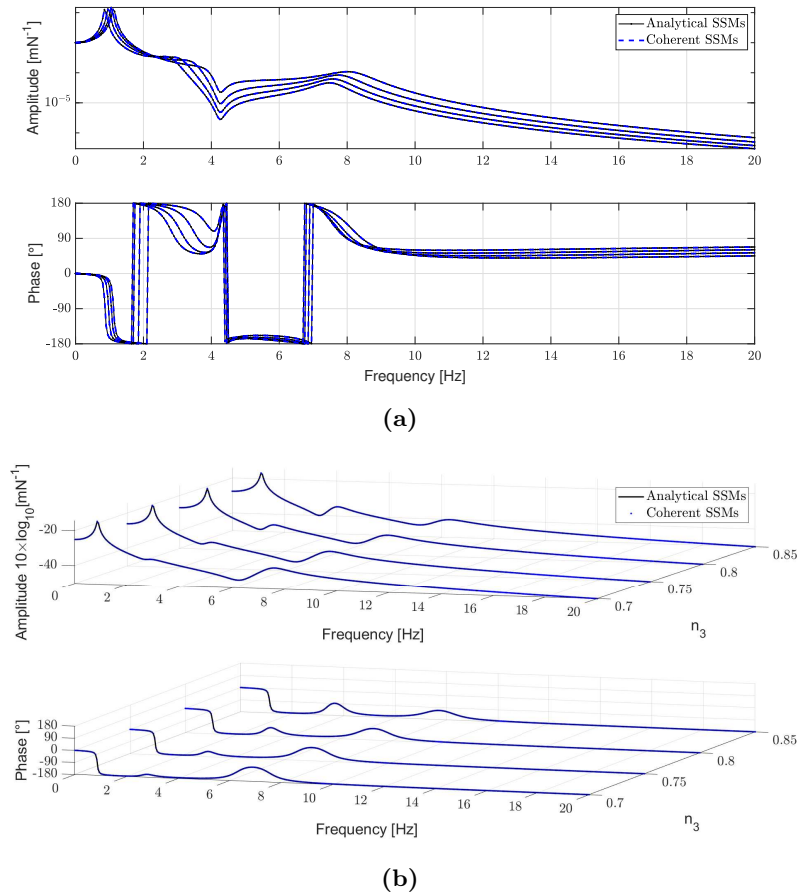
Figure 5.5: Comparison of two displacement FRFs of the set of analytically determined models with the same FRFs of the coherent set of state-space models to be exploited to define a LPV model representative of component C: a) displacement FRF, whose output and input are the DOFs c_2 and c_3, respectively; b) driving point displacement FRF, whose output and input is the DOF c_1.

1 and 1.15, of n_2 between 0.85 and 1 and of n_3 between 0.7 and 0.85 (see table 5.2), respectively.

5.2.3 Experimental Validation

Here, the strategy proposed in section 5.2.1 will be exploited to compute an interpolating LPV model representative of the time-varying dynamics of assembly A (presented in section 4.2.3), when submitted to a temperature run-up. To start, we will describe the performed experimental test to characterize the time-varying dynamics of assembly A. Then, an interpolating LPV model representative of the time-varying dynamic behaviour of assembly A will be set-up. Finally, the interpolated state-space models computed from the defined LPV model will be, firstly, used to reconstruct the measured time-domain accelerations during the performed experimental test. Subsequently, these interpolated models will be exploited with the Minimum-Variance Unbiased (MVU) estimator together with the measured time-domain responses to predict the time-domain

(a)

(b)
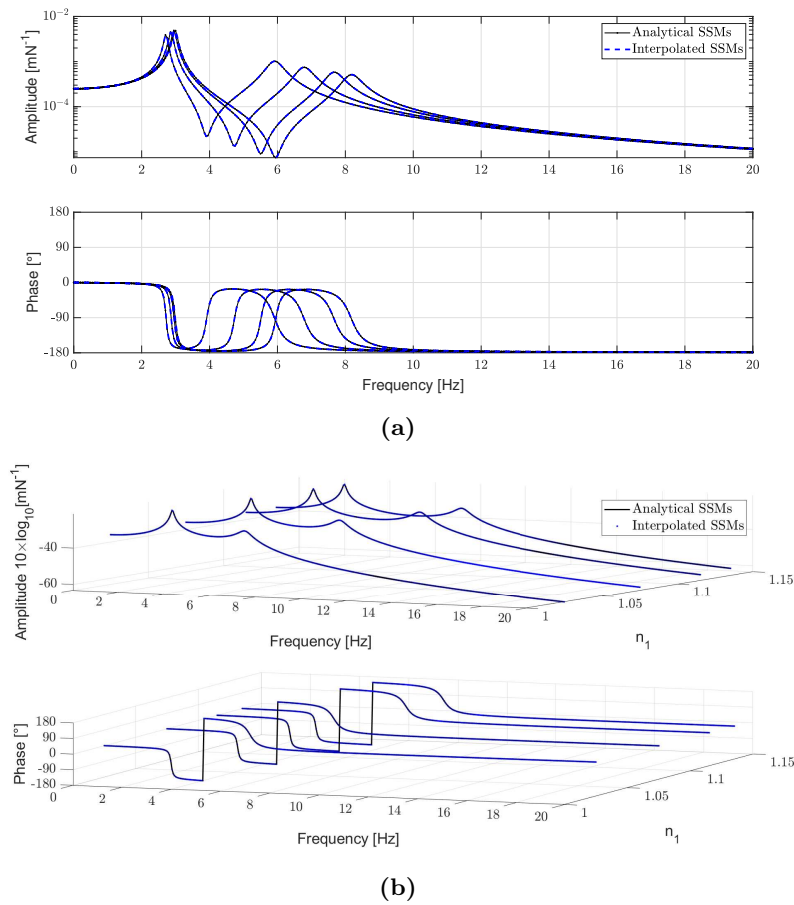
Figure 5.6: Comparison of two displacement FRFs of the analytically determined state-space models representative of system A submitted to the fixed conditions reported in table 5.3 with the same FRFs of the interpolated models obtained by exploiting the constructed LPV model of component A: a) driving point displacement FRF, whose output and input is the DOF a_1; b) displacement FRF, whose output and input are the DOFs a_2 and a_1, respectively.

load applied on assembly A during the conducted experimental test. To demonstrate the benefit of taking into account the variation on the dynamics of assembly A, the obtained results will be compared with the time-domain reconstructions obtained by ignoring the time-domain variations on the dynamics of this system.

Testing Campaign

To experimentally validate the strategy discussed in section 5.2.1 to construct LPV models, the assembly A (presented in section 4.2.3), which is composed by two aluminum crosses connected by a rubber mount, will be analyzed.

To promote time-domain variations on the dynamic behaviour of assembly A, this system was experimentally tested inside of a climate chamber (see figure 5.9), where it was exposed to a six minute temperature run-up. During this temperature run-up, the temperatures of the air inside the climate chamber and at the surface of the rubber

(a)

(b)
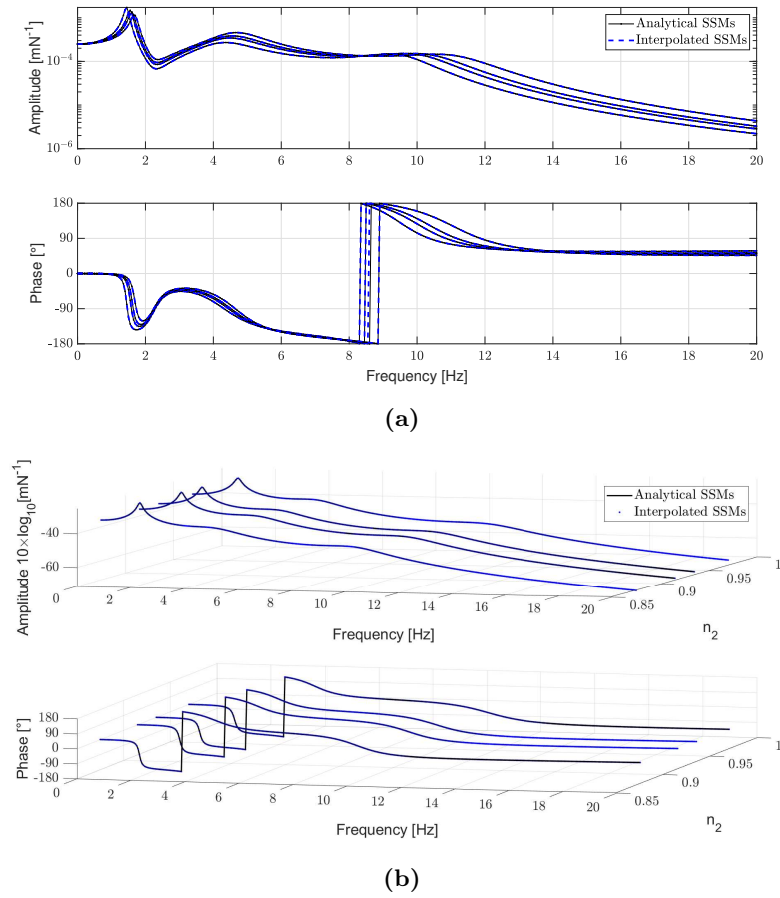
Figure 5.7: Comparison of two displacement FRFs of the analytically determined state-space models representative of system B submitted to the fixed conditions reported in table 5.3 with the same FRFs of the interpolated models obtained by exploiting the constructed LPV model of component B: a) displacement FRF, whose output and input are the DOFs b_2 and b_3, respectively; b) displacement FRF, whose output and input are the DOFs b_3 and b_1, respectively.

mount were continuously registered by two thermocouples. These temperatures are reported in figure 5.10.

By observing figure 5.10, it is clear that the temperature at the surface of the mount increased from, roughly, 14 °C to, approximately, 35.2 °C. This temperature variation promoted a continuous change on the dynamics of the rubber mount over time (see section 5.2). Hence, leading to time-domain variations on the dynamic behaviour of assembly A.

While submitted to the temperature run-up, the assembly A was continuously excited by a shaker. The force applied by this device was permanently registered by a load cell. Moreover, three accelerometers were instrumented in each cross to measure the acceleration responses of the system. To control the band of excited frequencies, the shaker was provided with a random signal defined as:

(a)

(b)
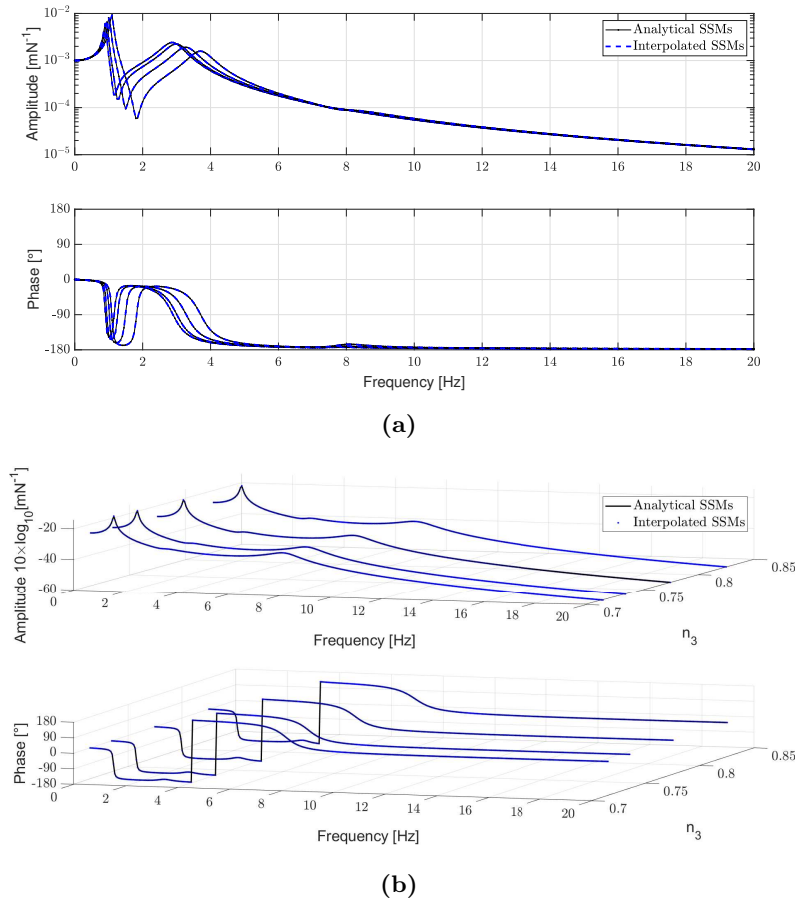
Figure 5.8: Comparison of two displacement FRFs of the analytically determined state-space
models representative of system C submitted to the fixed conditions reported in
table 5.3 with the same FRFs of the interpolated models obtained by exploiting
the constructed LPV model of component C: a) driving point displacement FRF,
whose output and input is the DOF c_1; b) displacement FRF, whose output and
input are the DOFs c_1 and c_2, respectively.

$$v(t_k) = \sum_{f=10}^{250} \gamma_{f,k} cos(2 \times 2\pi f + \theta_{f,k}) \tag{5.18}$$

where, subscript k denotes the kth discrete time instant and $\gamma_{f,k}$ and $\theta_{f,k}$ are Gaussian
distributed stochastic variables, whose means are, respectively, 5×10^{-2} V and 0 rad,
whereas the standard deviations of $\gamma_{f,k}$ and $\theta_{f,k}$ are, respectively, 1×10^{-2} V and 2
rad.

It is worth mentioning that we could have fed the shaker with any kind of signal,
provided that it enables the excitation of frequencies belonging to the frequency band
of interest (i.e. between 2×10^1 Hz to 5×10^2 Hz, see section 4.2.3), because the sole aim
of this section is to evaluate the accuracy of the LPV models constructed by exploiting
the strategy presented in section 5.2.1 to characterize the dynamics of real structures
presenting time-varying dynamic behaviour.
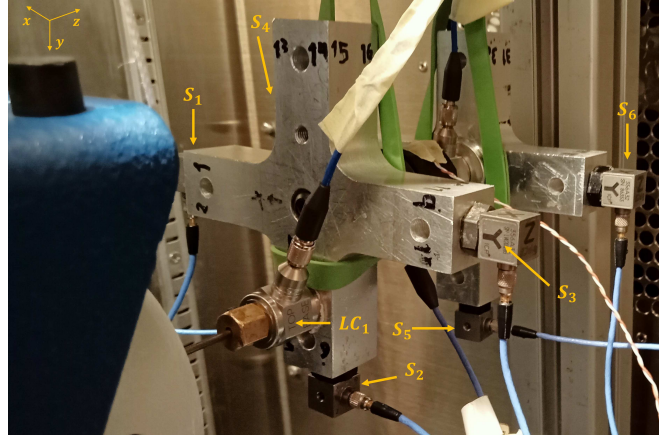
Figure 5.9: Exploited test set-up to experimentally characterize the dynamics of assembly A, when submitted to a temperature run-up [7].
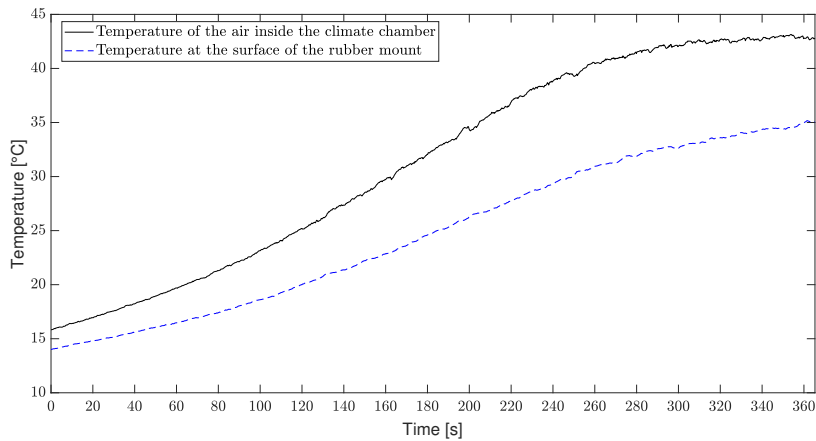
Figure 5.10: Temperatures of the air inside the climate chamber (black solid curve) and at the surface of the rubber mount (blue dashed curve) over time.

Computation of the Linear Parameter Varying model

The strategy presented in section 5.2.1 will be here used to define a LPV model representative of the dynamics of assembly A, when submitted to the described temperature run-up. To start, we must define a set of fixed operating conditions for which LTI state-space models will be estimated. As the dynamics of assembly A changes over time due to variations on the temperature of the rubber mount (from now on denoted as T_{rb}), this temperature will be considered as the scheduling parameter governing the dynamics of assembly A. In this way, to prevent the need of performing extrapolation, we will define two fixed operating conditions to be associated with temperatures at the surface of the rubber mount of 14 ℃ and 35.2 ℃. In addition, to avoid abrupt variations on the dynamics of assembly A between consecutive fixed operating conditions, three LTI state-space models representative of assembly A for rubber mount temperatures of 20 ℃, 25 ℃ and 30 ℃ will be estimated.

To estimate the intended set of LTI state-space models, we must start by computing

the FRFs of assembly A, when the surface of the rubber mount is at the temperatures associated with the selected fixed operating conditions (i.e. 14 ℃, 20 ℃, 25 ℃, 30 ℃ and 35.2 ℃). Besides computing these sets of FRFs, we will also calculate a set of FRFs representative of assembly A for T_{rb} =27.5 ℃. This set of FRFs will serve as reference to evaluate the accuracy of the LPV model to be constructed.

The intended sets of FRFs will be computed directly from the time-domain acceleration signals measured by the accelerometers and from the time-domain load signal measured with the load cell. Thereby, to compute each set of FRFs, chunks of the time-domain acceleration signals and of the time-domain load signal will be exploited. To establish the initial time instant of the chunks of the time-domain acceleration and load signals to compute each set of FRFs, we will look in the curve of the registered temperatures at the surface of the rubber mount (see figure 5.10) for the time instant corresponding to the temperature associated with the set of FRFs under computation minus, approximately, 0.5 ℃. Identically, to establish the final time instants of the chunks of signals to be used to compute each set of FRFs, we will look in the curve of the registered temperatures at the surface of the rubber mount (see figure 5.10) for the time instant corresponding to the temperature associated with the set of FRFs under construction plus, roughly, 0.5 ℃.

The defined initial and final time instants of the chunks of time-domain signals used to determine each of the intended sets of FRFs (i.e. representative of the system at 14 ℃, 20 ℃, 25 ℃, 27.5 ℃, 30 ℃ and 35.2 ℃) and the correspondent measured temperatures at the surface of the rubber mount at those time instants are reported in table 5.4.

Table 5.4: Initial and final time instants associated with the chunks of signals used to determine each set of FRFs and temperatures measured at the surface of the rubber mount at those time instants [7].

T_{rb} (℃)	$t_{initial}$ (s)	t_{final} (s)	$T_{rb,initial}$ (℃)	$T_{rb,final}$ (℃)
14	11	38	14.5	15.5
20	113.5	127	19.5	20.5
25	178.5	192	24.5	25.5
27.5	211	223	27	28
30	241.5	252.5	29.5	30.5
35.2	352	361	34.5	35.2

Note that we have decided to establish the initial and final time instants of the chunks of time-domain signals as described in table 5.4 to allow the computation of several averages of each set of FRFs. Moreover, the set of FRFs of the system for T_{rb} =14 ℃ was computed from chunks of signals, whose initial time instant is associated with a rubber mount temperature of 14.5 ℃ (see table 5.4). We have made this choice to ensure that during the full time-interval included in the chunks of signals used to

compute the FRFs for T_{rb} =14 ℃, the system was being properly excited. In fact, at the beginning of the performed experimental test, the assembly A was at rest. Thus, it is not recommended to compute sets of FRFs by using chunks of data including the initial time-instants of the measured time-domain signals. On the other hand, we do not expect that a variation of 0.5 ℃ on the rubber mount temperature leads to important changes on the FRFs of assembly A. For this reason, by using the defined chunks of time-domain signals, we expect to compute accurate FRFs representative of the dynamics of assembly A for T_{rb} =14 ℃.

The defined chunks of signals (see table 5.4) were used to compute the intended sets of FRFs (i.e. for rubber mount temperatures of 14 ℃, 20 ℃, 25 ℃, 27.5 ℃, 30 ℃ and 35.2 ℃) by exploiting an overlap process with 50% of overlap to enable the computation of more averages of each set of FRFs. On top of this, to reduce the effect of leakage, we have also applied an Hanning window on the output and input time-domain signals used to determine each average of each set of FRFs (see [123]).

Figure 5.11 reports the comparison of the computed FRFs, whose output and input are, respectively, S_4^y (where, superscript denotes the direction of the output) and LC_1^z (where, superscript denotes the direction of the input) (see figure 5.9), of the system under study at the fixed operating conditions selected to define a LPV model representative of the dynamics of assembly A (i.e. for rubber mount temperatures of 14 ℃, 20 ℃, 25 ℃, 30 ℃ and 35.2 ℃).
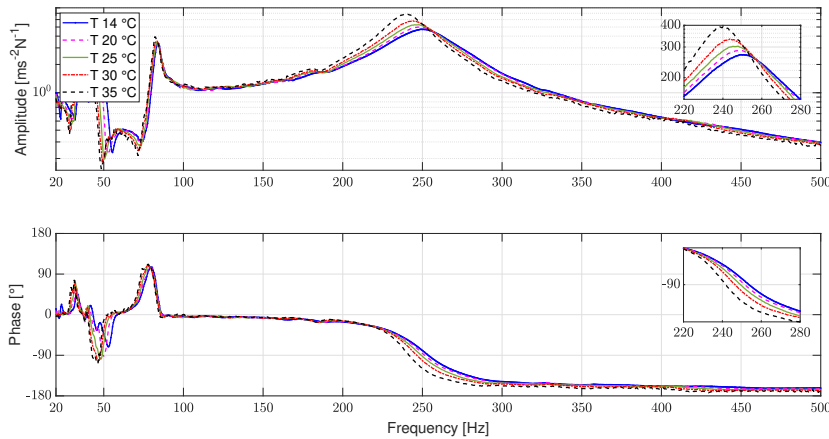
Figure 5.11: Comparison of the determined FRFs of assembly A, when the surface of the rubber mount is at 14 ℃, 20 ℃, 25 ℃, 30 ℃ and 35.2 ℃, whose output and input are, respectively, S_4^y and LC_1^z.

In figure 5.11, we can clearly observe that the FRFs of assembly A change with the rubber mount temperature, in particular, for frequencies between 2×10^2 Hz and 3×10^2 Hz. Furthermore, as the temperature of the rubber mount increases, the amplitude of the resonance of the FRFs of assembly A included in this frequency band increases and its natural frequency decreases. In fact, these observations were expected, because the value of the dynamic stiffness of rubber mounts is known to drop with the increment of

the temperature at which they are subjected (see [124],[125]). On top of this, in figure 5.11, we can also notice that between rubber mount temperature values associated with consecutive selected fixed operating conditions, the FRFs of assembly A change smoothly. This is a clear indication that the set of selected fixed operating conditions is suitable to compute the intended LPV model.

At this point, the LTI state-space models associated with the selected fixed operating conditions can be computed from the respective determined sets of FRFs (from now on denoted as measured FRFs). To compute these models, we will, firstly, estimate modal parameters from the measured set of FRFs representative of assembly A for $T_{rb} =14$ ℃, by using the Simcenter Testlab$^\text{\textregistered}$ implementation of PolyMAX (see, [22]) and ML-MM (see, [70]) algorithms. Then, to compute modal parameters representative of the dynamics of the system at the other selected fixed operating conditions, the modal parameters identified from the set of measured FRFs associated with a rubber mount temperature of 14 ℃ will be updated by using the ML-MM algorithm. All the modal parameters will be estimated without assuming a proportionally damped modal model. Subsequently, by using the estimated modal parameters and the approaches presented in sections 3.2 and 3.3.2, LTI state-space models representative of assembly A at the selected fixed operating conditions will be computed.

At the end of this process, five LTI state-space models representative of each selected fixed operating condition were obtained. Each of these models is made of five in-band pairs of complex conjugate poles, of two RCMs that model the contribution of the lower out-of-band modes in the frequency band of interest, of two other RCMs, whose task is modelling the contribution of the upper out-of-band modes in the frequency band of interest and of two RCMs responsible for imposing Newton's second law (see section 3.3.2). The RCMs used to include the contribution of the lower out-of-band modes were defined by choosing a value for their natural frequencies of 1×10^{-1} Hz, while the RCMs responsible for including the contribution of the upper out-of-band modes and for imposing Newton's second law were set-up by choosing a value for their natural frequencies of 1.5×10^3 Hz. Moreover, the value of the damping ratio of these RCMs was selected to be 1×10^{-1} (see section 3.2).

In figure 5.12, the measured acceleance FRF, whose output and input are, respectively, S_5^z and LC_1^z, of assembly A for $T_{rb} =30$ ℃, is compared with the same FRF of the correspondent estimated state-space model.

By analyzing figure 5.12, it is clear that the measured FRF of assembly A is very well-matched by the correspondent FRF of the estimated state-space model. Thus, we may conclude that the estimated LTI state-space model represents an accurate description of the dynamics of assembly A for $T_{rb} =30$ ℃. Moreover, identical match quality was observed between the FRFs of the computed state-space models representative of the other fixed operating conditions and the correspondent measured FRFs. Therefore, we may conclude that all the LTI state-space models were successfully computed.

Before computing the intended LPV model, the set of estimated state-space models
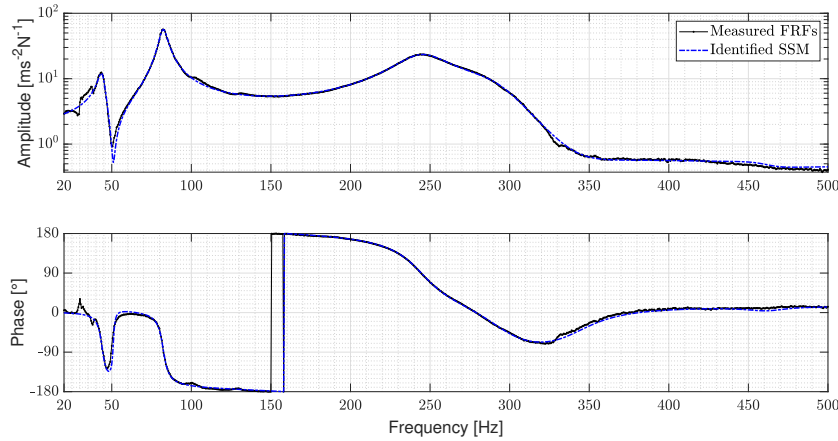
Figure 5.12: Comparison of the measured accelerance FRF, whose output and input are, respectively, S_5^z and LC_1^z, of the assembly A for $T_{rb} =$30 ℃, with the same FRF of the correspondent estimated state-space model.

must be coherently represented by exploiting the strategy outlined in section 5.2.1. Then, the obtained coherent set of models can be used to define the intended LPV model by following the strategy described in section 5.2.1. Nevertheless, to compute this LPV model, we are also required to select the degree χ of the homogeneous polynomial dependency of the LPV model on the parameterized values of the scheduling parameter (i.e. rubber mount temperature) associated with each of the estimated LTI models. However, we have no knowledge regarding the dependency of the dynamics of assembly A on the rubber mount temperature. For this reason, to define a degree of dependency that enables the construction of a reliable LPV model representative of assembly A, we will construct different LPV models by choosing the value of χ to be 1, 2, 3 and 4. The 2-norms of the error vectors (see expression 5.17) associated with the solved linear-least squares problems to compute each of these LPV models is indicated in table 5.5.

Table 5.5: 2-norms of the error vectors (see expression 5.17) associated with the solved linear-least squares problems to define LPV models by selecting the value of χ to be 1, 2, 3 and 4.

χ	1	2	3	4
$||E(p)||$	49.9402	27.0592	18.0371	4.3743×10^{-11}

From table 5.5, it is evident that the 2-norm of the error vector associated with the solved linear least-squares problem to calculate the LPV model by selecting $\chi = 4$ is very close to zero. Thus, by using this LPV model, we are capable of computing state-space models representative of the dynamics of the system submitted to the selected set of fixed operating conditions presenting state-space matrices elements closely matching the elements of the identified LTI models. Thereby, presuming that the set of identified LTI state-space models well captures the influence of the temperature of

the rubber mount over the dynamics of assembly A, we expect the LPV model defined by assuming $\chi = 4$ to be accurate to describe the dynamics of assembly A for rubber mount temperatures ranging from 14 ℃ to 35.2 ℃. Hence, the interpolated models computed from the defined LPV model representative of the dynamics of assembly A, when submitted to fixed operating conditions in between the selected ones to compute the LPV model, are expected to be accurate.

In case that the LPV model is, indeed, accurate, the FRFs of the computed interpolated models must not change abruptly for rubber mount temperatures ranging from 14 ℃ to 35.2 ℃ (see figure 5.11). Moreover, the variation of the FRFs of the interpolated models with the rubber mount temperature must follow the same trend observed for the measured sets of FRFs (see figure 5.11). Figure 5.13 reports a surface obtained from the FRF, whose output and input are, respectively, S_4^y and LC_1^z, of the computed interpolated state-space models representative of the dynamics of assembly A for rubber mount temperatures between 14 ℃ and 35.2 ℃ and spaced by 0.1 ℃.
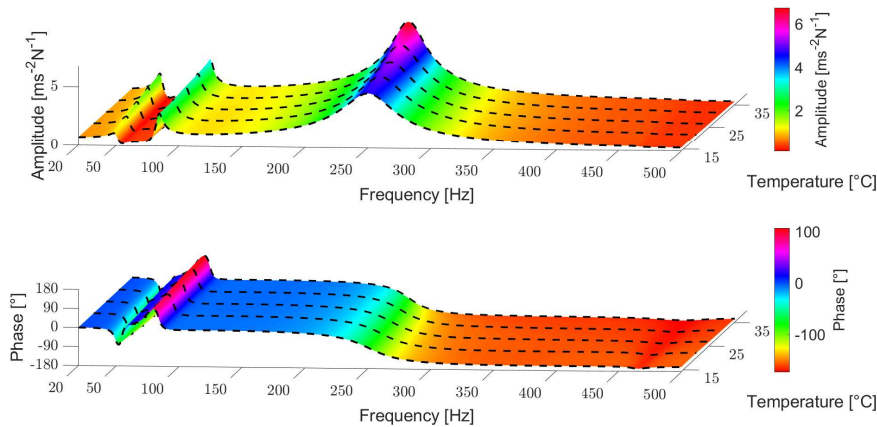
Figure 5.13: Surface constructed from the accelerance FRF, whose output and input are, respectively, S_4^y and LC_1^z, of the interpolated state-space models representative of the dynamics of assembly A for rubber mount temperatures between 14 ℃ and 35.2 ℃ and spaced by 0.1 ℃.

By analyzing figure 5.13, it is clear that the FRF of the interpolated state-space models varies smoothly with the rubber mount temperature. It was found that the other FRFs of the interpolated state-space models also vary smoothly with this temperature. Furthermore, the variation of the FRFs of the interpolated models with the rubber mount temperature follows the same trend observed for the measured sets of FRFs (see figure 5.11). Thereby, these observations indicate that the LPV model is correctly set-up and that it is accurate to characterize the dynamics of assembly A, when the rubber mount temperature is between 14 ℃ and 35.2 ℃.

To further evaluate the accuracy of the constructed LPV model, this model was exploited to compute an interpolated state-space model representative of assembly A for $T_{rb} = 27.5$ ℃. In figure 5.14, the accelerance FRF of this interpolated model, whose

output and input is S_2^Z and LC_1^z, respectively, is compared with the correspondent measured FRF.
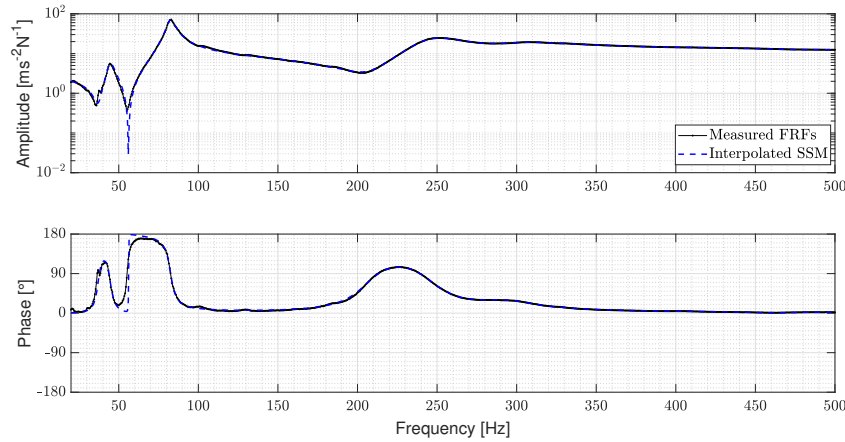
Figure 5.14: Comparison of the measured accelerance FRF, whose output and input is S_2^z and LC_1^z, respectively, of assembly A, when the rubber mount is at 27.5 ℃, with the same accelerance FRF of the correspondent interpolated state-space model obtained by exploiting the defined LPV model by selecting $\chi = 4$.

By analyzing figure 5.14, we may conclude that the measured accelerance FRF of assembly A, when the rubber mount is at 27.5 ℃, is very well-matched by the same FRF of the correspondent interpolated model obtained with the constructed LPV model. Thereby, further proving that the LPV model constructed by selecting $\chi = 4$ is valid to characterize the time-varying dynamics of assembly A.

Time-domain responses simulation and time-domain load identification

As first analysis, the time-domain responses measured during the performed experimental test (see section 5.2.3) will be reconstructed by exploiting the interpolated models computed from the constructed LPV model (see section 5.2.3) together with the measured time-domain load signal applied by the shaker. Additionally, to demonstrate the benefit of considering the time-domain variations on the dynamics of assembly A, the same time-domain responses will be reconstructed by solely exploiting the estimated LTI model representative of the dynamics of the assembly A for $T_{rb} = 14$ ℃.

Note that to restrict our analysis to frequencies for which variations on the rubber mount temperature lead to the most important variations on the measured FRFs of assembly A (see figure 5.11), the measured time-domain responses and load signals will be filtered with a band-pass filter presenting passband frequencies ranging from 1.2×10^2 Hz to 3.5×10^2 Hz.

In figures 5.15 and 5.16, it is reported the comparison of the measured time-domain response of two different outputs of assembly A with the correspondent reconstructed responses obtained by using the measured time-domain load signal with i) the identified LTI model of assembly A for $T_{rb} = 14$ ℃ and with ii) the interpolated state-space models

computed at each time sample from the defined LPV model of assembly A.
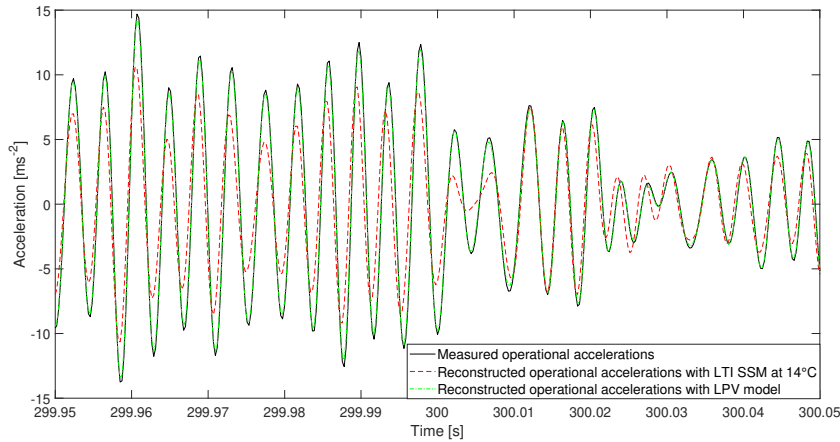
Figure 5.15: Comparison of the experimentally acquired time-domain response of output S_7^z with the predicted response of the same output obtained by i) exploiting the identified LTI model representative of the dynamics of assembly A, when the rubber mount is at 14 ℃, and by ii) exploiting the interpolated state-space models calculated at each time sample by using the defined LPV model.
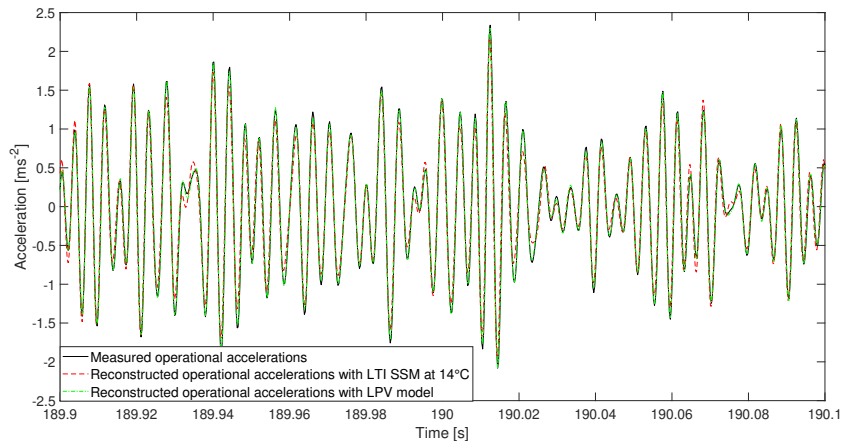
Figure 5.16: Comparison of the experimentally acquired time-domain response of output S_8^y with the predicted response of the same output obtained by i) exploiting the identified LTI model representative of the dynamics of assembly A, when the rubber mount is at 14 ℃, and by ii) exploiting the interpolated state-space models calculated at each time sample by using the defined LPV model.

Figures 5.15 and 5.16 demonstrate that the measured time-domain responses are very well-matched by the correspondent predicted responses by exploiting the interpolated models computed from the constructed LPV model. Moreover, it is evident that the time-domain responses predicted with the LTI state-space model representative of assembly A for T_{rb} =14 ℃ are less accurate. This is, particularly, evident at time instants for which the rubber mount temperature is higher (see figures 5.10 and 5.15). Thereby, it is straightforward to conclude that the methodology described in section

3.2 is valid to determine accurate LPV models characterizing the dynamics of real components, presenting time-varying dynamic behaviour. On top of this, the performed comparison clearly illustrates the benefit in terms of the quality of the predicted time-domain responses of taking into account the time-domain variations on the dynamics of assembly A.

At this point, we will exploit the experimentally acquired responses together with the MVU estimator presented in [126] to reconstruct the measured time-domain load signal (see appendix G). Figure 5.17 reports the comparison of the measured time-domain load signal with the predicted time-domain load signal by exploiting the acquired time-domain responses and the MVU estimator together with the following state-space models: a) LTI model representative of the dynamics of assembly A for T_{rb} =14 ℃ and b) by using the interpolated state-space models computed at each time sample with the defined LPV model.

Once again, to restrict our study to frequencies for which variations on the rubber mount temperature lead to the most important variations on the measured FRFs of assembly A (see figure 5.11), the measured time-domain responses and load signals were filtered with a band-pass filter presenting passband frequencies ranging from 1.2×10^2 Hz to 3.5×10^2 Hz. Moreover, as during the performed experimental test (see section 5.2.3) the assembly A was not properly excited by the shaker in the x direction (see figure 5.9), the time-domain load applied by the shaker was reconstructed without using the time-domain responses measured in this direction.

Note also that, to implement the MVU estimator, we must know the state vector at the initial time-instant and the associated covariance matrix. On top of this, we must also define the covariance matrices associated with both process and measurement noises (see appendix G). At the beginning of the conducted experimental test (see section 5.2.3), assembly A was in steady-state. For this reason, the state vector and its associated covariance matrix were assumed to be null. The covariance matrix associated with the process noise was also defined to be a null matrix, because the identified LTI models and the constructed LPV model demonstrated to be able to accurately describe the dynamic behaviour of assembly A (see section 5.2.3). Moreover, the covariance matrix associated with the measurement noise was defined from the statistical noise properties of the accelerometers reported by the manufacture (see [127]) and by presuming that the measurement noise of the used accelerometers is not correlated with each other. In this way, the covariance matrix associated with the measurement noise was defined to be $6.16 \times 10^{-6} \times [I]$, where $[I]$ is a $n_{out} \times n_{out}$ identity matrix (where, n_{out} represents the number of exploited outputs to predict the load applied by the shaker).

From the analysis of figure 5.17, it is evident that the measured time-domain load signal is very well-matched by the load signal predicted with the interpolated models computed from the defined LPV model. On top of this, it is clear that the load signal predicted with the LTI model representative of assembly A for T_{rb} =14 ℃ is not
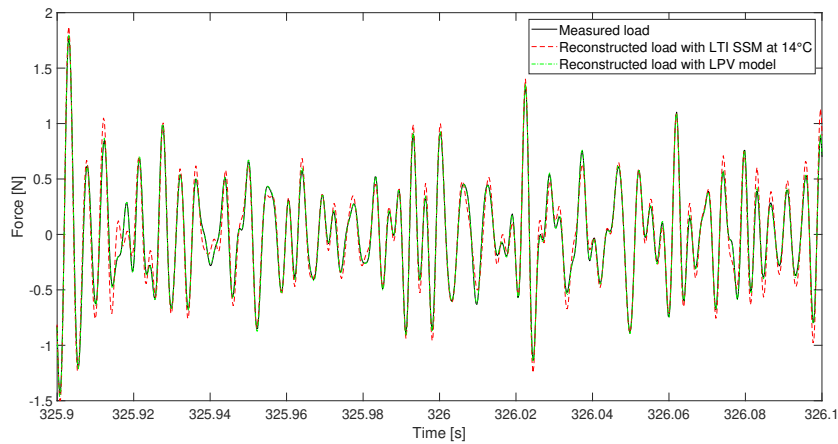
Figure 5.17: Comparison of the measured time-domain load with the time-domain loads predicted by exploiting the experimentally acquired time-domain responses and the MVU estimator together with: a) the identified LTI model representative of the dynamics of assembly A for T_{rb} =14 ℃ and with b) the interpolated models determined at each time-sample with the defined LPV model.

matching so well the measured time-domain load signal. Thus, we may conclude that to accurately reconstruct time-domain load signals, possible time-domain variations on the dynamics of the mechanical systems under study must not be ignored. Moreover, it is once again evident that the computed LPV model accurately describes the time-varying dynamic behaviour of assembly A. Hence, we may claim that the approach presented in section 5.2.1 is experimentally validated to set-up interpolating LPV models.

5.3   Transfer Path Analysis

In this section, we will start by presenting a brief review of some state-of-the-art Transfer Path Analysis (TPA) techniques (section 5.3.1). Then, the state-space realizations of both matrix-inverse classical TPA and in-situ component-based TPA methods are presented in sections 5.3.2 and 5.3.3, respectively.

5.3.1   State-of-the-art

TPA has revealed to be a valuable family of techniques to identify and assess the importance of transmission paths of noise and vibration from sources (active components, e.g. engines) to passive components (see, [128]). The TPA problem is in general represented by an assembled structure composed of a source in operation connected to a passive component through rigid connections or via connecting elements. As the source is under operation, its internal mechanisms originate structural and acoustical excitation that is transmitted to the passive system through structural and airborne transfer paths, respectively. The passive system is assumed to not receive any excitation besides the one transmitted through these transfer paths.

In practice, the performance of TPA usually aims at lessen the transmission of noise and vibration from the active to the passive components. Applications of this concept can be found in diverse areas, such as, in the automotive (see, for instance, [129], [130], [131], [132]) and in the aerospace industries (see, for example, [133], [134], [135]). Following the general framework for TPA presented by Van der Seijs et al. in [94], we will divide the TPA techniques in three different groups, namely, in the classical TPA, component-based TPA and transmissibility-based TPA methods.

The classical TPA methods aim at identifying a set of connecting forces acting at the interface between the active and passive components. These forces can, then, be used to compute the operational responses on the intended DOFs (commonly, denoted as target DOFs) at the passive side of the assembled structure (i.e. source connected to the passive system) resultant from the excitation provided by the active component. In the family of classical TPA methods are included approaches that make use of different strategies to compute this set of connecting forces. We can start by mentioning the direct force method, which makes use of force transducers installed at the interface between the active and passive components to measure the intended set of connecting forces. While this method might be adequate to deal with massive structures (see, [128]), when analyzing smaller mechanical systems the instrumentation of force sensors at the interface between the active and passive components is many times impossible due to lack of room or inconvenient, because it changes the mounting conditions between the components. On top of this, the measurement of the connecting forces on all intended DOFs might not be possible. Another technique belonging to the classical TPA family is the mount stiffness method (see, [128], [136]). This technique is applicable, when the active and passive components are connected by flexible mounts. To determine the connecting forces, the mounts are assumed to respect the assumptions underlying IS (see section 2.5.1), being the connecting forces determined by using the diagonal dynamic stiffness terms of the mounts and the difference between the displacements at the interface of the active and passive systems (see, bottom equation of expression (2.59)) [94]. An important drawback of this approach is that some mounts do not obey the assumptions underlying IS.

Lastly, we may also refer the widely popular matrix-inverse classical TPA method. This method determines the connecting forces between the active and passive components by solving an inverse problem involving operational responses collected at the interface and/or at the passive side of the assembled structure (i.e. active component connected to the passive system) and a model characterizing the dynamics of the passive system (for example, set of FRFs or a state-space model). However, it is well-known that the inverse force identification problem is ill-posed [137]. In practice, to make the inverse problem better conditioned, it is common to determine the connecting forces in an over-determined fashion by exploiting operational responses acquired at a number of DOFs at least two times higher than the number of connecting forces to be determined (see [136], [50], [94]). The location of these DOFs (also known as indicator

DOFs) must be close to the interface between the active and passive components to properly observe the full set of connecting forces. On top of this, to further improve the conditioning of the inverse problem, the use of regularization methods is common. In frequency-domain, the matrix-inverse method is usually regularized by either truncating the lowest singular values (see, for instance, [138]) or by exploiting the Tikhonov regularization approach [139], [140] (see, for example, the force identification strategies presented in [141], [142]).

In time-domain, many techniques enabling the identification of time-domain forces by solving inverse problems were proposed. Even though, many of these approaches were developed without specifically targeting the determination of connecting forces in the context of TPA, they can be exploited for this purpose. An example of these techniques is the adaptive algorithm proposed in [143], which was directly derived from the Least Mean Square algorithm [144]. By following the approach presented in [143], the time-domain forces are estimated recursively based on the error between the measured operational responses and the operational responses computed with the estimated forces. Thus, avoiding the need of performing possible ill-conditioned matrix inversions (see, [96]). Another force identification method was derived in [145]. This approach estimates the time-domain forces by using the inverse Markov parameters of the system under study together with measured operational responses. Moreover, to regularize the inverse problem, Tikhonov regularization is applied. In [146], a method that reconstructs time-domain forces by using an inverse structural filter that takes as input the operational responses of the system under analysis was presented. In this approach, the inverse problem is regularized by truncating the lowest singluar values. More recently, a novel force identification method based on the use of a precise time-step integration method for Markov parameters (PTIM-MP) together with the Tikhonov regularization approach was also proposed in [147]. Finally, we can mention some of the Kalman filter versions derived from the original work proposed by Kalman in [148] to solve the inverse force identification problem. Examples of these works are the dual Kalman filter proposed by Azam et al. in [149] and the Augmented Kalman Filter (AKF) presented by Lourens et al. in [150].

The family of component-based TPA methods aims at determining sets of forces that are an inherent property of the active components alone. These forces are usually addressed as equivalent forces. The interesting feature of these forces is that they can be used together with a model characterizing the dynamics of the assembled structure (i.e. source connected to passive system) to simulate the operational responses (i.e. when the source is running) on its passive side. Additionally, the equivalent forces of a given active component can be exploited to determine the operational responses on the passive side of any assembled system made of this component connected to any other passive system, provided that the operational excitation exerted by the active component is the same. This is possible, because these forces are an inherent property of the active component alone. However, as discussed in [26], [151], [94] these equivalent

forces cannot be used to predict the operational responses on the active side of the assemblies (i.e. on DOFs belonging to the active component).

To determine the equivalent forces of a given active component, we can follow different methodologies. For example, we may think of exploiting the blocked force method. This approach is based on the fact that if the boundary of the active component is completely blocked, while it is running, the reaction forces at the interface of the active system are, actually, its equivalent forces (see, for instance, [94], [50]). Thus, in this situation, the equivalent forces can be measured by using force transducers. In contrast, one may think of measuring the interface operational responses of the source by leaving it completely free. It can be proven that these free interface responses are also an inherent property of the source being related to the equivalent forces. Indeed, in frequency domain, one can compute the equivalent forces by using the inverted driving point interface FRFs of the source and its free interface responses (see, for instance, [152]).

However, in practice, these methods are hard to apply. On the one hand, the blocked force method requires the source to be blocked in all directions by a test bench presenting infinite stiffness. On the other hand, the measurement of free interface responses is challenging, because to be able to operate, the sources need to be mounted. Therefore, we expect the blocked force method to perform better at low frequencies, for which the interface of the source can be assumed to behave as a rigid body, whereas the characterization of active components by using free interface responses is expected to be more accurate for higher frequencies [94]. To surpass the practical difficulties inherent to both discussed component-based TPA methods, we may exploit the approach presented by de Klerk and Rixen in [151]. In this method, the operational tests are conducted with the source connected to a regular test-bench. During these tests, interface operational responses and connecting forces are collected. Then, by using these measured quantities, the equivalent forces can be computed as reported in [151]. The main drawback of this method is that it requires the measurement of collocated responses and forces in all directions and for all the connection points of the source with the test-bench. To avoid the need of measuring the forces at these connection points, Van der Seijs et al. proposed in [153] an approach that enables the determination of the equivalent forces by only using measured interface responses. Nevertheless, by exploiting this method, we are required to hold two models, one characterizing the dynamics at the interface of the source and another one characterizing the dynamics of the test-bench, while the approach proposed in [151] only requires the use of one model describing the dynamics at the interface of the source.

In the family of the component-based TPA techniques, it is also included the widely popular in-situ component-based TPA method (see, [154],[155]). This approach determines the equivalent forces by solving an inverse problem involving a model characterizing the dynamics of the assembled system (i.e. source connected to the passive system) and operational responses measured at the interface or/and at the passive side of the

assembly. In this way, by using this method we are able to calculate the equivalent forces without using special test-rigs and without dismounting any component, which makes this method very attractive to the scientific community. Yet, one must guarantee that the assembled system is only excited by forces applied on the active side. Thereby, the in-situ component-based TPA method is very similar to the matrix-inverse method. The main difference is that the in-situ TPA method is based on solving an inverse problem involving a model characterizing the dynamics of the assembled structure, while the matrix-inverse method is based on solving an inverse problem that involves a model describing the dynamics of the passive system. Thus, the strategies described above to better the conditioning of the inverse problem, when applying the matrix-inverse method still hold for the in-situ component-based TPA approach. Moreover, the time-domain approaches discussed above to implement the matrix-inverse method can also be exploited to implement the in-situ component-based TPA method. In literature, several works and studies exploiting the in-situ component-based TPA approach can be found, see for example, [156], [97], [157], [158], [159], [160].

Lastly, we may also mention the pseudo-forces method proposed in [161]. In this method, a given source is characterized by pseudo-forces placed on its outer surface. These forces are computed by solving an inverse problem involving a model characterizing the dynamics of the assembled system and operational responses acquired at the interface or/and at the passive side of the assembly. Thereby, the in-situ component-based TPA method is completely identical to the pseudo-forces method, in case that the pseudo-forces are assumed to be positioned at the interface between the source and the passive component. In [162], the pseudo-forces method was successfully applied to characterize an air-compressor mounted on a framework.

The family of transmissibility-based TPA methods aims at identifying and evaluating the importance of the paths of noise and vibration from the source to the passive system. In this way, the responses at the target DOFs are commonly decomposed into partial contributions coming from the operational responses measured at the indicators. To determine these partial contributions, this family of methods makes use of transmissibilities that are a property of the passive system alone (see, for instance, [163], [94]). In [164], Magrans proposed a method based on two steps that is capable of performing the decomposition of the operational responses at the target DOFs in terms of the responses at the indicators. The first step involves the measurement of a set of so-called general transmissibilities, whereas in the second step operational responses are acquired, while the source is under operation. Nevertheless, the general transmissibilities cannot be used to evaluate the contribution of the indicator responses to the target responses, instead we must use the so-called direct transmissibilities (also known in literature as global transmissibilities) that can be computed from the general transmissibilities (see, for instance, [164], [165]). This approach (also known as Global Transmissibility Direct Transmissibility method (see, for example, [166], [167])) has already demonstrated to lead to robust results, even when dealing with applications

involving real mechanical systems (see, [168], [169]).

To alleviate the experimental effort required by the approach proposed in [164], Noumura and Yoshida proposed a novel approach in [170] commonly denoted as Operational Transfer Path Analysis (OTPA). This method proposes the performance of several experimental tests during which the source is running under different operational conditions. By performing these tests, we aim at collecting operational responses at the target and indicator DOFs representative of several independent excitation cases. Then, the transmissibilities can be computed, for example, with the H_1 estimator (see, for instance, [21], [123]), by using the cross-power spectra matrix between the target and indicator DOFs and the auto-power spectra matrix of the indicators. Thereby, this method holds the important advantage of being a single step approach, allowing the determination of transmissibilities and the analysis of the transmission paths by solely exploiting operational data. Nevertheless, to properly estimate the transmissibilities, the auto-power spectra matrix of the indicators must be well-conditioned. Yet, the generation of independent excitation scenarios is difficult specially at low frequencies [171]. To improve the conditioning of the problem, we may, for instance, truncate the lowest singular values of the auto-power spectra matrix of the indicators. However, as discussed in [171], [172], this approach may lead to the computation of incorrect transmissibilities. For detailed discussions on the limitations of the OTPA method the readers are forward to [173], [171], [174], [175], [172]. Guidelines on how to apply this method in practice and a practical tire noise application are discussed in [176]. An application of OTPA in the context of time-domain auralisation can also be found in [177].

Finally, we may also mention the Operational Path Analysis with eXogenous Inputs (OPAX) method (see, [178], [179]). OPAX was developed with the aim of combining the advantages of both OTPA and classical TPA methods. In this approach, the connecting forces of the target assembly (i.e. active component rigidly connected to a passive system or connected via flexible mounts) are computed by exploiting the mount-stiffness classical TPA method. In case that the dynamics of the mounts are unknown, one can exploit models to parameterise they dynamic stiffness (for instance, single DOF models or multi-band models [179]). The parameters of these models can then be determined by solving a linear least-squares problem involving a model representative of the dynamics of the passive system and operational responses measured at the interface of the source and passive systems and at the indiator and/or target DOFs. If the assembled structure under study is composed of a source rigidly connected to a passive system, it is suggested to exploit the mount-stiffness method by using passive-side interface operational responses together with a narrow-band mount model (see, [179]). Then, by using the connecting forces together with a model representative of the dynamics of the passive system, the path contributions to the passive side DOFs of interest can be determined. The main disadvantage of this approach is that it requires the use of a model characterizing the dynamics of the passive system. If this model is to be de-

termined experimentally, we are required to perform experimental tests on the passive system alone.

Here, as mentioned in section 5.1, we will focus our attention on the matrix-inverse classical TPA and on the in-situ component-based TPA methods. In particular, we aim at presenting the state-space realizations of these methods that will be exploited in section 5.4 to determine connecting and equivalent forces, when analyzing mechnical systems presenting time-varying dynamic behaviour.

5.3.2   State-space realization of the matrix inverse method

In this section, we will present the state-space realization of the matrix inverse method. This approach will be presented to demonstrate, which state-space models and operational responses must be used to compute connecting forces in time-domain by exploiting the state-space formulation. To simplify, here, we will assume that the estimation of the connecting forces is performed in a linear-least squares sense. However, the force identification problem is known to be ill-posed. For this reason, when identifying forces from measured operational responses, the use of a linear-least squares approach is not recommended, because it generally leads to the amplification of the noise present in the measured operational responses (see, for example, [146],[147]). Thus, to estimate connecting forces by using measured operational responses, one must exploit more robust approaches, for instance, joint input-state estimation algorithms (see, for example, [126], [180]) and the Augmented Kalman filter (AKF) (see, for example, [150], [181], [182]).

To present the state-space realization of the matrix inverse method, we will consider the assembled structure AB depicted in figure 5.18 composed by a source A and a passive system B rigidly connected. In this figure, four different sets of DOFs can be observed. A set of internal DOFs a located on the source A, where the internal force generated by its internal mechanism is applied, a set of interface DOFs b, a set of indicator DOFs c and a set of target DOFs d.

Let us now, virtually separate the mechanical systems composing the assembled structure shown in figure 5.18. After performing this virtual operation, the mechanical systems of the assembled structure can be represented as shown in figure 5.19. In this figure, it is possible to observe the connecting forces, which are responsible for keeping the source and passive systems connected, acting on the interface of both mechanical
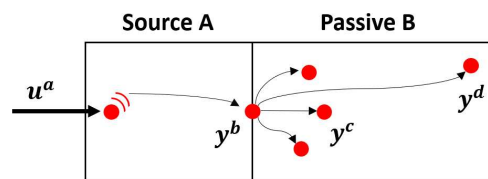
Figure 5.18: Assembled structure made of a source and a passive component rigidly connected.

systems.
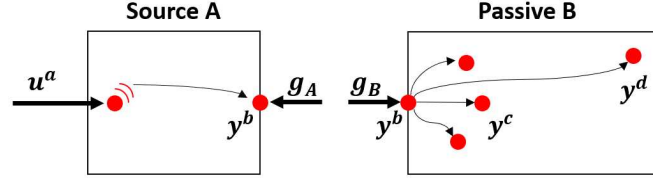
Figure 5.19: Assembled structure virtually separated.

To identify the connecting forces acting on the interfaces of the source and passive component in time-domain, one may think on using force transducers. Nevertheless, this would require the placement of these transducers in between the interfaces of the source and passive system. As argued in [94], for many applications, the instrumentation of these force transducers is neither desired nor even possible. In alternative, we may also think on using the LM-SSS method (see section 2.2.3) to define a state-space model, whose outputs are the connecting forces intended to be identified. This state-space model can simply be set-up by using the state equation of the coupled model given in expression (2.75) and the first equation of the system of equations (2.73). Thus, by using these equations and by retaining a unique set of inputs (see section 2.3.4), the intended state-space model can be obtained as follows:

$$
\begin{aligned}
\{\dot{\bar{x}}(t)\} &= [\bar{A}_{AB}(t)]\{\bar{x}(t)\} + \left[\bar{B}_{AB}(t)\right]\left\{\bar{u}_{AB}(t)\right\} \\
\{\lambda_C(t)\} &= \left[C^g_{AB}(t)\right]\{\bar{x}(t)\} + \left[D^g_{AB}(t)\right]\{\bar{u}_{AB}(t)\}
\end{aligned}
\tag{5.19}
$$

with,

$$
\begin{aligned}
[\bar{A}_{AB}(t)] &= [A_{S,D}(t)] - [B_{S,D}(t)][B_C]^T([B_C][D^{accel}_{S,D}(t)][B_C]^T)^{-1}[B_C][C^{accel}_{S,D}(t)] \\
[\bar{B}_{AB}(t)] &= [B_{S,D}(t)] - [B_{S,D}(t)][B_C]^T([B_C][D^{accel}_{S,D}(t)][B_C]^T)^{-1}[B_C][D^{accel}_{S,D}(t)] \\
[C^g_{AB}(t)] &= ([B_C][D^{accel}_{S,D}(t)][B_C]^T)^{-1}[B_C][C^{accel}_{S,D}(t)] \\
[D^g_{AB}(t)] &= ([B_C][D^{accel}_{S,D}(t)][B_C]^T)^{-1}[B_C][D^{accel}_{S,D}(t)] \\
\{\bar{u}_{AB}(t)\} &= \left\{\bar{u}^a_{AB}(t) \quad \bar{u}^b_{AB}(t) \quad \bar{u}^c_{AB}(t) \quad \bar{u}^d_{AB}(t)\right\}^T
\end{aligned}
\tag{5.20}
$$

while, $[A_{S,D}(t)]$, $[B_{S,D}(t)]$, $[C_{S,D}(t)]$ and $[D_{S,D}(t)]$ are given as follows:

$$
\begin{aligned}
[A_{S,D}(t)] &= \begin{bmatrix} A_A(t) & \\ & A_B(t) \end{bmatrix}, \quad [B_{S,D}(t)] = \begin{bmatrix} B_A(t) & \\ & B_B(t) \end{bmatrix} \\
[C^{accel}_{S,D}(t)] &= \begin{bmatrix} C^{accel}_A(t) & \\ & C^{accel}_B(t) \end{bmatrix}, \quad [D^{accel}_{S,D}(t)] = \begin{bmatrix} D^{accel}_A(t) & \\ & D^{accel}_B(t) \end{bmatrix}
\end{aligned}
\tag{5.21}
$$

where, subscripts A and B denote, respectively, variables associated with the source

and with the passive system, subscript AB represents variables associated with the assembled structure AB, while $\{\lambda_C(t)\}$ is given as hereafter.

$$\begin{Bmatrix} g_A(t) \\ g_B(t) \end{Bmatrix} = -[B_C]^T\{\lambda_C(t)\} \qquad (5.22)$$

By analyzing expressions (5.19) and (5.22), it is clear that if $[B_C]$ (see section 2.2.1) is set-up by assigning negative unitary coefficients to the interface DOF of the source, $\{\lambda_C(t)\} = \{g_A(t)\}$. In contrast, if $[B_C]$ is defined by assigning negative unitary coefficients to the interface DOFs of the passive system, $\{\lambda_C(t)\} = \{g_B(t)\}$.

It is worth mentioning that in expression (5.19) the state-space matrices were assumed to be dependent on time, because by using state-space models to calculate the connecting forces in time-domain, we can take into account possible variations on the dynamics of the source and of the passive component (see section 5.2). Thus, from now on, when working on time-domain, the state-space matrices of the state-space models will be assumed to be time-dependent.

Even though by using LM-SSS we can compute the intended connecting forces, we are required to know the excitation forces generated by the internal mechanism of the source (see expression (5.19)). In practice, these internal forces are unknown and impossible to be measured [94]. Thus, to circumvent the need of measuring the forces generated by the internal mechanism of the source, we may exploit the matrix inverse method. This method enables the computation of the connecting forces by using a representation of the dynamics of the passive system (e.g. FRFs or state-space model) together with the operational responses measured at the passive system or at the interface between this component and the source, provided that the passive system is only excited by the source [94]. In the frequency domain, this method can be exploited to compute the connecting forces as follows [94]:

$$\{G_B(j\omega)\} = \begin{bmatrix} H_B^{bb,accel}(j\omega) \\ H_B^{cb,accel}(j\omega) \\ H_B^{db,accel}(j\omega) \end{bmatrix}^{\dagger} \begin{Bmatrix} \ddot{Y}_{AB}^b(j\omega) \\ \ddot{Y}_{AB}^c(j\omega) \\ \ddot{Y}_{AB}^d(j\omega) \end{Bmatrix} \qquad (5.23)$$

where, superscripts d and c denote, respectively, variables related to the target and indicator DOFs (see figure 5.18). Expression (5.23) can be rewritten by using the state-space matrices of a state-space model representative of the dynamics of the passive system as given hereafter.

$$\{G_B(j\omega)\} = \begin{bmatrix} [C_B^{b,accel}](j\omega[I] - [A_B])^{-1}[B_B^b] + [D_B^{bb,accel}] \\ [C_B^{c,accel}](j\omega[I] - [A_B])^{-1}[B_B^b] + [D_B^{cb,accel}] \\ [C_B^{d,accel}](j\omega[I] - [A_B])^{-1}[B_B^b] + [D_B^{db,accel}] \end{bmatrix}^{\dagger} \begin{Bmatrix} \ddot{Y}_{AB}^b(j\omega) \\ \ddot{Y}_{AB}^c(j\omega) \\ \ddot{Y}_{AB}^d(j\omega) \end{Bmatrix} \qquad (5.24)$$

To estimate the connecting forces in time-domain, we may exploit the inverted

acceleration state-space model of the passive system (see appendix A) as follows:

$$\{\dot{x}_B(t)\} = [A_B^{inv}(t)]\{x_B(t)\} + \left[B_B^{inv}(t)\right] \begin{Bmatrix} \ddot{y}_{AB}^b(t) \\ \ddot{y}_{AB}^c(t) \\ \ddot{y}_{AB}^d(t) \end{Bmatrix}$$

$$\{g_B(t)\} = \left[C_B^{inv}(t)\right]\{x_B(t)\} + \left[D_B^{inv}(t)\right] \begin{Bmatrix} \ddot{y}_{AB}^b(t) \\ \ddot{y}_{AB}^c(t) \\ \ddot{y}_{AB}^d(t) \end{Bmatrix} \qquad (5.25)$$

where,

$$[A_B^{inv}(t)] = [A_B(t)] - [B_B^b(t)][D_B^{bcd,b}(t)]^\dagger[C_B^{bcd}(t)]$$

$$[B_B^{inv}(t)] = [B_B^b(t)][D_B^{bcd,b}(t)]^\dagger$$

$$[C_B^{inv}(t)] = -[D_B^{bcd,b}(t)]^\dagger[C_B^{bcd}(t)] \qquad (5.26)$$

$$[D_B^{inv}(t)] = [D_B^{bcd,b}(t)]^\dagger$$

while, $[C_B^{bcd}(t)]$ and $[D_B^{bcd,b}(t)]$ are given below.

$$[C_B^{bcd}(t)] = \begin{bmatrix} C_B^{b,accel}(t) \\ C_B^{c,accel}(t) \\ C_B^{d,accel}(t) \end{bmatrix}, \quad [D_B^{bcd,b}(t)] = \begin{bmatrix} D_B^{bb,accel}(t) \\ D_B^{cb,accel}(t) \\ D_B^{db,accel}(t) \end{bmatrix} \qquad (5.27)$$

For the sake of completeness, in expressions (5.23), (5.24) and (5.25) the connecting forces are calculated by exploiting measured operational responses at the interface, indicators and targets location. However, in practice it is common to determine those forces by only using operational responses measured at the indicators [94]. Indeed, the measured responses at the target DOFs are generally not used to estimate the connecting forces, because the number of target DOFs is commonly small and these DOFs are many times placed far away from the interface. Hence, they do not properly observe the connecting forces. On the other hand, the responses at the interface DOFs are usually difficult to be measured. Conversely, the location of the indicator DOFs is specially chosen to be accessible and close to the interface between the source and the passive system to ensure a proper observation of the full set of connecting forces. On top of this, the number of these DOFs is typically at least two times higher than the number of connecting forces to be identified to guarantee over-determination [136], [94] and hence, better conditioning of the feedthrough matrix to be inverted.

Note that as the matrix inverse method requires the characterization of the dynamics of the passive system, we are demanded to dismount this system from the assembly where it is included, in case that its characterization is to be experimentally performed. In addition, we must bear in mind that the connecting forces are a property of the assembly (i.e. source connected to the passive system) (see expression (5.19)), thus this

set of forces is not transferable to an assembled system composed by the same source connected to a different passive component.

5.3.3   State-Space realization of the in-situ component-based TPA method

In this section, we will present the state-space realization of the in-situ component-based TPA method. This approach will be presented to demonstrate, which state-space models and operational responses must be used to compute equivalent forces in time-domain by exploiting the state-space formulation. Once again, for the sake of simplicity, we will assume that the estimation of the equivalent forces is performed in a linear-least squares sense. However, as mentioned in section 5.3.2, when the forces are to be estimated from measured operational responses, the use of a linear-least squares approach is not recommended. Hence, when estimating equivalent forces from measured operational responses, one must exploit more robust techniques, for instance, joint input-state estimation algorithms (see, for example, [126], [180]) and the Augmented Kalman filter (AKF) (see, for example, [150], [181], [182]).

To start, let us once again consider the assembled structure shown in figure 5.20a, which is composed by a source A and a passive system B rigidly connected. The family of the component-based TPA methods aims at determining a set of forces that when applied on the source at rest, reproduce the operational responses at the passive system. This is illustrated in figure 5.20b. These estimated forces are usually denoted as equivalent forces and are an inherent property of the source itself. Thus, these forces can be used to simulate the operational responses on the passive side of any assembly composed by the same source connected to any passive system [94], [34].

By analyzing figures 5.20, it is evident that the operational responses at the indicator DOFs can be computed by following two different strategies. On the one hand, we may compute these operational responses by exploiting the internal forces originated by the internal mechanism of the source, on the other hand, we can determine the operational responses by using the equivalent forces of the source. Thus, by following both strategies and assuming that we aim at computing the acceleration operational responses at the indicators, we may define the following identity

(a) Operational responses resultant from the forces originated by the internal mechanisms of the source.

(b) Operational responses resultant from the equivalent forces computed with component-based TPA.
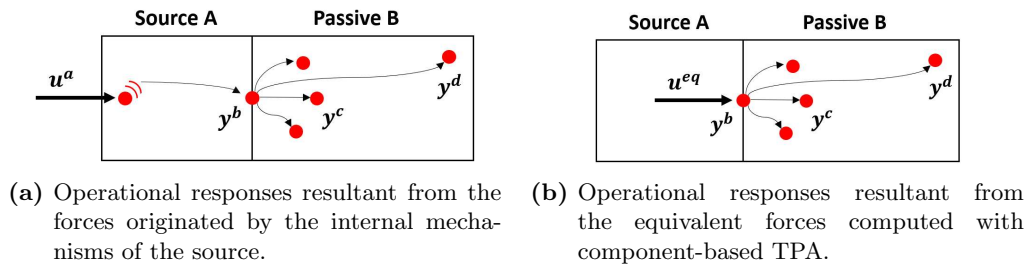
Figure 5.20: Assembly composed by a source and a passive system rigidly connected.

$$\left[\bar{H}_{AB}^{db,accel}(j\omega)\right]\left\{U^{b,eq}(j\omega)\right\} = \left[\bar{H}_{AB}^{da,accel}(j\omega)\right]\left\{U_{AB}^{a}(j\omega)\right\} \tag{5.28}$$

where, $\left\{U^{b,eq}(j\omega)\right\} \in \mathbb{C}^{n_J \times 1}$ is the vector containing the equivalent forces of the source in the frequency domain. By exploiting LM-FBS (see section 2.2.2) and by dropping $[\bullet]$, $\{\bullet\}$ and $(j\omega)$ for ease of readability, we may rewrite expression (5.28) as given below (see, for instance, [94]).

$$H_B^{db,accel} E_{AB} H_A^{bb,accel} U^{b,eq} = H_B^{db,accel} E_{AB} H_A^{ba,accel} U_{AB}^a \tag{5.29}$$

where, E_{AB} is given below.

$$E_{AB} = (H_A^{bb,accel} + H_B^{bb,accel})^{-1} \tag{5.30}$$

Expression (5.29) can be rewritten as hereafter:

$$U^{b,eq} = (H_A^{bb,accel})^{-1} H_A^{ba,accel} U_{AB}^a \tag{5.31}$$

by using the state-space model of the source, we may define $\left[H_A^{bb,accel}(j\omega)\right]$ and $\left[H_A^{ba,accel}(j\omega)\right]$ as given below.

$$\begin{aligned} H_A^{bb,accel} &= C_A^{b,accel}(j\omega I - A_A)^{-1} B_A^b + D_A^{bb,accel} \\ H_A^{ba,accel} &= C_A^{b,accel}(j\omega I - A_A)^{-1} B_A^a + D_A^{ba,accel} \end{aligned} \tag{5.32}$$

Analyzing expressions (5.31) and (5.32), we may realize that the equivalent forces are, indeed, a property of the source itself. To compute the equivalent forces in time-domain, we may exploit the inverted acceleration state-space model (see appendix A) representative of the assembled structure as follows:

$$\begin{aligned} \{\dot{x}_A^{inv}(t)\} &= \left[A_A^{inv}(t)\right]\{x_A^{inv}(t)\} + \left[B_A^{b,inv}(t)\right]\{\ddot{y}_A^b(t)\} \\ \{u^{b,eq}(t)\} &= \left[C_A^{b,inv}(t)\right]\{x_A^{inv}(t)\} + \left[D_A^{bb,inv}(t)\right]\{\ddot{y}_A^b(t)\} \end{aligned} \tag{5.33}$$

where,

$$\begin{aligned} [A_A^{inv}(t)] &= [A_A(t)] - [B_A^b(t)][D_A^{bb,accel}(t)]^{-1}[C_A^{b,accel}(t)] \\ [B_A^{inv}(t)] &= [B_A^b(t)][D_A^{bb,accel}(t)]^{-1} \\ [C_A^{inv}(t)] &= -[D_A^{bb,accel}(t)]^{-1}[C_A^{b,accel}(t)] \\ [D_A^{inv}(t)] &= [D_A^{bb,accel}(t)]^{-1} \end{aligned} \tag{5.34}$$

while, the acceleration responses $\{\ddot{y}_A^b(t)\}$ can be computed by exploiting the state-space model given below.

$$\{\dot{x}_A(t)\} = [A_A(t)]\{x_A(t)\} + \left[B_A^a(t)\right]\left\{u_A^a(t)\right\}$$

$$\left\{\ddot{y}_A^b(t)\right\} = \left[C_A^{b,accel}(t)\right]\{x_A(t)\} + \left[D_A^{ba,accel}(t)\right]\left\{u_A^a(t)\right\} \tag{5.35}$$

By exploiting expression (5.33) and (5.35), we can compute the intended set of time-domain equivalent forces, however we are required to know the internal forces originated by the internal mechanisms of the source. As mentioned in section 5.3.2, these internal forces are unknown and impossible to be measured in practice. Thus, to compute the equivalent forces, we may, for instance, exploit the in-situ method proposed by Moorhouse and Elliott (see [154],[155]). This method enables the calculation of the equivalent forces by using a representation of the dynamics of the assembled structure (e.g. FRFs or state-space model) together with operational responses measured at the passive system or at the interface between this component and the source, provided that the passive system is only excited by the source [94]. In this way, by using this method we are able to calculate the equivalent forces without using special test-rigs and without dismounting any component. By following this approach, the equivalent forces at the interface between the source and the passive system can be computed as hereafter.

$$\left\{U^{b,eq}(j\omega)\right\} = \begin{bmatrix} \bar{H}_{AB}^{bb,accel}(j\omega) \\ \bar{H}_{AB}^{cb,accel}(j\omega) \\ \bar{H}_{AB}^{db,accel}(j\omega) \end{bmatrix}^{\dagger} \begin{Bmatrix} \ddot{\bar{Y}}_{AB}^b(j\omega) \\ \ddot{\bar{Y}}_{AB}^c(j\omega) \\ \ddot{\bar{Y}}_{AB}^d(j\omega) \end{Bmatrix} \tag{5.36}$$

Alternatively, by exploiting a state-space model representative of the dynamics of the assembled structure (see figure 5.20a), expression (5.36) can be rewritten as given below.

$$\left\{U^{b,eq}(j\omega)\right\} = \begin{bmatrix} [\bar{C}_{AB}^{b,accel}](j\omega[I] - [\bar{A}_{AB}])^{-1}[\bar{B}_{AB}^b] + [\bar{D}_{AB}^{bb,accel}] \\ [\bar{C}_{AB}^{c,accel}](j\omega[I] - [\bar{A}_{AB}])^{-1}[\bar{B}_{AB}^b] + [\bar{D}_{AB}^{cb,accel}] \\ [\bar{C}_{AB}^{d,accel}](j\omega[I] - [\bar{A}_{AB}])^{-1}[\bar{B}_{AB}^b] + [\bar{D}_{AB}^{db,accel}] \end{bmatrix}^{\dagger} \begin{Bmatrix} \ddot{\bar{Y}}_{AB}^b(j\omega) \\ \ddot{\bar{Y}}_{AB}^c(j\omega) \\ \ddot{\bar{Y}}_{AB}^d(j\omega) \end{Bmatrix} \tag{5.37}$$

To compute the equivalent forces in time-domain by using the in-situ method, we may exploit the state-space model of the assembled structure as follows:

$$\{\dot{\bar{x}}(t)\} = \left[\bar{A}_{AB}^{inv}(t)\right]\{\bar{x}(t)\} + \left[\bar{B}_{AB}^{b,inv}(t)\right] \begin{Bmatrix} \ddot{\bar{y}}_{AB}^b(t) \\ \ddot{\bar{y}}_{AB}^c(t) \\ \ddot{\bar{y}}_{AB}^d(t) \end{Bmatrix}$$

$$\left\{u^{b,eq}(t)\right\} = \left[\bar{C}_{AB}^{bcd,inv}(t)\right]\{\bar{x}(t)\} + \left[\bar{D}_{AB}^{bcd,b,inv}(t)\right] \begin{Bmatrix} \ddot{\bar{y}}_{AB}^b(t) \\ \ddot{\bar{y}}_{AB}^c(t) \\ \ddot{\bar{y}}_{AB}^d(t) \end{Bmatrix} \tag{5.38}$$

where,

$$[\bar{A}_{AB}^{inv}(t)] = [\bar{A}_{AB}(t)] - [\bar{B}_{AB}^{b}(t)][\bar{D}_{AB}^{bcd,b}(t)]^{\dagger}[\bar{C}_{AB}^{bcd}(t)]$$
$$[\bar{B}_{AB}^{b,inv}(t)] = [\bar{B}_{AB}^{b}(t)][\bar{D}_{AB}^{bcd,b}(t)]^{\dagger}$$
$$[\bar{C}_{AB}^{bcd,inv}(t)] = -[\bar{D}_{AB}^{bcd,b}(t)]^{\dagger}[\bar{C}_{AB}^{bcd}(t)] \tag{5.39}$$
$$[\bar{D}_{AB}^{bcd,b,inv}(t)] = [\bar{D}_{AB}^{bcd,b}(t)]^{\dagger}$$

while, $[\bar{C}^{bcd}(t)]$ and $[\bar{D}^{bcd,b}(t)]$ are given below.

$$\left[\bar{C}_{AB}^{bcd}(t)\right] = \begin{bmatrix} \bar{C}_{AB}^{b,accel}(t) \\ \bar{C}_{AB}^{c,accel}(t) \\ \bar{C}_{AB}^{d,accel}(t) \end{bmatrix}, \quad \left[\bar{D}_{AB}^{bcd,b}(t)\right] = \begin{bmatrix} \bar{D}_{AB}^{bb,accel}(t) \\ \bar{D}_{AB}^{cb,accel}(t) \\ \bar{D}_{AB}^{db,accel}(t) \end{bmatrix} \tag{5.40}$$

It is worth mentioning that, for the sake of completeness, in expressions (5.36), (5.37) and (5.38), we have assumed that the equivalent forces are computed from the measured operational responses at the interface, indicator and target DOFs. However, for the reasons presented in section 5.3.2, in practice the equivalent forces are in general computed by only using operational responses measured at the indicator DOFs.

5.4   Numerical Validation

In this section, the state-space realizations of the matrix inverse method (see section 5.3.2) and of the in-situ component-based TPA (see section 5.3.3) will be applied on numerical TPA cases. The two assemblies depicted in figure 5.21 will be analyzed. The assembly AB is composed by the substructures A and B studied in section 5.2.2 rigidly connected, while assembly AC is composed by the substructure A rigidly connected to the substructure C, which was also analyzed in section 5.2.2.

In the following, we will assume that the substructure A is a source, while substruc-
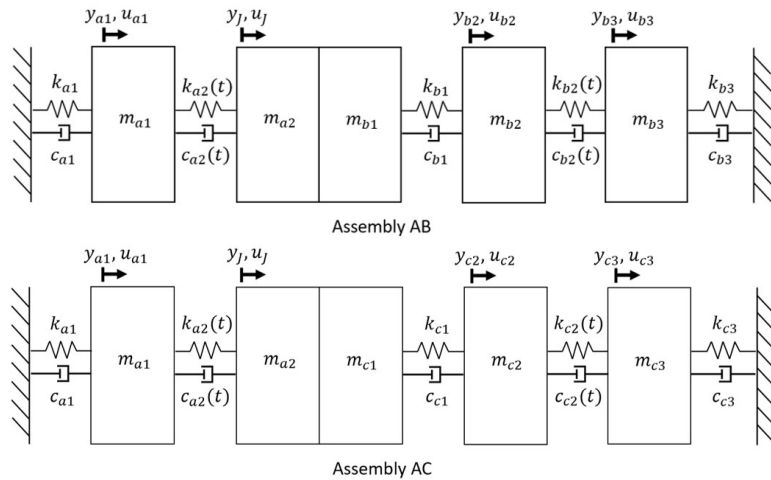
Figure 5.21: Assembled structures AB and AC [6].

tures B and C are two different passive components. Additionally, we will assume that the mechanical properties of the three substructures are time-varying and dependent on the three time-varying parameters presented in section 5.2.2 (i.e. n_1, n_2 and n_3), whose variation over time is given in figure 5.2. Moreover, assemblies AB and AC (see figure 5.21) will be analyzed for a time period of 4 s. During this time period, we will presume that the source (substructure A) is turned on during 1 s originating a transient load at DOF a_1 of 10 N. Then, the source is shut down and hence, the force acting on DOF a_1 during the remaining 3 s drops to zero.

We will start this section by applying the state-space realization of the matrix inverse method to determine the connecting forces acting on the interface of assembly AB (section 5.4.1). Afterwards, in section 5.4.2 the state-space realization of the in-situ component-based TPA method will be applied to determine the equivalent forces of substructure A (which is assumed to be an active component).

5.4.1   Numerical Validation of the state-space realization of the matrix inverse method

In this section, we will start by computing the analytical time-domain connecting force acting on the interface of component B. This force will then serve as reference to evaluate the accuracy of the state-space realization of the matrix-inverse method presented in section 5.3.2. To compute the intended analytical time-domain connecting force, we will define at each time sample a state-space model as given in expression (5.19). These state-space models must be computed by using the models representative of the dynamics of components A and B at each time sample (computed in section 5.2.2) in accordance with expressions (5.20). Moreover, the mapping matrix $[B_C]$ involved in the computation of the intended models must be set-up by assigning negative unitary values to the interface DOFs of substructure B. Thereby, the computed state-space models will enable the determination of the connecting force acting on the interface of substructure B instead of leading to the determination of the connecting force acting on the interface of substructure A (which is equal in intensity and opposite in direction) (see section 5.3.2). In this way, by using the force generated by the internal mechanism of source A and by discretizing the computed state-space models with a sampling frequency of 2×10^4 Hz and by exploiting the first-order-hold (foh) method (see [183]), the analytical time-domain connecting force acting on the interface of component B can be determined as follows:

$$\{\bar{x}_{AB,k+1}\} = [\bar{A}_{AB,k}]\{\bar{x}_{AB,k}\} + \left[\bar{B}_{AB,k}\right] \begin{Bmatrix} \bar{u}^{a_1}_{AB,k} \\ \bar{u}^{J}_{AB,k} \\ \bar{u}^{b_2}_{AB,k} \\ \bar{u}^{b_3}_{AB,k} \end{Bmatrix}$$

$$\{g_{B,k}\} = \left[C^{g}_{AB,k}\right]\{\bar{x}_{AB,k}\} + \left[D^{g}_{AB,k}\right] \begin{Bmatrix} \bar{u}^{a_1}_{AB,k} \\ \bar{u}^{J}_{AB,k} \\ \bar{u}^{b_2}_{AB,k} \\ \bar{u}^{b_3}_{AB,k} \end{Bmatrix} \qquad (5.41)$$

where, subscript AB denotes variables associated with a state-space model representative of the dynamics of assembly AB, while k represents the time sample under analysis.

At this point, by exploiting the state-space realization of the matrix inverse method (see section 5.3.2), we will compute the connecting force acting on the interface of substructure B in time-domain by using two different approaches. Nevertheless, before being able to exploit the matrix inverse method, we must compute the operational responses of assembly AB. To determine these operational responses, we will start by constructing at each time sample state-space models representative of the dynamics of assembly AB directly from its mechanical properties. Again, for the sake of simplicity, the damping matrix of assembly AB at each time sample will be defined from the respective stiffness matrix by replacing the stiffness terms with the damping ones. Then, by using the input force generated by the source (substructure A) and by discretizing the computed state-space models with a sampling frequency of 2×10^4 Hz and by using the foh method, the time-domain operational responses of assembly AB can be determined as given below.

$$\{x_{AB,k+1}\} = \left[A_{AB,k}\right]\{x_{AB,k}\} + \left[B_{AB,k}\right] \begin{Bmatrix} u^{a_1}_{AB,k} \\ u^{J}_{AB,k} \\ u^{b_2}_{AB,k} \\ u^{b_3}_{AB,k} \end{Bmatrix}$$

$$\begin{Bmatrix} \ddot{y}^{a_1}_{AB,k} \\ \ddot{y}^{J}_{AB,k} \\ \ddot{y}^{b_2}_{AB,k} \\ \ddot{y}^{b_3}_{AB,k} \end{Bmatrix} = \left[C^{accel}_{AB,k}\right]\{x_{AB,k}\} + \left[D^{accel}_{AB,k}\right] \begin{Bmatrix} u^{a_1}_{AB,k} \\ u^{J}_{AB,k} \\ u^{b_2}_{AB,k} \\ u^{b_3}_{AB,k} \end{Bmatrix} \qquad (5.42)$$

Note that, from now on the state-space models involved in calculations/simulations performed in time-domain will always be discretized with the foh method and by using a sampling frequency of 2×10^4 Hz.

After having determined the operational responses of assembly AB, we can exploit the state-space realization of the matrix inverse method to compute the time-domain connecting force acting on the interface of substructure B. To start, the intended

connecting force will be calculated by exploiting the state-space realization of the matrix inverse method with the computed operational responses at the interface DOF and at the DOF b_2 of assembly AB and by using the discretized analytically determined models representative of the dynamics of substructure B at each time sample (see section 5.2.2). Afterwards, the connecting force will be re-determined by following the same procedure, but by exploiting discretized state-space models computed at each time sample from the LPV model representative of the dynamics of component B calculated in section 5.2.1.

It is worth mentioning that, as discussed in section 5.3.2, it is not usual to determine connecting forces by exploiting operational responses measured at the interface between the source and the passive system. Nevertheless, in this numerical example, we were forced to exploit the operational responses measured at the interface of assembly AB, because to implement the state-space realization of the matrix inverse method we are required to invert the feedthrough matrix of substructure B. As the mass matrices of this substructure are assumed to be diagonal, the feedthrough matrices of the state-space models computed from its mechanical properties will be diagonal as well. For this reason, to avoid the inversion of null matrices, we performed the estimation of the connecting force acting on the interface of substructure B by using the operational responses at the interface of assembly AB. In contrast, when dealing with structures, whose dynamics is represented by state-space models estimated from experimentally acquired data, the state-space realization of the matrix inverse method can be exploited without using the operational responses at the interface between the source and the passive side, because the feedthrough matrices of models estimated from measured data are not diagonal.

Figure 5.22a shows the comparison of the analytical connecting force with the two estimations of the connecting force obtained by exploiting the state-space realization of the matrix inverse method (see expression (5.19)). Moreover, figure 5.22b shows the comparison of the operational acceleration response of assembly AB at DOF b_3 with the operational acceleration response estimated at the same DOF by using the connecting forces obtained by implementing the state-space realization of the matrix inverse method with the discretized analytical models of substructure B and with the discretized models of the same substructure computed by using the correspondent interpolating LPV model (see section 5.2.2).

By observing figure 5.22a, we conclude that the connecting force computed by exploiting the state-space realization of the matrix inverse method with discretized analytical models is perfectly matching the analytical connecting force. Additionally, the operational response at DOF b_3 computed by using this connecting force with the discretized analytical models of component B is also perfectly matching the analytical operational response at DOF b_3 of assembly AB (see figure 5.22b). Thus, showing that the state-space realization of the matrix inverse method is indeed valid to compute time-domain connecting forces (see section 5.3.2) even when dealing with components
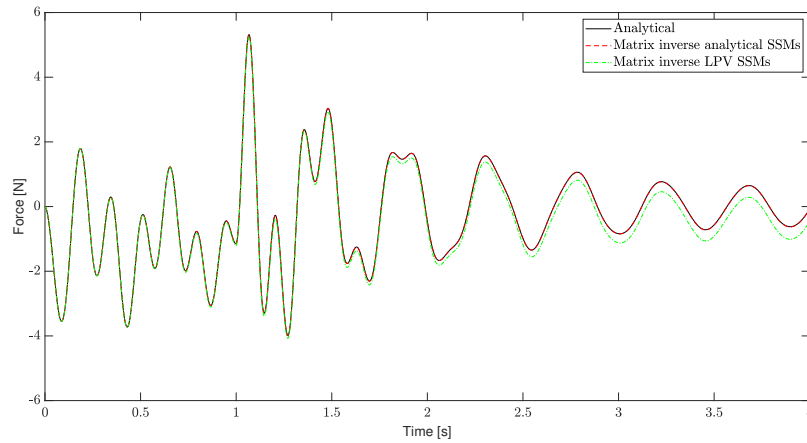
(a) Connecting force.
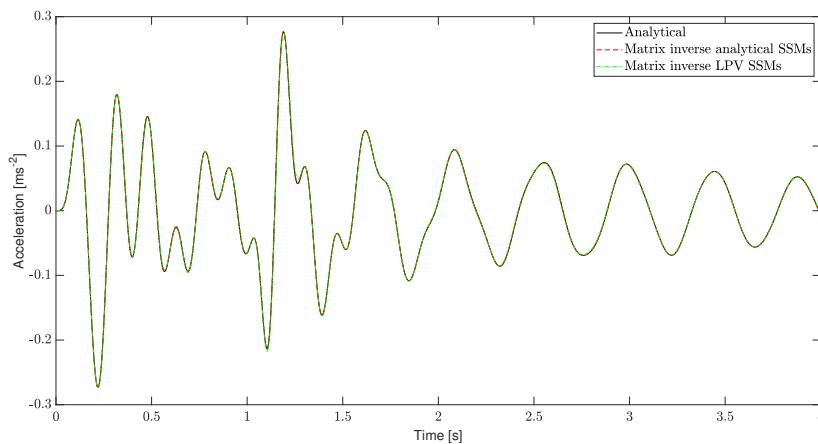
(b) Operational acceleration response at DOF b_3 of assembly AB.

Figure 5.22: Comparison of the computed connecting force and of the operational acceleration response at the DOF b_3 of assembly AB by following three different methodologies: analytically (represented by the black solid curve); by using the analytically determined models representative of the dynamics of substructure B at each time sample (represented by the red dashed curve) and by using state-space models representative of component B computed at each time sample by exploiting the correspondent constructed LPV model (represented by the green dash-dotted curve).

presenting time-varying dynamic behaviour.

Moreover, by further analyzing figure 5.22a, it is clear that the connecting force estimated by exploiting the state-space realization of the matrix inverse method with discretized state-space models computed from the interpolating LPV model of substructure B is well matching the analytical connecting force. On top of this, the operational response at DOF b_3 of assembly AB can be accurately reconstructed by using the estimated connecting force (see figure 5.22b). Therefore, we may conclude that the use of an interpolating LPV model to take into account the time-varying behaviour of mechanical systems, while computing connecting forces is a valid approach.

To demonstrate the benefit of taking into account the time-varying behaviour of component B, the connecting force was re-calculated by assuming that the parameter n_2 is kept constant and equal to one during the time period under analysis. Figure 5.23a shows the comparison of the analytical connecting force with: i) the same force obtained by using the state-space realization of the matrix inverse method with discretized state-space models representative of component B determined at each time sample from the correspondent LPV model (see section 5.2.2) and ii) with the discretized analytical state-space model of component B for $n_2 = 1$. In figure 5.23b, it is also shown the comparison of the reference operational acceleration response at DOF b_3 of assembly AB with the operational acceleration responses predicted by the following approaches: a) by exploiting the discretized state-space models of component B computed at each time sample from the correspondent estimated LPV model (see section 5.2.2) with the connecting force obtained through approach i) and b) by exploiting the discretized analytical state-space model of component B associated with $n_2 = 1$ with the connecting force determined from approach ii).

By analyzing figure 5.23a, it is evident that the connecting force computed by taking into account the time-varying dynamic behaviour of component B by exploiting the correspondent constructed LPV model (see section 5.2.2) is better matching the analytical connecting force than the estimation obtained by using the analytical state-space model associated with $n_2 = 1$, which neglects the time-varying dynamic behaviour of component B. Moreover, the same conclusions can be taken when comparing the reconstructed operational response at DOF b_3 of assembly AB by using each of the estimated connecting forces. These observations clearly demonstrate that to accurately determine connecting forces by using the matrix inverse method, we must take into account possible time-domain variations on the dynamics of the target structures.

5.4.2 Numerical Validation of the state-space realization of the in-situ component-based TPA method

Here, we will start by computing the time-domain analytical equivalent force of component A. This force will be computed in two steps. Firstly, the operational acceleration responses at the interface of component A (see expression (5.35)) will be
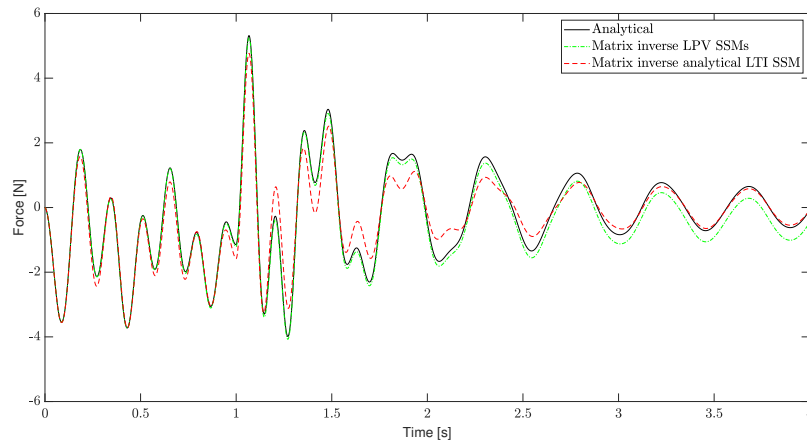
(a) Connecting force.
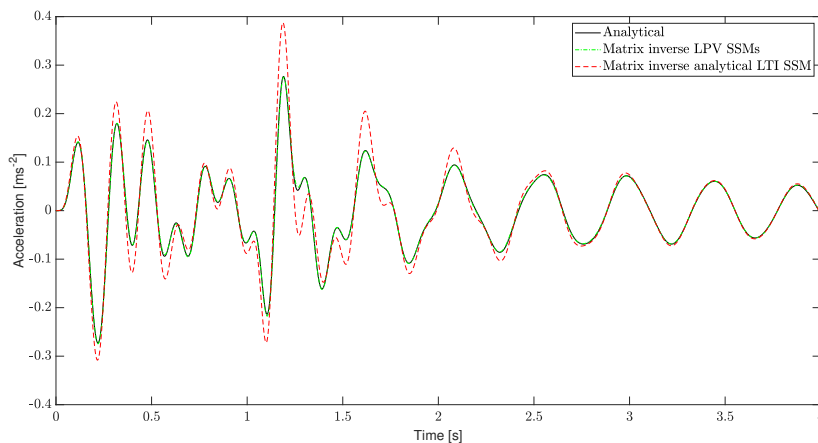
(b) Operational acceleration response at DOF b_3 of assembly AB.

Figure 5.23: Comparison of the computed connecting force and of the operational acceleration response at the DOF b_3 of assembly AB by following three different methodologies: analytically (represented by the black solid curve), by using state-space models representative of component B computed at each time sample by exploiting the correspondent constructed LPV model (represented by the green dash-dotted curve) and by using the analytical state-space model of component B associated with $n_2 = 1$ (represented by the red dashed curve).

determined from the applied force at DOF $a1$ and by using the discretized analytically determined state-space models (see section 5.2.2) representative of the dynamics of this substructure at each time instant. Then, the intended equivalent force will be calculated by exploiting those operational responses and the discretized inverted analytical acceleration models representative of component A at each time sample (see expression (5.33)).

To evaluate the accuracy of the in-situ component-based TPA method (see section 5.3.3), when dealing with substructures presenting time-varying dynamics, the time-domain equivalent force of component A will be re-estimated by using this method with the operating acceleration responses at the interface DOF and at DOFs b_2 and b_3 of assembly AB together with discretized acceleration models representative of the dynamics of assembly AB at each time sample. The acceleration models of assembly AB will be computed by using two different methodologies. Firstly, the intended models will be calculated by using LM-SSS to couple the analytically determined displacement models representative of substructures A and B (see section 5.2.2) at each time sample. To remove the originated redundant states from each of the computed coupled models, we will exploit the post-processing procedure presented in section 2.3.3 that makes use of a state Boolean localization matrix, while to eliminate the redundant DOFs of each of the computed coupled models, the method presented in section 2.3.4 will be used. In the second strategy, the intended coupled models will be obtained by exploiting LM-SSS to couple the displacement models representative of the dynamics of substructures A and B at each time sample computed by using the interpolating LPV models defined in section 5.2.2. It is important to mention that the state-space models computed from the LPV models were transformed into UCF, before being coupled. This was done, because the state-space models estimated from the defined LPV models are represented in complex diagonal form (see sections 5.2.1 and 5.2.2). Thus, to be able to compute minimal-order coupled models, we were required to transform these models into UCF (see section 2.3.2) before coupling them. Once again, the originated redundant states and DOFs of each of the coupled state-space models were eliminated by using, respectively, the post-processing procedure presented in section 2.3.3 that makes use of a state Boolean localization matrix and the post-processing procedure presented in section 2.3.4. Obviously, by following both described strategies, we obtain displacement coupled state-space models representative of assembly AB at each time sample. Thus, these models must be double-differentiated to compute the intended acceleration state-space models to be exploited in the state-space realization of the in-situ component-based TPA method (see section 5.3.3).

To demonstrate that the calculated equivalent forces are indeed, a property of the source and that they can be used to predict the responses on the passive side of structures made of the same source and different passive systems, coupled state-space models representative of assembly AC will also be computed by using the analytical models of substructures A and C at each time sample and by exploiting the models of the same

components computed from the respective constructed LPV models at each time sample (see section 5.2.2). The elimination of the originated redundant states and DOFs from the computed coupled models will be done by exploiting the same post-processing procedures used to eliminate the redundant states and DOFs from the computed coupled models representative of assembly AB.

In figure 5.24a, the time-domain analytical equivalent force of component A is compared with the equivalent force computed by using the following approaches: a) time-domain equivalent force obtained by exploiting the state-space realization of the in-situ component-based TPA method with the discretized coupled models obtained by coupling the analytically determined models representative of substructures A and B at each time sample and b) time-domain equivalent force determined by exploiting the state-space realization of the in-situ component-based TPA approach with the discretized coupled models calculated by coupling the interpolated models representative of the dynamics of components A and B at each time sample obtained from the respective interpolating LPV models constructed in section 5.2.2. Figure 5.24b reports the comparison of the analytical operational acceleration response at DOF c_3 of assembly AC (computed by following the methodology used to calculate the analytical operational responses of assembly AB in section 5.4.1) with the operational acceleration responses at the same DOF computed by exploiting the following approaches: i) operational acceleration response obtained by using the equivalent force computed through approach a) with the discretized coupled models of AC obtained by coupling at each time sample the analytical models representative of substructures A and C and ii) operational acceleration response estimated by using the equivalent force computed with approach b) together with the discretized coupled models of AC determined by coupling at each time sample the state-space models representative of the dynamics of substructures A and C computed by using the respective interpolating LPV models defined in section 5.2.2.

By observing figure 5.24a, it is clear that the equivalent force computed by exploiting methodology a) is perfectly matching the analytical one. Moreover, by analyzing figure 5.24b, it is clear that the analytical operational response at the DOF $c3$ of assembly AC is perfectly matched by the correspondent operational response computed by using the equivalent force obtained from approach b). Thus, demonstrating that the equivalent forces obtained by using the state-space realization of the in-situ component-based TPA are in fact, an inherent property of the source and hence, that can be used to predict the operational responses on the passive side of assemblies composed by the same source connected to any different passive system.

Further analyzing figure 5.24a, it is evident that the analytical equivalent force of component A is well-matched by the equivalent force computed with approach b). Furthermore, the operational response at the DOF c_3 of assembly AC computed with approach ii) is well-matching the analytical one (see figure 5.24b). Therefore, we may conclude that the use of the state-space realization of the in-situ component-based TPA
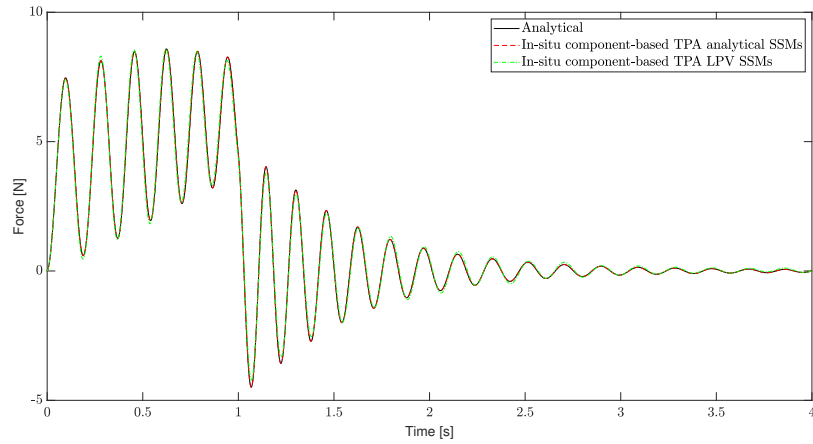
(a) Time-domain equivalent force of component A.
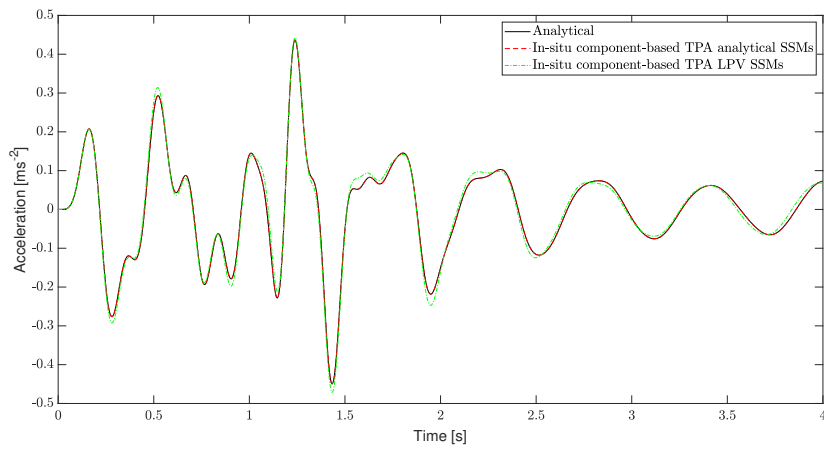
(b) Operational acceleration response at DOF c_3 of assembly AC.

Figure 5.24: Comparison of the time-domain equivalent force of component A and of the operational acceleration response at the DOF c_3 of assembly AC obtained by exploiting three different approaches.

method together with coupled models obtained by coupling state-space models computed from LPV models is an accurate approach to calculate time-domain equivalent forces, when dealing with assemblies, whose dynamics is time-dependent.

As final analysis, to evaluate the importance of taking into account the time-domain variation on the dynamics of assembly AB, we will compute an additional estimation of the equivalent force of component A by exploiting the state-space realization of the in-situ method with the discretized acceleration analytical state-space model of assembly AB associated with $n_1 = n_2 = 1$ and by using the analytical operational acceleration responses of assembly AB at the interface DOF and at DOFs b_2 and b_3 (from now on denoted as methodology c)). In figure 5.25a, it is reported the comparison of the analytical equivalent force of component A with the same equivalent force estimated by exploiting approaches b) and c). Moreover, in figure 5.25b, it is reported the comparison of the analytical operational acceleration response at the DOF c_3 of assembly AC with the operational response at the same DOF computed with approach ii) and by using the equivalent force computed with approach c) together with the discretized acceleration analytical state-space model representative of assembly AC associated with $n_1 = 1$ and $n_3 = 0.7$ (from now on denoted as approach iii)).

By analyzing figure 5.25a, we may conclude that the equivalent force obtained by exploiting approach c) (by neglecting the time-dependency of the dynamics of assembly AB) does not represent a good estimation of the analytical equivalent force. On top of this, the operational acceleration response at DOF c_3 of assembly AC obtained through methodology iii) is poorly matching the correspondent analytical response (see figure 5.25b). The poor quality of the estimated equivalent force obtained with approach c) and of the operational response at DOF c_3 of assembly AC predicted by using approach iii) is a direct consequence of ignoring the time-varying dynamic behaviour of assemblies AB and AC (see figure 5.25b). Hence, it is evident that to estimate accurate equivalent forces and to exploit them to predict the operational responses at the passive side of assemblies composed by the same source and different passive systems, we must not ignore possible time-domain variations on the dynamics of the assemblies under analysis.

Note that, to compute the equivalent force of component A by exploiting the state-space realization of the in-situ component-based TPA method, we have used the interface operational responses of assembly AB. In practice, it is not common to determine equivalent forces by using interface operational responses (see section 5.3.3). However, in this section we dealt with analytically modelled substructures/assemblies, whose mass matrices are assumed to be diagonal and hence, that are characterized by state-space models presenting diagonal feedthrough matrices. Thus, if the operational responses at the interface of assembly AB were not used, we would be demanded to invert null matrices. When dealing with real assemblies, whose state-space models are estimated from experimentally acquired data, we can exploit the state-space realization of the in-situ component-based TPA method without using operational responses
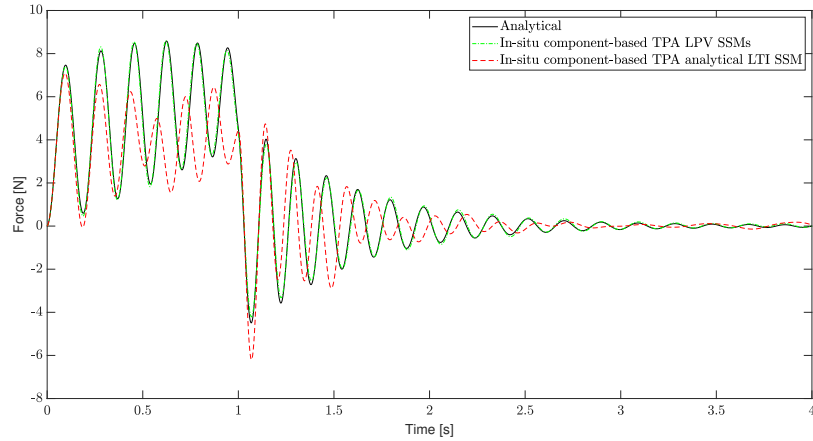
(a) Time-domain equivalent force of component A.
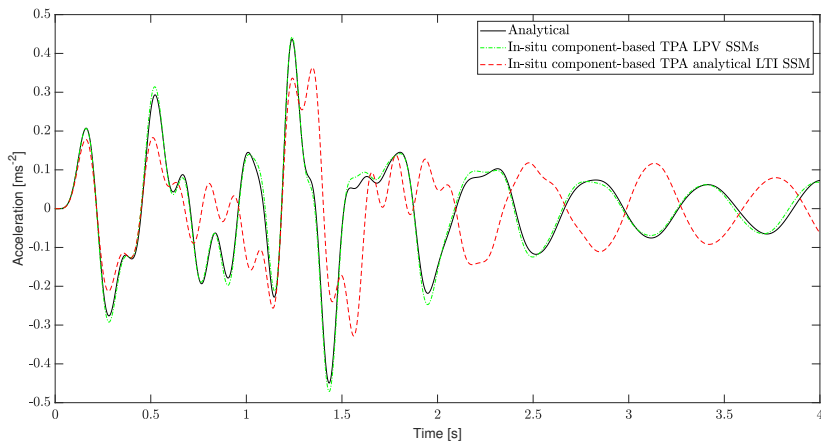
(b) Operational acceleration response at DOF c_3 of assembly AC.

Figure 5.25: Comparison of the time-domain equivalent force of component A and of the operational acceleration response at the DOF c_3 of assembly AC determined by exploiting two different strategies that take into account the time-domain variation on the dynamics of assemblies AB and AC with the equivalent force and operational acceleration response at the DOF c_3 of assembly AC estimated by exploiting a strategy that ignores the time-dependency of the dynamics of assemblies AB and AC.

collected at their interface, because the feedthrough matrices of state-space models estimated from measured data are not diagonal.

Chapter 6

Conclusion

6.1 Conclusions

In this thesis, we have analyzed and discussed in detail the limitations of the state-of-the-art SSS methods (see chapter 2). A similar debate on the limitations of the state-of-the-art approaches to experimentally identify state-space models was also conducted in chapter 3. Along with these discussions, novel methodologies to mitigate the pointed limitations were proposed. This led to a detailed and justified presentation of all the steps to be performed from the experimental identification of state-space models to the computation of stable accurate coupled state-space models. As a result, chapters 2, 3 and 4 demonstrate a substantial evolution of the state-of-the-art that enables the determination of accurate stable coupled state-space models from unstable coupled models originated from the performance of DS operations with non-passive models representative of complex substructures. Moreover, in chapter 5 we have also proposed two novel applications of LPV models in time-domain TPA. These applications clearly demonstrate the benefit of using the state-space formulation and the SSS methods in time-domain TPA applications involving mechanical systems presenting time-domain variations on their dynamics. In the following, conclusions for these three main topics are presented.

State-Space Substructuring

The LM-SSS method was exploited in sections 4.1.1 and 4.2.3 to perform decoupling and coupling operations with state-space models representative of analytical and real mechanical systems, respectively. The accurate results reported on those sections clearly demonstrate that LM-SSS is a reliable SSS method. On top of this, LM-SSS showed to be capable of performing decoupling and coupling operations with models previously transformed into coupling form. In addition, the novel post-processing procedures presented in section 2.3.3 showed to be able to correctly eliminate the redundant states originated from the performance of SSS operations with LM-SSS leading,

in this way, to the computation of accurate minimal-order coupled models. The post-processing procedure presented in section 2.3.4 also demonstrated to perform well, enabling a correct retention of a unique set of DOFs from the coupled state-space models computed with LM-SSS. Moreover, the novel coupling form, denoted UCF, proposed in section 2.3.2 demonstrated to be applicable on state-space models representative of analytical and real mechanical systems. UCF and the coupling form presented in [8] showed to perform similarly. Nevertheless, as discussed in section 2.3.2, UCF presents the relevant advantage of not requiring the selection of a subspace from a nullspace.

In sections 4.1.2 and 4.2.4, the state-space realization of IS demonstrated to be a reliable approach to compute models representative of diagonal apparent mass terms of CEs, whose dynamic behaviour can be accurately characterized by the assumptions underlying IS (see sections 4.1 and 4.2.4). Moreover, the use of these models to introduce the dynamics of CEs into the LM-SSS coupling formulation via compatibility relaxation demonstrated to be an accurate approach to compute coupled models representative of substructures connected by CEs suitable for being characterized by IS (see section 4.2.5). The novel post-processing procedures presented in section 2.5.2 showed to be reliable to eliminate the extra states originated from the performance of coupling operations with LM-SSS via compatibility relaxation leading to the computation of accurate minimal-order coupled models.

Furthermore, by analyzing the rubber mount models computed in the context of the experimental substructuring case analyzed in section 4.2, it is evident that the state-space models determined by exploiting the state-space realization of IS present a significant lower number of states than the models identified by performing decoupling operations with LM-SSS or by implementing primal state-space disassembly operations. This is observed, because the state-space realization of IS does not make use of decoupling operations to compute the rubber mount models. Therefore, these models are not composed by spurious modes and hence, they are made of a relevant lower number of states than the models computed by implementing decoupling with LM-SSS or by performing primal state-space disassembly operations. On top of this, the coupled models determined by including the CEs into LM-SSS via compatibility relaxation are made of a significant lower number of states than the coupled state-space models computed with LM-SSS or with primal state-space assembly. Once again, this is justified by the fact that the rubber mount models used in the LM-SSS method and in the primal state-space assembly formulation are identified from decoupling/disassembly operations and hence, they are contaminated by spurious modes. Thereby, it is straightforward to conclude that the state-space realization of IS is the most suitable approach to identify models of CEs, while LM-SSS via compatibility relaxation is the most adequate approach to include the dynamics of CEs into the LM-SSS formulation. However, the user must bare in mind that both state-space realization of IS and LM-SSS via compatibility relaxation rely on the assumptions underlying IS. Therefore, their application must be restricted in frequency and must be applied on CEs, whose dynamic behaviour is ade-

quate for being characterized by IS (see sections 2.5.1 and 4.2.4), i.e. the contribution of the mass of the CEs must be unimportant for their dynamics in the frequency range of interest and the CEs must not present relevant cross couplings between their DOFs.

Estimation of state-space models

The novel method proposed in section 3.3.2 demonstrated to be accurate to strictly impose Newton's second law on state-space models representative of analytical (see sections 4.1.1 and 4.1.2) and real mechanical systems (see sections 4.2.2 and 5.2.3). Moreover, it was shown that the proposed novel approach presents two important advantages over the state-of-the-art method presented in [5]. On the one hand, the method developed in section 3.3.2 does not rely on the use of undamped RCMs to impose Newton's second law. On the other hand, by using the approach here proposed, Newton's second law can be imposed by using RCMs presenting lower natural frequencies than by exploiting the method outlined in [5] (see section 4.2.2). Therefore, we may claim that the method proposed in section 3.3.2 is, particularly, interesting to set-up state-space models that, besides strictly respecting Newton's second law, are adequate for being exploited in time-domain simulations.

In addition, the novel strategy developed in section 3.5 to impose stability on unstable coupled models was experimentally validated in section 4.2.6. This approach demonstrated to be robust enough to compute an accurate coupled state-space model from an unstable coupled model resultant from the performance of several SSS operations involving models estimated from the measured FRFs of many mechanical systems. This approach holds the advantages of not strictly requiring the use of iterative algorithms and of being simple to apply. Furthermore, in section 4.2.6, we have clearly shown that, in contrast with the originally computed unstable coupled model, the determined stable coupled model is adequate for performing time-domain simulations. In this way, by exploiting the approach proposed in section 3.5, it is possible to compute accurate stable coupled models by performing SSS operations with non-passive state-space models estimated from experimentally acquired data.

State-space models and SSS methods in TPA

The local approach discussed in section 5.2.1 showed to be capable of computing interpolating LPV models that accurately describe the dependency of the dynamics of three analytical mechanical systems on scheduling parameters (see section 5.2.2). Moreover, in section 5.2.3, this approach lead to the determination of an interpolating LPV model that accurately describes the temperature dependency of the dynamics of a real assembled structure. Indeed, by exploiting this LPV model, very good estimations of the time-domain responses of this assembled structure, when submitted to a temperature run-up, could be performed. Accurate estimations of the time-domain

load applied on this structure during the performed temperature run-up could also be obtained by using the computed LPV model. It was also evident that ignoring the temperature dependency of the dynamics of the assembled structure leads to lower-quality predictions of the time-domain responses and of the time-domain load applied on this structure. Thereby, this case study motivates the exploitation of LPV models to describe the dependency of the dynamics of more complex structures on scheduling parameters. Alternatively, one may think on using interpolating LPV models to characterize the dependency of the dynamics of simple components (such as, rubber mounts) on scheduling parameters and subsequently, introduce them in complex structures via SSS.

To validate the novel applications of LPV models in TPA proposed in chapter 5, the three substructures analyzed in section 5.2.1 were once again studied, by assuming that their dynamic behaviour is continuously changing over time and by presuming that one of those substructures is a source (hence, it generates excitation) and that the other two are passive systems. The use of the LPV models computed in section 5.2.2 together with the state-space realization of the matrix-inverse method demonstrated to lead to the computation of an accurate estimation of the time-domain connecting force (see section 5.4.1). Moreover, it was found that an accurate prediction of the time-domain equivalent force could be performed by exploiting coupled models computed at each time-sample with LM-SSS (by coupling interpolated models calculated from the interpolating LPV models) together with the state-space realization of the in-situ component-based TPA method (see section 5.4.2). Moreover, in sections 5.4.1 and 5.4.2, it is clearly shown that if the time-varying dynamics of the analytical substructures are ignored, the quality of the estimated connecting and equivalent forces is significantly deteriorated. Thus, this study clearly demonstrates the suitability of the state-space formulation and SSS methods to tackle time-domain TPA applications involving mechanical systems, whose dynamics vary over time.

6.2   Future Research

Many research topics must still be investigated to improve the SSS methods and the methodologies to experimentally estimate state-space models suitable for being exploited in SSS operations. In the following, some of these research topics are proposed by the author:

- **Automatic selection of the natural frequencies of the RCMs included in state-space models:** When computing complete state-space models, it is common to use RCMs to include the contribution of the lower and upper out-of-band modes (see section 3.2). Additionally, in section 3.3.2, we proposed the use of RCMs to impose Newton's second law on the constructed complete state-

space models. As discussed in sections 3.2 and 3.3.2, to define these RCMs we are required to select their natural frequencies and damping ratios. The value of the damping ratio of these RCMs must be selected to be the minimum value that allows the performance of stable time-domain simulations with the complete state-space model under construction, while the natural frequency of the RCMs responsible for modelling the contribution of the lower out-of-band modes can be selected with freedom to make sure that the FRFs of these RCMs well match the contribution of the lower out-of-band modes. Nonetheless, the selection of optimal values for the natural frequencies of the RCMs responsible for including the contribution of the upper out-of-band modes and for imposing Newton's second law on state-space models must be performed in an iterative fashion by following a "try and error" approach. Thus, it would be convenient to possibly get to a mathematical expression that allows the user to directly calculate optimal values for the natural frequencies of these RCMs.

- **Uncertainty quantification:** In this thesis, the state-space models representative of real mechanical systems are estimated from modal parameters identified from their measured FRFs. Therefore, the random uncertainties in the measured FRFs will definitely influence the accuracy of the identified modal parameters and hence, will be propagated during the performance of SSS operations. Thereby, we propose the performance of a study on the quantification and propagation of measurement uncertainties in SSS operations.

- **Model order reduction:** It is evident that the coupled state-space models computed in chapter 4 are composed by a significant larger number of states than the strictly needed to characterize the dynamics of the assembled structures. This is definitely a consequence of using a large amount of modes to compute the state-space models in order to make sure that their FRFs match as closely as possible the measured FRFs of the components that they represent. Nevertheless, the use of model order reduction techniques will always make the models computed with SSS techniques more appealing to be exploited in time-domain applications (e.g. in real-time applications). Moreover, as discussed in section 2.5, the state-space models originated from decoupling operations include the dynamics of the decoupled substructures twice and hence, they are contaminated with pairs of spurious modes. Thus, the use of model order reduction techniques could be the solution to eliminate these undesired modes.

- **Direct computation of state-space models representative of inverted diagonal dynamic stiffness terms of CEs:** As the inversion of a given state-space model involves the inversion of its feedthrough matrix, by exploiting the state-space realization of IS (see section 2.5.4), it is only possible to determine state-space models representative of inverted diagonal apparent mass terms of

CEs. This is problematic, because to compute the correspondent state-space model representative of the inverted diagonal dynamic stiffness terms of the CEs, we would be required to invert its state matrix, which may lead to numerical problems associated with ill-conditioned matrix inversions. Moreover, this prevents the computation of displacement coupled state-space models by using LM-SSS via compatibility relaxation (see section 2.5.1) and hence, the methodology proposed in section 3.5 cannot be used to stabilize the coupled state-space models computed with this SSS technique. To overcome this difficulty, one may think on determining the inverted diagonal dynamic stiffness terms of the CEs by using IS in the frequency domain. Then, a state-space model could be estimated from these FRFs by exploiting the methodology presented in section 3.2. However, this is not recommended, because the IS method assumes that the CEs are massless. Therefore, no resonances are expected to be observed on the inverted diagonal dynamic stiffness terms of the CEs obtained with IS. The absence of resonances will certainly make the estimation of modal parameters harder and hence, it will be more difficult to construct the intended state-space models. Thus, it is necessary to investigate an alternative approach to compute models representative of the inverted diagonal dynamic stiffness terms of CEs.

- **Experimental validation of the novel applications of LPV models in TPA:** The use of LPV models together with the matrix-inverse classical TPA and the in-situ component-based TPA methods demonstrated to be promising to compute connecting and equivalent time-domain forces, respectively, when dealing with components presenting time-varying dynamics (see section 5.4). Nevertheless, these approaches were tested in numerical cases. To assess their robustness, it is essential to apply them on experimental cases, involving real mechanical systems, whose dynamics change over time.

References

[1] R.S.O. Dias, M. Martarelli, and P. Chiariotti. Lagrange Multiplier State-Space Substructuring. *Journal of Physics: Conference Series*, 2041(1):012016, 2021. doi:10.1088/1742-6596/2041/1/012016.

[2] R.S.O. Dias, M. Martarelli, and P. Chiariotti. Including connecting elements into the lagrange multiplier state-space substructuring formulation. *Journal of Sound and Vibration*, 546:117445, 2023. doi:https://doi.org/10.1016/j.jsv.2022.117445.

[3] R.S.O. Dias, M. Martarelli, and P. Chiariotti. On the use of lagrange multiplier state-space substructuring in dynamic substructuring analysis. *Mechanical Systems and Signal Processing*, 180:109419, 2022. doi:https://doi.org/10.1016/j.ymssp.2022.109419.

[4] A. Liljerehn and T.J.S. Abrahamsson. Dynamic sub-structuring with passive state-space components. In *Proceedings of ISMA 2014 - International Conference on Noise and Vibration Engineering and USD 2014 - International Conference on Uncertainty in Structural Dynamics*, pages 3879–3890, Leuven, Belgium, 2014.

[5] A. Liljerehn. *Machine Tool Dynamics – A Constrained State-space Substructuring Approach (Doctoral thesis)*. Chalmers University Technology, Götenborg, Sweden, 2016.

[6] R.S.O. Dias, M. Martarelli, and P. Chiariotti. In-Situ Component-Based TPA for Time-Variant Dynamic Systems: A State-Space Formulation. In Matthew Allen, Walter D'Ambrogio, and Dan Roettgen, editors, *Dynamic Substructures, Volume 4*, pages 73–87, Cham, 2024. Springer Nature Switzerland.

[7] R.S.O. Dias, M. Martarelli, and P. Chiariotti. On the prediction of the time-varying behavior of dynamic systems by interpolating state-space models. *Journal of Physics: Conference Series*, (submitted for publication).

[8] Per Sjövall and Thomas Abrahamsson. Component system identification and state-space model synthesis. *Mechanical Systems and Signal Processing*, 21:2697–2714, 2007. URL https://doi.org/10.1016/j.ymssp.2007.03.002.

[9] T.-J. Su and J.-N. Juang. Substructure system identification and synthesis. *Journal of Guidance, Control and Dynamics*, 17(5):1087–1095, 1994.

[10] R.S.O. Dias, M. Martarelli, and P. Chiariotti. State-space domain virtual point transformation for state-space identification in dynamic substructuring. In *Proceedings of ISMA 2022 - International Conference on Noise and Vibration Engineering and USD 2022 - International Conference on Uncertainty in Structural Dynamics*, pages 1627–1638, Leuven, Belgium, 2022.

[11] R.S.O. Dias, M. Martarelli, and P. Chiariotti. On the computation of stable coupled state-space models for dynamic substructuring applications. *Mechanical Systems and Signal Processing*, 205:110807, 2023. doi:https://doi.org/10.1016/j.ymssp.2023.110807.

[12] D. de Klerk, D.J. Rixen, and S.N. Voormeeren. General framework for dynamic substructuring: History, Review, and Classification of Techniques. *AIAA J.*, 46 (5):1169–1181, 2008. URL `https://doi.org/10.2514/1.33274`.

[13] D.R. Martinez, T.G. Carne, D.L. Gregory, and A.K. Miller. Combined experimental/analytical modeling using component mode synthesis. In *Proceedings of the AIAA/ASME/ACE/AHS Structures, Structural Dynamics and Materials Conference*, pages 140–152, Palm Springs, CA, USA, 1984.

[14] R.R. Craig and M.C. Bampton. Coupling of substructures for dynamic analyses. *AIAA Journal*, 6(7):1313–1319, 1968. URL `https://doi.org/10.2514/3.4741`.

[15] R.H. Macneal. A hybrid method of component mode synthesis. *Computers & Structures*, 1(4):581–601, 1971. doi:10.1016/0045-7949(71)90031-9. URL `https://hal.science/hal-01537661`.

[16] S. Rubin. Improved component-mode representation for structural dynamic analysis. *AIAA Journal*, 13(8):995–1006, 1975. doi:10.2514/3.60497. URL `https://hal.science/hal-03620411`.

[17] S. W. B. Klaassen and D. J. Rixen. Using SEMM to Identify the Joint Dynamics in Multiple Degrees of Freedom Without Measuring Interfaces. In Andreas Linderholt, Matthew S. Allen, Randall L. Mayes, and Daniel Rixen, editors, *Dynamic Substructures, Volume 4*, pages 87–99, Cham, 2020. Springer International Publishing.

[18] S. N. Voormeeren, P. L. C. van der Valk, and D. J. Rixen. Practical aspects of dynamic substructuring in wind turbine engineering. In Tom Proulx, editor, *Structural Dynamics and Renewable Energy, Volume 1*, pages 163–185, New York, NY, 2011. Springer New York.

[19] S. N. Voormeeren. *Dynamic substructuring methodologies for integrated dynamic analysis of wind turbines (Ph.D.thesis)*. Delft University of Technology, Delft, The Netherlands, 2012.

[20] E. Barten, M. V. van der Seijs, and D. de Klerk. A complex power approach to characterise joints in experimental dynamic substructuring. In Matt Allen, Randy Mayes, and Daniel Rixen, editors, *Dynamics of Coupled Structures, Volume 1*, pages 281–296, Cham, 2014. Springer International Publishing.

[21] D.J. Ewins. *Modal Testing: Theory, Practice and Application*. Research Studies Press Ltd., Second Edition, Hertfordshire, England, 2000.

[22] Bart Peeters, Herman Van der Auweraer, Patrick Guillaume, and Jan Leuridan. The polymax frequency-domain method: a new standard for modal parameter estimation? *Schock and Vibration*, 11:395–409, 2004.

[23] Dennis de Klerk, Daniel J. Rixen, and Jasper de Jong. The frequency based substructuring (FBS) method reformulated according to the dual domain decomposition method. In *Proceedings of the 24th International Modal Analysis Conference*, St. Louis, MO, USA, 2006.

[24] D.J. Rixen. *Substructuring and Dual Methods in Structural Analysis*. Université de Liège, Liège, Belgium, 1997.

[25] Daniel J. Rixen. A dual craig–bampton method for dynamic substructuring. *Journal of Computational and Applied Mathematics*, 168(1):383–391, 2004. doi:https://doi.org/10.1016/j.cam.2003.12.014. Selected Papers from the Second International Conference on Advanced Computational Methods in Engineering (ACOMEN 2002).

[26] Dennis de Klerk. *Dynamic Response Characterization of Complex Systems through Operational Identification and Dynamic Substructuring, PhD thesis*. Delft University of Technology, Delft, Netherlands, 2009.

[27] M.V. van der Seijs. *Experimental Dynamic Substructuring Analysis and Design Strategies for Vehicle Development (PhD thesis)*. Delft University of Technology, Delft, The Netherlands, 2016.

[28] H. Anton and C. Rorres. *Elementary linear algebra : applications version*. WILEY, 11th edition edition, 2013.

[29] M.S. Allen, R.L. Mayes, and E.J. Bergman. Experimental modal substructuring to couple and uncouple substructures with flexible fixtures and multi-point connections. *Journal of Sound and Vibration*, 329(23):4891–4906, 2010. doi:https://doi.org/10.1016/j.jsv.2010.06.007. URL https://www.sciencedirect.com/science/article/pii/S0022460X10003792.

[30] M.S. Allen and R.L. Mayes. Comparison of FRF and modal methods for combining experimental and analytical substructures. In *Proceedings of the 25th International Modal Analysis Conference*, Orlando, FL, USA, 2007.

[31] W. D'Ambrogio and A. Sestieri. Unified approach to substructuring and structural modification problems. *Shock and Vibration*, 11(3):295–309, 2004.

[32] B. Jetmundsen, R.L. Bielawa, and W.G. Flannelly. Generalized frequency domain substructure synthesis. *Journal of the American Helicopter Society*, 33:55–64, 1988.

[33] M. Haeussler, S.W.B. Klaassen, and D.J. Rixen. Experimental twelve degree of freedom rubber isolator models for use in substructuring assemblies. *Journal of Sound and Vibration*, 474:115253, 2020. URL `https://doi.org/10.1016/j.jsv.2020.115253`.

[34] Jesus Ortega Almiron, Fabio Bianciardi, Patrick Corbeels, Rupert Ullmann, and Wim Desmet. Mount characterization analysis in the context of FBS for Component-based TPA on a wiper system. In *Forum Acusticum*, pages 2011–2018, Lyon, France, 2020. doi:10.48465/fa.2020.0251. URL `https://hal.science/hal-03235436`.

[35] A.E. Mahmoudi, D.J. Rixen, and C.H. Meyer. Comparison of Different Approaches to Include Connection Elements into Frequency-Based Substructuring. *Experimental Techniques*, 2020. doi:10.1007/s40799-020-00360-1.

[36] Walter D'Ambrogio and Annalisa Fregolent. Direct hybrid formulation for substructure decoupling. In R. Mayes, D. Rixen, D.T. Griffith, D. De Klerk, S. Chauhan, S.N. Voormeeren, and M.S. Allen, editors, *Topics in Experimental Dynamics Substructuring and Wind Turbine Dynamics, Volume 2*, pages 89–107, New York, NY, 2012. Springer New York.

[37] F. Trainotti, T. Bregar, S.W.B. Klaassen, and D.J. Rixen. Experimental decoupling of substructures by singular vector transformation. *Mechanical Systems and Signal Processing*, 163:108092, 2022. doi:https://doi.org/10.1016/j.ymssp.2021.108092.

[38] S.N. Voormeeren and D.J. Rixen. A family of substructure decoupling techniques based on a dual assembly approach. *Mechanical Systems and Signal Processing*, 27:379–396, 2012. doi:https://doi.org/10.1016/j.ymssp.2011.07.028. URL `https://www.sciencedirect.com/science/article/pii/S0888327011003177`.

[39] M. Allen, D. Rixen, M.V. van der Seijs, P. Tiso, T. Abrahamsson, and R. Mayes. *Substructuring in Engineering Dynamics*. Springer International Publishing, 2020.

[40] Mahmoud Elkafafy and Bart Peeters. A Robust Identification of Stable MIMO Modal State Space Models. In Brandon J. Dilworth, Timothy Marinone, and Michael Mains, editors, *Topics in Modal Analysis & Parameter Identification, Volume 8*, pages 81–95, Cham, 2023. Springer International Publishing.

[41] M. Gibanica. *Experimental-Analytical Dynamic Substructuring: a state-space approach, Master's Thesis*. Chalmers University Technology, Götenborg, Sweden, 2013.

[42] Mladen Gibanica, Anders T. Johansson, Anders Liljerehn, Per Sjövall, and Thomas Abrahamsson. Experimental-analytical dynamic substructuring of ampair testbed: A state-space approach. In: M. Allen, R. Mayes, D.Rixen (eds) Dynamics of Coupled Structures. *Conference Proceedings of the Society for Experimental Mechanics Series. Springer International Publishing.*, 1:1–14, 2014. URL `https://doi.org/10.1007/978-3-319-04501-6_1`.

[43] M. Scheel, M. Gibanica, and A. Nord. State-space dynamic substructuring with the transmission simulator method. *Experimental Techniques*, 43:325–340, 2019. doi:10.1007/s40799-019-00317-z. URL `https://doi.org/10.1007/s40799-019-00317-z`.

[44] Benjamin Kammermeier, Johannes Mayet, and Daniel J. Rixen. Hybrid substructure assembly techniques for efficient and robust optimization of additional structures in late phase nvh design: A comparison. In Andreas Linderholt, Matthew S. Allen, Randall L. Mayes, and Daniel Rixen, editors, *Dynamic Substructures, Volume 4*, pages 35–45, Cham, 2020. Springer International Publishing.

[45] F. Lembregts, J.Leuridan, and H. Van Brussel. Frequency domain direct parameter identification for modal analysis: State space formulation. *Mechanical Systems and Signal Processing*, 4:65–75, 1990. doi:10.1016/0888-3270(90)90041-I. URL `https://doi.org/10.1016/0888-3270(90)90041-I`.

[46] Mladen Gibanica and Thomas J.S. Abrahamsson. Identification of physically realistic state-space models for accurate component synthesis. *Mechanical Systems and Signal Processing*, 145:106906, 2020. doi:https://doi.org/10.1016/j.ymssp.2020.106906.

[47] Maren Scheel. *State-Space Experimental-Analytical Dynamic Substructuring Using the Transmission Simulator, Master's Thesis*. Chalmers University Technology, Götenborg, Sweden, 2015.

[48] Marco A. M. Lasso. Linear vector space derivation of new expressions for the pseudo inverse of rectangular matrices. *Journal of Applied Research and Technology*, 5(3):150–159, 2007. URL `https://doi.org/10.22201/icat.16656423.2007.5.03.528`.

[49] Anders Liljerehn and Thomas Abrahamsson. Experimental–analytical substructure model sensitivity analysis for cutting machine chatter prediction. In R. Mayes, D. Rixen, D.T. Griffith, D. De Klerk, S. Chauhan, S.N. Voormeeren, and M.S. Allen, editors, *Topics in Experimental Dynamics Substructuring and Wind Turbine Dynamics, Volume 2*, pages 11–20, New York, NY, 2012. Springer New York.

[50] J.O. Almirón. *Component based TPA for virtual vehicle noise and vibration prediction, PhD Thesis.* Katholieke Universiteit Leuven, 2022.

[51] J.W.R. Meggitt, A.S. Elliott, A.T. Moorhouse, and H.K. Lai. In situ determination of dynamic stiffness for resilient elements. *Journal of mechanical engineering science*, 230(6):986–993, 2015. doi:10.1177/0954406215618986.

[52] J. Zhen, T.C. Lim, and G.Q. Lu. Determination of system vibratory response characteristics applying a spectral-based inverse sub-structuring approach. part i: analytical formulation. *International Journal of Vehicle Noise and Vibration*, 2004. doi:10.1504/IJVNV.2004.004066.

[53] J. Wang, G. Sun, L. Lu, and Q. Wang. General formulation of inverse substructuring method for multicoordinate coupled system. *Advances in Mechanical Engineering*, 2014:1–7, 2014. doi:10.1155/2014/475128.

[54] J.W.R. Meggit. *On In-situ Methodologies for the Characterisation and Simulation of Vibro-Acoustic Assemblies, PhD Thesis.* University of Salford, 2017.

[55] J.W.R. Meggitt and A.T. Moorhouse. The in-situ decoupling of resiliently coupled substructures. In *Proceedings of the 24th International Congress on Sound and Vibration*, London, UK, 2017.

[56] M. Haeussler, S. Klaassen, and D. Rixen. Comparison of substructuring techniques for experimental identification of rubber isolators dynamic properties. In *Proceedings of ISMA 2018 - International Conference on Noise and Vibration Engineering and USD 2018 - International Conference on Uncertainty in Structural Dynamics*, pages 3999–4014, Leuven, Belgium, 2018.

[57] L. Ljung. *System Identification Theory for the User.* 2nd Edition, Prentice Hall, Upper Saddle River, NJ, 1999.

[58] Peter Van Overschee and Bart De Moor. N4SID: Subspace algorithms for the identification of combined deterministic-stochastic systems. *Automatica*, 30(1):75–93, 1994. doi:https://doi.org/10.1016/0005-1098(94)90230-5. Special issue on statistical signal processing and control.

[59] P. van Overschee and B. De Moor. *Subspace Identification for Linear Systems, Theory - Implementation - Applications.* Kluwer Academic Press, 1996.

[60] T. McKelvey, H. Akcay, and L. Ljung. Subspace-based multivariable system identification from frequency response data. *IEEE Transactions on Automatic Control*, 41(7):960–979, 1996. doi:10.1109/9.508900.

[61] M. Richardson and D. Formenti. Parameter estimation from frequency response measurements using rational fraction polynomials. In *Proceedings of the 1st International Modal Analysis Conference*, pages 167–186, Orlando, Florida, USA, 1982.

[62] H. Van der Auweraer and J. Leuridan. Multiple input orthogonal polynomial parameter estimation. *Mechanical Systems and Signal Processing*, 1(3):259–272, 1987. doi:https://doi.org/10.1016/0888-3270(87)90103-8.

[63] P. Guillaume, P. Verboven, and S. Vanlanduit. Frequency-domain maximum likelihood identification of modal parameters with confidence intervals. In *Proceedings of the 23rd International Seminar on Modal Analysis (ISMA23)*, pages 359–366, Leuven, Belgium, 1998.

[64] Nimish Pandiya, Christian Dindorf, and Wim Desmet. A single step modal parameter estimation algorithm: Computing residues from numerator matrix coefficients of rational fractions. In Brandon Dilworth and Michael Mains, editors, *Topics in Modal Analysis & Testing, Volume 8*, pages 97–106, Cham, 2021. Springer International Publishing.

[65] Nimish Pandiya and Wim Desmet. Direct estimation of residues from rational-fraction polynomials as a single-step modal identification approach. *Journal of Sound and Vibration*, 517:116530, 2022. doi:https://doi.org/10.1016/j.jsv.2021.116530. URL `https://www.sciencedirect.com/science/article/pii/S0022460X21005575`.

[66] P. Guillaume, P. Verboven, S. Vanlanduit, H. Van der Auweraer, and B. Peeters. A poly-reference implementation of the least-squares complex frequency domain-estimator. In *Proceedings of the 21st International Modal Analysis Conference*, Kissimmee, FL, USA, 2003.

[67] Mahmoud El-kafafy, Tim De Troyer, Bart Peeters, and Patrick Guillaume. Fast maximum-likelihood identification of modal parameters with uncertainty intervals: a modal model-based formulation. *Mechanical Systems and Signal Processing*, 37:422–439, 2013. URL `https://doi.org/10.1016/j.ymssp.2013.01.013`.

[68] Mahmoud El-kafafy, Tim De Troyer, and Patrick Guillaume. Fast maximum-likelihood identification of modal parameters with uncertainty intervals: A modal model formulation with enhanced residual term. *Mechanical Systems and Signal Processing*, 48:49–66, 2014. URL `https://doi.org/10.1016/j.ymssp.2014.02.011`.

[69] Mahmoud El-kafafy, Giampiero Accardo, Bart Peeters, Karl Janssens, Tim De Troyer, and Patrick Guillaume. A fast maximum likelihood-based estimation of a modal model. In Michael Mains, editor, *Topics in Modal Analysis, Volume 10*, pages 133–156, Cham, 2015. Springer International Publishing.

[70] Mahmoud El-Kafafy, Bart Peeters, Patrick Guillaume, and Tim De Troyer. Constrained maximum likelihood modal parameter identification applied to structural dynamics. *Mechanical Systems and Signal Processing*, 72-73:567–589, 2016. URL `http://dx.doi.org/10.1016/j.ymssp.2015.10.030`.

[71] W. Heylen, S. Lammens, and P. Sas. *Modal Analysis Theory and Testing*. KUL Press, Leuven, Belgium, 1997.

[72] N.M.M. Maia and J.M.M. Silva. *Theoretical and Experimental Modal Analysis*. Research Studies Press, Baldock, England, 1997.

[73] J. He and Z. Fu. *Modal Analysis*. Butterworth-Heinemann, Oxford, England, 2001.

[74] M. El-Kafafy. *Design and validation of improved modal parameter estimators, PhD Thesis*. Vrije Universiteit Brussel, Brussels, Belgium, 2013.

[75] Mahmoud El-Kafafy, Bart Peeters, Theo Geluk, and Patrick Guillaume. A robust test-based modal model identification method for challenging industrial cases. *Proceedings*, 2(8), 2018. doi:10.3390/ICEM18-05196. URL `https://www.mdpi.com/2504-3900/2/8/378`.

[76] A. Bylin, M. Gibanica, and T.J.S. Abrahamsson. Experimental-analytical state-space synthesis of passenger car components. *In: Proceedings of ISMA 2018 - International Conference on Noise and Vibration Engineering and USD 2018 - International Conference on Uncertainty in Structural Dynamics, Leuven, Belgium*, 2018.

[77] S. Boyd, L. El Ghaoui, E. Feron, and V. Balakrishnan. *Linear matrix inequalities in system and control theory*. SIAM, Philadelphia, 1994.

[78] C.P. Coelho, J. Phillips, and L.M. Silveira. A convex programming approach for generating guaranteed passive approximations to tabulated frequency-data. *IEEE Transactions on Computer-Aided Design of Integrated Circuits and Systems*, 23 (2):293–301, 2004. doi:10.1109/TCAD.2003.822107.

[79] Huabo Chen and Jiayuan Fang. Enforcing bounded realness of s parameter through trace parameterization. In *Electrical Performance of Electrical Packaging (IEEE Cat. No. 03TH8710)*, pages 291–294, 2003. doi:10.1109/EPEP.2003.1250052.

[80] Giuseppe C. Calafiore, Alessandro Chinea, and Stefano Grivet-Talocia. Subgradient techniques for passivity enforcement of linear device and interconnect macromodels. *IEEE Transactions on Microwave Theory and Techniques*, 60(10): 2990–3003, 2012. doi:10.1109/TMTT.2012.2211610.

[81] S. Grivet-Talocia. Passivity enforcement via perturbation of hamiltonian matrices. *IEEE Transactions on Circuits and Systems I: Regular Papers*, 51(9): 1755–1769, 2004. doi:10.1109/TCSI.2004.834527.

[82] Stefano Grivet-Talocia and Bjorn Gustavsen. *Passive macromodeling: Theory and applications.* John Wiley & Sons, 2015.

[83] Jan De Caigny, Juan F. Camino, and Jan Swevers. Interpolating model identification for SISO linear parameter-varying systems. *Mechanical Systems and Signal Processing*, 23(8):2395–2417, 2009. doi:https://doi.org/10.1016/j.ymssp.2009.04.007.

[84] Jan De Caigny, Rik Pintelon, Juan F. Camino, and Jan Swevers. Interpolated Modeling of LPV Systems. *IEEE Transactions on Control Systems Technology*, 22(6):2232–2246, 2014. doi:10.1109/TCST.2014.2300510.

[85] Francesco Ferranti and Yves Rolain. A local identification method for linear parameter-varying systems based on interpolation of state-space matrices and least-squares approximation. *Mechanical Systems and Signal Processing*, 82:478–489, 2017. ISSN 0888-3270. doi:https://doi.org/10.1016/j.ymssp.2016.05.037.

[86] F. Felici, J.W. van Wingerden, and M. Verhaegen. Subspace identification of MIMO LPV systems using a periodic scheduling sequence. *Automatica*, 43:1684–1697, 2007. URL `https://doi.org/10.1016/j.automatica.2007.02.027`.

[87] Maarten V. van der Seijs, D. D. van den Bosch, Daniel J. Rixen, and Dennis de Klerk. An improved methodology for the virtual point transformation of frequency response functions in dynamic substructuring. In *Proceedings of the 4th ECCOMAS Thematic Conference on Computational Methods in Structural Dynamics and Earthquake Engineering (COMPDYN)*, pages 4334–4347, Kos Island, Greece, 2013.

[88] M. Häußler and Daniel Jean Rixen. Optimal transformation of frequency response functions on interface deformation modes. In Matthew S. Allen, Randall L. Mayes, and Daniel Jean Rixen, editors, *Dynamics of Coupled Structures, Volume 4*, pages 225–237, Cham, 2017. Springer International Publishing.

[89] G.H. Golub and C.F.V. Loan. *Matrix Computations.* The Johns Hopkins University Press, 3rd edition edition, 1996.

[90] E. Balmès. Frequency domain identification of structural dynamics using the pole/residue parametrization. In *Proceedings of 14th International Modal Analysis Conference*, pages 540–546, Dearborn, MI, USA, 1996.

[91] J.L.M. Zabala. *State-space formulation for structure dynamics, Master Thesis.* Massachusetts Institute of Technology, Cambridge, Massachusetts, USA, 1996.

[92] H.R. Harrison and T. Nettleton. *Advanced Engineering Dynamics.* Butterworth-Heinemann, 1st edition edition, 1997.

[93] J.B. Hoagg, S.L. Lacy, R.S. Erwin, and D.S. Bernstein. First-order-hold sampling of positive real systems and subspace identification of positive real models. In *Proceedings of the 2004 American Control Conference*, volume 1, pages 861–866 vol.1, 2004. doi:10.23919/ACC.2004.1383714.

[94] Maarten V. van der Seijs, Dennis de Klerk, and Daniel J. Rixen. General framework for transfer path analysis: History, theory and classification of techniques. *Mechanical Systems and Signal Processing*, 68-69:217–244, 2016. doi:https://doi.org/10.1016/j.ymssp.2015.08.004.

[95] Matthew S. Allen and Thomas G. Carne. Delayed, multi-step inverse structural filter for robust force identification. *Mechanical Systems and Signal Processing*, 22(5):1036–1054, 2008. doi:https://doi.org/10.1016/j.ymssp.2007.11.022.

[96] M. Sturm, A. T. Moorhouse, T. Alber, and F. F. Li. Force reconstruction using an adaptive algorithm in time domain. In *Proceedings of ISMA 2012 - International Conference on Noise and Vibration Engineering and USD 2012 - International Conference on Uncertainty in Structural Dynamics*, pages 3617–3630, Leuven, Belgium, 2012.

[97] M. Sturm, A. T. Moorhouse, W. Kropp, and T.H. Alber. Robust calculation of simultaneous multichannel blocked force signatures from measurements made in-situ using an adaptive algorithm in time domain. In *Proceedings of the 20th International Congress on Sound and Vibration (ICSV)*, pages 1610–1617, Bangkok, Thailand, 2013.

[98] Marco Lovera, Carlo Novara, Paulo Lopes dos Santos, and Daniel Rivera. Guest editorial special issue on applied LPV modeling and identification. *IEEE Transactions on Control Systems Technology*, 19(1):1–4, 2011. doi:10.1109/TCST.2010.2090416.

[99] Carlo Novara, Fredy Ruiz, and Mario Milanese. Direct identification of optimal sm-LPV filters and application to vehicle yaw rate estimation. *IEEE Transactions on Control Systems Technology*, 19(1):5–17, 2011. doi:10.1109/TCST.2010.2070505.

[100] Zoltán Szabó, Andrés Marcos, David Mostaza Prieto, Murray L. Kerr, Gábor Rödönyi, József Bokor, and Samir Bennani. Development of an integrated LPV/lft framework: Modeling and data-based validation tool. *IEEE Transactions on Control Systems Technology*, 19(1):104–117, 2011. doi:10.1109/TCST.2010.2072783.

[101] Mara Tanelli, Danilo Ardagna, and Marco Lovera. Identification of LPV state space models for autonomic web service systems. *IEEE Transactions on Control Systems Technology*, 19(1):93–103, 2011. doi:10.1109/TCST.2010.2063250.

[102] Jan De Caigny, Juan F. Camino, and Jan Swevers. Interpolation-Based Modeling of MIMO LPV Systems. *IEEE Transactions on Control Systems Technology*, 19(1):46–63, 2011. doi:10.1109/TCST.2010.2078509.

[103] Guillaume Mercère, Halldor Palsson, and Thierry Poinot. Continuous-time linear parameter-varying identification of a cross flow heat exchanger: A local approach. *IEEE Transactions on Control Systems Technology*, 19(1):64–76, 2011. doi:10.1109/TCST.2010.2071874.

[104] Paulo Lopes dos Santos, Teresa-P. Azevedo-Perdicoúlis, José A. Ramos, J. L. Martins de Carvalho, Gerhard Jank, and J. Milhinhos. An LPV modeling and identification approach to leakage detection in high pressure natural gas transportation networks. *IEEE Transactions on Control Systems Technology*, 19(1):77–92, 2011. doi:10.1109/TCST.2010.2077293.

[105] C.A.J. Beijers and A. de Boer. Numerical modelling of rubber vibration isolators. In *Tenth International Conference on Sound and Vibration*, Stockholm, Sweeden, 2003.

[106] T. Roncen, J.-J. Sinou, and J.-P. Lambelin. Experiments and nonlinear simulations of a rubber isolator subjected to harmonic and random vibrations. *Journal of Sound and Vibration*, 451:71–83, 2019. doi:https://doi.org/10.1016/j.jsv.2019.03.017.

[107] Lawton H. Lee and Kameshwar Poolla. Identification of Linear Parameter-Varying Systems Using Nonlinear Programming. *Journal of Dynamic Systems, Measurement, and Control*, 121(1):71–78, 1999. ISSN 0022-0434. doi:10.1115/1.2802444. URL https://doi.org/10.1115/1.2802444.

[108] Federico Felici, Jan-Willem van Wingerden, and Michel Verhaegen. Subspace identification of MIMO LPV systems using a periodic scheduling sequence. *Automatica*, 43(10):1684–1697, 2007. doi:https://doi.org/10.1016/j.automatica.2007.02.027.

[109] Bart Paijmans, Wim Symens, Hendrik Van Brussel, and Jan Swevers. Identification of interpolating affine LPV models for mechatronic systems with one varying parameter. *European Journal of Control*, 14(1):16–29, 2008. doi:https://doi.org/10.3166/ejc.14.16-29.

[110] J. De Caigny, J.F. Camino, B. Paijmans, and J. Swevers. An application of interpolating gain-scheduling control. *IFAC Proceedings Volumes*, 40(20):88–93, 2007. doi:https://doi.org/10.3182/20071017-3-BR-2923.00015. 3rd IFAC Symposium on System Structure and Control.

[111] Gary J. Balas. Linear, parameter-varying control and its application to a turbofan engine. *International Journal of Robust and Nonlinear Control*, 12(9):763–796, 2002. doi:https://doi.org/10.1002/rnc.704. URL `https://onlinelibrary.wiley.com/doi/abs/10.1002/rnc.704`.

[112] M. Steinbuch, R. van de Molengraft, and A. van der Voort. Experimental modelling and LPV control of a motion system. In *Proceedings of the 2003 American Control Conference, 2003.*, volume 2, pages 1374–1379, 2003. doi:10.1109/ACC.2003.1239782.

[113] C. Paige. Properties of numerical algorithms related to computing controllability. *IEEE Transactions on Automatic Control*, 26(1):130–138, 1981. doi:10.1109/TAC.1981.1102563.

[114] Marco Lovera and Guillaume Mercere. Identification for gain-scheduling: a balanced subspace approach. In *2007 American Control Conference*, pages 858–863, 2007. doi:10.1109/ACC.2007.4282899.

[115] B. Moore. Principal component analysis in linear systems: Controllability, observability, and model reduction. *IEEE Transactions on Automatic Control*, 26(1):17–32, 1981. doi:10.1109/TAC.1981.1102568.

[116] A. Laub, M. Heath, C. Paige, and R. Ward. Computation of system balancing transformations and other applications of simultaneous diagonalization algorithms. *IEEE Transactions on Automatic Control*, 32(2):115–122, 1987. doi:10.1109/TAC.1987.1104549.

[117] Qinghua Zhang and Lennart Ljung. LPV system common state basis estimation from independent local lti models. *IFAC-PapersOnLine*, 48(28):190–195, 2015. doi:https://doi.org/10.1016/j.ifacol.2015.12.123.

[118] Qinghua Zhang and Lennart Ljung. From structurally independent local lti models to LPV model. *Automatica*, 84:232–235, 2017. doi:https://doi.org/10.1016/j.automatica.2017.06.006.

[119] Qinghua Zhang, Lennart Ljung, and Rik Pintelon. On local lti model coherence for LPV interpolation. *IEEE Transactions on Automatic Control*, 65(8):3671–3676, 2020. doi:10.1109/TAC.2019.2948898.

[120] V. Verdult and M. Verhaegen. Subspace identification of piecewise linear systems. In *2004 43rd IEEE Conference on Decision and Control (CDC) (IEEE Cat. No.04CH37601)*, volume 4, pages 3838–3843 Vol.4, 2004. doi:10.1109/CDC.2004.1429336.

[121] J.H. Yung. *Gain scheduling for geometrically nonlinear flexible space structures (PhD dissertation)*. Massachusetts Institute of Technology, Cambridge, MA, USA, 2002.

[122] J. Brewer. Kronecker products and matrix calculus in system theory. *IEEE Transactions on Circuits and Systems*, 25(9):772–781, 1978. doi:10.1109/TCS.1978.1084534.

[123] Peter Avitabile. *Modal testing: a practitioner's guide.* John Wiley & Sons, 2017.

[124] Dao Gong, Yu Duan, Kang Wang, and Jinsong Zhou. Modelling rubber dynamic stiffness for numerical predictions of the effects of temperature and speed on the vibration of a railway vehicle car body. *Journal of Sound and Vibration*, 449: 121–139, 2019. ISSN 0022-460X. doi:https://doi.org/10.1016/j.jsv.2019.02.037.

[125] J. Wojtowicki and S. Lecuru. Characterization and modelling of mounts for electric powertrains. In *Proceedings of the 12th International Styrian Noise, Vibration & Harshness Congress: The European Automotive Noise Conference*, pages 952–964, 2022.

[126] Steven Gillijns and Bart De Moor. Unbiased minimum-variance input and state estimation for linear discrete-time systems with direct feedthrough. *Automatica*, 43(5):934–937, 2007. ISSN 0005-1098. doi:https://doi.org/10.1016/j.automatica.2006.11.016.

[127] Accelerometer, icp®, triaxial, model 356a32. `https://www.pcb.com/products?m=tld356a32`, Accessed: 2023-05-15.

[128] J. W. Verheij. *Multi-path sound transfer from resiliently mounted ship board machinery: experimental methods for analyzing and improving noise control (Ph.D.thesis).* Delft University of Technology, Delft, The Netherlands, 1982.

[129] F. Penne. Shaping the sound of the next-generation bmw. In *Proceedings of ISMA 2004 - International Conference on Noise and Vibration Engineering*, pages 25–39, Leuven, Belgium, 2004.

[130] H. Van der Auweraer, P. Mas, S. Dom, A. Vecchio, K. Janssens, and P. van de Ponseele. Transfer path analysis in the critical path of vehicle refinement: The role of fast, hybrid and operational path analysis. *SAE Technical Paper 2007-01-2352*, 2007. URL `http://dx.doi.org/10.4271/2007-01-2352`.

[131] P. Wagner, F. Bianciardi, P. Corbeels, and A. Hülsmann. High frequency source characterization of an e-motor using component-based TPA. *SIA NVH Comfort 2021*, 2021.

[132] P. Wagner, P. Hülsmann, and M. Van Der Seijs. Application of dynamic substructuring in nvh design of electric drivetrains. In *Proceedings of ISMA 2020 - International Conference on Noise and Vibration Engineering and USD 2020 - International Conference on Uncertainty in Structural Dynamics*, pages 3365–3382, Leuven, Belgium, 2020.

[133] Seyed Ehsan Mir-Haidari and Kamran Behdinan. On the vibration transfer path analysis of aero-engines using bond graph theory. *Aerospace Science and Technology*, 95:105516, 2019. doi:https://doi.org/10.1016/j.ast.2019.105516.

[134] Julie M. Harvie and Maarten van der Seijs. Application of transfer path analysis techniques to the boundary condition challenge problem. In Chad Walber, Patrick Walter, and Steve Seidlitz, editors, *Sensors and Instrumentation, Aircraft/Aerospace, Energy Harvesting & Dynamic Environments Testing, Volume 7*, pages 157–166, Cham, 2020. Springer International Publishing.

[135] Simon Prenant, Thomas Padois, Valentin Rolland, Manuel Etchessahar, Thomas Dupont, and Olivier Doutres. Effects of mobility matrices completeness on component-based transfer path analysis methods with and without substructuring applied to aircraft-like components. *Journal of Sound and Vibration*, 547: 117541, 2023. doi:https://doi.org/10.1016/j.jsv.2022.117541.

[136] P. J. G. Van Der Linden and H. Floetke. Comparing inverse force identification and the mount-stiffness force identification methods for noise contribution analysis. In *Proceedings of ISMA 2004 - International Conference on Noise and Vibration Engineering*, pages 2971–2985, Leuven, Belgium, 2004.

[137] J. M. Starkey and G. L. Merrill. On the ill-conditioned nature of indirect force measurement techniques. *International Journal of Analytical and Experimental Modal Analysis*, 4(3):103–108, 1989.

[138] A. N. Thite and D. J. Thompson. The quantification of structure-borne transmission paths by inverse methods. part 1: Improved singular value rejection methods. *Journal of Sound and Vibration*, 264(2):411–431, 2003. doi:https://doi.org/10.1016/S0022-460X(02)01202-6.

[139] A. N. Tikhonov and V. Y. Arsenin. *Solutions of Ill-Posed Problems.* John Wiley and Sons, New York, USA, 1977.

[140] D. Calvetti, S. Morigi, L. Reichel, and F. Sgallari. Tikhonov regularization and the l-curve for large discrete ill-posed problems. *Journal of Computational and Applied Mathematics*, 123(1):423–446, 2000. doi:https://doi.org/10.1016/S0377-0427(00)00414-3.

[141] A. N. Thite and D. J. Thompson. The quantification of structure-borne transmission paths by inverse methods. part 2: Use of regularization techniques. *Journal of Sound and Vibration*, 264(2):433–451, 2003. doi:https://doi.org/10.1016/S0022-460X(02)01203-8.

[142] Hyoung Gil Choi, Anand N. Thite, and David J. Thompson. Comparison of methods for parameter selection in tikhonov regularization with application to inverse force determination. *Journal of Sound and Vibration*, 304(3):894–917, 2007. doi:https://doi.org/10.1016/j.jsv.2007.03.040.

[143] W. Kropp and K. Larsson. Force estimation in the time domain by applying an lms algorithm. In *Proceedings of Noise and Vibration: Emerging Methods (Novem)*, Saint-Raphaël, France, 2005.

[144] B. Widrow and M. E. Hoff. Adaptive switching circuits. In *Proceedings of Western Electric Show and Convention*, pages 96–104, Los Angeles, California, USA, 1960.

[145] D. C. Kammer. Input Force Reconstruction Using a Time Domain Technique. *Journal of Vibration and Acoustics*, 120(4):868–874, 10 1998. doi:10.1115/1.2893913. URL https://doi.org/10.1115/1.2893913.

[146] A. Steltzner and D. Kammer. Input force estimation using an inverse structural filter. In *Proceedings of the 17th International Modal Analysis Conference*, pages 954–960, Kissimmee, FL, USA, 1999.

[147] Y.M. Mao, X.L. Guo, and Yan Zhao. A state space force identification method based on markov parameters precise computation and regularization technique. *Journal of Sound and Vibration*, 329(15):3008–3019, 2010. doi:https://doi.org/10.1016/j.jsv.2010.02.012.

[148] R. E. Kalman. A New Approach to Linear Filtering and Prediction Problems. *Journal of Basic Engineering*, 82(1):35–45, 1960. doi:10.1115/1.3662552. URL https://doi.org/10.1115/1.3662552.

[149] Saeed Eftekhar Azam, Eleni Chatzi, and Costas Papadimitriou. A dual kalman filter approach for state estimation via output-only acceleration measurements. *Mechanical Systems and Signal Processing*, 60-61:866–886, 2015. doi:https://doi.org/10.1016/j.ymssp.2015.02.001.

[150] E. Lourens, E. Reynders, G. De Roeck, G. Degrande, and G. Lombaert. An augmented kalman filter for force identification in structural dynamics. *Mechanical Systems and Signal Processing*, 27:446–460, 2012. ISSN 0888-3270. doi:https://doi.org/10.1016/j.ymssp.2011.09.025.

[151] D. de Klerk and D.J. Rixen. Component transfer path analysis method with compensation for test bench dynamics. *Mechanical Systems and Signal Processing*, 24(6):1693–1710, 2010. doi:https://doi.org/10.1016/j.ymssp.2010.01.006.

[152] Daniel J. Rixen, Anthonie Boogaard, Maarten V. van der Seijs, Gert van Schothorst, and Tjeerd van der Poel. Vibration source description in substructuring: A theoretical depiction. *Mechanical Systems and Signal Processing*, 60-61:498–511, 2015. ISSN 0888-3270. doi:https://doi.org/10.1016/j.ymssp.2015.01.024.

[153] M.V. van der Seijs, E.A. Pasma, D. de Klerk, and D.J. Rixen. A robust transfer path analysis method for steering gear vibrations on a test bench. In *Proceedings of the International Conference on Noise and Vibration Engineering (ISMA)*, pages 3967–3980, Leuven, Belgium, 2014.

[154] Andrew Elliott and Andy T. Moorhouse. Characterisation of structure borne sound sources from measurement in-situ. *The Journal of the Acoustical Society of America*, 123:3176–3176, 2008. doi:10.1121/1.2933261.

[155] A.T. Moorhouse, A.S. Elliott, and T.A. Evans. In situ measurement of the blocked force of structure-borne sound sources. *Journal of Sound and Vibration*, 325(4):679–685, 2009. doi:https://doi.org/10.1016/j.jsv.2009.04.035.

[156] A.S. Elliott. *Characterisation of structure borne sound sources in-situ (Ph.D.thesis)*. University of Salford, Salford, United Kingdom, 2009.

[157] A.S. Elliott, A.T. Moorhouse, T. Huntley, and S. Tate. In-situ source path contribution analysis of structure borne road noise. *Journal of Sound and Vibration*, 332(24):6276–6295, 2013. ISSN 0022-460X. doi:https://doi.org/10.1016/j.jsv.2013.05.031.

[158] M. Sturm, T. Alber, A. Moorhouse, D. Zabel, and Z. Wang. The in-situ blocked force method for characterization of complex automotive structure-borne sound sources and its use for virtual acoustic prototyping. In *Proceedings of ISMA 2016 - International Conference on Noise and Vibration Engineering and USD 2016 - International Conference on Uncertainty in Structural Dynamics*, pages 3647–3662, Leuven, Belgium, 2016.

[159] M. Haeussler, D.C. Kobus, and D.J. Rixen. Parametric design optimization of e-compressor nvh using blocked forces and substructur-

ing. *Mechanical Systems and Signal Processing*, 150:107217, 2021. doi:https://doi.org/10.1016/j.ymssp.2020.107217.

[160] Jesús Ortega Almirón, Fabio Bianciardi, Patrick Corbeels, Nicola Pieroni, Peter Kindt, and Wim Desmet. Vehicle road noise prediction using component-based transfer path analysis from tire test-rig measurements on a rolling tire. *Journal of Sound and Vibration*, 523:116694, 2022. doi:https://doi.org/10.1016/j.jsv.2021.116694.

[161] M.H.A. Janssens and J.W. Verheij. A pseudo-forces methodology to be used in characterization of structure-borne sound sources. *Applied Acoustics*, 61(3): 285–308, 2000. doi:https://doi.org/10.1016/S0003-682X(00)00035-9.

[162] M.H.A Janssens, J.W Verheij, and T Loyau. Experimental example of the pseudo-forces method used in characterisation of a structure-borne sound source. *Applied Acoustics*, 63(1):9–34, 2002. doi:https://doi.org/10.1016/S0003-682X(01)00023-8.

[163] A.M.R. RIBEIRO, J.M.M. SILVA, and N.M.M. MAIA. On the generalisation of the transmissibility concept. *Mechanical Systems and Signal Processing*, 14(1): 29–35, 2000. doi:https://doi.org/10.1006/mssp.1999.1268.

[164] F.X. Magrans. Method of measuring transmission paths. *Journal of Sound and Vibration*, 74(3):321–330, 1981. doi:https://doi.org/10.1016/0022-460X(81)90302-3.

[165] F. X. Magrans, P. V. Rodríguez, and G. C. Cousin. Low and mid-high frequency advanced transmission path analysis. In *Proceedings of the 12th International Congress on Sound and Vibration 2005*, page 3292–3299, Lisbon, Portugal, 2005.

[166] O. Guasch and F.X. Magrans. The global transfer direct transfer method applied to a finite simply supported elastic beam. *Journal of Sound and Vibration*, 276 (1):335–359, 2004. doi:https://doi.org/10.1016/j.jsv.2003.07.032.

[167] Oriol Guasch. Direct transfer functions and path blocking in a discrete mechanical system. *Journal of Sound and Vibration*, 321(3):854–874, 2009. doi:https://doi.org/10.1016/j.jsv.2008.10.006.

[168] Oriol Guasch, Carlos García, Jordi Jové, and Pere Artís. Experimental validation of the direct transmissibility approach to classical transfer path analysis on a mechanical setup. *Mechanical Systems and Signal Processing*, 37(1):353–369, 2013. doi:https://doi.org/10.1016/j.ymssp.2013.01.006.

[169] Àngels Aragonès, Jordi Poblet-Puig, Kevin Arcas, Pere Vicens Rodríguez, Francesc Xavier Magrans, and Antonio Rodríguez-Ferran. Experimental

and numerical study of advanced transfer path analysis applied to a box prototype. *Mechanical Systems and Signal Processing*, 114:448–466, 2019. doi:https://doi.org/10.1016/j.ymssp.2018.05.030.

[170] K. Noumura and J. Yoshida. Method of transfer path analysis for vehicle interior sound with no excitation experiment. In *Proceedings of FISITA, F2006D183*, 2006.

[171] P. Gajdatsy, K. Janssens, L. Gielen, P. Mas, and H. Van der Auweraer. Critical assessment of operational path analysis: effect of coupling between path inputs. In *Acoustics 08 Conference*, Paris, France, 2008.

[172] P. Gajdatsy, K. Janssens, Wim Desmet, and H. Van der Auweraer. Application of the transmissibility concept in transfer path analysis. *Mechanical Systems and Signal Processing*, 24(7):1963–1976, 2010. doi:https://doi.org/10.1016/j.ymssp.2010.05.008.

[173] Peter Gajdatsy, Karl Janssens, Ludo Gielen, Peter Mas, and Herman Van Der Auweraer. Critical assessment of operational path analysis: mathematical problems of transmissibility estimation. *The Journal of the Acoustical Society of America*, 123:3869–3869, 2008. doi:10.1121/1.2935749. URL `https://doi.org/10.1121/1.2935749`.

[174] P. Gajdatsy, K. Janssens, L. Gielen, P. Mas, and H. Van der Auweraer. Critical assessment of operational path analysis: mathematical problems of transmissibility estimation. In *Acoustics 08 Conference*, Paris, France, 2008.

[175] P. Gajdatsy, K. Janssens, L. Gielen, P. Mas, and H. Van der Auweraer. Critical assessment of operational path analysis: effect of neglected paths. In *ICSV Conference*, Daejeon, Korea, 2008.

[176] D. de Klerk and A. Ossipov. Operational transfer path analysis: Theory, guidelines and tire noise application. *Mechanical Systems and Signal Processing*, 24 (7):1950–1962, 2010. doi:https://doi.org/10.1016/j.ymssp.2010.05.009.

[177] M. Vorländer and P. Dietrich. Transfer path analysis and synthesis for auralization. In *39th Congreso Espanol de Acústica 2008*, Coimbra, Portugal, 2008.

[178] K. Janssens, P. Mas, P. Gajdatsy, L. Gielen, and H. Van der Auweraer. A novel path contribution analysis method for test-based nvh troubleshooting. In *Proceedings of the International Conference on Noise and Vibration Engineering (ISMA)*, pages 3673–3683, Leuven, Belgium, 2008.

[179] Karl Janssens, Peter Gajdatsy, Ludo Gielen, Peter Mas, Laurent Britte, Wim Desmet, and Herman Van der Auweraer. OPAX: A new transfer path analysis

method based on parametric load models. *Mechanical Systems and Signal Processing*, 25(4):1321–1338, 2011. doi:https://doi.org/10.1016/j.ymssp.2010.10.014.

[180] K. Maes, A.W. Smyth, G. De Roeck, and G. Lombaert. Joint input-state estimation in structural dynamics. *Mechanical Systems and Signal Processing*, 70-71: 445–466, 2016. doi:https://doi.org/10.1016/j.ymssp.2015.07.025.

[181] F. Naets, J. Cuadrado, and W. Desmet. Stable force identification in structural dynamics using kalman filtering and dummy-measurements. *Mechanical Systems and Signal Processing*, 50-51:235–248, 2015. ISSN 0888-3270. doi:https://doi.org/10.1016/j.ymssp.2014.05.042.

[182] S. Vettori, E. Di Lorenzo, B. Peeters, M.M. Luczak, and E. Chatzi. An adaptive-noise augmented kalman filter approach for input-state estimation in structural dynamics. *Mechanical Systems and Signal Processing*, 184:109654, 2023. doi:https://doi.org/10.1016/j.ymssp.2022.109654.

[183] G. F. Franklin, D. J. Powell, and M. L. Workman. *Digital Control of Dynamic Systems*. Prentice Hall, 3rd edition, 1997.

Appendix A

Inverting state-space models

To demonstrate how the inversion of state-space models can be performed, let us consider a generic acceleration model as given below.

$$\{\dot{x}(t)\} = [A]\{x(t)\} + [B]\{u(t)\}$$
$$\{\ddot{y}(t)\} = [C^{accel}]\{x(t)\} + [D^{accel}]\{u(t)\} \tag{A.1}$$

Solving the output equations of the state-space model given in expression (A.1) to find the value of $\{u(t)\}$, we may define the following expression.

$$\{u(t)\} = [D^{accel}]^{-1}(\{\ddot{y}(t)\} - [C^{accel}]\{x(t)\}) \tag{A.2}$$

By using equation (A.2), the state equations of the state-space model given by expression (A.1) can be rewritten as given hereafter.

$$\{\dot{x}(t)\} = [A]\{x(t)\} + [B][D^{accel}]^{-1}(\{\ddot{y}(t)\} - [C^{accel}]\{x(t)\}) \tag{A.3}$$

By using equations (A.3) and (A.2), the inverted state-space model can be computed as follows:

$$\{\dot{x}(t)\} = [A^{inv}]\{x(t)\} + [B^{inv}]\{\ddot{y}(t)\}$$
$$\{u(t)\} = [C^{inv}]\{x(t)\} + [D^{inv}]\{\ddot{y}(t)\} \tag{A.4}$$

where, matrices $[A^{inv}]$, $[B^{inv}]$, $[C^{inv}]$ and $[D^{inv}]$ are given hereafter.

$$[A^{inv}] = [A] - [B][D^{accel}]^{-1}[C^{accel}], \quad [B^{inv}] = [B][D^{accel}]^{-1}$$
$$[C^{inv}] = -[D^{accel}]^{-1}[C^{accel}], \quad [D^{inv}] = [D^{accel}]^{-1} \tag{A.5}$$

Appendix B

Negative form of a state-space model representative of apparent mass

To demonstrate how to define the negative form of a state-space model representative of apparent mass, let us consider the following acceleration state-space model directly derived from the mass, stiffness and damping matrices of a given mechanical system (see [45]).

$$\{\dot{x}(t)\} = [A]\{x(t)\} + [B]\{u(t)\}$$
$$\{\ddot{y}(t)\} = [C^{accel}]\{x(t)\} + [D^{accel}]\{u(t)\}$$

(B.1)

where, matrices $[A]$, $[B]$, $[C^{accel}]$ and $[D^{accel}]$ are given below.

$$[A] = \begin{bmatrix} -M^{-1}V & -M^{-1}K \\ I & 0 \end{bmatrix}, \quad [B] = \begin{bmatrix} M^{-1} \\ 0 \end{bmatrix}$$
$$[C^{accel}] = \begin{bmatrix} -M^{-1}V & -M^{-1}K \end{bmatrix}, \quad [D^{accel}] = \begin{bmatrix} M^{-1} \end{bmatrix}$$

(B.2)

By using expression (A.5), we may invert the state-space model given in expression (B.1) to obtain the correspondent apparent mass model. The state-space matrices of this model are given below.

$$[A^{apm}] = [A] - [B][D^{accel}]^{-1}[C^{accel}]$$

$$= \begin{bmatrix} -M^{-1}V & -M^{-1}K \\ I & 0 \end{bmatrix} - \begin{bmatrix} M^{-1} \\ 0 \end{bmatrix} \left[M^{-1}\right]^{-1} \begin{bmatrix} -M^{-1}V & -M^{-1}K \end{bmatrix}$$

$$= \begin{bmatrix} -M^{-1}V & -M^{-1}K \\ I & 0 \end{bmatrix} - \begin{bmatrix} -M^{-1}V & -M^{-1}K \\ 0 & 0 \end{bmatrix} = \begin{bmatrix} 0 & 0 \\ I & 0 \end{bmatrix}$$

$$[B^{apm}] = [B][D^{accel}]^{-1} = \begin{bmatrix} M^{-1} \\ 0 \end{bmatrix} \left[M^{-1}\right]^{-1} = \begin{bmatrix} I \\ 0 \end{bmatrix} \tag{B.3}$$

$$[C^{apm}] = -[D^{accel}]^{-1}[C^{accel}] = -\left[M^{-1}\right]^{-1} \begin{bmatrix} -M^{-1}V & -M^{-1}K \end{bmatrix} = \begin{bmatrix} V & K \end{bmatrix}$$

$$[D^{apm}] = [D^{accel}]^{-1} = \left[M^{-1}\right]^{-1} = [M]$$

In [47],[43], it was argued that to compute the negative form of a state-space model, its $[M]$, $[K]$ and $[V]$ matrices must be multiplied by -1. Thereby, we may define the negative form of the state-space matrices given in expression (B.3) as follows

$$[A^{apm}_{neg}] = \begin{bmatrix} 0 & 0 \\ I & 0 \end{bmatrix}, \quad [B^{apm}_{neg}] = \begin{bmatrix} I \\ 0 \end{bmatrix}$$

$$[C^{apm}_{neg}] = [-V \quad -K], \quad [D^{apm}_{neg}] = \begin{bmatrix} -M \end{bmatrix} \tag{B.4}$$

where, subscript *neg* denotes a state-space matrix transformed into negative form.

By observing expression (B.4), it is evident that to define the negative form of a state-space model representative of apparent mass, we must multiply its output and feedthrough matrices by -1. Note that this procedure continues to be valid to compute the negative form of state-space models defined in the modal domain.

Appendix C

Displacement and velocity coupled models with LM-SSS via compatibility relaxation

Here, the expressions developed in section 2.5.1 to compute acceleration coupled state-space models by using LM-SSS with compatibility relaxation (see expressions (2.144)) will be modified to directly provide displacement and velocity coupled models. The displacement, velocity and acceleration models of a given mechanical system present the same state and input matrices. Hence, we are only required to perform modifications on the expressions associated with the computation of the output and feedthrough matrices of the acceleration coupled model.

Let us start by rewriting the expressions responsible for computing matrices $[\tilde{C}^{accel}]$ and $[\tilde{D}^{accel}]$ by using displacement state-space matrices as follows (see expression (2.78)):

$$[\tilde{C}_S^{accel}] = C_{S,D}^{disp} A_{S,D} A_{S,D} - (C_{S,D}^{disp} A_{S,D} B_{S,D}) B_C^T E_{CRd} B_C C_{S,D}^{disp} A_{S,D} A_{S,D}$$

$$[\tilde{C}_M^{accel}] = (C_{S,D}^{disp} A_{S,D} B_{S,D}) B_C^T E_{CRd} C_{M,D}^{disp} A_{M,D} A_{M,D} \tag{C.1}$$

$$[\tilde{D}_S^{accel}] = C_{S,D}^{disp} A_{S,D} B_{S,D} - (C_{S,D}^{disp} A_{S,D} B_{S,D}) B_C^T E_{CRd} B_C (C_{S,D}^{disp} A_{S,D} B_{S,D})$$

where, matrix $[E_{CRd}]$ is given below.

$$[E_{CRd}] = (B_C (C_{S,D}^{disp} A_{S,D} B_{S,D}) B_C^T + (C_{M,D}^{disp} A_{M,D} B_{M,D}))^{-1} \tag{C.2}$$

By using the relations between the output and feedthrough matrices of acceleration and displacement state-space models (see expression (2.78)), we may define the following expressions to compute the output and feedthrough matrices of the displacement coupled model.

$$[\tilde{C}_S^{disp}] = C_{S,D}^{disp} - (C_{S,D}^{disp} A_{S,D} B_{S,D}) B_C^T E_{CRd} B_C C_{S,D}^{disp}$$

$$[\tilde{C}_M^{disp}] = (C_{S,D}^{disp} A_{S,D} B_{S,D}) B_C^T E_{CRd} C_{M,D}^{disp}$$

$$[\tilde{D}_S^{disp}] = C_{S,D}^{disp} A_{S,D} B_{S,D} - (C_{S,D}^{disp} A_{S,D} B_{S,D}) B_C^T E_{CRd} B_C (C_{S,D}^{disp} A_{S,D} B_{S,D}) -$$

$$\tilde{C}^{disp} \tilde{A} \tilde{B} = 0 \tag{C.3}$$

From the relations between the acceleration and velocity output and feedthrough matrices (see, [45]), we may establish expressions to compute both output and feedthrough matrices of the velocity coupled state-space model as follows:

$$[\tilde{C}_S^{vel}] = C_{S,D}^{disp} A_{S,D} - (C_{S,D}^{disp} A_{S,D} B_{S,D}) B_C^T E_{CRd} B_C C_{S,D}^{disp} A_{S,D}$$

$$[\tilde{C}_M^{vel}] = (C_{S,D}^{disp} A_{S,D} B_{S,D}) B_C^T E_{CRd} C_{M,D}^{disp} A_{M,D} \tag{C.4}$$

$$[\tilde{D}_S^{vel}] = C_{S,D}^{disp} B_{S,D} - (C_{S,D}^{disp} A_{S,D} B_{S,D}) B_C^T E_{CRd} B_C (C_{S,D}^{disp} B_{S,D})$$

where, if the coupled state-space model obeys Newton's second law $[C_{S,D}^{disp} B_{S,D}^{disp}] = [0]$ [45],[8], hence $[\tilde{D}_S^{vel}] = [0]$.

As mentioned above, the state and input matrices of displacement, velocity and acceleration state-space models are the same and are given in expression (2.144). Nevertheless, those expressions can also be easily rewritten in terms of displacement state-space matrices.

Appendix D

LSFD matrices construction

In this section, the construction of $[\hat{A}(L, \lambda, j\omega)]$ (see expression (3.66)) will be mathematically proven. It will also be shown how this matrix must be set-up, when using LSFD with mobility or accelerance reference FRFs. Furthermore, the implementation of LSFD by assuming that both upper and lower residual matrices are null will also be presented.

Let us start by considering the following modal model composed by a single pair of complex conjugate poles and defined for a single frequency line:

$$[H_{ref}(j\omega)]_1 = \left(\frac{\{\psi_1\}\{l_1\}}{j\omega_1 - \lambda_1} + \frac{\{\psi_1\}^*\{l_1\}^*}{j\omega_1 - \lambda_1^*} \right) + \frac{[LR]}{(j\omega_1)^2} + [UR] \qquad (D.1)$$

where, $[H_{ref}(j\omega)]$ represents the displacement reference FRFs.

Let us now define $\{\psi_1\}$, $\frac{\{l_1\}}{j\omega_1 - \lambda_1}$ and $\frac{\{l_1\}^*}{j\omega_1 - \lambda_1^*}$ as hereafter.

$$\{\psi_1\} = \{a\} + \{b\}j \qquad (D.2)$$

$$\frac{\{l_1\}}{j\omega_1 - \lambda_1} = \{c\} + \{d\}j \qquad (D.3)$$

$$\frac{\{l_1\}^*}{j\omega_1 - \lambda_1^*} = \{e\} + \{f\}j \qquad (D.4)$$

By using expressions (D.2), (D.3) and (D.4), we may redefine the terms $\frac{\{\psi_1\}\{l_1\}}{j\omega_1 - \lambda_1}$ and $\frac{\{\psi_1\}^*\{l_1\}^*}{j\omega_1 - \lambda_1^*}$ as given below.

$$\frac{\{\psi_1\}\{l_1\}}{j\omega_1 - \lambda_1} = (\{a\} + \{b\}j)(\{c\} + \{d\}j) = \{a\}\{c\} + \{a\}\{d\}j + \{b\}\{c\}j - \{b\}\{d\} \quad (D.5)$$

$$\frac{\{\psi_1\}^*\{l_1\}^*}{j\omega_1 - \lambda_1^*} = (\{a\} - \{b\}j)(\{e\} + \{f\}j) = \{a\}\{e\} + \{a\}\{f\}j - \{b\}\{e\}j + \{b\}\{f\} \quad (D.6)$$

From expressions (D.1), (D.5) and (D.6), we may express $[H_{ref}(j\omega)]_1$ as follows

$$[H_{ref}(j\omega)]_1 = \{a\}\{c\} + \{a\}\{d\}j + \{b\}\{c\}j - \{b\}\{d\} + \{a\}\{e\}$$
$$+ \{a\}\{f\}j - \{b\}\{e\}j + \{b\}\{f\} + \frac{[LR]}{(j\omega_1)^2} + [UR] \tag{D.7}$$

thus, we may also write

$$\left[\hat{H}_{ref}(j\omega)\right]_1 = \begin{bmatrix} \{a\}\{c\} - \{b\}\{d\} + \{a\}\{e\} + \{b\}\{f\} + \frac{[LR]}{(j\omega_1)^2} + [UR] \\ \{a\}\{d\} + \{b\}\{c\} + \{a\}\{f\} - \{b\}\{e\} \end{bmatrix}^T \tag{D.8}$$

with,

$$\left[\hat{H}_{ref}(j\omega)\right]_1 = \begin{bmatrix} \Re([H_{ref}(j\omega)]_1) & \Im([H_{ref}(j\omega)]_1) \end{bmatrix} \tag{D.9}$$

or, by representing equation (D.8) in matrix form, we may define the expression given below.

$$\left[\hat{H}_{ref}(j\omega)\right]_1 = \begin{bmatrix} \{a\} & \{b\} & [LR] & [UR] \end{bmatrix} \begin{bmatrix} \{c\} + \{e\} & \{d\} + \{f\} \\ -\{d\} + \{f\} & \{c\} - \{e\} \\ \frac{[I]}{(j\omega_1)^2} & [0] \\ [I] & [0] \end{bmatrix} \tag{D.10}$$

By using equation (3.65), expression (D.10) can be rewritten as follows:

$$\left[\hat{H}_{ref}(j\omega)\right]_1 = \begin{bmatrix} [\Upsilon]_1 & [LR] & [UR] \end{bmatrix} \left[\hat{A}(L, \lambda, j\omega)\right]_1 \tag{D.11}$$

with,

$$[\Upsilon]_1 = \begin{bmatrix} \Re(\{\psi_1\}) & \Im(\{\psi_1\}) \end{bmatrix} \tag{D.12}$$

where, $\left[\hat{A}(L, \lambda, j\omega)\right]_1$ is given as:

$$\left[\hat{A}(L, \lambda, j\omega)\right]_1 = \begin{bmatrix} [\hat{a}_\Re(L, \lambda, j\omega)]_1 & [\hat{a}_\Im(L, \lambda, j\omega)]_1 \\ \left[\hat{b}_\Re(\omega)\right]_1 & [0] \end{bmatrix} \tag{D.13}$$

while, $[\hat{a}_\Re(L, \lambda, j\omega)]_1$, $[\hat{a}_\Im(L, \lambda, j\omega)]_1$ and $\left[\hat{b}_\Re(\omega)\right]_1$ are given hereafter.

$$[\hat{a}_\Re(L, \lambda, j\omega)]_1 = \begin{bmatrix} \Re(\frac{\{l_1\}}{j\omega_1 - \lambda_1}) + \Re(\frac{\{l_1^*\}}{j\omega_1 - \lambda_1^*}) \\ -\Im(\frac{\{l_1\}}{j\omega_1 - \lambda_1}) + \Im(\frac{\{l_1^*\}}{j\omega_1 - \lambda_1^*}) \end{bmatrix} \tag{D.14}$$

$$[\hat{a}_{\Im}(L, \lambda, j\omega)]_1 = \begin{bmatrix} \Im(\frac{\{l_1\}}{j\omega_1 - \lambda_1}) + \Im(\frac{\{l_1^*\}}{j\omega_1 - \lambda_1^*}) \\ \Re(\frac{\{l_1\}}{j\omega_1 - \lambda_1}) - \Re(\frac{\{l_1^*\}}{j\omega_1 - \lambda_1^*}) \end{bmatrix} \qquad \text{(D.15)}$$

$$\left[\hat{b}_{\Re}(\omega)\right]_1 = \begin{bmatrix} \frac{[I]}{(j\omega_1)^2} \\ [I] \end{bmatrix} \qquad \text{(D.16)}$$

Expressions (D.11) and (D.13) conclude the mathematical proof for the construction of $\left[\hat{A}(L, \lambda, j\omega)\right]$, when exploiting LSFD with displacement reference FRFs. If mobility reference FRFs are to be used, we have to rewrite expression (D.11) as follows:

$$\left[\hat{H}_{ref}^{vel}(j\omega)\right]_1 = j\omega_1 \left[\hat{H}_{ref}(j\omega)\right]_1 = \begin{bmatrix} [\Upsilon]_1 & [LR] & [UR] \end{bmatrix} \left[\hat{A}^{vel}(L, \lambda, j\omega)\right]_1 \qquad \text{(D.17)}$$

where, $\left[\hat{A}^{vel}(L, \lambda, j\omega)\right]_1$ is given below.

$$\left[\hat{A}^{vel}(L, \lambda, j\omega)\right]_1 = j\omega_1 \left[\hat{A}(L, \lambda, j\omega)\right]_1 \qquad \text{(D.18)}$$

While, in case LSFD is implemented with acceleration reference FRFs, expression (D.11) must be rewritten as follows

$$\left[\hat{H}_{ref}^{accel}(j\omega)\right]_1 = (j\omega_1)^2 \left[\hat{H}_{ref}(j\omega)\right]_1 = \begin{bmatrix} [\Upsilon]_1 & [LR] & [UR] \end{bmatrix} \left[\hat{A}^{accel}(L, \lambda, j\omega)\right]_1 \qquad \text{(D.19)}$$

where, $\left[\hat{A}^{accel}(L, \lambda, j\omega)\right]_1$ is given hereafter.

$$\left[\hat{A}^{accel}(L, \lambda, j\omega)\right]_1 = (j\omega_1)^2 \left[\hat{A}(L, \lambda, j\omega)\right]_1 \qquad \text{(D.20)}$$

If LSFD is to be used by assuming that the lower and upper residual matrices are null, we must re-establish expression (D.11) as follows:

$$\left[\hat{H}_{ref}(j\omega)\right]_1 = \left[\Upsilon\right]_1 \left[\mathring{A}(L, \lambda, j\omega)\right]_1 \qquad \text{(D.21)}$$

where, $\left[\mathring{A}(L, \lambda, j\omega)\right]_1$ is given below.

$$\left[\mathring{A}(L, \lambda, j\omega)\right]_1 = \begin{bmatrix} [\hat{a}_{\Re}(L, \lambda, j\omega)]_1 & [\hat{a}_{\Im}(L, \lambda, j\omega)]_1 \end{bmatrix} \qquad \text{(D.22)}$$

When exploiting mobility reference FRFs, expression (D.22) must be rewritten as follows:

$$\left[\hat{H}_{ref}^{vel}(j\omega)\right]_1 = \left[\Upsilon\right]_1 \left[\mathring{A}^{vel}(L, \lambda, j\omega)\right]_1 = \left[\Upsilon\right]_1 j\omega_1 \left[\mathring{A}(L, \lambda, j\omega)\right]_1 \qquad \text{(D.23)}$$

while, when using acceleration FRFs, expression (D.22) must be redefined as given

below.

$$\left[\hat{H}_{ref}^{accel}(j\omega)\right]_1 = \left[\Upsilon\right]_1 \left[\mathring{A}^{accel}(L,\lambda,j\omega)\right]_1 = \left[\Upsilon\right]_1 (j\omega_1)^2 \left[\mathring{A}(L,\lambda,j\omega)\right]_1 \qquad (D.24)$$

It is worth mentioning that, although we have used a modal model composed by a single pair of complex conjugate poles and defined for a single frequency line to mathematically demonstrate how to set-up the matrices involved in the LSFD method, the same methodology is applicable, when dealing with modal models made of an unlimited number of pairs of complex conjugate poles and defined for an unlimited number of frequency lines.

Appendix E

LSFD by applying the real mode constraint

In this section, the implementation of LSFD by applying the real mode constraint together with displacement, velocity and accelerance reference FRFs will be discussed. Moreover, it will be shown how to exploit this constrained version of LSFD by assuming that both lower and upper residual matrices are null.

Having in mind that the estimation of real modes is equivalent to model a given structure by assuming that it has a proportional damping (see, for example [70]), let us consider the following proportionally damped modal model composed by a single pair of complex conjugate poles and defined for a single frequency line (see, for example, [70]):

$$[H_{ref}(j\omega)]_1 = \left(\frac{j\{\psi_1\}\{l_1\}}{j\omega_1 - \lambda_1} + \frac{-j\{\psi_1\}\{l_1\}}{j\omega_1 - \lambda_1^*} \right) + \frac{[LR]}{(j\omega_1)^2} + [UR] \tag{E.1}$$

where, $[H_{ref}(j\omega)]$ represents the displacement reference FRFs.

Let us now define $\{\psi_1\}$, $\frac{\{l_1\}}{j\omega_1 - \lambda_1}$ and $\frac{\{l_1\}}{j\omega_1 - \lambda_1^*}$ as hereafter.

$$\{\psi_1\} = \{a\} \tag{E.2}$$

$$\frac{\{l_1\}}{j\omega_1 - \lambda_1} = \{b\} + \{c\}j \tag{E.3}$$

$$\frac{\{l_1\}}{j\omega_1 - \lambda_1^*} = \{d\} + \{e\}j \tag{E.4}$$

By using expressions (E.2), (E.3) and (E.4), we may rewrite the terms $\frac{j\{\psi_1\}\{l_1\}}{j\omega_1 - \lambda_1}$ and $\frac{-j\{\psi_1\}\{l_1\}}{j\omega_1 - \lambda_1^*}$ as given below.

$$\frac{j\{\psi_1\}\{l_1\}}{j\omega_1 - \lambda_1} = j\{a\}(\{b\} + \{c\}j) = \{a\}\{b\}j - \{a\}\{c\} \tag{E.5}$$

$$\frac{-j\{\psi_1\}\{l_1\}}{j\omega_1 - \lambda_1^*} = -j\{a\}(\{d\} + \{e\}j) = -\{a\}\{d\}j + \{a\}\{e\} \tag{E.6}$$

From expressions (E.1), (E.5) and (E.6), we may express $[H_{ref}(j\omega)]_1$ as follows

$$[H_{ref}(j\omega)]_1 = \{a\}\{b\}j - \{a\}\{c\} - \{a\}\{d\}j + \{a\}\{e\} + \frac{[LR]}{(j\omega_1)^2} + [UR] \tag{E.7}$$

thus, we may also write

$$\left[\hat{H}_{ref}(j\omega)\right]_1 = \left[-\{a\}\{c\} + \{a\}\{e\} + \frac{[LR]}{(j\omega_1)^2} + [UR] \quad \{a\}\{b\} - \{a\}\{d\}\right] \tag{E.8}$$

with,

$$\left[\hat{H}_{ref}(j\omega)\right]_1 = \left[\Re([H_{ref}(j\omega)]_1) \quad \Im([H_{ref}(j\omega)]_1)\right] \tag{E.9}$$

or, by representing equation (E.8) in matrix form, we may define the expression given below.

$$\left[\hat{H}_{ref}(j\omega)\right]_1 = \left[\{a\} \quad [LR] \quad [UR]\right]\begin{bmatrix} -\{c\} + \{e\} & \{b\} - \{d\} \\ \frac{[I]}{(j\omega_1)^2} & [0] \\ [I] & [0] \end{bmatrix} \tag{E.10}$$

Expression (E.10) can also be rewritten as follows:

$$\left[\hat{H}_{ref}(j\omega)\right]_1 = \left[\{\psi_1\} \quad [LR] \quad [UR]\right]\left[\hat{A}^{PD}(L, \lambda, j\omega)\right]_1 \tag{E.11}$$

where, $\left[\hat{A}^{PD}(L, \lambda, j\omega)\right]_1$ is given as:

$$\left[\hat{A}^{PD}(L, \lambda, j\omega)\right]_1 = \begin{bmatrix} \left[\hat{a}_\Re^{PD}(L, \lambda, j\omega)\right]_1 & \left[\hat{a}_\Im^{PD}(L, \lambda, j\omega)\right]_1 \\ \left[\hat{b}_\Re^{PD}(\omega)\right]_1 & [0] \end{bmatrix} \tag{E.12}$$

while, $\left[\hat{a}_\Re^{PD}(L, \lambda, j\omega)\right]_1$, $\left[\hat{a}_\Im^{PD}(L, \lambda, j\omega)\right]_1$ and $\left[\hat{b}_\Re^{PD}(\omega)\right]_1$ are given hereafter.

$$\left[\hat{a}_\Re^{PD}(L, \lambda, j\omega)\right]_1 = \left[-\Im(\frac{\{l_1\}}{j\omega_1 - \lambda_1}) + \Im(\frac{\{l_1\}}{j\omega_1 - \lambda_1^*})\right] \tag{E.13}$$

$$\left[\hat{a}_\Im^{PD}(L, \lambda, j\omega)\right]_1 = \left[\Re(\frac{\{l_1\}}{j\omega_1 - \lambda_1}) - \Re(\frac{\{l_1\}}{j\omega_1 - \lambda_1^*})\right] \tag{E.14}$$

$$\left[\hat{b}_\Re^{PD}(\omega)\right]_1 = \begin{bmatrix} \frac{[I]}{(j\omega_1)^2} \\ [I] \end{bmatrix} \tag{E.15}$$

By using expression (E.11), the real mode shapes, the lower and upper residual

matrices can be estimated in a linear-least squares sense as given below.

$$\left[\{\psi_1\} \quad [LR] \quad [UR] \right] = \left[\hat{H}_{ref}(j\omega) \right]_1 \left[\hat{A}^{PD}(L, \lambda, j\omega) \right]_1^\dagger \tag{E.16}$$

Expressions (E.16) concludes the presentation of LSFD by applying the real mode constraint, when exploiting displacement reference FRFs. If mobility reference FRFs are to be used, we have to rewrite expression (E.11) as follows:

$$\left[\hat{H}_{ref}^{vel}(j\omega) \right]_1 = j\omega_1 \left[\hat{H}_{ref}(j\omega) \right]_1 = \left[\{\psi_1\} \quad [LR] \quad [UR] \right] \left[\hat{A}^{PD,vel}(L, \lambda, j\omega) \right]_1 \tag{E.17}$$

where, $\left[\hat{A}^{PD,vel}(L, \lambda, j\omega) \right]_1$ is given below.

$$\left[\hat{A}^{PD,vel}(L, \lambda, j\omega) \right]_1 = j\omega_1 \left[\hat{A}^{PD}(L, \lambda, j\omega) \right]_1 \tag{E.18}$$

Whereas, if accelerance reference FRFs are used, expression (E.11) must be rewritten as follows

$$\begin{aligned} \left[\hat{H}_{ref}^{accel}(j\omega) \right]_1 &= (j\omega_1)^2 \left[\hat{H}_{ref}(j\omega) \right]_1 \\ &= \left[\{\psi_1\} \quad [LR] \quad [UR] \right] \left[\hat{A}^{PD,accel}(L, \lambda, j\omega) \right]_1 \end{aligned} \tag{E.19}$$

where, $\left[\hat{A}^{PD,accel}(L, \lambda, j\omega) \right]_1$ is given hereafter.

$$\left[\hat{A}^{PD,accel}(L, \lambda, j\omega) \right]_1 = (j\omega_1)^2 \left[\hat{A}^{PD}(L, \lambda, j\omega) \right]_1 \tag{E.20}$$

If this constrained version of LSFD is to be used by assuming that the lower and upper residual matrices are null, we must re-establish expression (E.11) as follows:

$$\left[\hat{H}_{ref}(j\omega) \right]_1 = \{\psi_1\} \left[\mathring{A}^{PD}(L, \lambda, j\omega) \right]_1 \tag{E.21}$$

where, $\left[\mathring{A}^{PD}(L, \lambda, j\omega) \right]_1$ is given below.

$$\left[\mathring{A}^{PD}(L, \lambda, j\omega) \right]_1 = \left[\left[\hat{a}_{\Re}^{PD}(L, \lambda, j\omega) \right]_1 \quad \left[\hat{a}_{\Im}^{PD}(L, \lambda, j\omega) \right]_1 \right] \tag{E.22}$$

When exploiting mobility reference FRFs, expression (E.22) must be rewritten as follows:

$$\left[\hat{H}_{ref}^{vel}(j\omega) \right]_1 = \{\psi_1\} \left[\mathring{A}^{PD,vel}(L, \lambda, j\omega) \right]_1 = \{\psi_1\} \, j\omega_1 \left[\mathring{A}^{PD}(L, \lambda, j\omega) \right]_1 \tag{E.23}$$

whereas, when using accelerance FRFs, expression (E.22) must be redefined as given below.

$$\left[\hat{H}_{ref}^{accel}(j\omega)\right]_1 = \{\psi_1\}\left[\mathring{A}^{PD,accel}(L,\lambda,j\omega)\right]_1 = \{\psi_1\}(j\omega_1)^2\left[\mathring{A}^{PD}(L,\lambda,j\omega)\right]_1 \quad \text{(E.24)}$$

It is worth mentioning that, even though we have used a modal model composed by a single pair of complex conjugate poles and defined for a single frequency line to present LSFD by applying the real mode constraint, this approach continues to be valid, when dealing with modal models made of an unlimited number of pairs of complex conjugate poles and defined for an unlimited number of frequency lines.

Appendix F

Suitability of the proposed RCMs to impose Newton's second law

Here, it will be mathematically proven that the RCMs proposed in section 3.3 are, indeed, suitable to impose Newton's second law on displacement state-space models. Let us start by assuming that we aim at imposing Newton's second law on a complete displacement state-space model computed by following the procedures presented in section 3.2. Thus, to be suitable to impose Newton's second law, the proposed RCMs must ensure that $[C_{full}^{INL,disp}][B_{full}^{INL}] = [0]$ and that the contribution of $[C_{ib}^{disp}][B_{ib}]$ is properly included in the correspondent complete velocity state-space model. To demonstrate that the proposed set of RCMs fulfil the first requirement, we must define $[C_{full}^{INL,disp}][B_{full}^{INL}]$ (see expression (3.47)) by remembering that $[C_{full}^{disp}][B_{full}] = [C_{ib}^{disp}][B_{ib}]$ (as argued in section 3.3) as follows.

$$[C_{full}^{INL,disp}][B_{full}^{INL}] = [C_{ib}^{disp}][B_{ib}] + [C_{CB}^{disp}][B_{CB}] \tag{F.1}$$

Further assuming that the state-space model to be forced to respect Newton's second law is of SISO type and by exploiting equations (3.42), (3.38), (3.39) and (3.40), we may define $[A_{CB}]$, $[B_{CB}]$ and $[C_{CB}^{vel}]$ as:

$$[A_{CB}] = \begin{bmatrix} -\xi_{CB}\omega_{CB} + j\omega_{CB}\sqrt{1-\xi_{CB}^2} & \\ & -\xi_{CB}\omega_{CB} - j\omega_{CB}\sqrt{1-\xi_{CB}^2} \end{bmatrix} \tag{F.2}$$

$$[B_{CB}] = \begin{bmatrix} -\frac{j}{2}\sqrt{\sigma_{CB}}W_{CB}^T \\ \frac{j}{2}\sqrt{\sigma_{CB}}W_{CB}^T \end{bmatrix} \tag{F.3}$$

$$[C_{CB}^{vel}] = \begin{bmatrix} \frac{\omega_{CB}}{\sqrt{1-\xi_{CB}^2}}\sqrt{\sigma_{CB}}P_{CB} & \frac{\omega_{CB}}{\sqrt{1-\xi_{CB}^2}}\sqrt{\sigma_{CB}}P_{CB} \end{bmatrix}. \tag{F.4}$$

By using expressions (F.2), (F.3), (F.4) and (3.45), it is evident that $[C_{CB}^{disp}]$ must be computed as hereafter.

$$[C_{CB}^{disp}] = [C_{CB}^{vel}][A_{CB}]^{-1} = \left[\begin{array}{c} \frac{\omega_{CB}\sqrt{\sigma_{CB}}P_{CB}}{\sqrt{1-\xi_{CB}^2}\left(-\xi_{CB}\omega_{CB}+j\omega_{CB}\sqrt{1-\xi_{CB}^2}\right)} \\ \frac{\omega_{CB}\sqrt{\sigma_{CB}}P_{CB}}{\sqrt{1-\xi_{CB}^2}\left(-\xi_{CB}\omega_{CB}-j\omega_{CB}\sqrt{1-\xi_{CB}^2}\right)} \end{array} \right]^T \qquad \text{(F.5)}$$

From equations (F.3) and (F.5) and after making some mathematical manipulations, we may define the following expression to compute $[C_{CB}^{disp}][B_{CB}]$.

$$[C_{CB}^{disp}][B_{CB}] = - \left[P_{CB}\sigma_{CB}V_{CB}^T \right] \qquad \text{(F.6)}$$

By exploiting expressions (3.37) and (F.6), equation (F.1) can be rewritten as given below.

$$[C_{full}^{INL,disp}][B_{full}^{INL}] = [P_{CB}\sigma_{CB}V_{CB}^T] - [P_{CB}\sigma_{CB}V_{CB}^T] = [0] \qquad \text{(F.7)}$$

Expression (F.7) proves that the proposed set of RCMs forces $[C_{full}^{INL,disp}][B_{full}^{INL}]$ to be a null matrix. To prove that these RCMs are also capable of including the contribution of $[C_{ib}^{disp}][B_{ib}]$ on the correspondent complete velocity state-space model, let us compute the FRFs of the velocity model given in expression (3.41) as given below.

$$[H_{CB}^{vel}(j\omega)] = [C_{CB}^{vel}](j\omega[I] - [A_{CB}])^{-1}[B_{CB}] + [C_{CB}^{disp}][B_{CB}] \qquad \text{(F.8)}$$

By using expressions (F.2), (F.3), (F.4) , (3.37) and (F.6) and after performing some mathematical manipulations, equation (F.8) can be redefined as hereafter.

$$[H_{CB}^{vel}(j\omega)] = \frac{\omega_{CB}^2[C_{ib}^{disp}][B_{ib}]}{-\omega^2 + 2j\omega\xi_{CB}\omega_{CB} + \omega_{CB}^2} - [C_{ib}^{disp}][B_{ib}] \qquad \text{(F.9)}$$

The right-hand side of expression (F.9) is composed by two different terms. The first has the role of including the contribution of $[C_{ib}^{disp}][B_{ib}]$ into the complete velocity state-space model, whereas the second ensures that $[C_{full}^{INL,disp}][B_{full}^{INL}] = [0]$ is always verified. Hence, the RCMs will be more accurate as the value of the first term is closer to $[C_{ib}^{disp}][B_{ib}]$. This will happen as the value selected for the natural frequencies of the RCMs increases and as the value selected for their damping ratios decreases. Thereby, we may claim that by properly selecting the value for the natural frequencies and damping ratios of the proposed set of RCMs (see section 3.3.2), we can use these RCMs to correctly force displacement state-space models to obey Newton's second law.

It is worth mentioning that the mathematical proofs here performed continue to be valid for MIMO state-space models.

Appendix G

Minimum-Variance Unbiased estimator

In this section, the Minimum-Variance Unbiased (MVU) estimator developed in [126] will be, briefly, presented. This approach enables the estimation of the inputs and of the states of a given system, provided that the state-space model of the system is known and that a set of response measurements of the system are available (for details, see [126],[180]). To initialize this algorithm, the user needs to provide an estimate of the initial state vector (i.e. $x_{[0|-1]}$) and its error covariance matrix $P_{x[0|-1]}$. In addition, the user must also know the covariance matrices associated with the process noise and with the measurement noise (see [126]). Assuming that the state-space matrices are known, time-varying and that have been previously discretized, we may present all steps to implement the MVU estimator as follows:

Input estimation:

$$
\begin{aligned}
\tilde{R}_k &= C_k P_{x[k|k-1]} C_k^T + R \\
M_k &= (D_k^T \tilde{R}_k^{-1} D_k)^{-1} D_k^T \tilde{R}_k^{-1} \\
u_{[k|k]} &= M_k(y_k - C_k x_{[k|k-1]}) \\
P_{p[k|k]} &= (D_k^T \tilde{R}_k^{-1} D_k)^{-1}
\end{aligned}
\tag{G.1}
$$

Measurement update:

$$
\begin{aligned}
K_k &= P_{x[k|k-1]} C_k^T \tilde{R}_k^{-1} \\
x_{[k|k]} &= x_{[k|k-1]} + K_k(y_k - C_k x_{[k|k-1]} - D_k u_{[k|k]}) \\
P_{x[k|k]} &= P_{x[k|k-1]} - K_k(\tilde{R}_k - D_k P_{p[k|k]} D_k^T) K_k^T \\
P_{xp[k|k]} &= P_{px[k|k]}^T = -K_k D_k P_{p[k|k]}
\end{aligned}
\tag{G.2}
$$

Time update:

$$x_{[k+1|k]} = A_k x_{[k|k]} + B_k u_{[k|k]}$$

$$[P_{x[k+1|k]}] = \begin{bmatrix} A_k & B_k \end{bmatrix} \begin{bmatrix} P_{x[k|k]} & P_{xp[k|k]} \\ P_{px[k|k]} & P_{p[k|k]} \end{bmatrix} \begin{bmatrix} A_k^T \\ B_k^T \end{bmatrix} + Q \qquad \text{(G.3)}$$

where, superscript k denotes the time sample under analysis, u_k is the estimated input vector at the kth time instant, Q is the covariance matrix associated with the process noise, R is the covariance matrix associated with the measurement noise and y_k is the measured output vector at the kth time instant. Subscript $[k|k-1]$ denotes the estimation of a given variable at time instant k given the measured output sequence $y_{\delta_{k-1}}$ with $\delta_{k-1} = 0, 1, 2, .., k-1$, while subscripts $[k+1|k]$ and $[k|k]$ represent the estimation of a given variable at time instants $k+1$ and k, respectively, given the measured output sequence y_{δ_k} with $\delta_k = 0, 1, 2, .., k$.

List of publications

Peer-reviewed journal publications

- R.S.O. Dias, M. Martarelli, and P. Chiariotti. On the computation of stable coupled state-space models for dynamic substructuring applications. *Mechanical Systems and Signal Processing*, 205:110807, 2023. doi:`https://doi.org/10.1016/j.ymssp.2023.110807`.

- R.S.O. Dias, M. Martarelli, and P. Chiariotti. Including connecting elements into the lagrange multiplier state-space substructuring formulation. *Journal of Sound and Vibration*, 546:117445, 2023. doi:`https://doi.org/10.1016/j.jsv.2022.117445`.

- R.S.O. Dias, M. Martarelli, and P. Chiariotti. On the use of lagrange multiplier state-space substructuring in dynamic substructuring analysis. *Mechanical Systems and Signal Processing*, 180:109419, 2022. doi:`https://doi.org/10.1016/j.ymssp.2022.109419`.

Conference proceedings publications

- R.S.O. Dias, M. Martarelli, and P. Chiariotti. On the prediction of the time-varying behavior of dynamic systems by interpolating state-space models. Journal of Physics: Conference Series, (submitted for publication).

- R.S.O. Dias, M. Martarelli, and P. Chiariotti. In-Situ Component-Based TPA for Time-Variant Dynamic Systems: A State-Space Formulation. In Matthew Allen, Walter D'Ambrogio, and Dan Roettgen, editors, *Dynamic Substructures, Volume 4*, pages 73–87, Cham, 2024. Springer Nature Switzerland.

- R.S.O. Dias, M. Martarelli, and P. Chiariotti. State-space domain virtual point transformation for state-space identification in dynamic substructuring. In *Proceedings of ISMA 2022 - International Conference on Noise and Vibration Engineering and USD 2022 - International Conference on Uncertainty in Structural Dynamics*, pages 1627–1638, Leuven, Belgium, 2022.

- R.S.O. Dias, M. Martarelli, and P. Chiariotti. Lagrange Multiplier State-Space Substructuring. *Journal of Physics: Conference Series*, 2041(1):012016, 2021. doi:`10.1088/1742-6596/2041/1/012016`.

Curriculum vitae

Rafael da Silva Oliveira Dias
30th November 1997, Porto, Portugal
rafaelsilvaoliveiradias@gmail.com

Professional Experience

January 2021 - December 2023
Marie Skłodowska-Curie fellow in ECO-DRIVE Project
Polytechnic University of Marche, Ancona, Italy

July 2023 - September 2023
Visiting researcher
BMW Group, Munich, Germany

August 2022 - November 2022
Visiting researcher
Siemens Industry Software NV, Leuven, Belgium

February 2020 - August 2020
Master's thesis student
Siemens Industry Software NV, Leuven, Belgium

Education

January 2021 - present
Doctorate in Industrial Engineering - curriculum in Mechanical Engineering
Polytechnic University of Marche, Ancona, Italy

September 2015 - July 2020
Master's degree in Mechanical Engineering
University of Porto, Porto, Portugal